Dissertations, Theses, and Masters Projects   Theses, Dissertations, & Master Projects

2014

Development of a Large-Scale Storm Surge and High-Resolution Sub-Grid Inundation Model for Coastal Flooding Applications: A Case Study during Hurricane Sandy

Jon Derek Loftis
VIMS, jdloftis@vims.edu

Follow this and additional works at: https://scholarworks.wm.edu/etd

Part of the Earth Sciences Commons, Geographic Information Sciences Commons, and the Oceanography Commons

Development of a Large-Scale Storm Surge and High-Resolution Sub-Grid Inundation Model

for Coastal Flooding Applications: A Case Study During Hurricane Sandy

_____

A Dissertation

Presented to

The Faculty of the School of Marine Science

The College of William and Mary in Virginia

In Partial Fulfillment

of the Requirements for the Degree of

Doctor of Philosophy

_____

by

Jon Derek Loftis

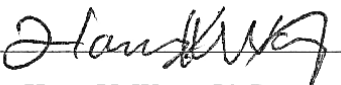2014

APPROVAL SHEET
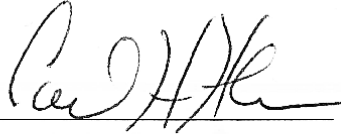
This dissertation is submitted in partial fulfillment of

the requirements for the degree of
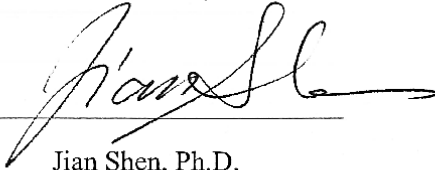
Doctor of Philosophy

_____

Jon Derek Loftis

Approved, by the Committee, April 2014
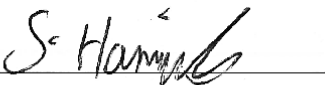
Harry V. Wang, Ph.D.
Committee Chairman/Advisor

Carl H. Hershner, Ph.D.

Jian Shen, Ph.D.

David R. Forrest, Ph.D.

Stuart E. Hamilton, Ph.D.
Center for Geospatial Analysis; College of W&M

i

TABLE OF CONTENTS

ACKNOWLEDGEMENTS

Of those who have been immensely helpful during the preparation of this dissertation, I would like to give special recognition to my advisor, Dr. Harry V. Wang, whose support and guidance throughout the course of this research effort has been invaluable to me. Harry has instilled in me an austere appreciation for precise science, as he guided me through the field of physical oceanography and estuarine coastal modeling.

I would also like to express my deepest gratitude to my dissertation committee members, Dr. Jian Shen, Dr. David Forrest, Dr. Carl Hershner, and Dr. Stu Hamilton, who have generously offered valuable remarks and constructive feedback at various stages of this dissertation effort. I also would like to thank Dr. Jim Perry, who graciously served as the official moderator for my qualifying exam and dissertation defense.

Furthermore, I would like to thank my current and former VIMS research colleagues, Senior Research Scientist Mac Sisson, Dr. Yi-Cheng Teng, Mr. Zhengui Wang, and Mr. Zhuo Liu for their help and encouragement during this study. Successful completion of this dissertation would not have been possible without the encouragement and support of the VIMS Three-Dimensional Estuarine Coastal Modeling Group.

Finally, I would like to give special thanks to my supporting wife, Rebekah, for her understanding and encouragement, and my parents and grandparents for their support and correspondence throughout this research endeavor.

LIST OF TABLES

LIST OF FIGURES

ABSTRACT

Coastal inundation initiated via storm surge by hurricanes and nor'easters along the U.S. East Coast is a substantial threat to residential properties, community infrastructure, and human life. During and after the storm, compounding with heavy precipitation and upland drainage, inundation can be caused by the combination of storm surge and river-induced inland flooding in various locations throughout the coastal plain. Thus, coastal inundation can be expanded from the open coast upstream into the tributaries of the New York Bay including the Hudson and East River systems. Given the cross-disciplinary nature of the dynamics (encompassing hydraulics, oceanography, and hydrology), and the complexity of the atmospheric forcing, a numerical model is the optimal approach for a comprehensive study of the hydrodynamics of coastal inundation.

This study will utilize the large-scale parallel SELFE model to simulate the storm surge and inundation caused by 2012 Hurricane Sandy utilizing different forecast wind and pressure fields. The large-scale numerical model made use of multiple inputs for atmospheric forcing and spatially covered a large domain area to account for large-scale oceanographic processes and output accurate model simulation of water levels. In a simultaneous effort, a street-level sub-grid inundation model coupled with Lidar-derived topography (UnTRIM^2) was employed to simulate localized flooding events in the New York Harbor.

Sub-grid modeling is a novel method by which water level elevations are efficiently calculated on a coarse computational grid, with discretized bathymetric depths and topographic heights stored on a sub-grid nested within each base grid cell, capable of addressing local friction parameters without resorting to solve the full set of equations. Sub-grid technology essentially allows velocity to be rationally and efficiently determined at the sub-grid level. This salient feature enables coastal flooding to be addressed in a single cross-scale model from the ocean to the upstream river channel without overly refining the grid resolution. To this end, high-resolution Digital Elevation Models (DEMs) were developed utilizing GIS from Lidar-derived topography for incorporation into a sub-grid model, for research into the plethora of practical research applications related to urban inundation in New York City.

SELFE large-scale storm tide simulations were successfully conducted for 2012 Hurricane Sandy using both the North American Regional Reanalysis (NARR), and the Regional Atmospheric Modeling System (RAMS) atmospheric hindcast model results as atmospheric inputs. Overall statistics using the 24km resolution NARR inputs observed an average R^2 value of 0.8994, a relative error of 11.77%, and a root-mean-squared error of 32.69cm for 10 NOAA observation stations. The 4km RAMS inputs performed noticeably better at all 10 stations with aggregate statistics yielding an average R^2 value of 0.9402, a relative error of 4.08%, and a root-mean-squared error of 19.22 cm. Since the RAMS atmospheric inputs possessed a higher spatial and temporal resolution than the NARR inputs for air pressure and wind speed, it was concluded that generally superior storm tide predictions could be expected from utilizing more reliable or better resolution atmospheric forecast products.

UnTRIM^2 results were obtained via sub-grid simulation of 2012 Hurricane Sandy in the New York Harbor with high-resolution topography and building heights embedded in the model sub-grid for New York City. Model performance was assessed via comparison with various verified field measurements: (1) Temporal comparison of NOAA and USGS permanent water level gauges, (2) USGS rapid deployment water level gauges, along with a spatial inundation comparison using (3) USGS-collected high water marks, (4) FEMA-collected data regarding inundated schools, (5) calculated area and distance differentials using FEMA's maximum extent of inundation map, and (6) known locations of inundated subway entrances. Temporal results verified the effectiveness of the sub-grid model's wetting and drying scheme via seven over land rapid deployment gauges installed and collected by the USGS with a mean R^2 of 0.9568, a relative error of 3.83%, and a root-mean-squared error of 18.15cm.

Spatial verification of the inundation depths predicted by the UnTRIM^2 model were addressed by comparison with 73 high water mark measurements collected by the USGS and by 80 FEMA-reported water level thicknesses at inundated schools throughout the sub-grid domain separated by state. Average statistics for the 73 USGS-recorded high water marks for New York and New Jersey were: 0.120 ± 0.085m and 0.347 ± 0.256m for root-mean-squared error $\pm$ standard deviation, respectively. The larger differences and errors reported in the point to point comparisons for New Jersey relative to New York were largely due to the lack building representation in the sub-grid DEM for the New Jersey side of the Hudson River, and was a significant indication that the representation of buildings as a physical impediment to fluid flow is critical to urban inundation modeling.

A maximum difference threshold was imposed for distance and area comparisons with FEMA's Hurricane Sandy flood map using the average distance differential rounded to 40m. This was done to minimize the impact of missing or added infrastructure such as highway overpasses along with Lidar-derived data limitations of physical impediments to fluid flow not accounted for in the model's DEM. The difference in the absolute mean distance between the maximum extent predicted by the street-level sub-grid model and the FEMA maximum inundation observation was 21.207m or $\approx$4 sub-grid pixels at 5m resolution for the entire sub-grid domain. The final area comparison resulted in an 85.17% area (49,253,687m^2) spatial match, with 7.57% area (4,376,726m^2) representing model over-prediction, and under-prediction area accounting for 7.27% (4,202,376m^2), with differences being attributed to lack of building representation in the FEMA maximum inundation map. Additionally, the implementation of the FEMA's spatial flood map data as a "bathtub" model derivative product of USGS interpolated high water marks and elevation data without regard for strong water current velocities or estuarine circulation can also account for regions with significant discrepancies.

Keywords: Storm Surge, Inundation, Sub-Grid, New York City, New York Harbor, Jersey City, Conveyance Approach, Unstructured Grids, UnTRIM, SELFE, Lidar, Lidar-Derived Topography

Development of a Large-Scale Storm Surge and High-Resolution Sub-Grid Inundation Model

for Coastal Flooding Applications: A Case Study During Hurricane Sandy

CHAPTER 1: Introduction

1.1   Literature Review

A storm surge is an aperiodically anomalous rise of sea level accompanied by a

tropical or extratropical storm system, wherein surge height is the distinction between the

observed sea level and the forecasted water level (NWS, 2009). Several distinct processes

can potentially alter the water level in tidal regions; the pressure effect, the wind effect,

the Coriolis Effect, the wave effect, and the rainfall effect (Harris, 1963). Coastal

inundation initiated via storm surge along the U.S. East Coast is a substantial threat to

residential properties, community infrastructure, and human life. Furthermore, prolonged

inundation from heavy precipitation and upland drainage during and after a storm has

passed can significantly increase coastal flood damage. There are additional implications

for inundated coastal habitats, as a major flood event can dramatically alter the regular

function of an ecosystem. In order to mitigate loss of human life and damage to coastal

properties, several numerical models have been developed to provide an early warning

system for storm surge and inundation events in various coastal study areas (Blumberg

and Mellor, 1987; Flather et al., 1991; Leuttich et al., 1992; Jelesnianski et al., 1992;

Westerink et al., 1994; Zhang et al., 2008; Casulli and Stelling, 2011; Arumala, 2012).

The storm surge model currently employed in forecast and hindcast efforts by the

U.S. government is the Seas, Lakes, and Overland Surge from Hurricane (SLOSH)

model. SLOSH was developed by the National Oceanic and Atmospheric Administration

(NOAA) (Jelesnianski et al., 1992), and effectively separates the U.S. East and Gulf

Coasts into 30+ overlapping basins with polar, elliptical, or hyperbolic shapes to produce

grids for modeling overland flooding (Glahn et al., 2009). Furthermore, for a structured

grid model like SLOSH to provide adequate coverage over a large domain area and

maintain fine-resolution near the coast without sacrificing computational efficiency, a

polar, elliptical, or hyperbolic grid with gradually spatially varying cell size is typically

utilized to represent an expansive model domain with some limitations (Zhang, K. et al.,

2008). This permits the model grid to cover a sizable basin extending from inland areas

potentially inundated via storm surge events, to the deeper waters of the open ocean

hundreds of kilometers from the shore. Due to geometric shape limitations of structured

grid cells, structured grid models typically prove to be inadequate in their representation

of complex shoreline geometry and deep shipping channels present in major waterways

(especially in the Chesapeake Bay). Likewise, the intransigent size limitations associated

with structured grids usually hampers their capability to cover a satisfactorily large

enough model domain to account for the remote wind effect (Blain et al., 1994; Shen and

Gong, 2009).

The Advanced Circulation (ADCIRC) model is a second-generation storm surge

model that makes use of a continuous Galerkin finite element numerical scheme, and a

generalized wave continuity equation to provide a dampened solution free of noise

(Westerink et al., 1994). ADCIRC uses an unstructured grid to resolve complex shoreline

geometry and accurately represent the bathymetry of shallow water, and currently uses a

large domain grid complete with an offshore boundary at approximately 1800 km from

the Chesapeake Bay entrance at 60°W longitude. This large domain grid has been utilized

by ADCIRC, the Finite Volume Community Ocean Model (FVCOM), and the Semi-

Implicit Eulerian-Lagrangian Finite Element model (SELFE) as part of the Southeastern

Universities Research Association coastal inundation modeling initiative as a testbed for modeling success (Luettich, 2011). This grid covers the entire the U.S. Atlantic Coast and Gulf of Mexico to surmount some of the shortcomings of most structured grid models like the Regional Ocean Modeling System (ROMS) and SLOSH. With this perceived advantage over structured grid models, ADCIRC has helped established successes for unstructured grid models on varying topics relevant in the field of physical oceanography, ranging from large-scale tide and storm surge modeling to inundation simulation (Blain et al., 1994; Westerink et al., 1994; Shen and Gong, 2009).

This study will make use of a robust semi-implicit finite difference/finite volume model for three dimensional flows, UnTRIM^2 (Unstructured Tidal Residual Intertidal Mudflat Model, Version 2). UnTRIM^2 has been formulated and proven on unstructured orthogonal grids (Casulli and Zanolli, 1998, 2002, 2005; Casulli, 1999; Casulli and Walters, 2000), and in recent years, the model has been shown to tremendously improve its formulation to inherently account for infinitesimally detailed sub-grid elevation features without substantially increasing computational effort. These advancements in UnTRIM^2 make it ideal for modeling inundation, which involves virtual representation of water flooding beyond complex geometric shorelines with many unique spatial features that can be greatly enhanced with improved resolution without the detriment of increased computing time (Casulli and Stelling, 2011).

Modeling in the mid-Atlantic Bight has been successfully performed previously with the serial version of SELFE (Cho, 2009). To expand upon this success, this study will make use of the MPI parallel version 3.1 of SELFE to capitalize on the additional computing power provided to process a large domain cast on a spherical coordinate

system. These features being of paramount importance for a large-scale super-regional model, the entire model domain covers the U.S. Atlantic coastline from 23°N to 47°N (Figure 1.1). This expansive curvilinear large domain grid covers from the Florida Keys to Nova Scotia out into the Atlantic Ocean to 62°W, and increases the likelihood of properly modeling the effects of an approaching tropical storm system.

Cho's (2009) dissertation focused upon 2003 Hurricane Isabel and 1999 Hurricane Floyd and baroclinic responses in the Chesapeake Bay as a result of these two tropical storm systems. Recently, 2011 Hurricane Irene followed a path similar to 1999 Hurricane Floyd across the Chesapeake Bay from the Southwest to Northeast across the Virginia Eastern Shore with congruent strength and intensity (Masters, 2011). The similarities in the two storm systems are scientifically important, as 2011 Hurricane Irene did substantially more flood damage than did 1999 Hurricane Floyd, making 2011 Hurricane Irene important for study within the scope of a large-scale storm surge model (Rugaber and Wagner, 2011; Walsh, 2011).

Recently, there has been a renewed interest for improving accuracy and reliability of storm surge and inundation models. This is attributed primarily to the severe damage left in the wake of 2012 Hurricane Sandy on the U.S. East Coast. In the dissertation by Teng (2012), considerable focus was placed on the incorporation of a Wind Wave Model into the 3-D hydrodynamic model, SELFE, to accurately model the forerunner of 2008 Hurricane Ike in the Gulf of Mexico. Additional focus on storm surge in scientific studies is also due in part to the potential increase in the strength and frequency of hurricanes associated with sea level rise concomitant with global climate change. This effort will provide physical oceanographers, government decision makers, and the general public

4

alike, with a better understanding of physical processes while advancing the operational

capabilities for improving real-time prediction systems (Blain et al., 1994; Wang et al.,

2005; Bernier and Thompson, 2006; Li et al., 2006; Kohut et al., 2006; Shen et al., 2006;

Gong et al., 2007, 2009; Shen, 2009; Cho, 2009; Xu et al., 2010).
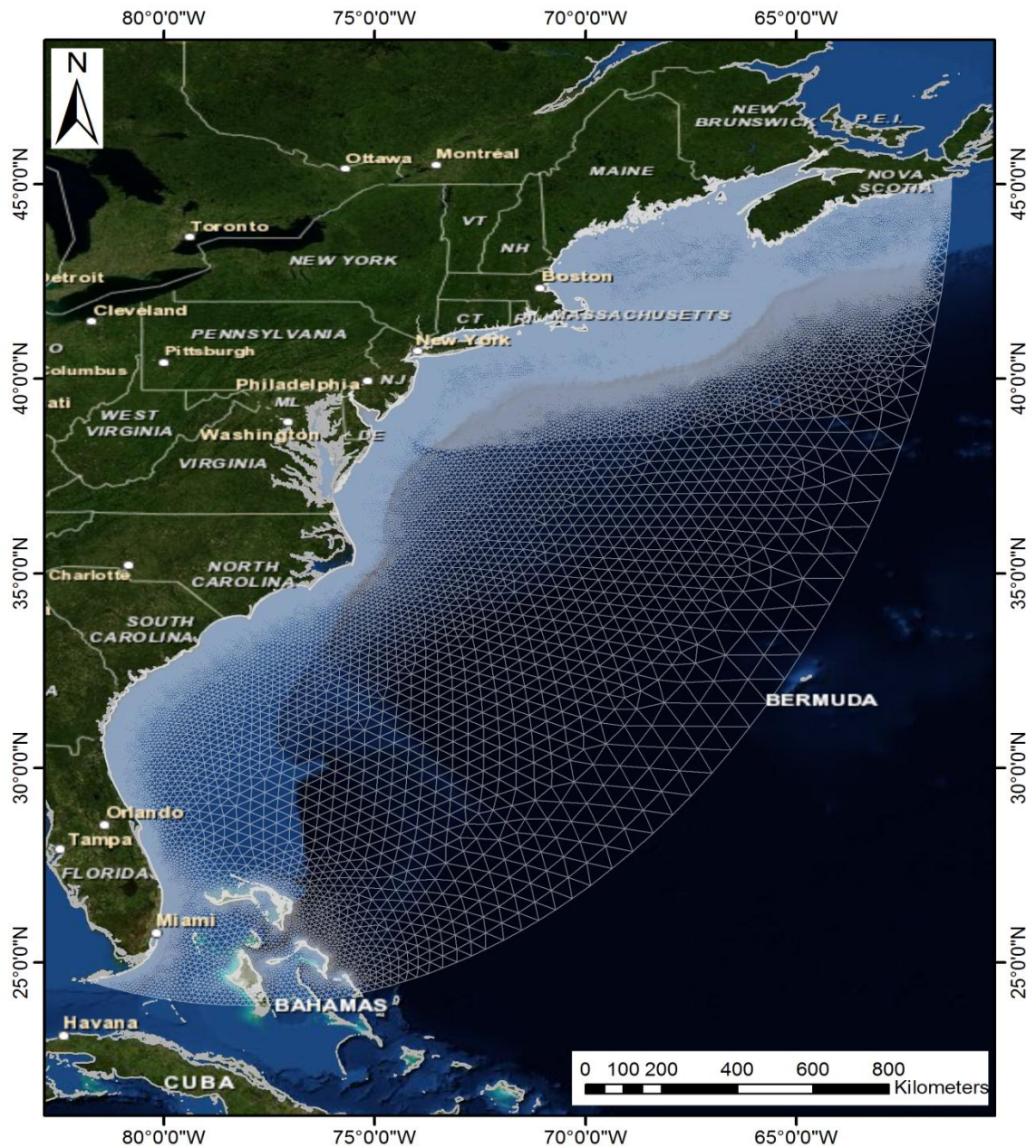
Figure 1.1. Large-scale storm tide model grid stretching from the Florida Keys to Nova
Scotia including detailed bathymetry in the New York Harbor and adjacent river systems.

Not only is there uncertainty associated with climatic regime changes in the foreseeable future, there is considerable uncertainty in forecasting wind and pressure fields used to force storm surge models. Temporally, increasing length of a forecast period likewise raises the uncertainty associated with the predicted wind for that time span. Spatially, all coastal regions heavily influenced by a passing storm surge must be covered in the model grid. Conceivably, the large-scale model grid shown in Figure 1.1 with detailed bathymetry in the New York Harbor and Long Island Sound could be used to model 2012 Hurricane Sandy. The grid envelops the U.S. East Coast from 23°N to 42°N including high-resolution topography for select areas of interest prone to inundation, and detailed bathymetry in the Hudson and East Rivers, the Long Island Sound, New York Bay, and Raritan Bay.

A successful method for improving the accuracy and reliability of storm surge inundation models has been to augment the resolution of the model domain using Light Detection And Ranging (LiDAR or Lidar). This technology is a quick and effective method to collect topographic data accurate to within a couple of centimeters in vertical resolution to populate a Digital Elevation Model (DEM) (Cobby et al., 2001). The use of Lidar data to prepare a high-resolution DEM to interpolate onto a model grid is of paramount importance in the interest of increasing model resolution for improved accuracy and reliability of hydrodynamic model results. The use of Lidar in unstructured model grids has already seen some successes in modeling inundation with close to 30m resolution using the Eulerian-Lagrangian CIRCulation (ELCIRC) model, the predecessor to the SELFE model (Shen, 2009; Gao, 2011). In the thesis by Shen (2009), ELCIRC was used to research the induced wave effect in association with 2006 Hurricane Ernesto.

Gao's thesis (2011) utilized a similar unstructured ELCIRC model grid with incorporated Lidar topography in the Hampton Roads region of Virginia in the central U.S. East Coast, to investigate the important roles played by the remote wind versus local wind effects on water level fluctuations in relation to efficient operational forecast modeling during Nor'easter Nor'Ida in November 2009. It was demonstrated in this study that Ekman transport is a key mechanism affecting the magnitude of storm surge inside the Chesapeake Bay during a long duration of continuous wind forcing (Gao, 2011). Taking this process a step further, inundation modeling using Lidar data could be further improved using a sub-grid modeling technique for improved resolution down to 5m grid resolution with nominal cost to computation time. Thus, the sub-grid modeling method using Lidar data is potentially ideal for improving real-time prediction in finite regions.

When water from Hurricane Sandy's storm surge floods into New York City, it will encounter complicated and unique developed land surfaces characterized by a wide range of features ranging from waterfront berms, streets, railroads, parks, highways, subway stations, bridges, to a variety building types. High-resolution hydrodynamic models can be used as a tool to evaluate the impact of these local features into the prediction of maximum storm surge extents in an ultra-urban environment. Even with ample computing resources available today, it is still insufficient to model all complex topographic features at the individual building scale or at street-level resolution. Recent research demonstrates that, provided Lidar data of topographic heights and sufficient bathymetric water depths, both of which can be collected with very high resolution, it has been recognized that the availability of detailed bathymetric data within a coarse grid model can be used to further improve model accuracy (Casulli, 2009; Loftis et al., 2013).

Currently, the highest-resolution DEM freely available along the U.S. East Coast is located within the region of the New York Harbor, comprised of a 1m resolution DEM derived from Lidar data with an average point spacing of 0.5m. This study aims to improve upon previous storm surge studies by incorporating Lidar topographic data into a sub-grid model capable of 5m resolution to resolve complicated geometry neglected by grid size limitations of the previous storm surge modeling efforts. As the highest grid resolution recorded from the previously discussed modeling efforts was 1 arc sec (≈30m resolution), sub-grid scalability (down to 5m resolution) is critical for correctly modeling the maximum extent of inundation in storm surge scenarios.

Visualization of inundation results is a valuable asset in illustrating the potential devastation associated with modeled or forecasted events, and has proven to be an accurate method of both representing and assessing damages in hindcast models. Moreover, flood warnings issued by various government authorities can sometimes be confusing or misinterpreted by the general public. An accurate inundation extent map superposed on orthophotographs and satellite imagery is proposed to draw attention to key societal and economic outcomes from flooding. In the interest of successfully conveying inundation model results to both scientific audiences and the general public most effectively, a Google Earth/Maps visualization using Keyhole Markup Language (KML) will be produced.

1.2   The Impact of 2012 Hurricane Sandy

Hurricane Sandy was the second-costliest hurricane on record (after 2005 Hurricane Katrina) to make landfall in the United States. While only a Category 1 storm

on the Saffir-Simpson scale when it made landfall in Atlantic City, NJ, Hurricane Sandy was directly responsible for 73 deaths, and amounted to more than $65 billion dollars in assessed damages in the United States (NOAA NCDC, 2013; Smith and Katz, 2013). Hurricane Sandy reached peak strength on October 25th as a Category 3 storm offshore of Cuba in the Caribbean Sea. On October 28th, while it was a Category 2 hurricane east of the Atlantic shelf break, the storm measured a wind swath of 1,100 miles (1,800 km) in diameter, making it (spatially) the largest Atlantic hurricane in recorded history (Gutner, 2012). Along the path of the storm across seven countries, a total of 286 people died with total international damage estimates surpassing $68 billion dollars (Smith and Katz, 2013). Hurricane Sandy directly impacted 24 states, including all coastal states across the U.S. eastern seaboard, with the most severe damage accounted for in New Jersey and New York (NOAA Service Assessment, 2012; NOAA NCDC, 2013).

Hurricane Sandy is distinguished as a unique Atlantic tropical storm system, given that it did not track along the typical path of hurricanes back out to sea following the Gulf Stream current between the U.S. East Coast and the Atlantic Shelf break (NOAA Service Assessment, 2012). Given the presence of a formidable cold front approaching from the west across the United States mainland, it was initially forecasted that Hurricane Sandy would be pushed back out to sea by the advancing front (Blake et al., 2013). However, the front weakened as it crossed the Appalachian Mountain Range, and the far-reaching effects of Sandy's winds could be felt more than 900km from the eye of the storm (Gutner, 2012). Early on October 29th, Hurricane Sandy abruptly veered westward towards the New York/New Jersey coast resulting in the heaviest storm surge impacts in the region of the New York Harbor and New York Bight (Blake et al., 2013, Smith and

Katz, 2013). The path of Hurricane Sandy was correctly predicted by the European Centre for Medium-Range Weather Forecasts (ECMWF) on October 23rd, nearly eight days prior to making landfall in the United States on October 29th at 22:00 GMT in Atlantic City (Vergano, 2012). The ECMWF forecast came four days before to the National Weather Service and National Hurricane Center confirmation of the hurricane predicted path with their own GFS wind forecast products on Oct. 27th (NOAA NCDC, 2013).

The New York Harbor resides at the confluence of the Hudson and East River systems where they empty into the New York Bay, forming one of the largest natural harbors in the world. The New York Harbor is a historically significant region with a variety of commercial and ecological resources, with management of the Port of New York and New Jersey being shared in a cooperative effort by the two different state governments (NOAA Service Assessment, 2012).

Sandy's storm surge hit the New York Harbor on October 29th, with dual storm surges approaching from the south through the New York Bay and from the east propagating via the Long Island Sound. New York City, NY, along with Jersey City, NJ, and Hoboken, NJ, were heavily impacted by the effect of the storm surge bottlenecking up the Hudson River and East River systems, with the storm surge flooding streets, tunnels, and subway lines; effectively cutting electrical power, as sub-surface electrical infrastructure became flooded via transit tunnels throughout the city. An estimated 66 million gallons of flood waters were pumped from the city's subway channels in the weeks after the storm had passed (MTA, 2012; PBS NOVA, 2012). The storm surge had also had lasting effects on surface infrastructure due to the flood damage inflicted upon

an electrical transformer at a ConEdison power substation, still in operation during the storm. The transformer exploded, as more than 3m of water height from the East River flooded over and around the facility's 10ft. tall containment wall, leaving more than 250,000 residences in lower Manhattan Island without power for nearly a week after Sandy had passed (PBS NOVA, 2012). Damage to infrastructure during Hurricane Sandy prompted ConEdison to stop power distribution from many other high-voltage lines as a preventative measure on Tuesday, October 30th, around Brooklyn and Staten Island servicing the New York Bay area after the passage of the storm as a precaution. This action left more than 160,000 homes and businesses without electrical power in these areas of New York City, with a total of more than 6 million people without power across the Northeastern U.S. (AP, 2012; USDOE, 2012). Given the valuable infrastructure to sustain the high population density in the surrounding New York City (8,336,697 residents, 27,550/sq mi (10,640/km^2)), and Jersey City (254,441 residents, 16,736.6/sq mi (6,462.0/km^2)), the Greater New York metropolitan area Harbor is a critically important region to protect (United States Census Bureau, 2012).

The primary effort of this dissertation will be to use 2012 Hurricane Sandy as a key case study to address the challenges associated with modeling large-scale storm tide processes such as storm surge and tide interaction and their associated impacts on inundation extents. Additionally, the inclusion of new technology utilizing sub-grid modeling coupled with high-resolution Lidar-derived topography, and the inclusion of complex building infrastructure to simulate the inundation observed in the ultra-urban environment around New York City and Jersey City in the New York Harbor region will provide for a detailed local analysis for 2012 Hurricane Sandy.

1.3   Scope of Study

Numerous storm surge models have been developed and applied along the U.S. East Coast, and they vary upon grid type (structured/unstructured) or upon the numerical schemes used (implicit, semi-implicit, explicit), with examples including SLOSH, ADCIRC, FVCOM, and others noted in the literature review (Jelesnianski, et al., 1992; Westerink et al., 1994; Zhang et al., 2008). This study will use SELFE, a semi-implicit finite element model using an Eulerian-Lagrangian scheme which is not restricted by the Courant Friedrichs-Lewy stability criterion, and thus permits the use of larger model time steps and robust computations (Zhang and Baptista, 2008). The Global 2-D mode of SELFE uses a spherical coordinate system, which will be applied for the simulation of 2012 Hurricane Sandy in a large-scale simulation covering entire U.S. Eastern Seaboard using hindcast atmospheric inputs. The goal of the large-scale approach is to ensure that storm tide driven by the hurricane from the ocean is accurately simulated in the major estuaries and waterways near the coast, with model results being evaluated for accuracy by verified NOAA tidal gauge observations.

In a simultaneous effort, a highly-resolved, sub-grid inundation model (Casulli and Stelling, 2011), will make use of Lidar-derived DEMs specifically produced for the New York City metropolitan area to address the extent, timing, and depth of inundation at the street-level during Hurricane Sandy. Given the variety of densely-compacted multi-scale topographic features included in an ultra-urban setting, a coarse grid cannot be efficiently scaled to incorporate all the unique objects, features, and scales. Thus, an efficient and plausible approach is to sub-divide the various scales and dimensions of buildings and streets down to the smallest basic unit of the sub-grid cell. Resolving

multiple features at the sub-grid scale permits calculation of form drag posed by those features and skin friction as the shallow surge propagates through the city streets during a flooding event. Furthermore, by utilizing a non-linear solver and the conveyance formulation for calculating the flow resistance, it effectively improves model accuracy to the street-level scale without the high computational cost of simulation on a fully-fledged high-resolution grid.

A multi-faceted approach will be used to address spatial verification of the inundation extent predicted by the street-level inundation model. These methods will include: point-to-point comparisons to validate flood water depth, along with multiple distance comparisons between FEMA's maximum flood extent map, and modeled street-level inundation results, and separate area comparisons along the New York and New Jersey banks of the Hudson River, the East River, and the Harlem River. Additionally, a suite of observations from NOAA tide gauges and USGS overland rapid-deployment gauges will be used to validate modeled results for timing and flood heights (NOAA Tides and Currents, 2012; McCallum et al., 2013).

1.4   Research Objectives, Assumptions, and Hypotheses

The primary objective is to develop an effective storm tide and inundation numerical model for predicting coastal inundation through the simulation of storm tide using a large-scale ocean model along the U.S. East Coast, and concomitantly, the inundation extent, timing, and depth at the street-level resolution for the Greater New York City area.

Specific research objectives addressed include:

1. Developing a large-scale storm tide model to address storm tide along with broad-scale ocean processes such as Ekman transport, to ensure that storm tide driven by Hurricane Sandy from the ocean is accurately simulated in the estuaries and waterways of the mid-Atlantic Bight, where the model results can be assessed by NOAA tide gauge measurements.

2. Addressing the localized inundation in the New York Harbor region at the street-level (5m resolution) using a sub-grid model with high-resolution topography measurements derived from Lidar instrumentation to accurately represent multi-scale topographic features, such as buildings with various scales and dimensions, where timing, depth, and extent of the inundation will be validated via USGS-collected field-verified measurements.

3. Evaluating the capability of sub-grid modeling, which uses a non-linear solver and the conveyance formula to improve model accuracy down to the street-level scale without the high computational costs of simulation on a fully-fledged high-resolution grid.

4. Producing visualization products using Google Earth to illustrate flooding extents predicted by the street-level inundation model to both scientific audiences and the general public.

The assumptions presumed by this study include:

1. A two-dimensional vertically-averaged model with pressure being hydrostatic, is a good approximation for the full three-dimensional hydrodynamic equations.

2.   Wind and pressure fields obtained from prominent atmospheric model outputs are reasonably accurate as the forcing functions for driving water level hindcast.

3.   The Lidar topography data with QA/QC can be imported into the sub-grid mesh to resolve buildings and the streets in the ultra-urban environment of metropolitan New York City.

The specific research hypotheses that will be addressed in this study include:

1.   For the large scale storm tide model, the application of harmonic tidal constituents to force the water level at the open boundary condition, ≈ 1500km from the U.S. mid-Atlantic Bight, is far enough (into the ocean) that there will be minimal interference by the hurricane system.

2.   The partial wetting and drying sub-grid inundation scheme, in the present form, is sufficient to model an ultra-urban landscape containing a wide range of spatial scales, and the results can be verified upon comparison with field-verified observation data.

Specifically, the event of Hurricane Sandy provided a testbed for:

a.   Ultra-urban settings include a variety of densely-compacted multiple-scale topographic features, with various scales and dimensions including: waterfront berms, streets, railroads, parks, highways, bridges, buildings of different shapes and sizes, etc.

b.   The USGS field observation program collected and verified field observations during Hurricane Sandy using rapid-deployment gauges to record water level, and high water marks (after the storm) were surveyed and meticulously recorded. Both data sets are valuable data sets which can

serve as useful tools for validation of inundation timing and depth from

rapid-deployment water level gauges and inundation area and depth in the

forms of reported high water marks.

3. Sub-grid modeling with a non-linear solver operated under the friction-dominated

conveyance formula is a reasonable approach to the simulation of street-level

inundation.

1.5   Chapter Outline

With the scope of work, research objectives, assumptions, and hypotheses in

mind, the dissertation is divided into seven chapters. The detailed contents of each

chapter are outlined as follows:

Chapter 2: The methodology associated with the large-scale storm tide model, SELFE,

and a detailed description of the grid, atmospheric forcing, and boundary

conditions used for the 2012 Hurricane Sandy forecast effort are introduced.

Chapter 3: Tidal calibration and storm tide simulation results using atmospheric hindcast

forcing for the large-scale storm tide model, SELFE, will be presented for

2012 Hurricane Sandy.

Chapter 4: The street-level sub-grid inundation model coupled with Lidar-derived

topography in UnTRIM^2, and a detailed description of the setup of the

boundary conditions will be described. The overland friction specification,

and atmospheric forcing used for the setup of 2012 Hurricane Sandy in the

New York Harbor will also be reviewed.

Chapter 5: Description of geospatial analysis methods used for pre- and post- processing of the observations and model results including Google Earth visualizations and animations are revealed.

Chapter 6: Presentation of temporal and spatial results for the street-level sub-grid inundation model, UnTRIM^2, and sensitivity tests for 2012 Hurricane Sandy in New York City, and around the New York Harbor is covered.

Chapter 7: Discussion of large-scale (SELFE) and sub-grid (UnTRIM2) model results including suggested methods and additional results obtained by addressing specific discrepancies between model prediction data and observations. Final conclusions of the dissertation are also presented at the end the chapter.

CHAPTER 2: Large-Scale Storm Tide Model Methodology

2.1   SELFE Model Description

SELFE is the Semi-implicit Eulerian-Lagrangian Finite Element model developed by Zhang and Baptista (2008). This study will utilize the parallel SELFE model to simulate the storm surge and inundation caused by hurricanes such as 2012 Hurricane Sandy in both forecasting and hindcast efforts. The model will serve as a broad scaling-resolution storm surge model with the application of being a practical choice for use in simulating large-scale to small-scale phenomena.

2.1.1   Governing Equations

The SELFE model is governed by the 3-Dimensional shallow-water equations with the Boussinesq approximation, along with associated transport equations for salinity and temperature. The equations are solved for free surface elevation, water velocities, salinity, and temperature of the water, in a Cartesian coordinate system as specified in Zhang and Baptista's model description (2008):

$$\nabla \cdot \vec{u} + \frac{\partial w}{\partial z} = 0 \tag{2-1}$$

$$\frac{\partial \eta}{\partial t} + \nabla \cdot \int_{-h}^{\eta} \vec{u} \, dz = 0 \tag{2-2}$$

$$\frac{D\vec{u}}{Dt} = \vec{f} - g\nabla\eta + \alpha g\nabla\varphi - \frac{1}{\rho_0}\nabla P_A + \frac{\partial}{\partial z}\left(v\frac{\partial \vec{u}}{\partial z}\right) - \frac{g}{\rho_0}\int_{z}^{\eta}\nabla\rho \, d\zeta + \nabla \cdot (\mu\nabla\vec{u}) \tag{2-3}$$

$$\frac{DS}{Dt} = \frac{\partial}{\partial z}\left(\kappa \frac{\partial S}{\partial z}\right) \tag{2-4}$$

$$\frac{DT}{Dt} = \frac{\partial}{\partial z}\left(\kappa \frac{\partial T}{\partial z}\right) + \frac{\dot{Q}}{\rho_0 C_p} \tag{2-5}$$

$$\frac{\partial p}{\partial z} = -\rho_0 g \tag{2-6}$$

where:

t : time [s];

x, y, z : Cartesian coordinates [m];

$\eta(x, y, t)$: free surface elevation [m];

∇ : horizontal gradient [m^{-1}];

$\vec{u}$: Cartesian horizontal water velocity components (u, v) [m s^{-1}];

w : vertical velocity [m s^{-1}];

h(x, y) : bathymetric depth [m];

f : Coriolis parameter [s^{-1}];

g : acceleration of gravity [m s^{-2}];

φ : tidal potential [m];

α : effective Earth elasticity factor [0.69];

$\rho(x, y, t)$: water density [kg m^{-3}] ;

ρ_0 : reference water density [kg m^{-3}] ;

$P_A(x, y, t)$: atmospheric pressure at the free surface [N m^{-2}];

S : salinity of the water [PSU];

T : temperature of the water (℃);

ν : vertical eddy viscosity [m^2 s^{-1}];

μ : horizontal eddy viscosity [m^2 s^{-1}];

κ : vertical eddy diffusivity for salt and heat [m^2 s^{-1}];

$\dot{Q}$: rate of absorption of solar radiation [W m^{-1}] ;

C_P : specific heat of water [J kg^{-1} K^{-1}].

The differential equation system for Equations (2-1) to (2-5) is closed with respect

to: the hydrostatic approximation (2-6), the equation of state, describing water density as

a function of salinity and temperature, and definition of the tidal potential and the

Coriolis Effect (Zhang et al., 2004). Furthermore, the system is closed via

parameterizations for both horizontal and vertical mixing through the turbulence closure

equations, and applicable initial and boundary conditions. The numerical algorithm

utilized in SELFE is explained at length in Zhang and Baptista (2008). Central features of SELFE include a differential equation system that the model solves using a semi-implicit methodology complete with finite-element and finite-volume schemes. SELFE uses the Eulerian-Lagrangian method to appropriately handle advection in the momentum equations. Advection terms in the transport equations are addressed using one of three different schemes including the default Eulerian-Lagrangian method described above, the total variation diminishing scheme, and the finite-volume upwind method. The horizontal grid structure is comprised of unstructured triangular grids, within which the orthogonality of the horizontal grid is not necessary (as in SELFE's predecessor, ELCIRC) since finite-element discretization is used. The vertical grid structure for SELFE permits the use of hybridized vertical coordinates including both terrain-following S-coordinate and rigid depth-specific Z-coordinate layers (Figure 2.1).

The SELFE model commences solving the barotropic pressure gradient term in the momentum equation with a semi-implicit schematization with the baroclinic pressure gradient term being solved for explicitly. Owing to the hydrostatic approximation, vertical velocity components are solved from Equation (2-1) upon ascertaining horizontal velocity components. The continuity equation discretized in the finite-element framework is solved in the weak form of a Galerkin-weighted residual statement. In the SELFE model, linear shape functions are utilized as weighted functions such that the linear shape functions used for the elevations are weighted functions wherein the two components of the horizontal velocity are solved from the momentum equation independently from one another upon determining the elevations.

Upon solving for elevation at all nodes, SELFE solves the momentum equation

(2-3) along each vertical column at the center of each element side. A semi-implicit

Galerkin finite-element method is used, with the pressure gradient and the vertical

viscosity terms being handled implicitly with all other terms treated explicitly. Once all

velocities at every element side are determined, the velocity at each node is computed by

a weighted average of all surrounding sides evaluated by proper interpolation in the

vertical. The velocity at each node is computed within each element from the three sides

using a linear shape function as an averaging technique and is kept discontinuous

between elements. This methodology encourages parasitic oscillations, so a Shapiro filter

is built into the model code as a smoothing function to suppress the static measurements

(Shapiro, 1970).

A finite-volume approach is applied to a typical prism, to solve for vertical

velocity, as depicted in Figure 2.1, because it serves as a diagnostic variable for local

volume conservation when a steep slope is present in the model grid bathymetry (Zhang

et al., 2004). In this case, vertical velocity is solved from the bottom to the surface, in

conjunction with the bottom boundary condition. The closure error between the

calculated w at the free surface and the surface kinematic boundary condition is an

indication of the local volume conservation error (Luettich et al., 2002). Since the

primitive formulation of the continuity equation is solved in the model, infinitesimal error

is associated with this closure methodology.

Recently, newer versions of SELFE (> v3.1) have a spherical coordinate option

which is based on the work by Comblen et al. (2009). Various 3-D Cartesian frames are

used to solve the equations in their original form. Since the distances are all measured in

the physical space, a very fine-resolution grid is achievable with these coordinates, and thus can be utilized to optimally simulate the entire East Coast by using this coordinate system for storm surge inundation research. Also, the new Global SELFE model has a barotropic two-dimensional mode which solves the depth-integrated barotropic shallow-water equations in spherical coordinates utilizing a finite-element solution:

$$\frac{\partial U}{\partial t} + U\frac{\partial U}{\partial x} + V\frac{\partial U}{\partial y} - fV = -g\frac{\partial}{\partial x}\left[\eta + \frac{P_A}{g\rho_0} - \alpha\varphi\right] + \frac{\tau_{SX,winds} + \tau_{SX,waves} - \tau_{bx}}{\rho_0 H} + X \quad (2\text{-}7)$$

$$\frac{\partial V}{\partial t} + U\frac{\partial V}{\partial x} + V\frac{\partial V}{\partial y} + fU = -g\frac{\partial}{\partial y}\left[\eta + \frac{P_A}{g\rho_0} - \alpha\varphi\right] + \frac{\tau_{Sy,winds} + \tau_{Sy,waves} - \tau_{by}}{\rho_0 H} + Y \quad (2\text{-}8)$$

$$\frac{\partial \eta}{\partial t} + \frac{\partial U}{\partial x} + \frac{\partial V}{\partial y} = 0 \quad\quad\quad\quad\quad\quad\quad\quad (2\text{-}9)$$

where U is the depth-integrated current in the x-direction, and V is the depth-integrated current in the y-direction, $\tau_{s,winds}$ is surface stress due to winds, and $\tau_{s,waves}$ is surface stress due to waves, with τ_b representing bottom stress. The formulations in the 2-D version utilize the 2-D shallow water equations for momentum in the x- (Equation 2-7) and y- (Equation 2-8) directions, and continuity (Equation 2-9). The X and Y represent additional terms not included, such as horizontal viscosity and wave-induced radiation stress. These terms can be treated explicitly, thus do not influence the stability condition.
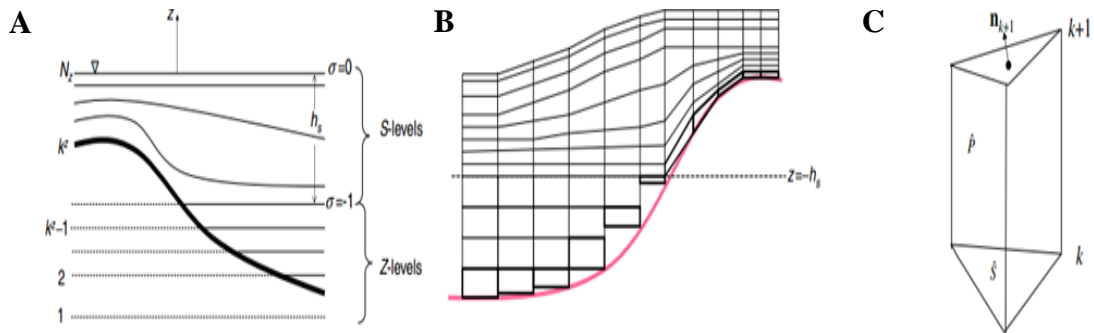
Figure 2.1. SELFE model vertical grid and hybridized coordinate system. A schematic representation of the terrain-following S-levels on top of the Z-levels in a vertical field of view (A). A vertical transect view of the discretized domain with bottom cells in red (B), and the basic computational unit of a triangular model grid element as a prism with uneven/non-parallel top and bottom faces (C) (adapted from Zhang and Baptista, 2008).

2.1.2 Initial and Boundary Conditions

The governing equations necessitate the initial condition (t=0) to be specified for unknown variables in each SELFE model simulation. These include initial values for water level elevation, water velocities, salinity, and temperature at a minimum. For example, initial conditions for salinity and temperature are parameterized via 'salt.ic' and 'temp.ic' initial condition input files with values at each grid node, respectively. Inclusion of additional parameters and/or tracers requires providing initial conditions for each parameter and/or tracer added. Given that only the barotropic mode of SELFE is utilized for storm tide simulations, the standard initial condition applied is the zero motion condition with a model "spin up" beginning at a date sufficiently prior to the storm event to account for tidal resonance in regions with relatively complex shoreline geometry. Tidal elevation is specified at the open boundary utilizing the 'bctides.in' input file by means of a hyperbolic ramp-up function called in the model's 'param.in' input file when tidal potential forcing is specified to be used. A hyperbolic tangent function is utilized to simulate the tide given a series of harmonic constituents with a typical duration of 1 to 2 days for a large domain such as those used in modeling 2012 Hurricane Sandy.

2.1.2.1 Surface Boundary Conditions

At the water's surface, the SELFE model imposes a balance between the internal Reynolds stress and the applied shear stress:

$$\rho_0 K_{mv}\left(\frac{\partial u}{\partial z}, \frac{\partial v}{\partial z}\right) = (\tau_{Wx}, \tau_{Wy}) \qquad \text{at} \qquad z = H_R + \eta \qquad (2\text{-}10)$$

Essential to modeling storm surge, the surface wind stress over the water at the air-sea interface may be approached using a variety of methods including parameterization of spatially and/or temporally varying surface shear stresses. A frequently used method for addressing the surface boundary condition involves utilizing a bulk aerodynamic algorithm to account for ocean surface fluxes under variable conditions of stability of the atmosphere (Zeng et al., 1998). This method is used when forcing SELFE using outputs obtained from an atmospheric model to drive storm surge simulations (Equation 2-11). Surface stresses may be evaluated utilizing:

$$(\tau_{Wx}, \tau_{Wy}) = \rho_a C_{Ds} \left| \overrightarrow{W} \right| (W_x, W_y) \tag{2-11}$$

where:
ρ_a : air density [kg/m^3];
C_{Ds} : wind drag coefficient;
$\overrightarrow{W}(x, y, t)$: wind velocity at 10m above the sea surface [m/s];
$\left| \overrightarrow{W} \right|$: wind magnitude with components of east-west (W_x) and north-south W_y [m/s];

The drag coefficient C_{Ds} is often empirically ascertained via curve-fitting utilizing observation measurements. In Garratt's (1977) formula (Equation 2-12), the equation related to C_{Ds} is in the form of a linear function:

$$C_d = (a + b \left| \overrightarrow{W} \right|) \times 10^{-3} \tag{2-12}$$

where a=0.75 and b=0.067 has been empirically ascertained from research literature as standard values for a and b are proposed by various preeminent authors in recent history as atmospheric and hydrodynamic research advances (Equation 2-13). The upper limit of the formula, 33 m/s, is based upon NOAA's Hurricane Research Division's notorious

study regarding direct measurements of overwater hurricane wind speeds in Powell et al. (2003). The lower limit of Equation (2-13), 4 m/s, is based upon the research performed by Donelan et al. (2004). For moderately strong winds, this formulation allows the degree of the momentum being transferred through the air-sea interface to increase with proportional growth in wind speed. C_{Ds} remains constant outside this range:

$$
\left.
\begin{array}{lll}
C_{Ds} = 0.75 \times 10^{-3} & \text{if} & |\overrightarrow{W}| \leq 4m/s \\[2ex]
C_{Ds} = \left(0.75 + 0.067|\overrightarrow{W}|\right) \times 10^{-3} & \text{if} & 4m/s \leq |\overrightarrow{W}| \leq 33m/s \\[2ex]
C_{Ds} = 2.64 \times 10^{-3} & \text{if} & 33m/s \leq |\overrightarrow{W}|
\end{array}
\right\}
\qquad (2\text{-}13)
$$

2.1.2.2 Bottom Boundary Conditions

The 3-Dimensional SELFE model is bounded at the bathymetric bottom surface. At the bottom boundary, the model maintains the balance between the frictional stress and internal Reynolds stress via Equation (2-14):

$$
(\tau_{bx}, \tau_{by}) = \rho_0 K_{mv} \left(\frac{\partial u}{\partial z}, \frac{\partial v}{\partial z} \right)_b \qquad \text{at} \qquad z = H_R - h \qquad (2\text{-}14)
$$

with bottom stress, (τ_{bx}, τ_{by}), defined as:

$$
(\tau_{bx}, \tau_{by}) = \rho_a C_{Db} \sqrt{u_b^2 + v_b^2} \, (u_b, v_b) \qquad (2\text{-}15)
$$

where u_b, v_b are bottom velocities, and C_{Db} is the bottom drag coefficient. Precise parameterization of C_{Db} is necessary to effectively simulate bottom frictional stress, and site-specific calibration is often warranted, given that C_{Db} is not uniform everywhere, but

instead is spatially and temporally varying. In lieu of using a constant C_{Db} throughout the entire domain, the logarithmic law is applied to calculate a spatially varying C_{Db} by specifying the local bottom roughness at each node (Equation 2-15). Spatially varying bottom friction requires a fine-scale discretization of the bottom bathymetry in the model grid to obtain reasonable approximations for C_{Db}. The 2-dimensional Global SELFE model driven via forecasted winds and tides uses a 2-D depth-averaged long wave formulation in conjunction with Manning's formula to calculate C_{Db}:

$$C_{Db} = \frac{gn^2}{h^{1/3}}$$
(2-16)

where *n* is the Manning coefficient. Manning's coefficient, *n*, is an empirically derived coefficient, with a higher values representing increased friction. It has a standard value of 0.025 (Henderson, 1966), and depends upon many factors including sinuosity and bottom roughness to yield typical values for C_{Db} between 0.001 and 0.003 (Equation 2-16). In estuaries, *n* varies greatly along the distance of the river, and can even vary within a small area of the river channel exhibiting different stages of flow. Due to the modeling emphasis in this study and the lack of direct site or field surveys, noted values for *n* other than the standard 0.025 are used from prominent papers studying the areas of interest to this study, and adjusted for optimal simulation results during tidal calibration.

2.1.2.3 Open Boundary Conditions

Tidal simulations using the SELFE model can make use of the traditional Dirichlet boundary condition at the grid's open boundary, for which water level elevation may be specified to a time series of specified known values. This open boundary forcing

methodology is less useful in large scale simulations, and conversely more convenient in estuaries where there are ample tidal recording stations available for comparison and minimal external influences to the movement of water volume.

For the large domain SELFE grid, values for the water elevation specified at the open boundary were calculated utilizing eight dominant tidal constituents obtained from Le Provost's FES95.2 global model (Le Provost et al., 1998). Upon completion of tidal simulation over the large domain, time-series water level data may be extracted at model grid nodes near stations of interest for comparison.

2.1.3 Coriolis Force and Parameters for Tidal Potential

The Earth's rotation is represented through the Coriolis acceleration in the momentum equations (Equations 2-3, 2-7, and 2-8). In 3-Dimensional space, the Coriolis acceleration, a_c, is:

$$a_c = \begin{pmatrix} 2\Omega v \sin \Phi - 2\Omega \omega \cos \Phi \\ -2\Omega u \sin \Phi \\ 2\Omega u \cos \Phi \end{pmatrix} \tag{2-17}$$

When vertical velocity, w, is much smaller than the horizontal components u and v, the expression in Equation (2-17) may be approximated using the Coriolis parameter (f):

$$a_c = \begin{pmatrix} fv \\ -fu \\ 0 \end{pmatrix} \tag{2-18}$$

where $f = 2\Omega \, sin(\Phi)$, and Ω is the angular rotation velocity of the Earth ($7.29 \times 10^{-5} rads^{-1}$). It is also assumed that the vertical Coriolis acceleration can be neglected with respect to

27

gravity *g* in Equation (2-18). To minimize coordinate translation inconsistencies when addressing Cartesian coordinates in a large domain, SELFE uses a β-plane approximation for *f* :

$$f = f_C + \beta_C \, (y - y_C) \tag{2-19}$$

where subscript $_C$ represents the mid-latitude of the domain and β is the local derivative of the Coriolis factor *f* in (2-19). The Global SELFE model makes use of the *f*-plane approximation is used when the horizontal domain is not > 100km, instead of the β-plane approximation, where the Coriolis parameter *f* may be presumed to be constant at its value at the center of the grid (for the grids simulating 2012 Hurricane Sandy, this is ≈ 37° N Latitude). To simulate large-scale tide, the tidal potential function defined in Reid (1990) given in the next Chapter (Equation 3-1), was utilized as a harmonic forcing for the SELFE model.

2.1.4 Wetting and Drying Scheme

A robust representation of wetting and drying is maintained in the SELFE model via inclusion of formulations similar to those in the standard UnTRIM model noted in Chapter 4 (Casulli and Cheng, 1992; Casulli and Zanolli, 1998). This robust approach to wetting and drying algorithms allows for accurate inundation simulation near the coastline with careful consideration for recording of indices. Once all unknowns have been calculated at the model time step n+1, free-surface indices are updated with newly-computed elevation values. Elements are considered dry if $h + \eta < 0.0001$, if not, then grid elements are considered to be wet. In the Global SELFE 2-D mode, when only one vertical layer is specified, this methodology is reduced to a semi-implicit scheme for

solving the corresponding two-dimensional shallow water equations (Equations 2-7 to 2-9). The resulting 2-D or 3-D wetting and drying algorithms in SELFE have been demonstrated to be efficient and accurate, while conserving mass. As such, the SELFE model, building upon the successes of its predecessors, has been documented to appropriately simulate flooding and drying in tidal flats and near-shore areas (Cho, 2009; Gong et al., 2009; Cho et al., 2012; Teng, 2012).

2.2   Model Setup and Configuration for 2012 Hurricane Sandy

2.2.1   Model Domain and Grid

The modeling effort for 2012 Hurricane Sandy will utilize a large-scale model grid developed for this study. The grid includes detailed resolution along the U.S. Northeast Atlantic coastline around where Hurricane Sandy made landfall. The new grid resolves many oceanic canyons and trenches along the Atlantic shelf break and includes detailed bathymetry of the Long Island Sound and Hudson River along with numerous embayments along the Northeastern U.S. coastline. The grid is comprised of 207,996 nodes and 392,013 elements, and extends from the U.S. shoreline out into the Atlantic Ocean to 62°W longitude (Figure 1.1). The grid features a curvilinear open boundary stretching from Key West, Florida, to Nova Scotia in Canada. This larger domain extent is necessary to completely include the large size of Hurricane Sandy's substantial wind influence of 1800km, given its unique track (Gutner, 2012). Spatial resolution scales from ≈50km at the grid's open boundary at Bermuda to ≈50m in the Hudson River near New York Harbor. The model grid includes 134 open boundary nodes where elevation forcing can be applied from the open ocean to capture tropical events making landfall

along the U.S. East Coast, the Caribbean Islands, and coastal Canada adjacent to the Atlantic Ocean. Additionally, there are four boundary nodes with a prescribed flux boundary condition near Wappingers Falls, 115.9km (72.0 miles) north of The Battery at the southern tip of Manhattan Island.

The grid makes use of a spatially varying Manning coefficient for bottom friction with a value of n=0.010 in the Hudson River, New York Harbor, and Raritan Bay, with n=0.045 along the relatively narrow and shallow channels of the East and Hudson Rivers, with a standard Manning coefficient for bottom friction of n=0.025 everywhere else in the domain. In Blumberg et al., a bottom drag coefficient of C_D=0.06 was utilized in the ECOM model to account for the higher friction conditions imposed in these narrow and shallow regions within the New York Harbor region for a successful tidal calibration (1999). The SELFE model grid resolution is 2-3 cells across for some areas of the East and Harlem Rivers, accounting for an appropriate conversion of Blumberg et al.'s C_D for these areas to a Manning coefficient of n=0.045 necessary to appropriately model the phase for a successful tidal calibration and storm surge using the Global SELFE 2-D Manning formulation for bottom friction (Manning, 1891; Blumberg et al., 1999).

In the interest of faster computational speed and forecast urgency, the 2-D barotropic mode assuming vertically averaged horizontal velocities will be utilized for the Hurricane Sandy forecasting effort. Simulations for Hurricane Sandy were performed via the parallel SELFE model using 64 nodes of the total available 72 dual-processors (Dell SC1435 chipset) available on the Typhoon sub-cluster of the SciClone heterogeneous high-performance computing platform at The College of William and Mary in 2013.

2.2.2 External Forcing and DEM Development

2.2.2.1 Atmospheric Forcing

Atmospheric pressure and wind fields were collected at 32km resolution for the NOAA's North American Mesoscale (NAM) model, and 24km resolution for NOAA's North American Regional Reanalysis (NARR) model as a reanalysis of the NAM wind product with some corrections to wind speed and direction within the formulation. Both NOAA atmospheric model products have a 3-hour forecast time interval. Additionally, 4km resolution atmospheric pressure and wind fields were obtained from the proprietary Regional Atmospheric Modeling System (RAMS) from an independent firm, WeatherFlow Inc., with a 1-hour temporal resolution (Figure 2.2).

Atmospheric model data outputs were retrieved and processed into NetCDF files for use with the 'sflux' input format (part of the utility library available at: http://www. stccmop.org/CORIE/modeling/selfe/utilities.html) compatible with the SELFE model located at Concurrently, tides were generated for the 'bctides.in' input file assuming a start time of 00:00 GMT on October 27, 2012, for the NAM & NARR wind simulations and a start time of 00:00 GMT on October 24, 2012, for the RAMS model wind product simulations. Start times for tidal inputs were selected based upon the earliest corresponding atmospheric product availability from their respective data sources.
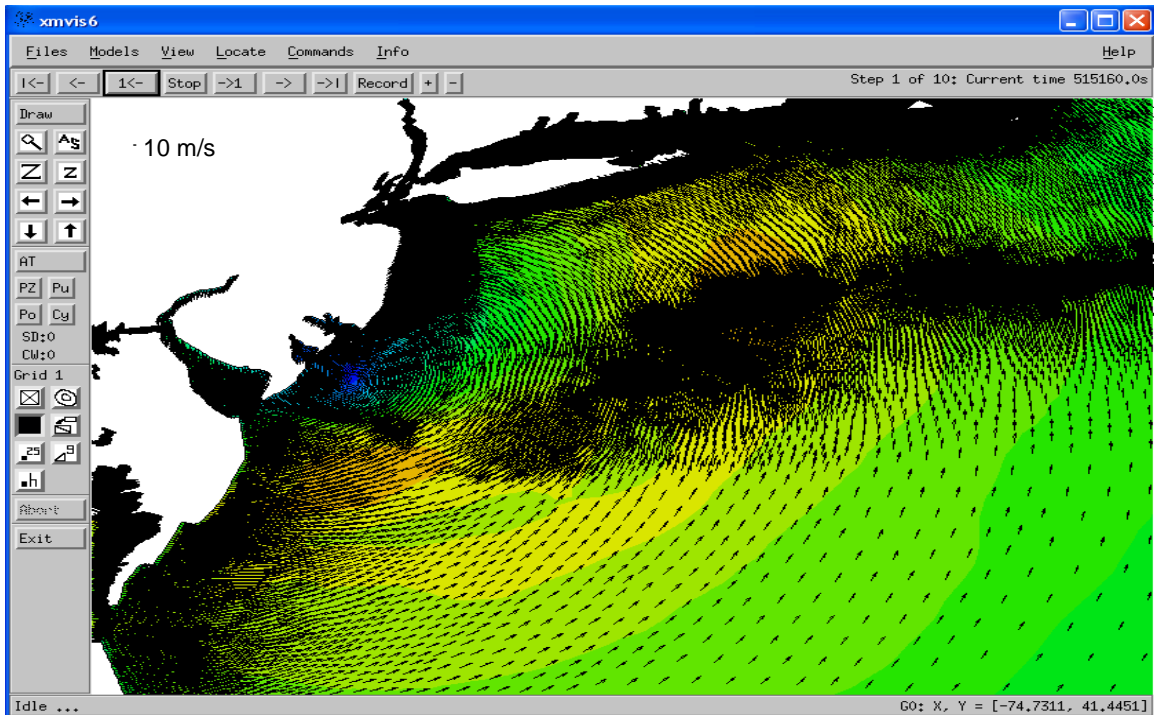
Figure 2.2. Weatherflow RAMS wind field shown in xmvis6, obtained from model output of wind velocities at grid nodes on October 29, 2012, at 23:00 GMT, with an approximate wind velocity of 25 m/s moving westward near Atlantic City, NJ.

2.2.2.2 Freshwater River Inflow

Hourly discharge data were obtained from the nearest USGS station to the Hudson River flux boundary of the grid, shown in Figure 1.1, near Wappingers Falls, adjacent to the Hudson River at Latitude 41°39'11"N, Longitude 73°52'21"W (Station #01646500). The hourly discharge data were converted from cubic feet/second to cubic meters/second and interpolated to a 5-minute time step to be prescribed as a flux boundary condition in the model input to apply to the four boundary nodes spanning the width of the Hudson River near Wappingers Falls. Discharge inputs were set to the time range of the model, from 00:00 GMT on October 17, 2012, and ending at 00:00 GMT on November 4, 2012.

2.2.2.3 Tidal Open Boundary Forcing

Tides are forced along the 134 nodes comprising the Atlantic open-ocean boundary utilizing eight dominant astronomical tidal constituents. Four semidiurnal constituents (M_2, N_2, S_2, and K_2) were used with four diurnal constituents (O_1, P_1, K_1, and Q_1) obtained via SMS 8.0 within the model control module for tidal forcing by the FES95.2 global model formulation for harmonic tides (Le Provost et al., 1998). Relevant tidal potential functions were forced within the model domain for each of the 134 boundary nodes using amplitude and phase calculated via the 'SELFE tidal utility package for the U.S. East Coast (c/o Dr. Ed Myers)'.

Periods, tidal potential constants, and Earth elasticity factors, which reduce the magnitude of the tidal potential forcing due to the Earth's tides are accounted for in the SELFE model's 'bctides.in' input file in a way which accounts for the nodal factor and equilibrium argument for boundary and interior domain forcing tidal constituents, based upon initiation time of the simulation. In the concerted forecasting effort for 2012 Hurricane Sandy, tides were generated for the 'bctides.in' input file assuming a start time of 00:00 GMT on October 27, 2012, for the NAM and NARR wind simulations and a start time of 00:00 GMT on October 24, 2012, for the RAMS model wind product simulations. Start times for tidal inputs were selected based upon corresponding wind product availability from their respective data sources.

2.2.2.4 Pre-Processing Development of DEM

Open-ocean and shelf bathymetric depths in this mesh were interpolated from NOAA's bathymetric sounding database, the Digital Nautical Charts database, and ETOPO1 1-minute gridded bathymetry world database (NOAA NGDC, 1999) (Table 2.1). Shelf contour data produced through the use of NOAA's Coastal Relief Model allowed for detailed resolution along the many shelf canyons within the Sargasso Sea in the Atlantic Northeast. Within the New York Harbor, detailed bathymetry extends beyond Yonkers, NY, up the Hudson River, throughout the New York Bay and Raritan Bay, and everywhere along the East River, Harlem River, and the Kill van Kull. Select low-elevation locations around the New York Harbor, Raritan Bay, and Atlantic City were included in the grid for the purposes of inundation using elevation DEMs retrieved from the USGS National Elevation Dataset. All SELFE grid nodes were referenced to an elevation interpolated from the DEM with the atmospheric inputs, open boundary, and flux boundary conditions specified from the previous section.

Table 2.1. Data sources and resolutions for represented topography and bathymetry for the grid used in the 2012 Hurricane Sandy modeling effort .

	Bathymetry Data	Resolution	Area
Bathymetry	NOAA Global Relief Model (ETOPO1)	1 arc min (≈1800m)	Atlantic Shelf/Ocean
	NOAA Coastal Relief Model	3 arc sec (≈90m)	Coastal Region & Chesapeake Bay
	NOAA Bathymetric Survey Data	1/3 arc sec (≈10m)	New York Harbor & Estuaries, Long Island Sound, Raritan Bay, and New York Bay
Topography	USGS National Elevation Dataset	1/3 arc sec (≈10m)	Low-elevation areas around New York Harbor, Raritan Bay, and Atlantic City

2.2.3 Observation Data Compiled during 2012 Hurricane Sandy

Verified observation data from 10 NOAA tide gauges along the Atlantic Coast including 3 within the Long Island Sound were utilized for comparison with model results for Hurricane Sandy. Binary model results were combined and post-processed utilizing the SELFE 'stations.in' input file with specified node numbers of the model grid corresponding to the location of related tide gauges. All tidal prediction and observation data were collected from their respective data sources at hourly and 6-minute intervals in meters relative to MSL from October 1, 2012, at 00:00 GMT through November 30, 2012, at 00:00 GMT for tidal calibration purposes and storm surge comparison with observation data using the statistical measures outlined in Appendix A. The peak at The Battery in the densely populated region of southern Manhattan notably reached heights greater than 3.5m (Figure 2.3). The tidal stations include: 4 Atlantic coastal stations, 3 in the Long Island Sound, and 3 around New York Bay and Raritan Bay; these stations are shown in Figure 2.4.
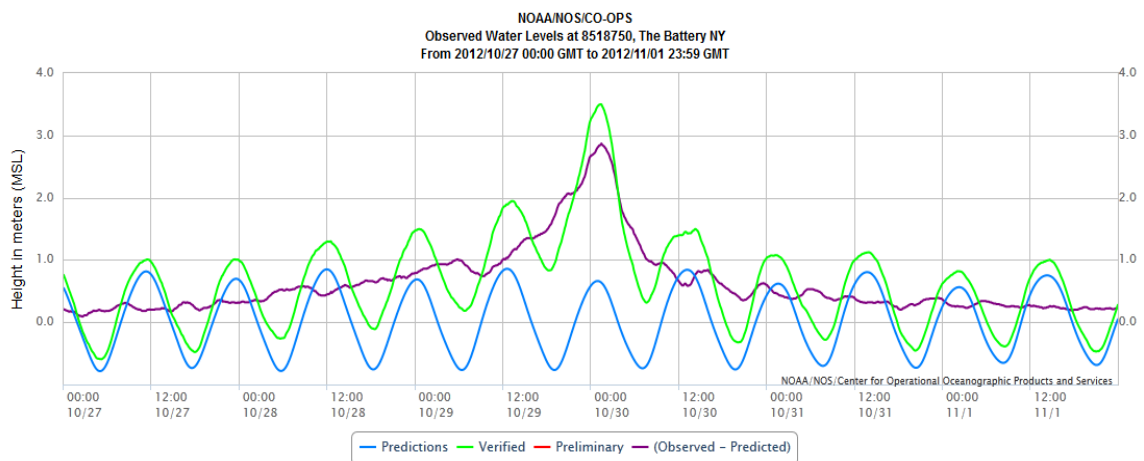
Figure 2.3. Hurricane Sandy water level observed at The Battery on the southern tip of Manhattan Island, NY, shown peaking at 3.501m (11.469ft.) at 01:24 GMT on Tuesday, October 30, 2012 (NOAA Tides and Currents, 2012).
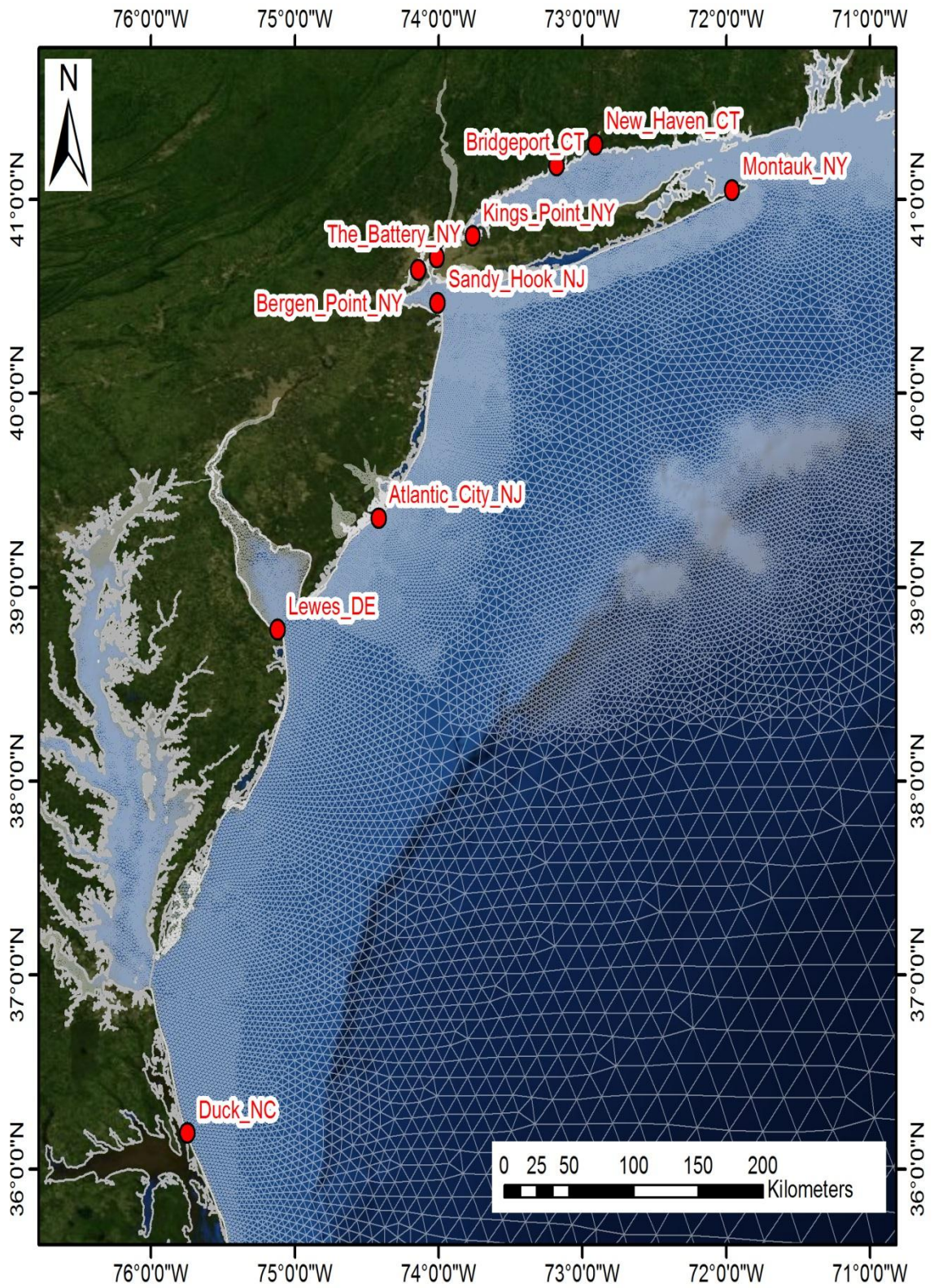
Figure 2.4. Map of U.S. Mid-Atlantic coast with SELFE model grid superposed in white with the locations of 10 NOAA water level observation stations in red.

CHAPTER 3: Large-Scale Storm Tide Model Results

3.1   Tidal Calibration and Harmonic Analysis Results

To ensure that the SELFE model properly simulated the long-period wave

propagation inside the New York Bay and Long Island Sound, a tidal calibration and

harmonic analysis was conducted. The Global SELFE 2-D model was run without

salinity and surface wind forcing, using only tidal sinusoidal motion at the curvilinear

open boundary. Eight harmonic tidal constituents were utilized along the 134 nodes at the

open boundary to force the astronomical tide in the Atlantic Ocean. Four semidiurnal

constituents (M_2, N_2, S_2, and K_2) and four diurnal constituents (O_1, P_1, K_1, and Q_1) were

obtained via SMS 8.0 via the FES95.2 global model formulation for harmonic tides

(LeProvost, et al., 1998), and were specified to calculate the water level at each element

of the open boundary based upon the following tidal formulation (Equation 3-1):

$$\eta(x, y, t) = \sum_i A_i(x, y) f_i(t_0) \cos[\sigma_i (t - t_0) + V_i(t_0) - \psi_i(x, y)] \qquad (3\text{-}1)$$

where the amplitude (of constituent i) is A_i, the frequency is σ_i, and the tidal phase is ψ_i.

The nodal factor is provided by f_i and the equilibrium argument via V_i. Between these

terms, only the tidal frequency is an absolute constant for a given constituent, as the

amplitudes and phases are spatially variable, yet temporally constant values. Conversely,

nodal factors and equilibrium arguments are spatially constant, but temporally variable

values, and are critically important to synchronize the SELFE model outputs with NOAA

observation data (Equation 3-1). The tidal simulation spanned 90 days and commenced

on 09/01/2012 at 00:00 GMT through 11/30/2012 at 00:00 GMT. The tidal calibration

made use of a 3-day spin up prior to the recording of numerical results via a hyperbolic tangent ramp-up function.

The standard Manning coefficient of n=0.025 was used to calculate the bottom friction for most of the areas within the domain with the following exceptions: (1) n=0.010 was used in the Hudson River, New York Harbor, and Raritan Bay, and (2) n=0.045 in the East River up to its junction with the Hudson River. These values were consistent with Blumberg et al.'s 1999 study in the New York Bight using the ECOM model. Additionally, factors which may reduce the tidal potential forcing due to the Earth's tide were also accounted for via nodal factor and equilibrium arguments in the 'bctides.in' input file. Locations of the selected NOAA tidal gauge stations used for tidal verification of the model are displayed on the map in Figure 2.4, with time series results for the month of September shown in Figures 3.1A-E and related statistics in Table 3.1.

Table 3.1. Statistical evaluation SELFE modeled tide and NOAA predicted tide for the 10 selected tide gauges.

Station	R^2	Relative Error (%)	RMS Error (cm)
Montauk, NY	0.9674	4.47	7.24
New Haven, CT	0.9915	0.61	7.44
Bridgeport, CT	0.9834	1.19	11.07
Kings Point, NY	0.9868	1.16	13.60
The Battery, NY	0.9692	1.71	9.13
Bergen Point, NY	0.9650	2.89	12.63
Sandy Hook, NJ	0.9809	1.52	9.46
Atlantic City, NJ	0.9915	1.57	8.04
Lewes, DE	0.9612	2.50	10.34
Duck, NC	0.9905	2.35	8.24
Mean Value	0.9787	2.00	9.72

Table 3.2A. Comparison of tidal amplitudes in meters relative to MSL for 4 major semidiurnal tidal constituents (top) and 4 diurnal tidal constituents (bottom) between SELFE modeled tide and NOAA predicted tide at 10 tide gauges along the U.S. East Coast.

Amplitude	M_2			S_2			N_2			K_2		
Station	Modeled	NOAA	Difference	Modeled	NOAA	Difference	Modeled	NOAA	Difference	Modeled	NOAA	Difference
Montauk, NY	0.300	0.305	-0.004	0.059	0.061	-0.002	0.072	0.072	0.001	0.015	0.003	0.012
New Haven, CT	0.913	0.907	0.006	0.118	0.155	-0.037	0.172	0.170	0.002	0.084	0.117	-0.033
Bridgeport, CT	0.938	1.006	-0.068	0.121	0.137	-0.016	0.177	0.181	-0.005	0.087	0.126	-0.039
Kings Point, NY	1.248	1.158	0.089	0.156	0.172	-0.017	0.239	0.227	0.013	0.145	0.195	-0.050
The Battery, NY	0.625	0.674	-0.049	0.058	0.087	-0.029	0.121	0.141	-0.020	0.024	0.063	-0.039
Bergen Point, NY	0.635	0.753	-0.118	0.063	0.072	-0.009	0.123	0.150	-0.027	0.024	0.071	-0.047
Sandy Hook, NJ	0.740	0.696	0.044	0.109	0.079	0.030	0.154	0.143	0.011	0.021	0.073	-0.052
Atlantic City, NJ	0.595	0.602	-0.007	0.096	0.089	0.008	0.125	0.127	-0.002	0.012	0.049	-0.037
Lewes, DE	0.608	0.624	-0.016	0.084	0.076	0.009	0.121	0.119	0.002	0.025	0.050	-0.025
Duck, NC	0.504	0.498	0.006	0.081	0.068	0.012	0.107	0.103	0.004	0.005	0.024	-0.019
Average	**0.711**	**0.722**	**-0.012**	**0.095**	**0.100**	**-0.005**	**0.141**	**0.143**	**-0.002**	**0.044**	**0.077**	**-0.033**
Std. Deviation	**-**	**-**	**0.058**	**-**	**-**	**0.020**	**-**	**-**	**0.013**	**-**	**-**	**0.019**

Amplitude (cont'd)	K_1			O_1			P_1			Q_1		
Station	Modeled	NOAA	Difference	Modeled	NOAA	Difference	Modeled	NOAA	Difference	Modeled	NOAA	Difference
Montauk, NY	0.076	0.071	0.005	0.062	0.050	0.012	0.025	0.021	0.004	0.014	0.014	0.000
New Haven, CT	0.082	0.088	-0.007	0.076	0.059	0.017	0.041	0.039	0.002	0.019	0.021	-0.002
Bridgeport, CT	0.082	0.075	0.007	0.076	0.058	0.018	0.041	0.028	0.013	0.019	0.019	0.000
Kings Point, NY	0.091	0.089	0.002	0.079	0.060	0.019	0.070	0.070	0.000	0.027	0.028	-0.002
The Battery, NY	0.084	0.106	-0.022	0.055	0.044	0.011	0.044	0.014	0.030	0.018	0.014	0.004
Bergen Point, NY	0.084	0.105	-0.020	0.055	0.045	0.010	0.040	0.010	0.029	0.017	0.014	0.003
Sandy Hook, NJ	0.095	0.105	-0.010	0.060	0.047	0.014	0.027	0.016	0.011	0.015	0.014	0.001
Atlantic City, NJ	0.092	0.112	-0.021	0.068	0.068	0.000	0.013	0.024	-0.012	0.012	0.012	0.000
Lewes, DE	0.090	0.105	-0.015	0.073	0.076	-0.003	0.011	0.029	-0.019	0.013	0.014	-0.001
Duck, NC	0.089	0.091	-0.002	0.068	0.054	0.013	0.009	0.016	-0.008	0.013	0.013	0.000
Average	**0.086**	**0.095**	**-0.008**	**0.067**	**0.056**	**0.011**	**0.032**	**0.027**	**0.005**	**0.017**	**0.016**	**0.000**
Std. Deviation	**-**	**-**	**0.011**	**-**	**-**	**0.007**	**-**	**-**	**0.016**	**-**	**-**	**0.002**

Table 3.2B. Comparison of tidal phase in degrees for 4 major semidiurnal tidal constituents (top) and 4 diurnal tidal constituents (bottom) between SELFE modeled tide and NOAA predicted tide at 10 tide gauges along the U.S. East Coast.

Phase	M_2			S_2			N_2			K_2		
Station	Modeled	NOAA	Difference	Modeled	NOAA	Difference	Modeled	NOAA	Difference	Modeled	NOAA	Difference
Montauk, NY	262.591	262.533	0.058	267.910	267.706	0.204	242.159	242.235	-0.076	275.504	276.944	-1.440
New Haven, CT	108.133	108.175	-0.041	132.947	132.455	0.492	84.876	84.998	-0.122	134.571	135.079	-0.509
Bridgeport, CT	111.331	111.430	-0.100	138.134	137.692	0.442	90.770	91.004	-0.234	138.174	138.441	-0.267
Kings Point, NY	117.665	117.640	0.025	143.411	142.563	0.848	96.051	96.095	-0.044	145.336	145.723	-0.387
The Battery, NY	19.185	19.240	-0.055	44.156	43.476	0.681	1.772	1.857	-0.085	45.972	45.897	0.074
Bergen Point, NY	21.341	21.481	-0.140	52.008	51.701	0.307	6.825	7.085	-0.260	49.708	49.683	0.025
Sandy Hook, NJ	12.214	6.013	6.201	33.169	38.876	-5.707	350.053	350.268	-0.215	32.403	33.017	-0.614
Atlantic City, NJ	361.484	361.511	-0.028	18.131	23.909	-5.778	337.185	337.327	-0.142	19.619	20.094	-0.475
Lewes, DE	31.373	31.555	-0.181	57.560	57.324	0.236	12.354	12.664	-0.310	54.101	54.074	0.027
Duck, NC	364.129	364.159	-0.030	22.474	22.184	0.290	339.118	339.276	-0.159	19.127	19.437	-0.310
Average	**140.945**	**140.374**	**0.571**	**90.990**	**91.789**	**-0.799**	**156.116**	**156.281**	**-0.165**	**91.451**	**91.839**	**-0.387**
Standard Deviation	**-**	**-**	**1.980**	**-**	**-**	**2.614**	**-**	**-**	**0.087**	**-**	**-**	**0.442**

Phase (cont'd)	K_1			O_1			P_1			Q_1		
Station	Modeled	NOAA	Difference	Modeled	NOAA	Difference	Modeled	NOAA	Difference	Modeled	NOAA	Difference
Montauk, NY	108.187	108.365	-0.178	141.470	141.967	-0.497	123.069	121.607	1.462	128.999	129.090	-0.091
New Haven, CT	194.956	195.031	-0.074	220.056	220.572	-0.516	208.057	207.142	0.915	214.304	214.604	-0.300
Bridgeport, CT	196.545	196.619	-0.073	221.156	221.683	-0.526	208.455	207.728	0.728	209.305	209.369	-0.064
Kings Point, NY	196.852	196.903	-0.051	222.407	222.921	-0.514	215.381	214.723	0.658	215.942	216.079	-0.137
The Battery, NY	184.259	184.475	-0.217	177.797	177.675	0.122	187.987	186.519	1.468	194.231	194.291	-0.060
Bergen Point, NY	187.561	187.821	-0.260	180.754	180.735	0.019	185.910	184.508	1.402	194.802	194.974	-0.172
Sandy Hook, NJ	180.294	180.542	-0.248	173.698	173.795	-0.097	184.355	182.521	1.835	186.414	186.575	-0.161
Atlantic City, NJ	187.798	188.199	-0.401	167.181	167.250	-0.069	183.185	180.381	2.803	171.829	171.956	-0.128
Lewes, DE	206.495	207.033	-0.537	189.929	190.153	-0.223	203.700	201.384	2.316	186.199	186.368	-0.169
Duck, NC	177.616	177.748	-0.131	193.877	194.230	-0.353	177.932	175.647	2.284	181.520	181.650	-0.130
Average	**182.056**	**182.273**	**-0.217**	**188.833**	**189.098**	**-0.265**	**187.803**	**186.216**	**1.587**	**188.355**	**188.496**	**-0.141**
Standard Deviation	**-**	**-**	**0.155**	**-**	**-**	**0.248**	**-**	**-**	**0.721**	**-**	**-**	**0.069**
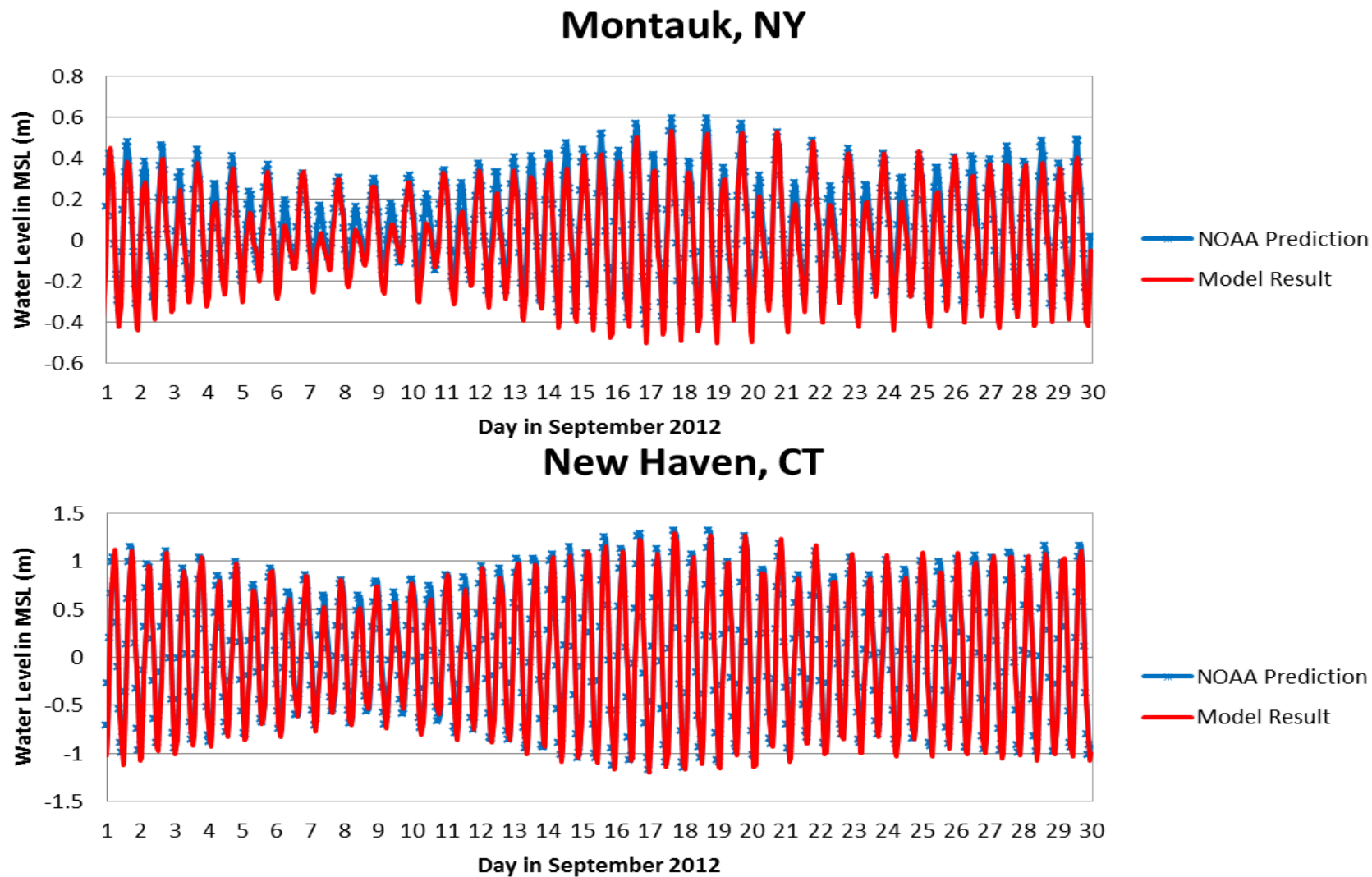
Figure 3.1A. Time series comparison of the SELFE model tidal calibration with NOAA predicted tide data during September 2012.

41
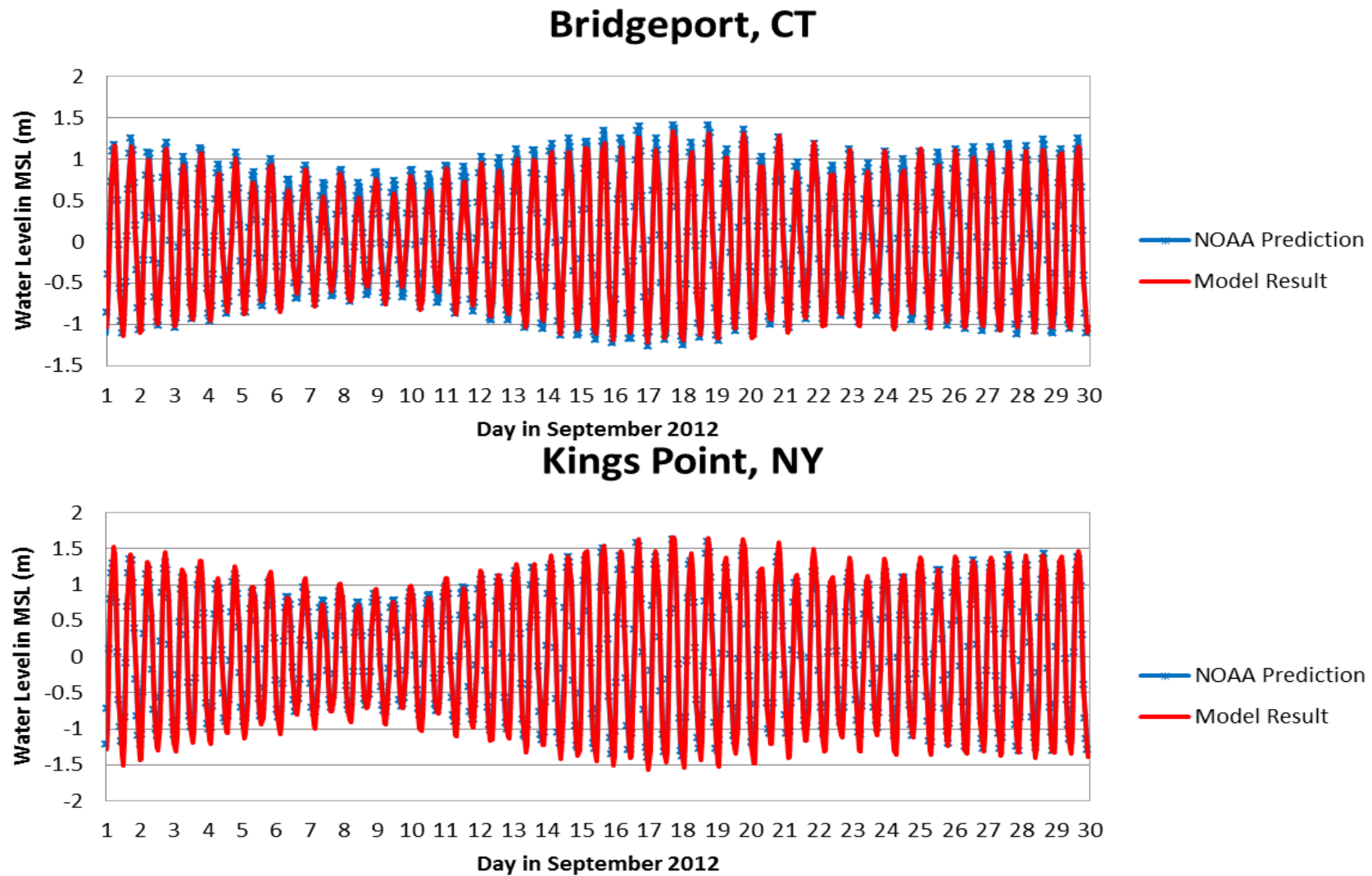
Figure 3.1B. Time series comparison of the SELFE model tidal calibration with NOAA predicted tide data during September 2012.
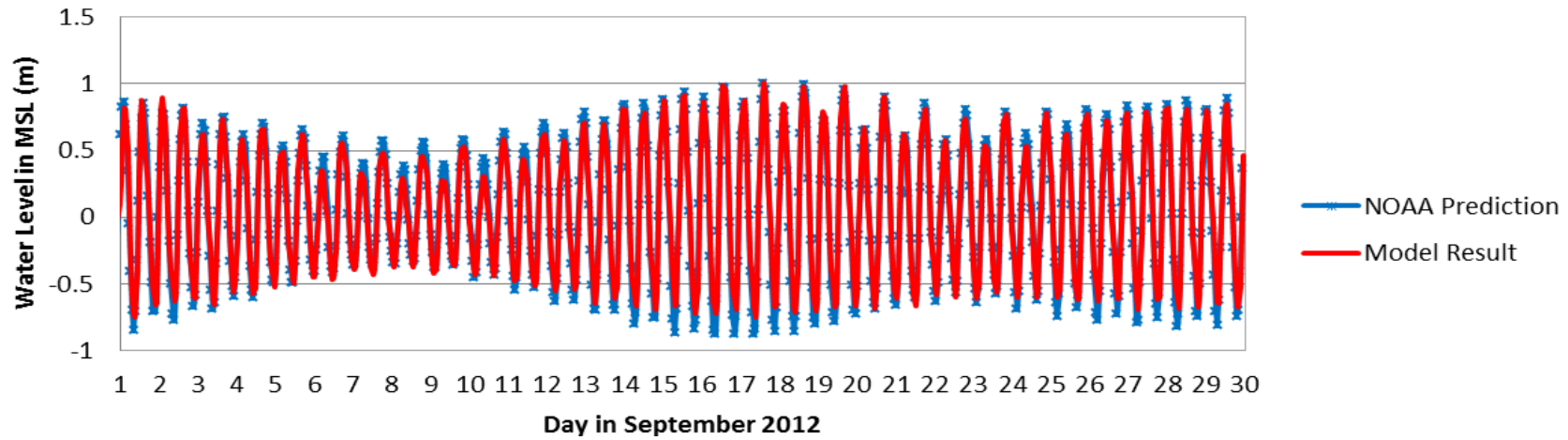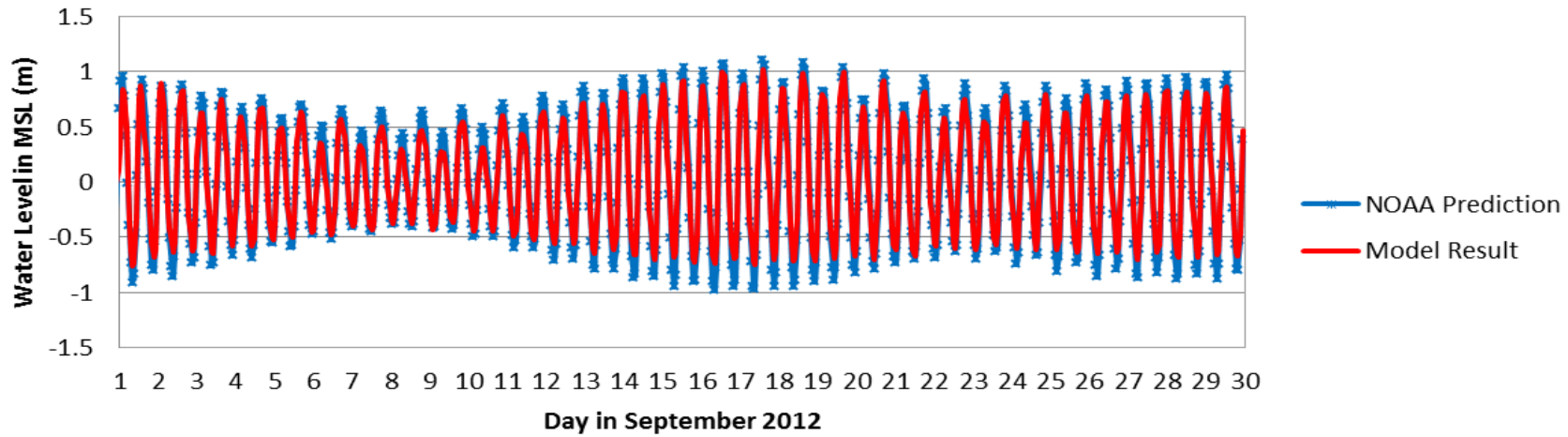
Figure 3.1C. Time series comparison of the SELFE model tidal calibration with NOAA predicted tide data during September 2012.
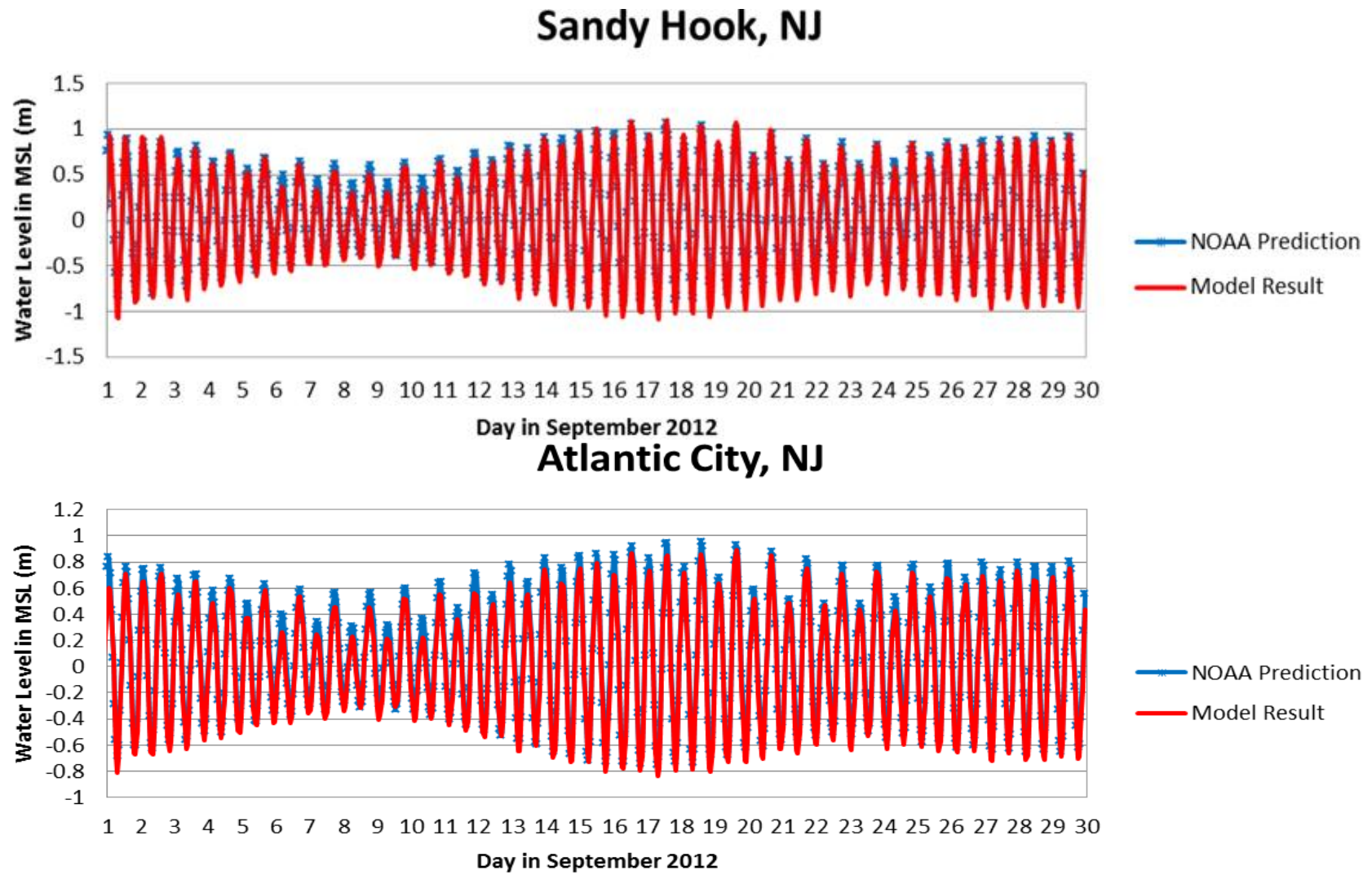
Figure 3.1D. Time series comparison of the SELFE model tidal calibration with NOAA predicted tide data during September 2012.
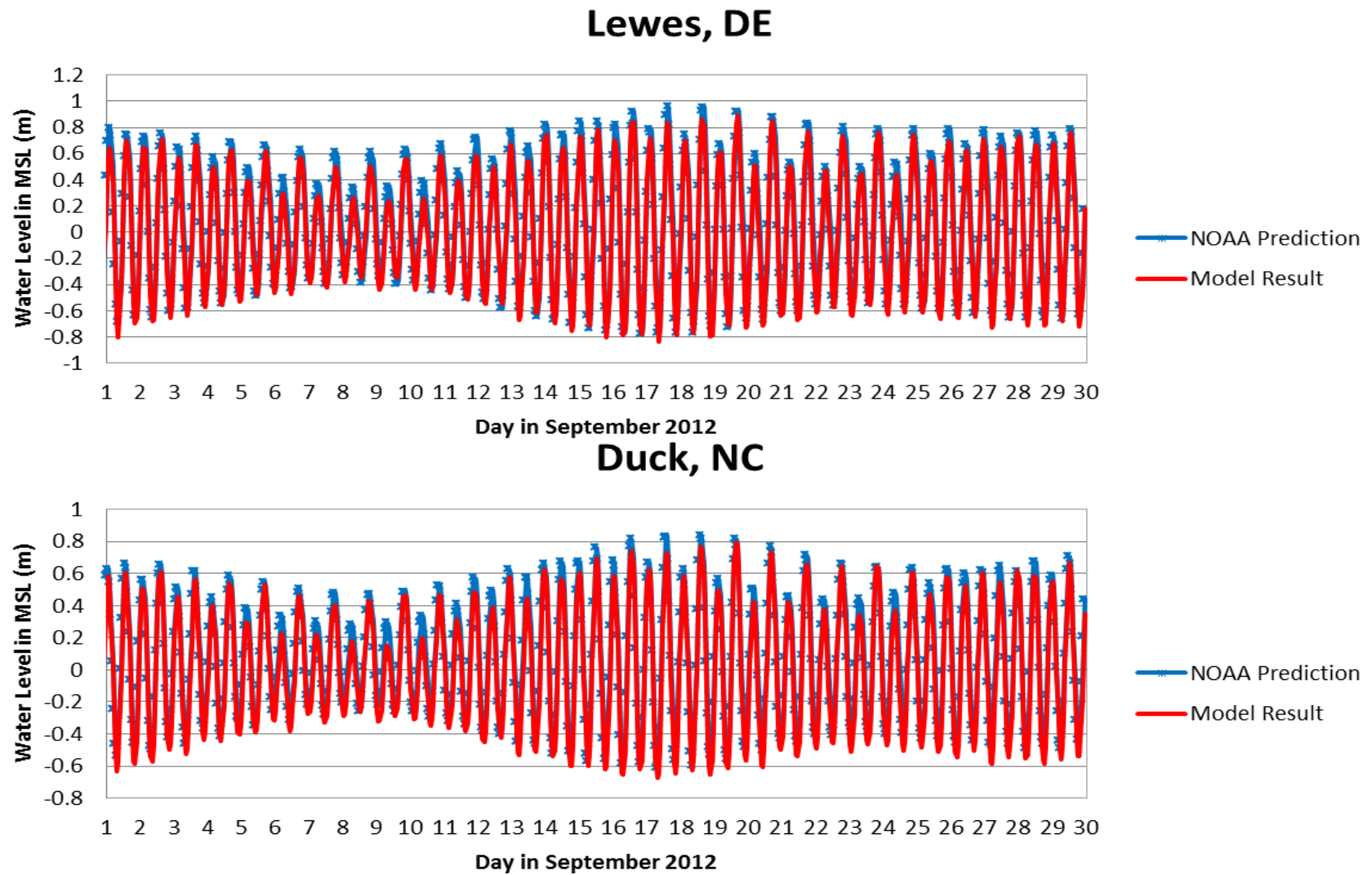
Figure 3.1E. Time series comparison of the SELFE model tidal calibration with NOAA predicted tide data during September 2012.

A harmonic analysis was conducted in MATLAB using the public domain software package 'T-Tide' (Pawlowicz et al., 2002), on tidal results from the last 90 days of hourly model outputs at 10 selected NOAA tide gauges along the U.S. East Coast near areas where Hurricane Sandy's impact was most evident. These stations were: Montauk, NY, New Haven, CT, Bridgeport, CT, Kings Point, NY, The Battery, NY, Bergen Point, NY, Sandy Hook, NJ, Atlantic City, NJ, Lewes, DE, and Duck, NC (Figure 2.4). Tidal prediction data were obtained from these NOAA gauges for the same time period for evaluation at each station, and analyzed for 4 major tidal constituents (Table 3.2). The overall statistical comparison yields excellent results upon application of the friction parameter adjustments noted in the previous paragraph, with an R^2 of 0.9787, a relative error of 2.00%, and a root-mean-squared error of 9.72cm (Table 3.2).

Data tables of tidal amplitude and tidal phase between modeled tide and NOAA observed tide for the 8 major harmonic constituents that the model is driven by at the open boundary are presented in Table 3.2A and Table 3.2B. The SELFE model accurately predicts tidal propagation along the U.S. Eastern Seaboard and embayments within the model grid with good accuracy. In the tidal amplitude comparison, the SELFE model simulates the amplitude of the dominant M_2 tidal constituent very well at all of the 10 stations with a mean difference of -0.012±0.058m (Table 3.2A). Nearly all of the 10 selected tide gauge stations showed a mean amplitude difference of less than 10% except for Bergen Point, NY (Figure 3.1C), where a 15.6% difference in M_2 tidal amplitude was observed (Table 3.2A). The principal solar diurnal constituent, S_2, had a mean difference of -0.005±0.020m between the modeled tide and NOAA observed tide. Stations positioned along the open coast provided a better comparison, while those located in

small tributaries of the Long Island Sound or in the New York Harbor were more likely to observe larger discrepancies in tidal amplitude. Small waterways and tributaries necessitate the use of higher grid resolution to resolve complex shoreline geometry and stark differences in bathymetry over diminutive distances, which is a particular challenge for very accurate water level modeling using gradually scaling resolution grids. The remaining principal semidiurnal constituents at the top of Table 3.2A had average harmonic differences of -0.002±0.013m for the N_2 and -0.033± 0.019m for the K_2 tidal constituent. As for the diurnal tidal amplitudes, the mean differences for the 10 stations of interest were -0.008±0.011m, 0.011±0.007m, 0.005±0.016m, and 0.000±0.002m, for K_1, O_1, P_1, and Q_1, respectively (Table 3.2A).

In the tidal phase comparison, Table 3.2B displays the mean difference of tidal phase between modeled tide and NOAA observed tide for the principal lunar and solar semidiurnal constituents, M_2 and S_2, was 0.571±1.980° and -0.799±2.614°, respectively. Sandy Hook, NJ, observed a shift in M_2 tide by 6.013° and in the S_2 tide by -5.707°, accounting for much of the deviation (Figure 3.1D). The N_2 constituent yielded an average phase difference of -0.165±0.087°, and the average difference for the K_2 constituent was -0.387±0.442°. The average phase differences for the diurnal constituents, K_1, O_1, P_1, and Q_1, were -0.217±0.155°, -0.265±0.248°, 1.587±0.721°, and -0.141±0.069°, respectively (Table 3.2B). The close tidal harmonic comparison for both amplitude and phase suggests that the SELFE large scale model grid of the U.S. East Coast including the New York Harbor and Long Island Sound is sufficient when compared with NOAA tidal prediction data tide. Thus, the new SELFE grid developed

for simulating 2012 Hurricane Sandy is quite proficient at modeling the characteristics of long-period wave propagation along the open coast and the New York Harbor.

3.2   Storm Tide Model Results for 2012 Hurricane Sandy

Hurricane Sandy formed in the Caribbean Sea on October 22, 2012, and intensified in strength as it tracked northward. The storm's maximum classification as a Category 3 Hurricane on the Saffir-Simpson scale occurred over the mid-Atlantic Bight just before abruptly veering to the northwest on October 28th. The unique shift in storm track was largely due to a large-scale wind flow pattern favoring an upper-level block over Greenland and a mid-level atmospheric trough coming from the U.S. Southeast. Consequently, Hurricane Sandy made landfall just north of Atlantic City near Brigantine, NJ, as a Category 1 Hurricane on October 29, 2012, at approximately 7:30 pm.

The landfall of Hurricane Sandy brought an atypically large storm tide with record-setting water levels observed along the coasts of New Jersey, New York City, and low elevation regions of the Long Island Sound. NOAA verified water level records observed peak storm tide elevation at The Battery, NY, Bergen Point, NY, Sandy Hook, NJ, Bridgeport, CT, New Haven, CT, at 2.74, 2.90, 2.44, 1.77, 1.69m (or 9.0, 9.53, 8.01, 5.82, 5.54ft) above mean higher-high water, respectively (NOAA Tides and Currents, 2012). The storm tide triggered significant flooding in New York in the Hudson River Valley, the East River, and the western portion of the Long Island Sound, with some of the most catastrophic flooding being observed along Staten Island and to the south along the New Jersey coast. The combination of the astronomical tide and storm surge is indicative of a storm tide, which is inherently related to a tropical or extratropical

atmospheric disturbance. In regions where tidal ranges are significantly large, storm surge can be particularly damaging when it occurs concurrently with a high tide. The opposite of this scenario was observed at Kings Point, NY, at the head of the Long Island Sound, where the peak storm surge occurred simultaneously with a tidal trough (Figure 3.2). The pier at Kings Point observed one of the highest storm surge heights during Hurricane Sandy due to its bottlenecked location at the relatively narrow mouth of the East River, compared to the substantially wider Long Island Sound. However, the observed storm tide could easily have been at least 2m higher had the storm surge occurred during high tide.

Upon calibration of tidal harmonics conducted in the previous section, external atmospheric forcings for air pressure and wind were applied to simulate storm surge and inundation along the U.S. East Coast during 2012 Hurricane Sandy. Since the modeled water level fluctuations along the open coast and within coastal embayments depend heavily upon the input meteorological conditions, forecast wind and pressure fields with higher accuracy ideally provide better hydrodynamic model predictions. In the upcoming sections, a comparison of the hydrodynamic influences of two atmospheric forecast model products, the North American Regional Reanalysis (NARR) model, and the Regional Atmospheric Modeling System (RAMS). A cursory comparison of wind velocities in the u and v directions in m/s has been made to demonstrate the relative accuracy of the forecast winds' speeds with observations recorded by NOAA's National Data Buoy Center (NDBC). The NDBC observations are compared at two stations: 44065 near the mouth of the Raritan Bay near the New York Harbor (Figure 3.3A), and CHLV2, near the mouth of the Chesapeake Bay (Figure 3.3B). While both forecast wind

fields compare reasonably well with the buoy observations (NOAA NBDC, 2012), the

RAMS wind product has a higher temporal resolution of one hour, while the NAM wind

field is updated every three hours. Regardless of the update frequency of the atmospheric

forcings, the SELFE model will temporally interpolate the input data to synchronize with

the model's time step. However, coarser temporal resolution will be interpolated over

longer periods of time, potentially missing high frequency shifts in wind and pressure.

The wind velocities for the NARR and RAMS inputs were amplified by 10% to

account for potential wave-induced mechanisms influencing water levels. Research

related to the influence of currents and wave interaction is being worked on, but is

beyond the scope of this dissertation. Since a wind-wave model was not utilized in these

storm tide simulations, wind velocities were increased by 10%, which translates to an

increase in wind stress of approximately 20% throughout the domain. The upcoming

sections address two different atmospheric models using unique wind and pressure fields

to drive the SELFE model in order to simulate the influence of 2012 Hurricane Sandy.
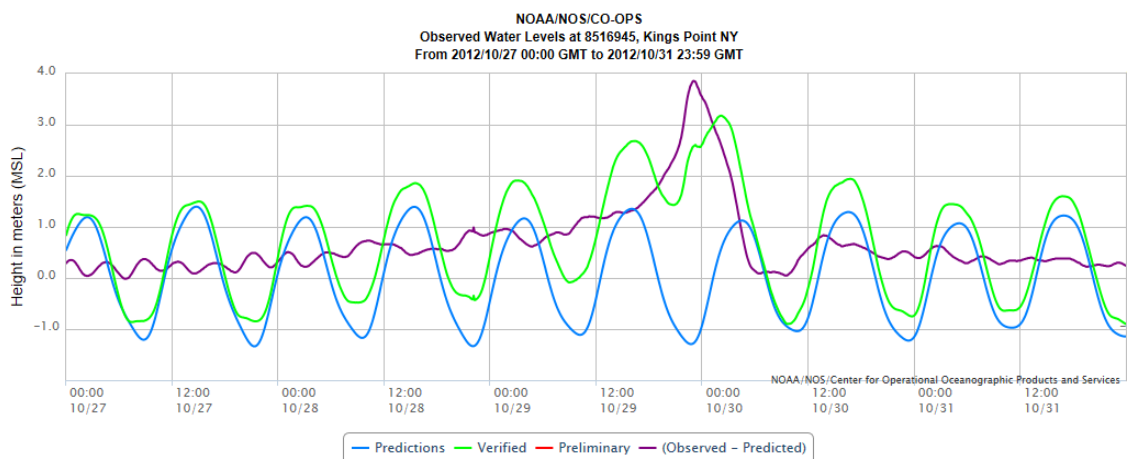
Figure 3.2. Hurricane Sandy water level observed at Kings Point, NY, at the head of the
Long Island Sound, shown peaking at 3.175m (10.416ft.) at 02:12 GMT on Tuesday,
October 30, 2012 (NOAA Tides and Currents, 2012).
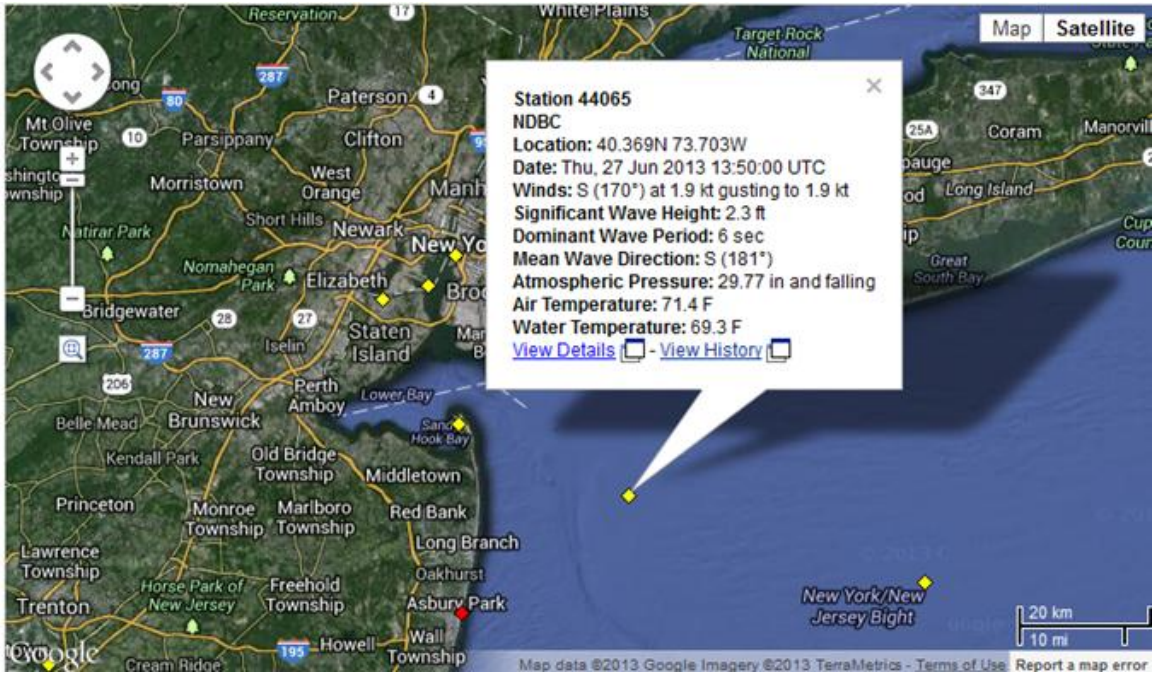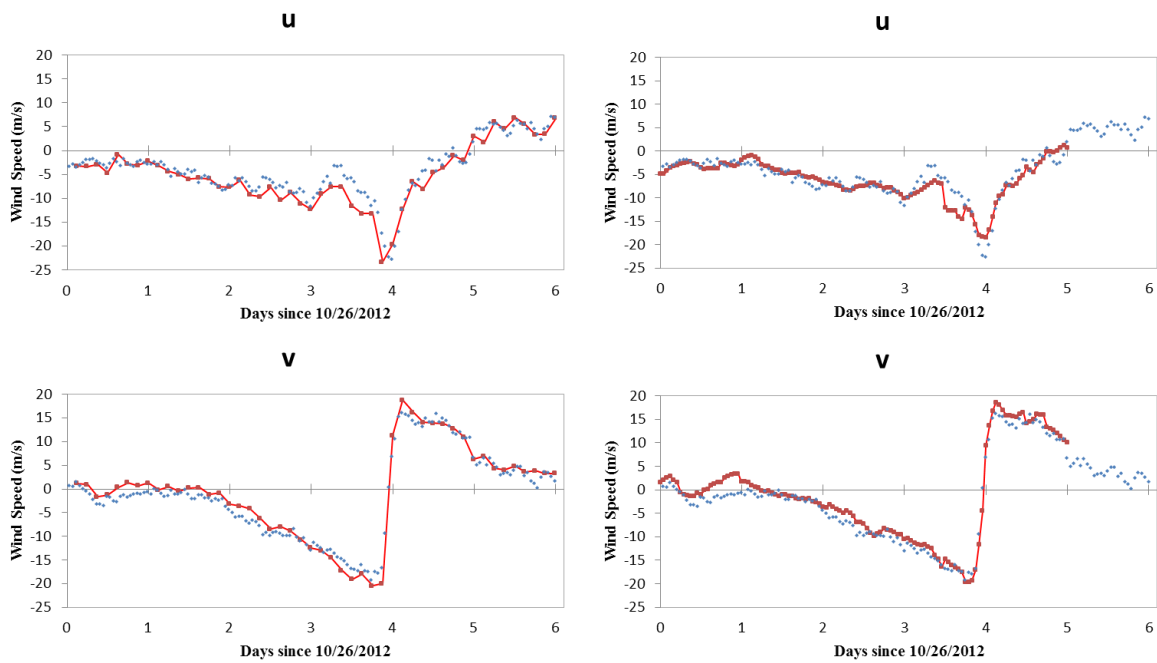
Figure 3.3A. Wind field comparisons for *u* and *v* wind velocities in m/s at Station 44065 near the mouth of the Raritan Bay near the New York Harbor using verified NOAA atmospheric observation data in blue, and forecast wind products displayed in red for NAM winds on the left and RAMS winds at right (NOAA NBDC, 2012).
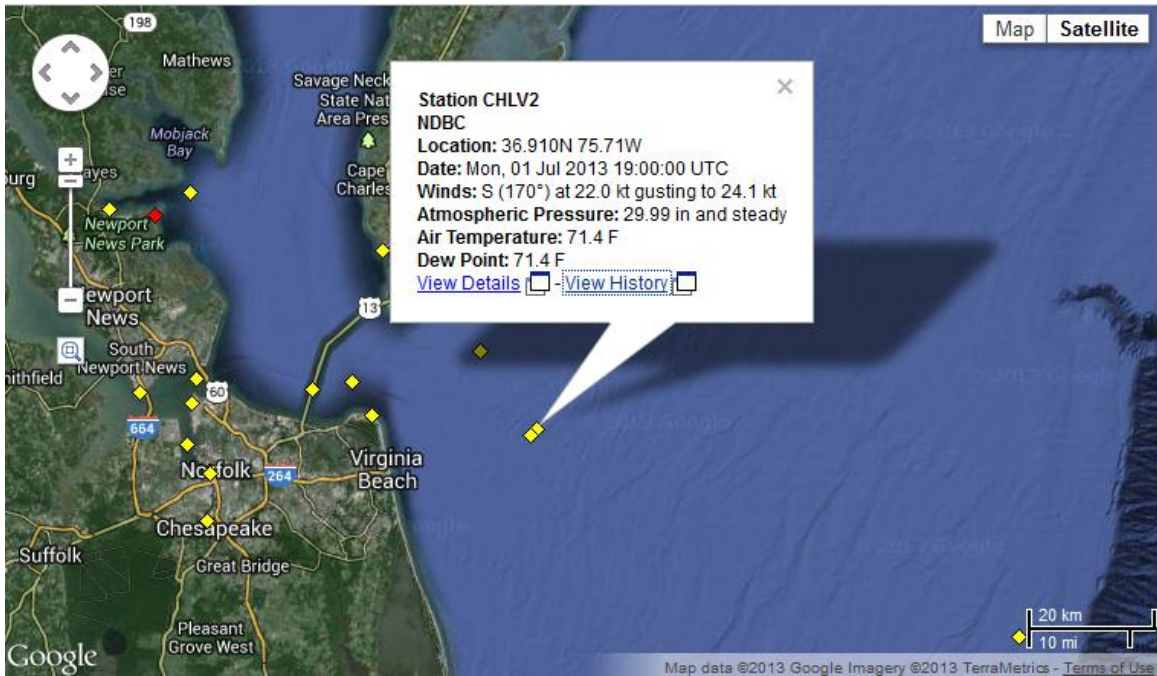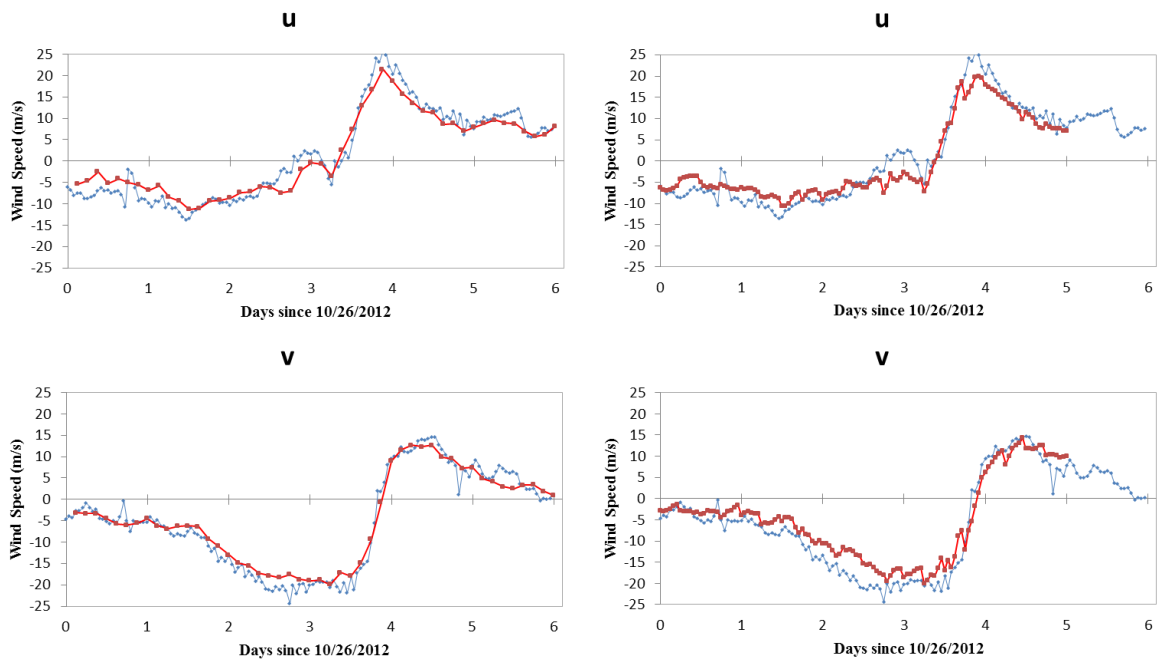
Figure 3.3B. Wind field comparisons for *u* and *v* wind velocities in m/s at Station CHLV2 near the mouth of the Chesapeake Bay using verified NOAA atmospheric observation data in blue, and forecast wind products displayed in red for NAM winds on the left and RAMS winds on the right. Observations retrieved from NOAA NBDC, 2012.

3.2.1 Storm Tide Simulation Results using NARR Atmospheric Forcing

The NARR atmospheric model outputs were retrieved at 24km resolution for Hurricane Sandy with a 3-hour update interval. Wind and pressure data were retrieved for the entire region covering the large scale SELFE model grid from 10/15/2012 at 00:00 GMT through 11/01/2012 at 00:00 GMT. Several 30-hour forecast series updating every 6 hours were combined to prepare the model input wind and pressure fields. Uncertainty in forecast accuracy increases the further into the future a model attempts to predict. Thus, a hindcast simulation using NARR forcings is conducted for comparison to yield the greatest potential for accuracy.

The storm tide results generated by the NARR wind, shown by the red lines in Figure 3.4A-E, demonstrate that the simulated water levels at each of the 10 NOAA stations were relatively accurate. Discrepancies in the model results suggested frequent fluctuations, especially during surge peaks when wind speed was strong, but were generally within 0.45m (Figure 3.4A-E & Table 3.3).

Stations positioned along the open coast performed generally better than those stations positioned far upriver or well within shallow embayments. Open coast stations included Montauk, NY, Sandy Hook, NJ, Atlantic City, NJ, Lewes, DE, and Duck, NC, with R^2 values ranging from 0.81 to 0.92. The relative error of these stations ranges from 10.16% at Atlantic City, NJ, to 17.75% at Duck, NC, and the root-mean-squared error ranges from 20.82cm at Montauk, NY, to 39.66cm at Sandy Hook, NJ. It should be noted that the observation data record at Sandy Hook was lost during the peak observed storm surge after 00:00GMT on October 30, 2012 (Figure 3.4D), and data were unavailable at

the station in Duck, NC, after 08:00GMT on October 29, 2012 (Figure 3.4E). Additionally, an apparent disturbance in the observation data record at Lewes, DE, exists between 22:00GMT on October 29, 2012, through 04:00GMT on October 30, 2012, accounting for some statistical incongruity with some of the other coastal stations (Figure 3.4E).

New Haven and Bridgeport, CT, within the Long Island Sound, compared reasonably well in phase, with R^2 values of 0.9292 and 0.9284, respectively. The amplitude differential is reasonably characterized with a 37.37cm and 41.64cm root-mean-squared error, respectively. Kings Point, NY, located at the head of the Long Island Sound where it joins with the East River, had an R^2 value of 0.9055, a relative error of 9.80%, but observed the highest root-mean-squared error of 45.51cm. Dual storm surges converging from the Long Island Sound, shown in the station's peak transitions in Figure 3.4A-B, and from the New York Bay up through the East River, observed in the peaks at the stations in Figure 3.4C-D, can account for the relatively large storm surge peak and larger error observed at Kings Point, NY. Reasonable comparisons were made using the NARR atmospheric forcings at the Battery at the confluence of the Hudson and East Rivers and at Bergen Point, NY, along the Kill van Kull connecting Newark Bay with the New York Bay. Based upon the complete analysis of the NARR results, predictive capacity of the SELFE hydrodynamic model is consistent with the relative quality of the NARR wind product being employed. Thus, a superior storm tide prediction would be anticipated if a more reliable or better resolution forecast wind were utilized.

Table 3.3. Statistical comparison between NOAA verified water level measurements and the model results obtained via forcing with 24km NARR wind and pressure fields.

Station	R^2	Relative Error (%)	RMS Error (cm)
Montauk, NY	0.8559	10.79	20.82
New Haven, CT	0.9292	11.25	37.37
Bridgeport, CT	0.9284	12.26	41.64
Kings Point, NY	0.9055	9.80	45.51
The Battery, NY	0.9305	9.13	32.08
Bergen Point, NY	0.9532	11.86	35.81
Sandy Hook, NJ	0.9286	12.39	39.66
Atlantic City, NJ	0.9113	10.16	25.36
Lewes, DE	0.8395	12.32	25.57
Duck, NC	0.8121	17.75	23.09
Mean Value	0.8994	11.77	32.69
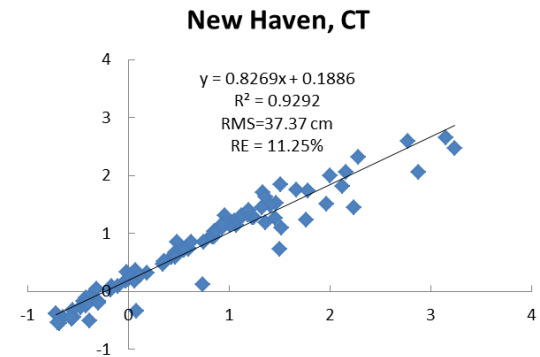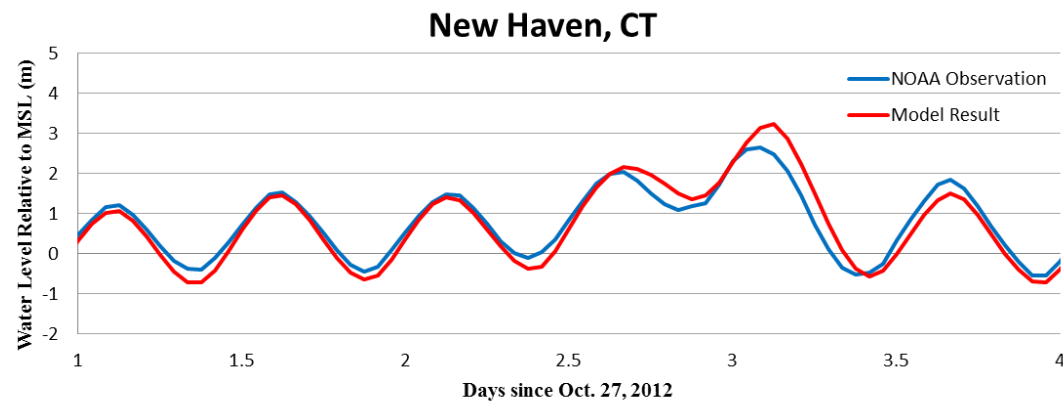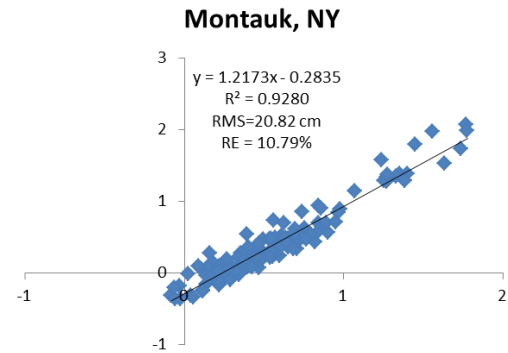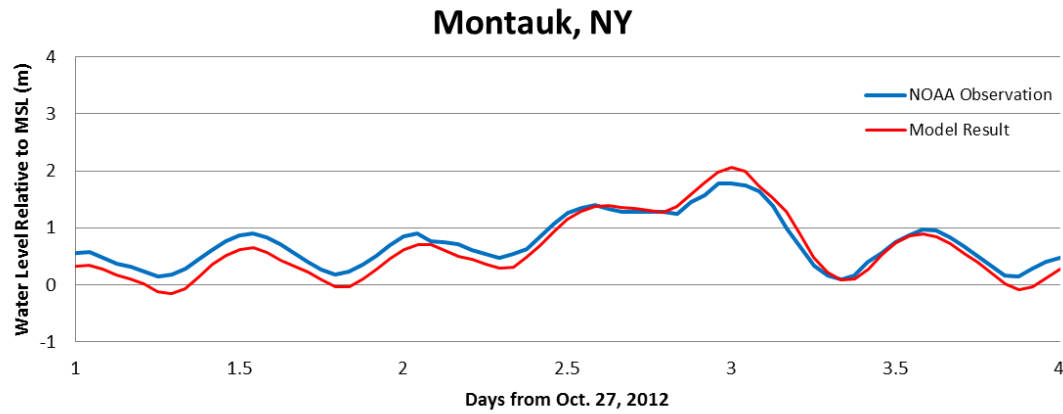
Figure 3.4A. Storm tide model results and NOAA verified water level comparison with time series (left) and statistical results (right).
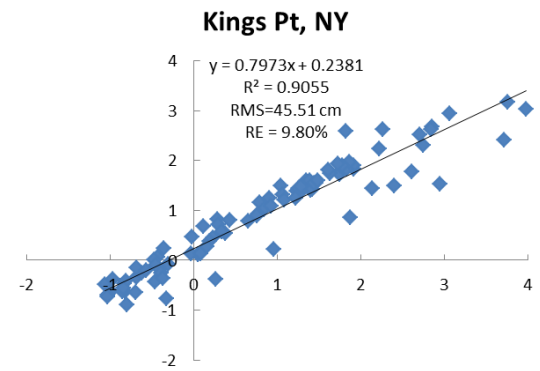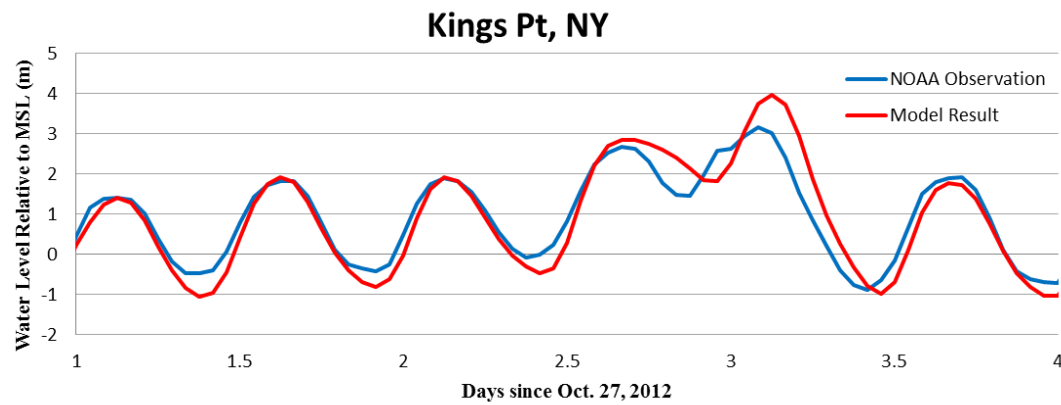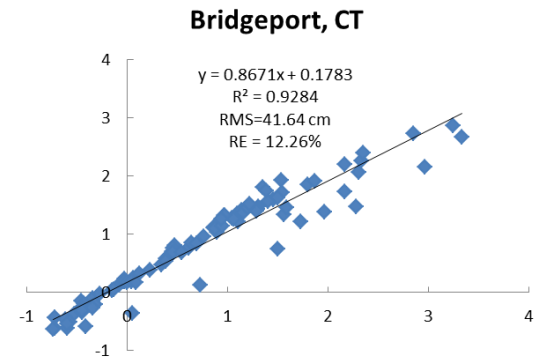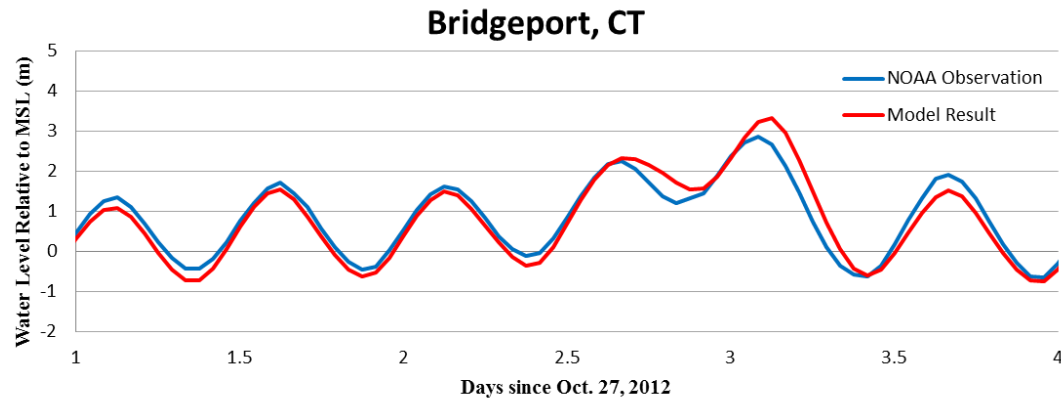
Figure 3.4B. Storm tide model results and NOAA verified water level comparison with time series (left) and statistical results (right).
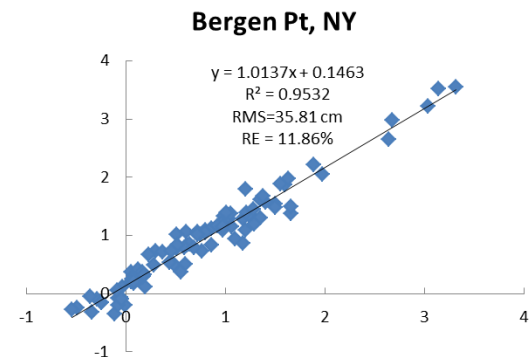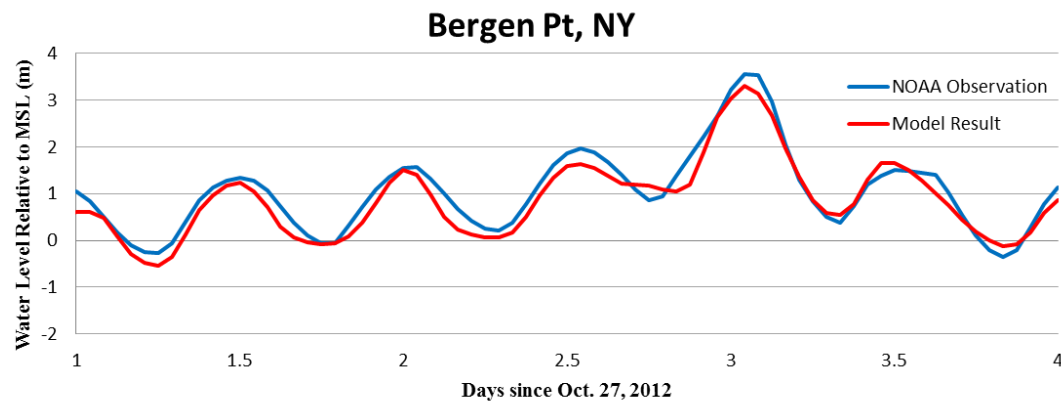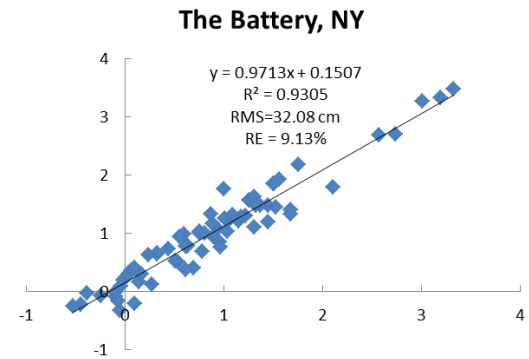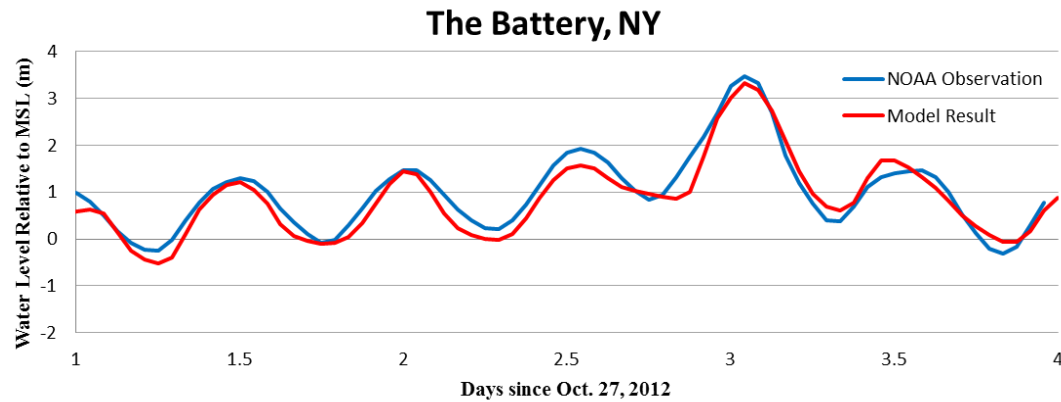
Figure 3.4C. Storm tide model results and NOAA verified water level comparison with time series (left) and statistical results (right).
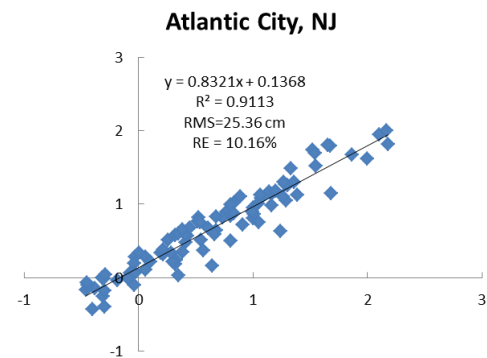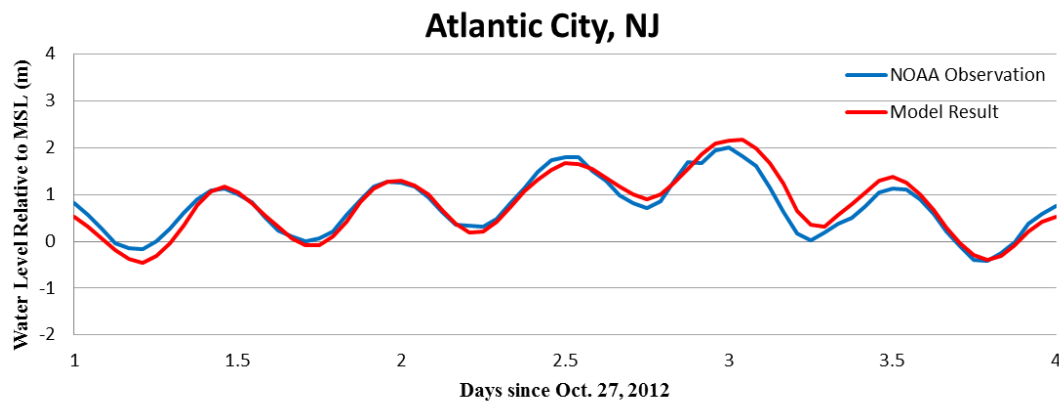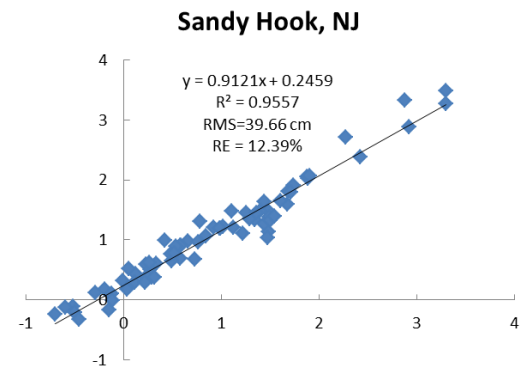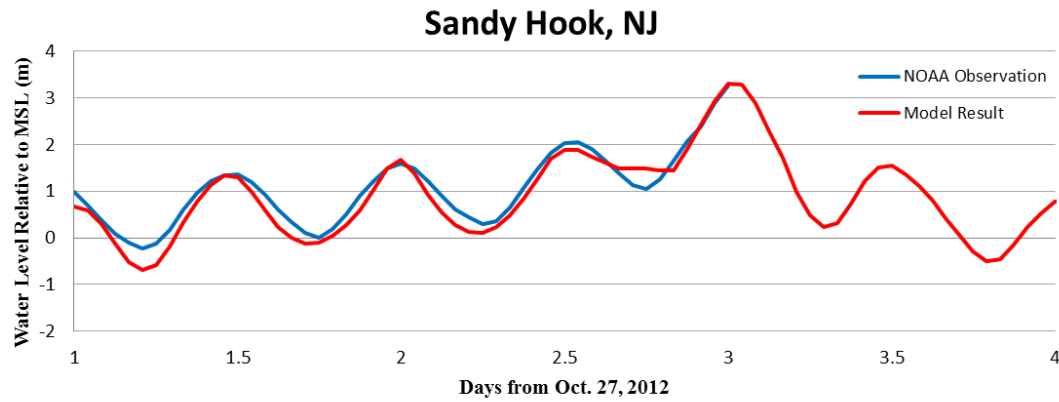
Figure 3.4D. Storm tide model results and NOAA verified water level comparison with time series (left) and statistical results (right).
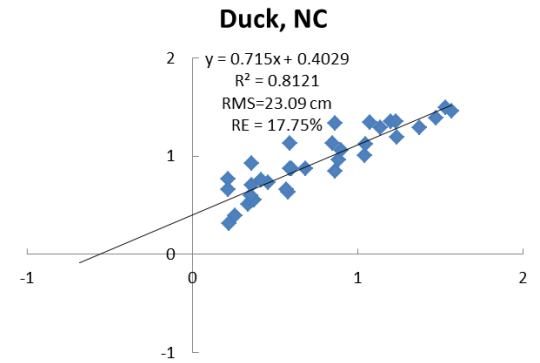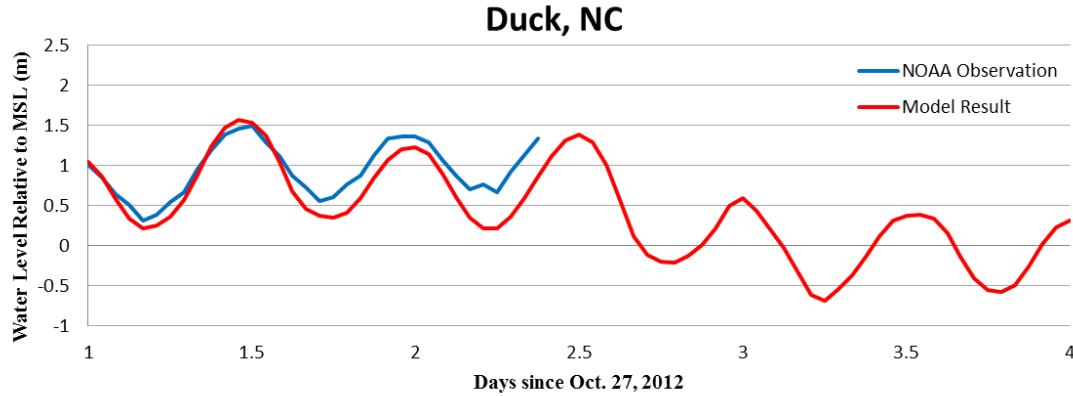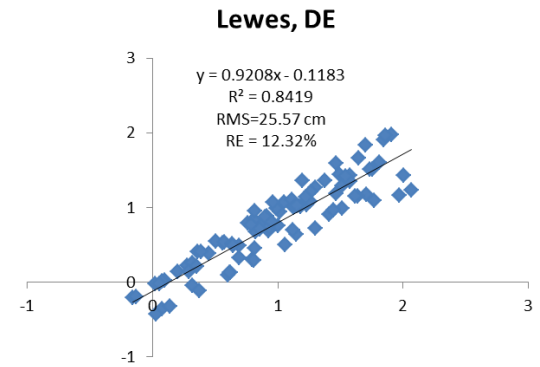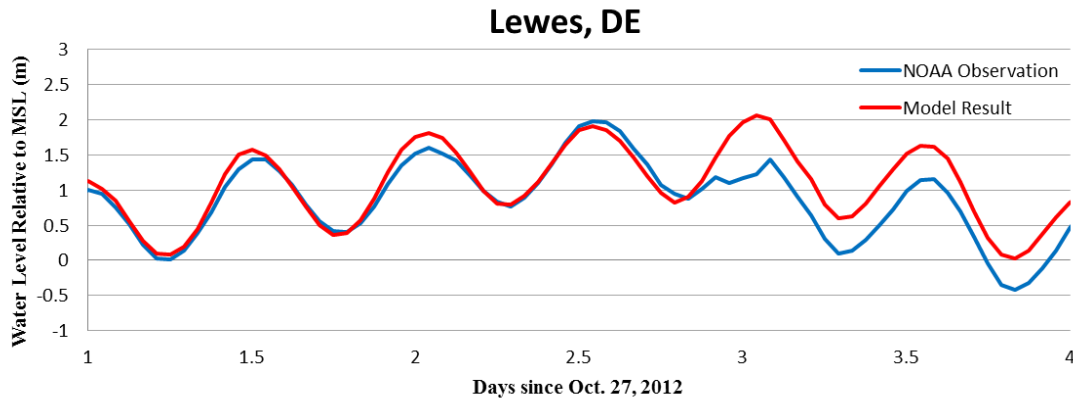
Figure 3.4E. Storm tide model results and NOAA verified water level comparison with time series (left) and statistical results (right).

3.2.2 Storm Tide Simulation Results using RAMS Atmospheric Forcing

The high-resolution winds for Hurricane Sandy were produced by an independent company, WeatherFlow, Inc. (http://www.weatherflow.com/) in hindcast mode. These atmospheric pressure and wind products are retrieved from the RAMS model output and used as an atmospheric input to drive the SELFE model. The wind field features coverage from 33.000 to 42.972˚N latitude and from 78.000 to 68.026˚W longitude with a resolution of 2.16 arc-seconds (≈4km resolution from north-south and ranging in resolution from 3.356km to 2.926km east-west).

The duration of the wind and pressure field data provided ranged from 10/24/2012 at 00:00 GMT through 10/31/2012 at 00:00 GMT, with a 1-hour temporal resolution. These atmospheric data products are a continuous hindcast simulation, being assembled in a similar fashion to the continuous NARR atmospheric data inputs. These are in contrast with the typical 30-hour forecast products updated every 3 or 6 hours. The product assimilates atmospheric observations from various sources, including Weatherflow's extensive network of meteorological stations. The SELFE model's atmospheric forcing field requires a fully expanded longitude-latitude grid, specific variable names, time units measured in days, and a time origin in a specific format to be read by the model's 'sflux' atmospheric input. The atmospheric data provided by Weatherflow were released as an interoperable NetCDF format, which can be adapted to the SELFE model input with minimal preprocessing effort. A short script utilizing NetCDF operators (such as 'ncap2', 'ncrename', and 'ncatted' from http://nco.sourceforge.net/) can augment and adjust the metadata of the Weatherflow product in less than 10 seconds of run time to support the SELFE model setup.

To account for the shorter data range and partial grid coverage extent of the hindcast RAMS model outputs as effective atmospheric inputs, the storm tide simulation utilized the model's hotstart option using the NARR atmospheric inputs to "spin-up" the storm tide simulation from 10/15/2012 at 00:00GMT for 9 days until 10/24/2012 at 00:00GMT. At this time, the rapid deployment 4km RAMS model inputs were utilized throughout the extent of the region covered, with the NARR atmospheric data being used at grid nodes outside the extent of the RAMS atmospheric data coverage along the periphery of the grid. Combination of the two wind products is handled via the 'sflux9c.f90' file to blend the two data sources and provide a complete atmospheric input for the entire simulation period when two atmospheric inputs are simultaneously specified.

Figure 3.5A-E displays the storm tide results at the 10 stations ranging in location from the Long Island Sound, through the New York Harbor, down along the Atlantic Coast to Duck, NC, shown in Figure 2.4, during the period from October 28, 2012, at 00:00GMT through October 31, 2012, at 00:00GMT. Figure 3.5A displays two stations in near the mouth of the Long Island Sound. A comparison of the timing of the peak water level water level illustrates the surge propagation from Montauk, NY, at the top of Figure 3.5A at the mouth of the Long Island Sound. As the surge propagated westward through the Long Island Sound toward Kings Point, NY, at the bottom of Figure 3.5B, the storm tide reached the peak water level elevation of 3.216m above MSL (Figure 3.2).

It is evident that there were two storm surges converging upon New York City during Hurricane Sandy; one from the New Jersey coast, and the other from the Long Island Sound propagating westward. Figure 3.5E combines two coastal stations in

Delaware and North Carolina, which are positioned within the 3rd and 4th quadrants of the Hurricane track where the counterclockwise wind motion has been weakened after passing over land. As the stations just north of Atlantic City, NJ (Figure 3.5A-D), were experiencing the maximum storm surge setup, these stations simultaneously experienced a water level set down, elucidated by the model results' response to the offshore wind field. It is also worth noting that the forerunner of the storm was so pronounced that it water levels were observed to consistently exceed the station's mean high water in Montauk, NY, for several days before storm made landfall through several days after.

SELFE model performance with the RAMS atmospheric inputs were better than the storm tide resulting from the NARR atmospheric forcing (Table 3.3) with a mean R^2 value of 0.9402, a mean relative error of 4.08%, and an overall root-mean-squared error of 19.22cm. The relative error was observed to be less than 7.0% for the 10 NOAA observation stations, except for Lewes, DE, for which there is an observation error noted in the previous section. Therefore, the model dependably represented the hydrodynamics correctly using the RAMS atmospheric inputs (Table 3.4).

Table 3.4. Statistical comparison between the model results obtained using the 4km RAMS wind and pressure fields and NOAA verified water level measurements.

Station	R^2	Relative Error (%)	RMS Error (cm)
Montauk, NY	0.8856	6.70	15.77
New Haven, CT	0.9701	3.33	24.02
Bridgeport, CT	0.9908	0.76	11.74
Kings Point, NY	0.9518	2.77	26.59
The Battery, NY	0.9741	1.55	15.16
Bergen Point, NY	0.9471	3.17	22.04
Sandy Hook, NJ	0.9610	2.14	15.02
Atlantic City, NJ	0.9377	4.70	19.65
Lewes, DE	0.8234	9.52	25.71
Duck, NC	0.9606	6.19	16.53
Mean Value	0.9402	4.08	19.22
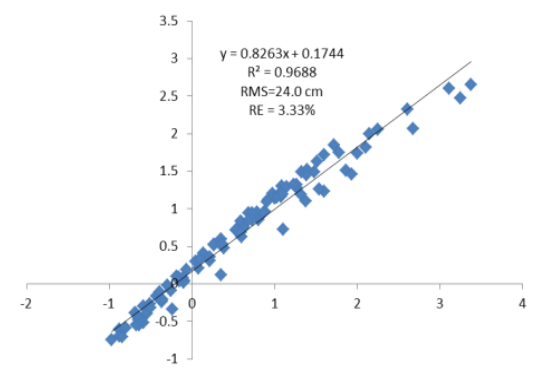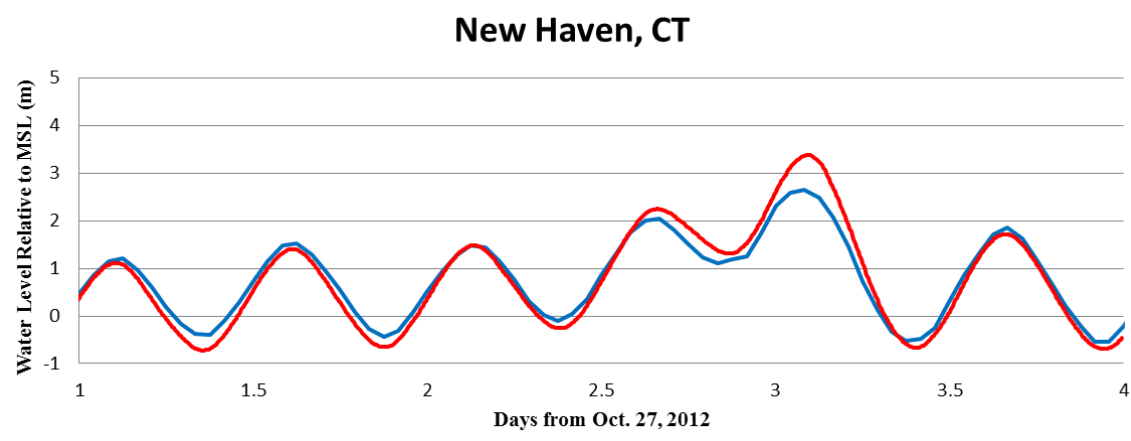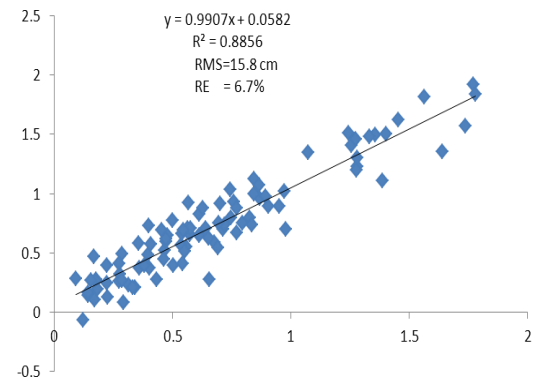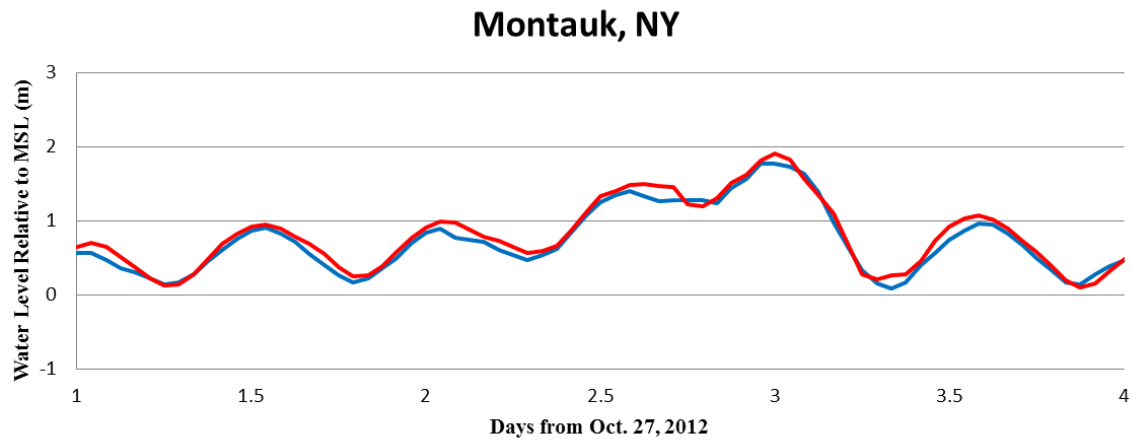
Figure 3.5A. Storm tide model results and NOAA verified water level comparison with time series (left) and statistical results (right).

Bridgeport, CT

Kings Pt, NY
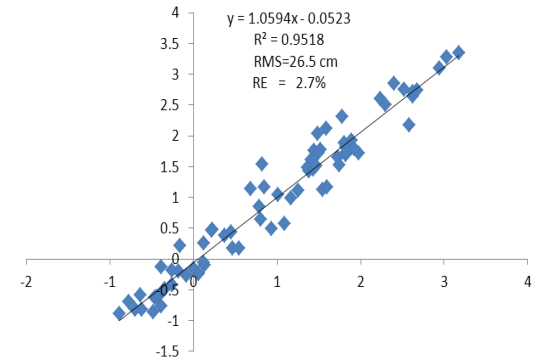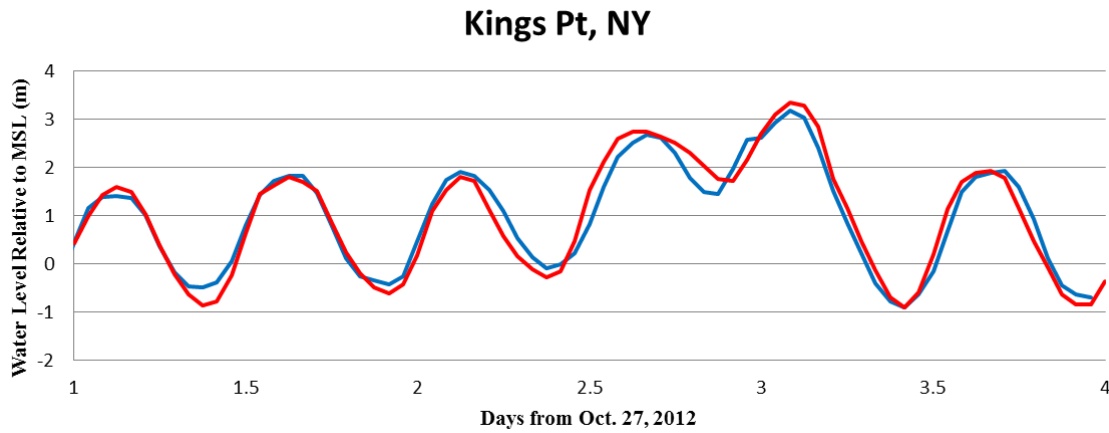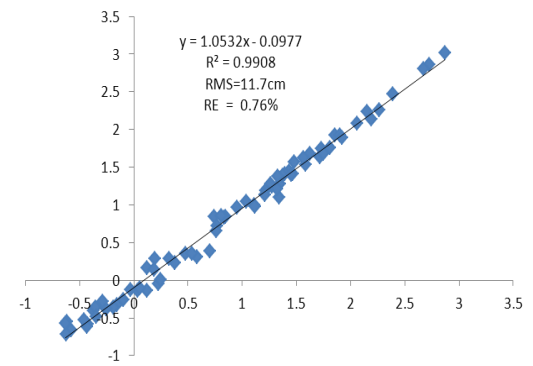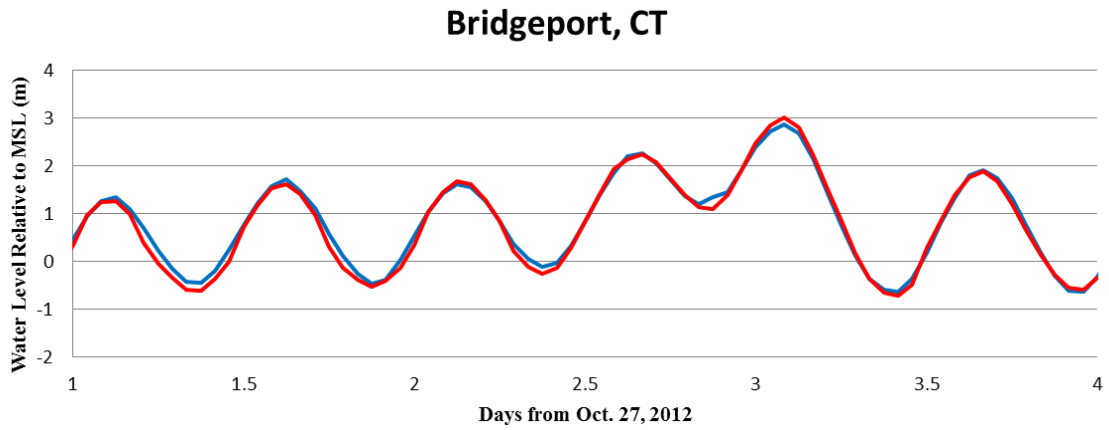
Figure 3.5B. Storm tide model results and NOAA verified water level comparison with time series (left) and statistical results (right).

The Battery, NY

y = 1.0525x - 0.0769
R² = 0.9741
RMS=15.1 cm
RE = 1.55%

Bergen Pt, NY

y = 0.9957x - 0.0868
R² = 0.9481
RMS=22.1 cm
RE = 3.17%
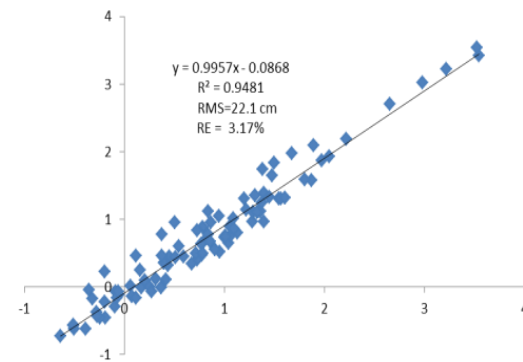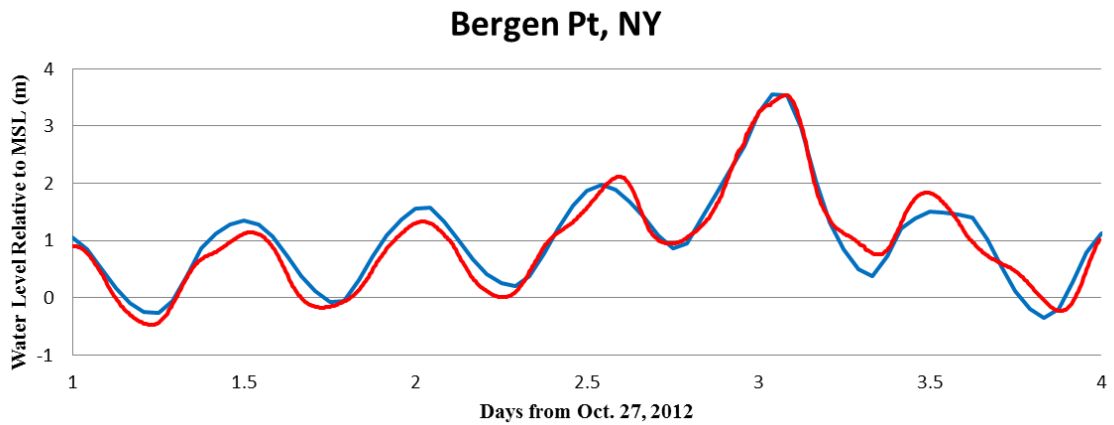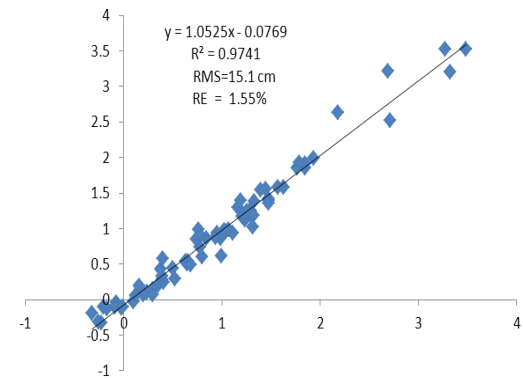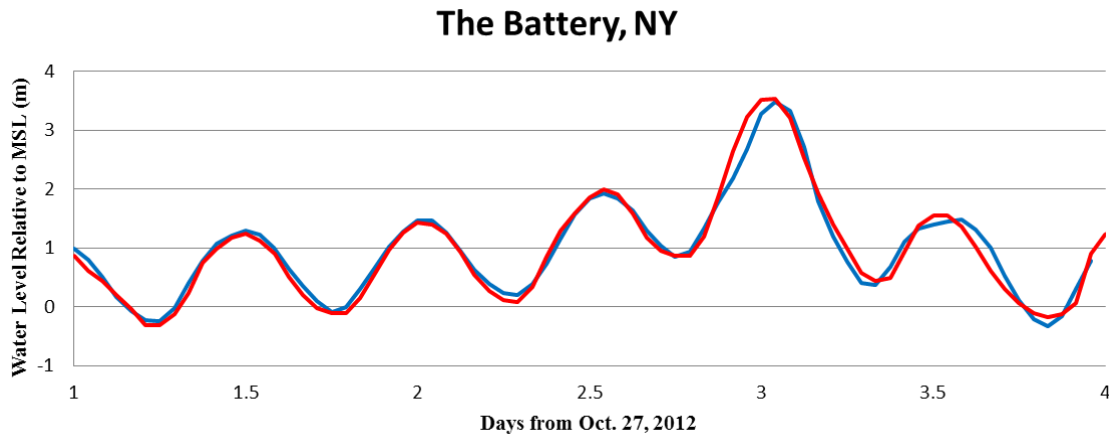
Figure 3.5C. Storm tide model results and NOAA verified water level comparison with time series (left) and statistical results (right).
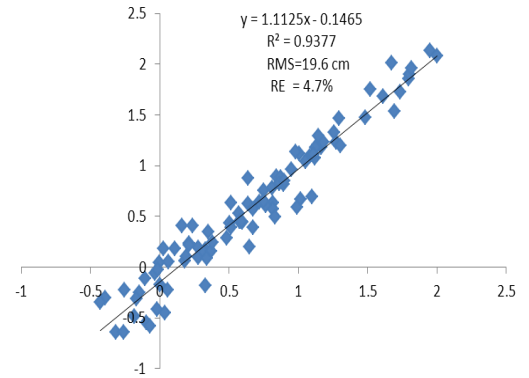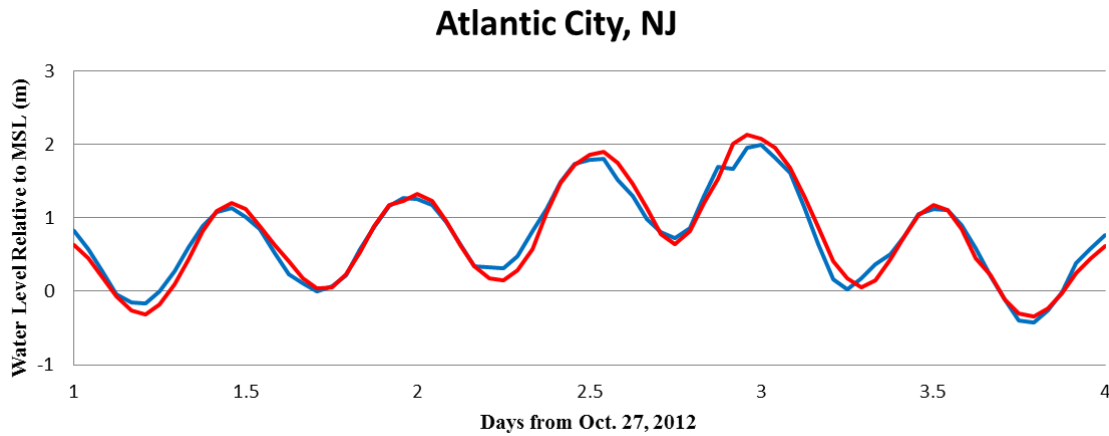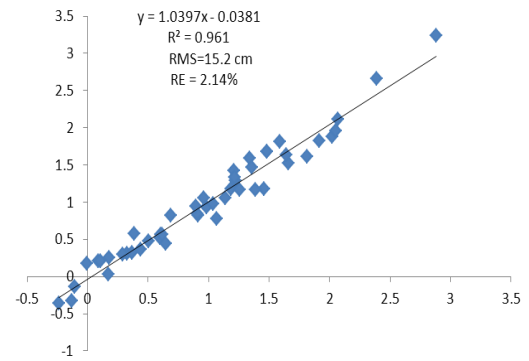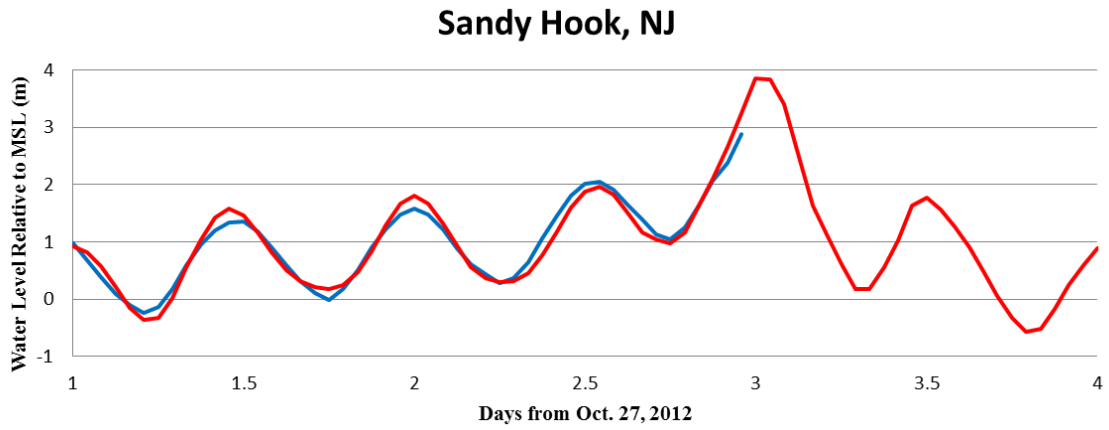
Figure 3.5D. Storm tide model results and NOAA verified water level comparison with time series (left) and statistical results (right).

Lewes, DE

y = 0.9682x + 0.0009
R² = 0.8234
RMS=25.7 cm
RE = 9.5%

Duck, NC

y = 1.1091x - 0.21
R² = 0.9634
RMS16.5 cm
RE = 6.19%
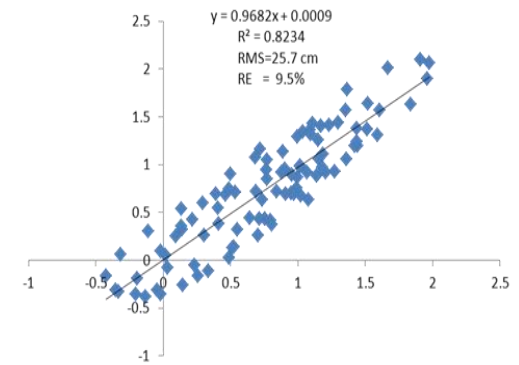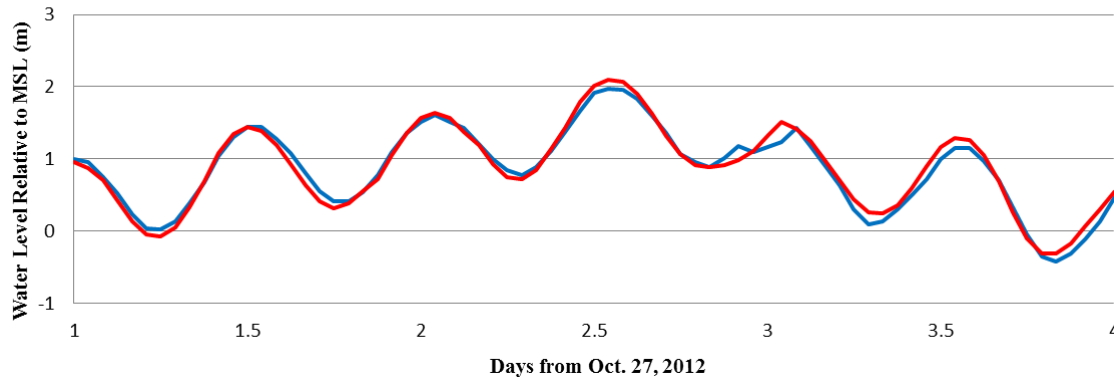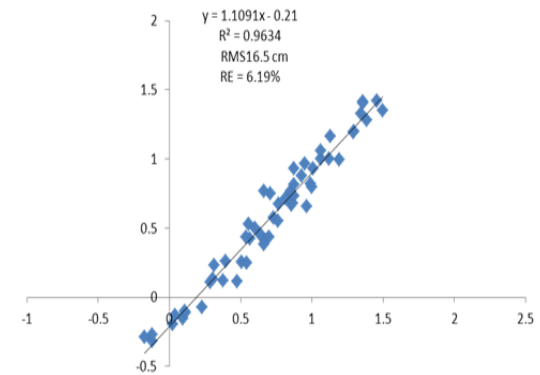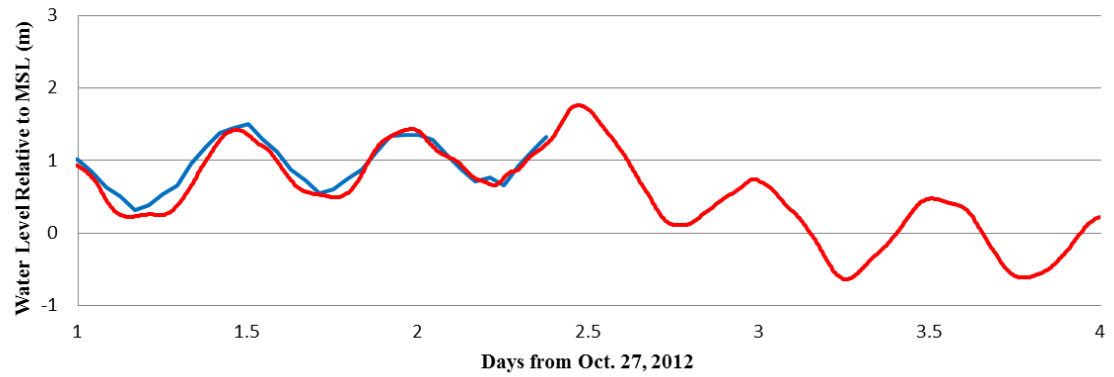
Figure 3.5E. Storm tide model results and NOAA verified water level comparison with time series (left) and statistical results (right).

CHAPTER 4: Street-Level Sub-Grid Inundation Model Methodology

4.1   UnTRIM^2 Model Description

The UnTRIM^2 model is utilized in this study to simulate storm surge and
inundation caused by hurricanes and nor'easters. The numerical algorithms of UnTRIM^2
are both robust, and relatively general (Casulli and Walters, 2000; Casulli and Zanolli,
2002; Casulli, 2009; Casulli and Stelling, 2011). A detailed model description can be
found in the above references. The model is governed by the three-dimensional shallow-
water equations with the Boussinesq approximation and the equations are solved for free
surface elevation, water velocities, and salinity in a Cartesian coordinate system. The
momentum equations (4-1 & 4-2) and the continuity equation (4-3) for three-dimensional
hydrostatic flows are:

$$\frac{\partial u}{\partial t} + u\frac{\partial u}{\partial x} + v\frac{\partial u}{\partial y} + w\frac{\partial u}{\partial z} - fv = -g\frac{\partial \eta}{\partial x} + v^h\left(\frac{\partial^2 u}{\partial x^2} + \frac{\partial^2 u}{\partial y^2}\right) + \frac{\partial}{\partial z}\left(v^v\frac{\partial u}{\partial z}\right) \tag{4-1}$$

$$\frac{\partial v}{\partial t} + u\frac{\partial v}{\partial x} + v\frac{\partial v}{\partial y} + w\frac{\partial v}{\partial z} + fu = -g\frac{\partial \eta}{\partial y} + v^h\left(\frac{\partial^2 v}{\partial x^2} + \frac{\partial^2 v}{\partial y^2}\right) + \frac{\partial}{\partial z}\left(v^v\frac{\partial v}{\partial z}\right) \tag{4-2}$$

$$\frac{\partial u}{\partial x} + \frac{\partial v}{\partial y} + \frac{\partial w}{\partial z} = 0 \tag{4-3}$$

where:

$u(x, y, z, t)$, $v(x, y, z, t)$, and $w(x, y, z, t)$: velocity in the x-, y-, and z-directions [m];
t : time [s];
$\eta(x, y, t)$: water surface elevation measured from the undisturbed water surface [m];
f : Coriolis force [s^{-1}];
g : gravitational acceleration [m s^{-2}];
v^h : coefficient of horizontal eddy viscosity [m^{2}s^{-1}];
v^v : coefficient of vertical eddy viscosity [m^{2}s^{-1}];

Coefficients for eddy viscosity can be derived from an appropriate turbulence closure model. Integrating the continuity equation over depth and using a kinematic condition at the free surface of the water yields the following free surface equation (4-4):

$$\frac{\partial \eta}{\partial t} + \frac{\partial}{\partial x}\left[\int_{-h}^{\eta} u \, dz\right] + \frac{\partial}{\partial y}\left[\int_{-h}^{\eta} v \, dz\right] = 0 \tag{4-4}$$

where $h(x, y)$ is the water depth measured from the undisturbed water surface such that $H(x, y, t) = h(x, y) + \eta(x, y, t)$ represents the total water depth. When wetting or drying is expected, the differential equations (4-1 through 4-4) are defined on a time-dependent horizontal domain $\Omega(t)$ defined as $\Omega(t) = \{(x, y): H(x, y, t) > 0\}$ (Casulli, 2009). The boundary conditions at the free surface (4-5) are specified via prescribed wind stresses:

$$\nu^v \frac{\partial u}{\partial z} = \gamma_T(u_a - u), \qquad \nu^v \frac{\partial v}{\partial z} = \gamma_T(v_a - v), \qquad \text{at } z = \eta \tag{4-5}$$

where u_a and v_a are the respective wind velocity components in the x- and y-directions, and γ_T is a non-negative wind stress coefficient dependent upon wind speed. At the sediment-water interface, the bottom friction (4-6) is specified via:

$$\nu^v \frac{\partial u}{\partial z} = \gamma_B u, \qquad \nu^v \frac{\partial v}{\partial z} = \gamma_B v, \qquad \text{at } z = -h \tag{4-6}$$

where γ_B is a non-negative bottom friction coefficient; γ_B can be given by the Manning-Chezy formulation, or via fitting to a turbulent boundary layer.

In the UnTRIM^2 numerical scheme, local volume conservation is assured via the finite volume formulation. Simultaneously, a finite volume method is utilized to discretize the free-surface two-dimensional equation at each polygon to guarantee local and global volume conservation. Transport equations are solved using the sub-cycle

upwind scheme, or by using the higher-resolution flux-limiter method (Casulli and Zanolli, 2005). Upon solving the transport equations, mass is also conserved locally and globally due to the finite-difference formulation.

The Eulerian-Lagrangian method is applied in the UnTRIM^2 numerical scheme to solve the momentum equations, since this method facilitates high-accuracy discretization of the non-linear advection terms. The advection term is solved via the Lagrangian method, which is computed independently with each time step by the method of characteristics applied to a fixed grid domain. This combined method is especially efficient when applied to unstructured Cartesian grids (Casulli and Walters, 2000; Casulli and Zanolli, 2002). When the momentum equations are solved, this method combines the advantages of the Eulerian method with the Lagrangian method, via merging the ease of a fixed Eulerian grid with the computational strength of the Lagrangian method. The advantage of the Eulerian-Lagrangian method is that a sharp front of velocity (like a storm surge or large river discharge) is easier to trace because the system matrix becomes diagonal and symmetrical (Casulli and Zanolli, 2002). Additionally, this method enables the use of larger time steps than without the scheme, since small grid size no longer places as great of a constraint on the Courant number (Casulli, 1999; Casulli and Walters, 2000; Casulli and Zanolli, 2002).

4.2   Model Setup and Configuration for 2012 Hurricane Sandy

4.2.1   Model Domain and Grid

UnTRIM^2 is an unstructured orthogonal grid model and differs from structured orthogonal grids (like those used with ROMS), in that orthogonal structured grids

exclusively consist of four-sided structured polygons. The unstructured orthogonal model can make use of both three and four-sided polygons. Orthogonality in an unstructured grid is defined by the assumption that, within every polygon, there is a center point such that the segment joining the centers of two adjacent polygons, and the side shared by the two polygons has a non-empty intersection and that they are perpendicular to one another (Casulli and Zanolli, 1998). Additionally, the SELFE model utilized in the large domain of this modeling effort is an unstructured grid model that has no requirement regarding the orthogonality of its grid elements. An UnTRIM^2 horizontal computational domain consists of a set of non-overlapping convex three or four-sided polygons. Each polygon side is designated as either a side of an adjacent polygon, or as a boundary of the grid.

More recent advancements in the UnTRIM^2 model allow for the use of a sub-grid mesh embedded within each base grid element with an inherent numerical scheme capable of partial wetting and drying (Casulli and Stelling, 2011). UnTRIM^2 possesses numerous other valuable properties including: high-order numerical accuracy, global and local mass conservation, and unconditional stability due to its computationally semi-implicit scheme. Greatest numerical accuracy is achieved when a uniform grid, comprised of uniform quadrilaterals (like squares) or equilateral triangles, is used. For this reason, many of the grids developed using Lidar-derived data have been scaled to square grids congruent to the native resolution of the topographic data contained in the DEM. The sub-grid model grid utilized to model 2012 Hurricane Sandy in the New York Harbor region makes use of a 200m base grid with a 40x40 nested 5m sub-grid within each grid cell (Figure 4.1). The grid is comprised of 11,959 nodes and 11,601 elements, covering an area of 29 x 37km, translating to 4,496,833 sub-grid cells at 5m resolution.
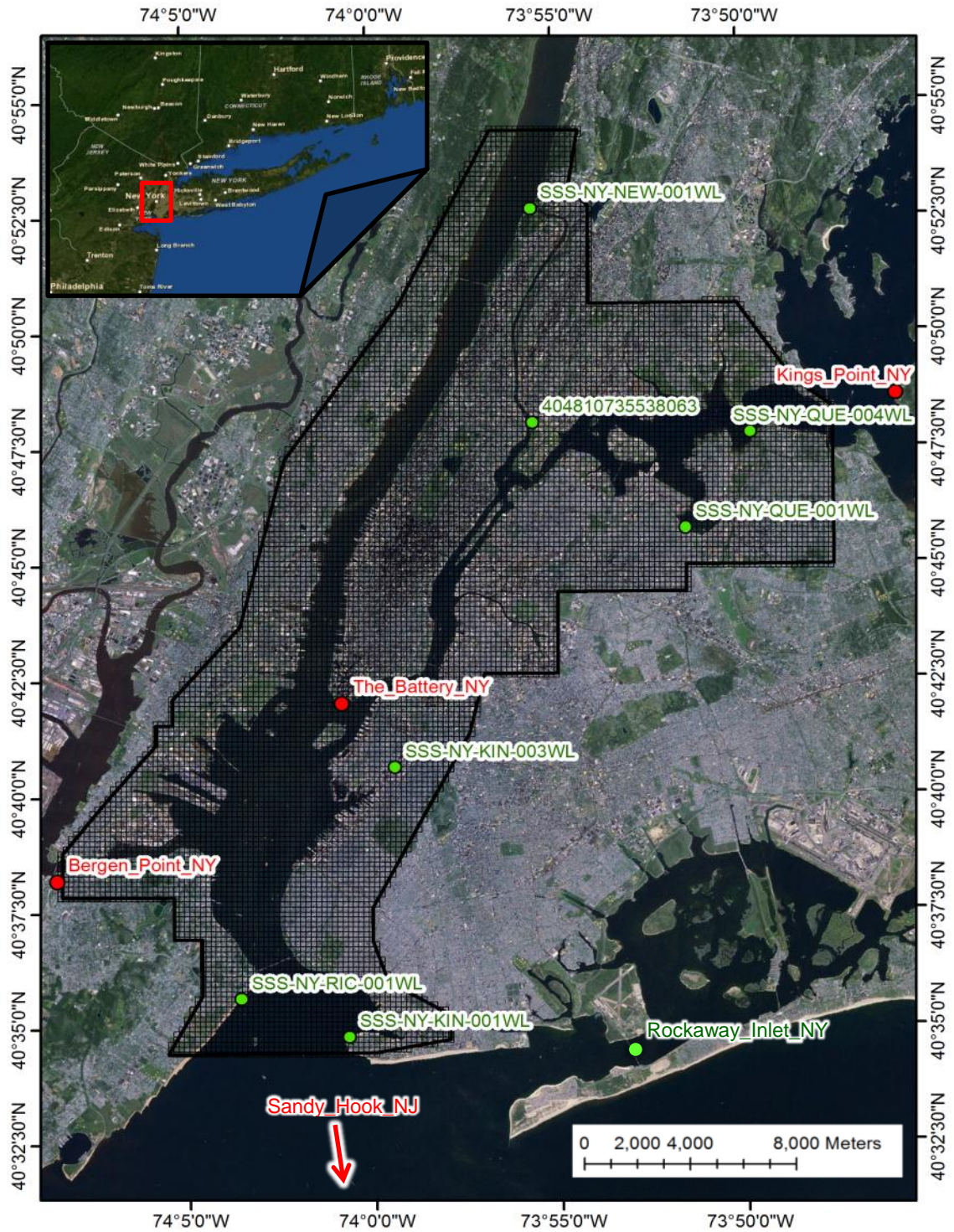
Figure 4.1. Location map of 4 NOAA tide gauges (**red**), and 8 USGS rapid deployment water level gauges (**green**) near the sub-grid domain utilized in the sub-grid modeling effort. Stations within the 200m base grid (**black**) were utilized for temporal verification of model results, while stations outside the grid were used for water elevation boundary forcing in the hindcast simulation driven via observation data.

Given a square grid, the normal velocity on the faces of each polygon is calculated at the center point of the face and the centers of two adjacent polygons are equally spaced from the shared face, minimizing the associated discretization error in these computations. An unstructured, non-uniform grid can be utilized with a larger associated discretization error (Casulli and Zanolli, 1998). Discretization error will propagate with increased simulation time, as is typical in computational simulations. If not utilizing a uniformly shaped unstructured grid, discretization error can be minimized when the polygon size and shape gradually vary throughout the flow region of the domain when using a uniform square-based grid with a uniform square sub-grid as shown near the southern tip of Manhattan Island with buildings included in Figure 4.2.
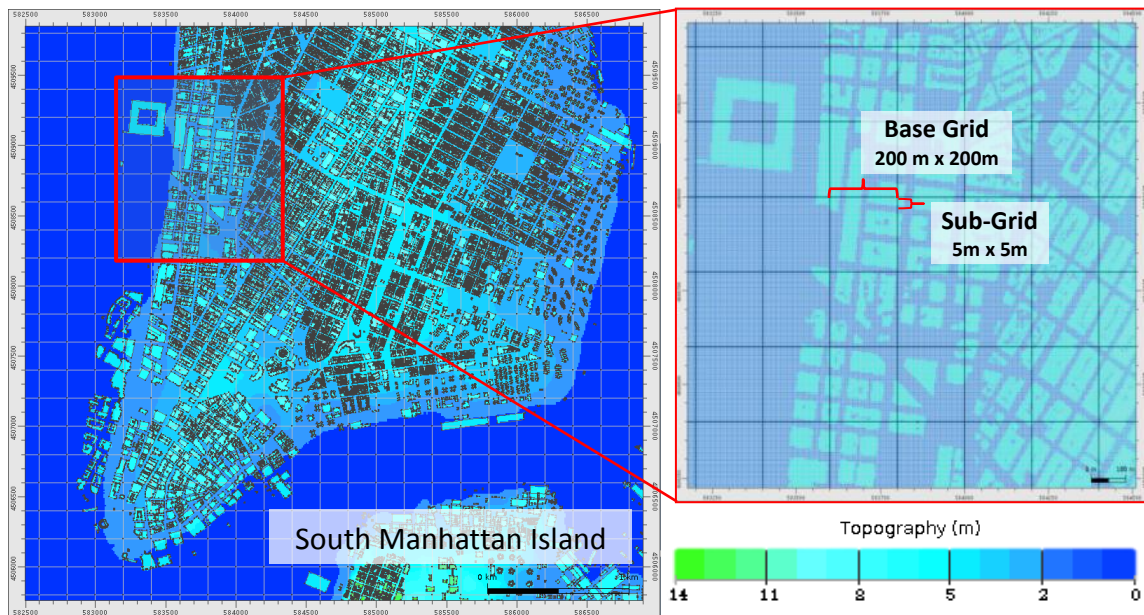
Figure 4.2. Representation of the square sub-grid used for modeling Hurricane Sandy in New York City in UnTRIM[2] at Manhattan Island just north of the Battery shown in Figure 4.1. The grid includes a uniform 200m resolution square base grid with a nested 40 x 40 5m resolution sub-grid. Lidar data are directly imported into the square sub-grid elements to effectively resolve buildings and streets. Coordinates are in UTM zone 18N.

4.2.1.1 Description of Sub-Grid Techniques

Sub-grid modeling is a novel method by which water level elevations on the sub-grid level can be obtained through the combination of water levels and velocities efficiently calculated at the coarse computational grid, the discretized bathymetric depths, and local friction parameters, without utilizing the excessive computing resources required to solve the full set of equations. Sub-grid technology essentially allows velocity to be determined efficiently at the sub-grid scale. This salient feature enables coastal flooding to be addressed in a single cross-scale model from the ocean to upstream river channels without overly refining the grid resolution. To this end, high-resolution DEMs will be developed using GIS from Lidar-derived topography for incorporation into a sub-grid model, for research into the plethora of practical research applications related to inundation.

When water from Hurricane Sandy's storm surge floods into New York City, it will encounter complex developed land surfaces characterized by a wide range of unique features ranging from waterfront berms, streets, railroads, parks, highways, subway stations, bridges, to a variety building types of different kinds. High-resolution hydrodynamic models are needed to appropriately consider the impact of these local features into the prediction of maximum storm surge extents. Even with ample computing resources available today, it is still insufficient to model all complex topographic features at the individual building scale or at street-level resolution. Recent research demonstrates that, provided Lidar data of topographic heights and sufficient bathymetric water depths, both of which can be collected with very high resolution, detailed bathymetric data within

a coarse grid model can be used to further improve model accuracy (Casulli, 2009; Loftis et al., 2013). This is the emerging consensus for the sub-grid modeling approach.

4.2.1.2 Nonlinear Solver for Sub-Grid Applications

The essence of sub-grid modeling is its nonlinear solver within the solution algorithm for the wetting and drying scheme. The primary benefit of sub-grid modeling is its accurate and efficient wetting and drying scheme, which is capitalized upon in this inundation study. Since a conventional model can only represent overland fluid flow as a single water level within each core computational cell, it is represented as an average water level across the entire region represented by that one cell, with a Boolean true or false value for the typical fluid dynamics parameter: 'is_wet'. Considering an element located along the edge of a shoreline where parts of the cell are wet while others areas of the cell are dry can only average the elevation across the cell, ultimately misrepresenting the fluid flow and spatial extent of water flooding into land areas.

A sub-grid, nested within base grid cells can store unique topographic and bathymetric terrain information at a variety of scales depending upon DEM resolution to sub-divide the model's core computational grid into smaller sections to allow for better representation of the flow velocities and flooding extent by allowing model elements to display as partially-wet or partially-dry, with the Boolean true or false value for the 'is_wet' parameter now applying to each sub-grid cell based upon its averaged elevation being negative or positive (Figure 4.3). The sub-grid helps to sub-divide the river cross-section into smaller separate areas in a manner analogous to the mean value theorem in calculus to better estimate the area underneath the curve for computation (Figure 4.4).

76
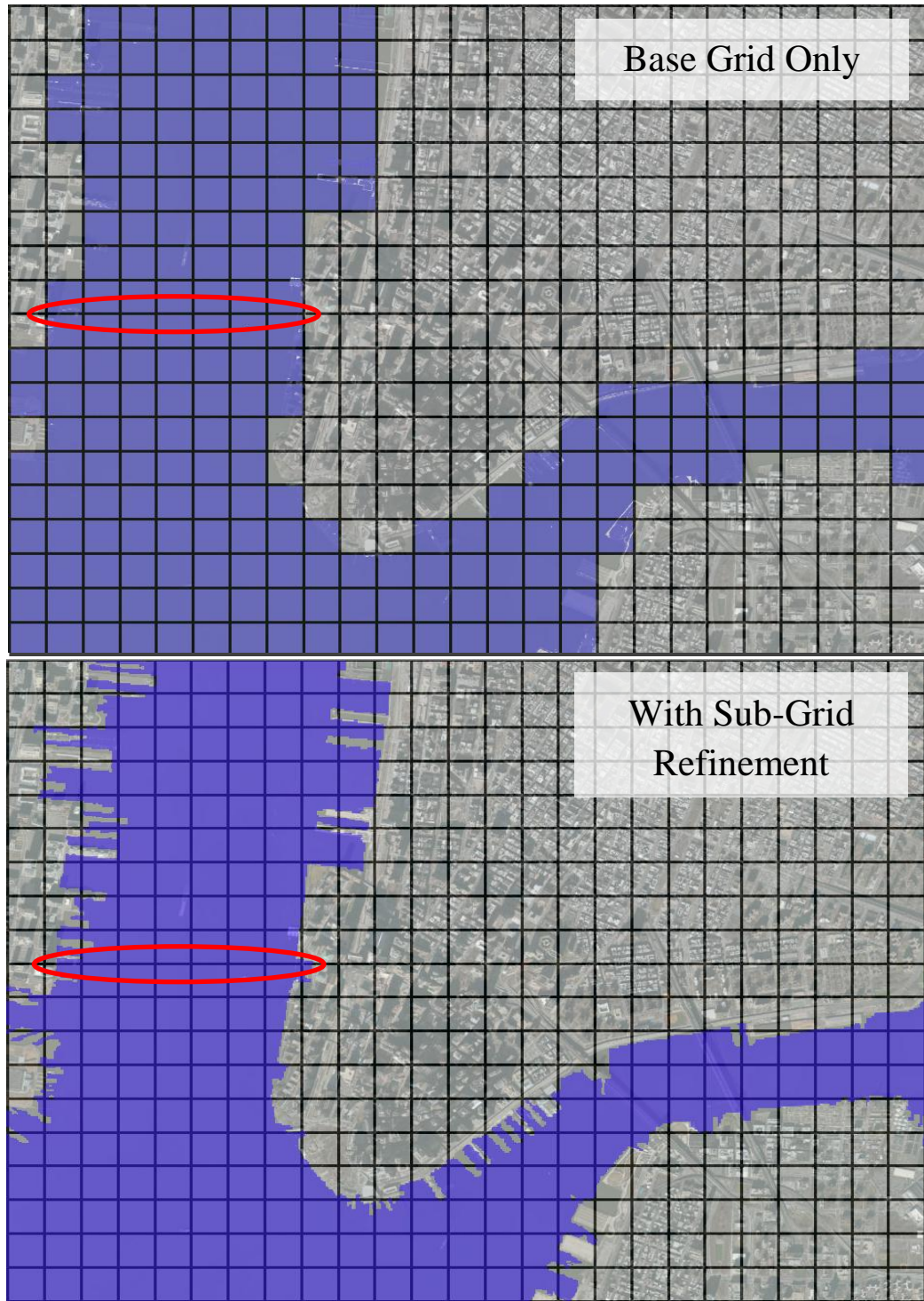
Figure 4.3. Two images depicting the 200m UnTRIM^2 model base grid near the tip of Manhattan at the confluence of the Hudson and East Rivers into the New York Bay without sub-grid refinement (top) and with 5m sub-grid refinement (bottom). The transect across the Hudson River bed enveloped in red is shown in Figure 4.4 detailing the sub-grid discretization methodology.
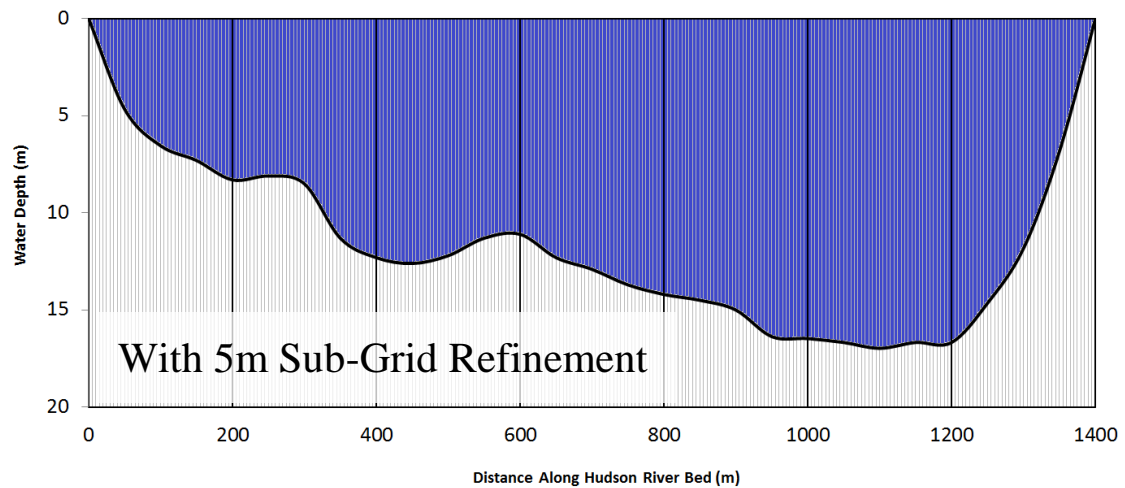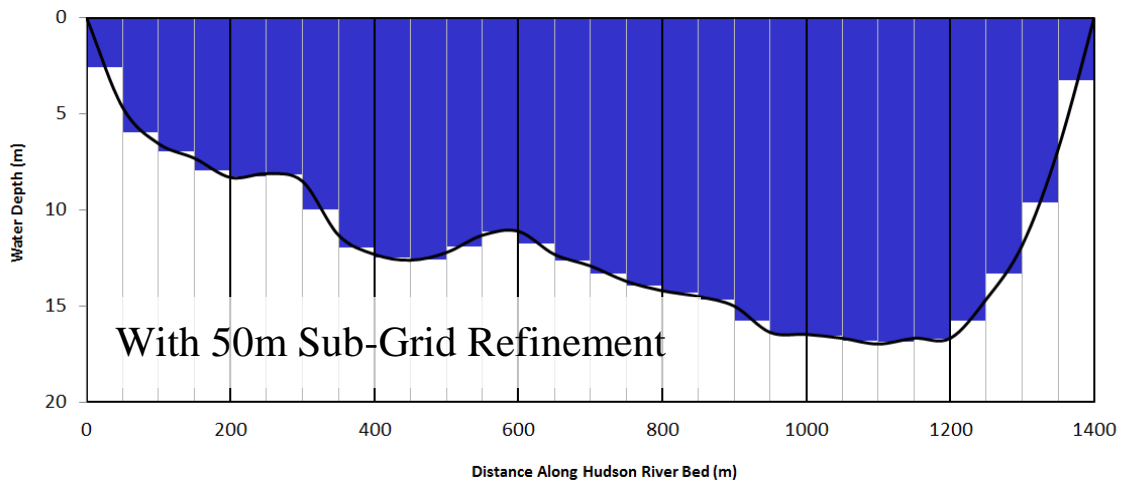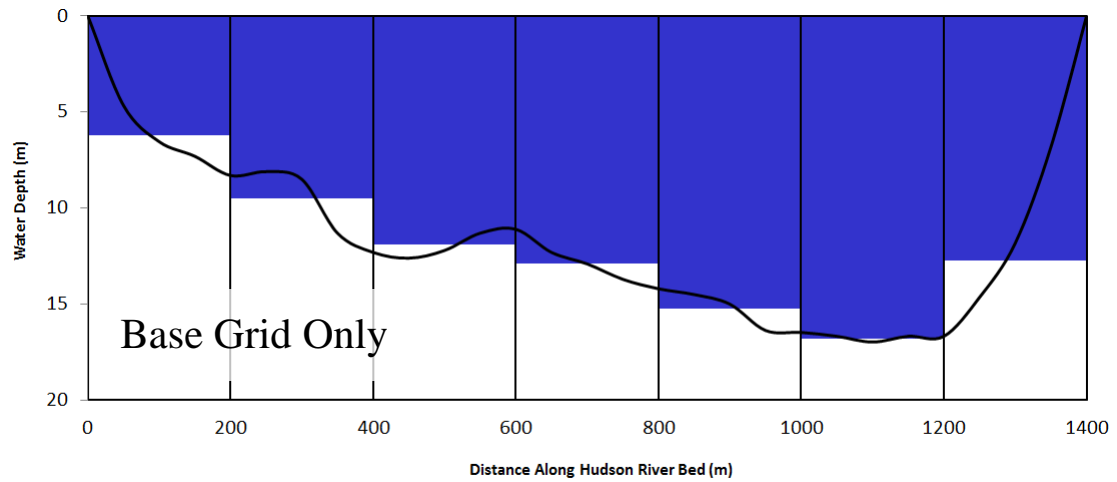
Figure 4.4. The transect across the Hudson River bed highlighted in red within Figure 4.3 is shown at the 200m base grid resolution without sub-grid refinement (top), with 4 subdivisions/cell for a 50m sub-grid (middle), and with 5m sub-grid refinement (bottom).

78

The sub-division methodology of the sub-grid essentially separates the base grid edges into more manageable pieces for computation in the model to estimate the cross-sectional area more accurately (as depicted in Figure 4.4), and thus the volume transport.

In Casulli's (2009) paper, the UnTRIM^2 sub-grid solution algorithm is referred to as a mildly nonlinear system for the free surface wherein the formulation for finite volume leads to a mildly nonlinear system for finite volume with respect to the free surface elevation. This nonlinear solver operates on the base grid cell sides, and is non-linear because as volume increases the slopes of the river banks are not uniform (Aldrighetti and Zanolli, 2005). Since the "container" holding the fluid is a complex shape, and not idealized flat walls perpendicular to a flat river bottom as depicted in Figure 4.5A, the fluid volume increases and decreases nonlinearly with the rise and fall of the free surface of the water with the tide as shown in Figure 4.5B (Casulli and Zanolli, 2012). Given the anomalous rise in the free surface of 3.5m observed at The Battery, NY, the storm surge causes a nonlinear increase in volume transport as the flood waters are not constrained by the riverbanks and freely flood into Jersey City and New York City as observed during Hurricane Sandy (Figure 4.5C).

Since cross section area is not calculated using only one average value for the base grid edge, as in the conventional modeling approach (Figure 4.3), but using multiple sections to estimate cross-sectional area using the divisions specified in the sub-grid; the wet volume (first term of the continuity equation times area) may be more accurately approximated (Figure 4.4), leading to more accurate non-linear volume transport calculations (Figure 4.5) (Casulli, 2009; Casulli and Stelling, 2011).

A likewise-comparison of a base grid against a sub-grid mesh of identical

resolution illustrates the classical modeling trade-off of favoring minimal computing time

over accuracy (Casulli and Zanolli, 2012). Ideally, the traditional modeling approach

would utilize a base grid only, at 5m resolution, and thus would involve minimal

approximation but become extremely computationally expensive. For example, the sub-

grid for New York City includes 4,496,833 sub-grid cells, which would need to be

resolved within the core computational grid in a conventional hydrodynamic model with

a 5m grid resolution. Furthermore, the same size domain at 1m resolution would require a

grid containing >110 million cells, thus requiring enormous computing power to simulate.

Therefore, attempting to resolve these unique topographic and bathymetric

differences in the conventional modeling sense is impractical. The sub-grid modeling

approach affords substantial computational savings via solving the shallow water

equations presented in Section 4.1 at the base computational grid while storing the

discretized bathymetric depths and Lidar-derived topographic heights within the sub-grid

(Casulli, 2009). Using the formulation presented in the next section, this study will

perform sensitivity tests using various resolution base grids to verify that there is minimal

decline in the computational accuracy in the New York Harbor during 2012 Hurricane

Sandy when utilizing the sub-grid non-linear solver (Casulli, 2009; Casulli and Stelling,

2011, Casulli and Zanolli, 2012). Sensitivity tests will be presented in the next chapter

regarding resolution of the core computational base grid that will be utilized to verify the

robustness of the partial wetting and drying scheme using over land gauges to compare

with street-level inundation model results with and without sub-grid refinement.

A. Linear Water Level Increase

3.5m Surge
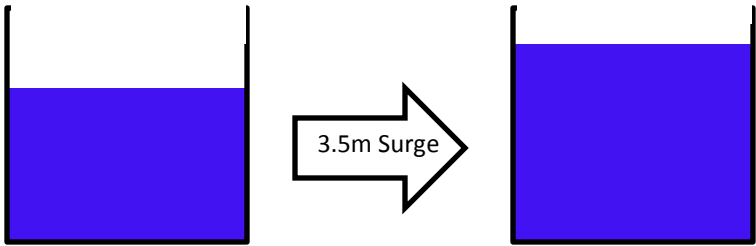
B. Nonlinear Water Level Increase

3.5m Surge
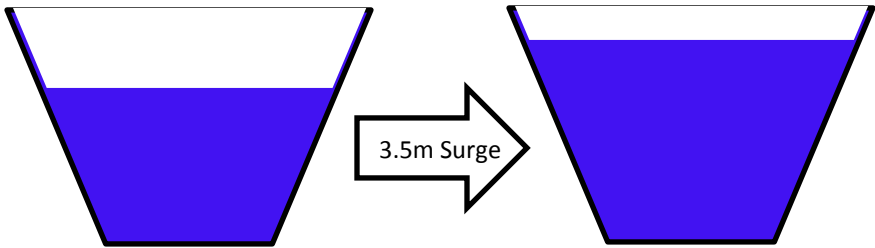
C. Modeled Nonlinear Water Level Increase

New Jersey

3.5m Surge

New York City

Water Depth (m)

5

10

15

20

0   200   400   600   800   1000   1200   1400

Distance Along Hudson River Bed (m)
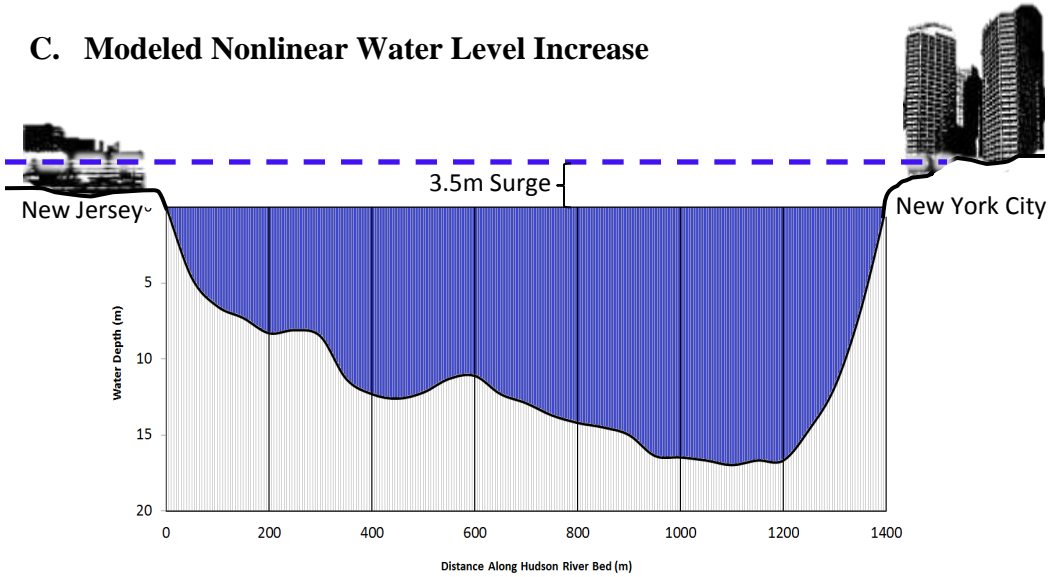
Figure 4.5A-C. Relational depiction of a linear (A), vs. the non-linear (B and C) water level and volume increase observed when utilizing sub-grid techniques in New York City during 2012 Hurricane Sandy's 3.5m storm surge observed at The Battery, NY.

4.2.1.3 Sub-Grid Model Formulation

The concept of a sub-grid nested within a coarse computational grid was

developed to utilize detailed bathymetric depths in order to model the spatial extent of

wetting and drying more accurately (Casulli, 2009). Using the imbedded sub-grid within

the coarse grid, it is possible to accurately determine the wet volume and cross-sectional

area of a coarse grid cell, which is required using the continuity equation (4-3). The water

levels and velocities are then computed on the coarse grid level to ensure the efficiency of

the model in each time step (Casulli and Zanolli, 2012). The sub-grid is then utilized as

an intermediate step to update volumes and cross-sectional areas, without the high

computational costs of simulation on a traditional complete high-resolution grid. The sub-

grid approach can generate velocities at the sub-grid level, and thus improve calculation

of the bottom stress (Stelling and Kerncamp, 2010). Assuming in the coarse grid model,

that the 2-D flow is dominated by friction, this results in the pressure gradient term being

balanced by the friction term in the momentum equation for each time step:

$$-g\frac{\partial \zeta}{\partial x} + cf\frac{U\|U\|}{h} = 0 \qquad (4\text{-}7)$$

where g is gravity, ζ is water surface elevation, and cf is the friction parameter (4-7).

This leads to:

$$U = \Omega\sqrt{\zeta_x} \quad \text{or} \quad \frac{U^2}{\Omega^2} = \zeta_x \qquad \text{where:} \qquad \Omega = \sqrt{\frac{gh}{cf}} \qquad (4\text{-}8)$$

and Ω is defined as conveyance velocity in (4-8). If we assume that the pressure gradient

within a time step is constant, the traditional approach leads to the velocity being constant

within a computation cell. In the sub-grid approach, however, it will allow the velocity field to vary within a coarse grid cell as follows. If we assume that every sub-grid has the same surface size, then each sub-grid velocity will obey:

$$\frac{cf_j}{gh_j}\left\|u_j\right\|^2 = \zeta_x = \text{constant} \tag{4-9}$$

where j is the index for each sub-grid cell (4-9), and the sub-grid velocities can be determined by the coarse grid velocity, $\|U\|$, with cf_j, and h_j, according to (4-10 & 4-11):

$$\frac{\|u_j\|}{\Omega_j} = \frac{\|U\|}{\Omega} \quad \text{for all } j \quad \rightarrow \quad \|u_j\| = \Omega_j \frac{\|U\|}{\Omega} \tag{4-10}$$

where:

$$\|U\| = \frac{\sum_{j=1}^{J} h_j\|u_j\|}{\sum_{j=1}^{J} h_j} \quad \text{and} \quad \Omega = \frac{\sum_{j=1}^{J} h_j\Omega_j}{\sum_{j=1}^{J} h_j} \tag{4-11}$$

Therefore, when the sub-grid approach is adopted, it enables the model to determine bottom friction more accurately from the sub-grid level, which can then be integrated to the entire cell instead of using the average velocity to obtain the average bottom friction.

4.2.1.4 Flow Resistance

Determining overland friction for flow resistance in urban areas is critical to accurately modeling inundation for high-resolution sub-grid applications. The calculation of friction is important in the interest of characterizing the resistance to fluid flow. In typical hydrodynamic studies, the effect of friction within the river channel must be

calibrated and parameterized in order to accurately assess fluid movement (Henderson, 1966; Dyer, 1986; Nitsche et al., 2012). When a storm surge brings fluid up on to land, the resistance to fluid movement at the bottom is significantly heightened due to skin friction, as the bottom boundary layer comprises a large portion of the water column, as the flood water depth may be only a meter or more (Christensen and Walton, 1980).

When not utilizing a high-resolution model grid in an urban setting, a very large friction parameter must be specified in the model in order to account for the insurmountable barrier to fluid flow posed by the presence of tall buildings in New York City as a form of macro-roughness. Any bottom roughness on a scale much greater than the wavelength of the approaching wave is characterized as macro-roughness, and such building features lead to turbulence and scattering of the wave, which is largely independent of wavelength and angle of incidence (Kökpinar, 2004; Nitsche et al., 2012). Flow and friction around buildings in a built-environment varies by two fundamental measurements: the width of the buildings, and the width of the street channels to accommodate fluid flow between them (Wang, 1983; Wang and Christensen, 1986). Given that buildings vary by shape and dimension, there is a nearly infinite variety of building shapes observed in a coastal ultra-urban environment such as New York City; each with its own flow resistance regime (Figure 4.6).

Laboratory experiments have been previously performed to determine friction specifications to account for the effect of form drag as fluid detours around buildings of various shapes and dimensions (Wang, 1983; Wang and Christensen, 1986). Additionally, laboratory prototypes of building configurations were constructed to determine that the width of the horizontal building face (facing the initial surge) divided

by the diagonal measurement between adjacent building corners correlates well with

form drag of the fluid around the building (Wang, 1983). If one does not wish to resolve

the streets between buildings, then form drag must be addressed as part of the overland

bottom friction specification. This effort will reasonably address the substantial

difference between the relatively small impact of bottom friction in a river channel,

which is carved by regular fluid flow over vast time scales, and the comparatively larger

friction over rough surfaces of a metropolitan city's infrastructure within the context of a

numerical model (Christensen, 1972; Wang, 1983; Wang and Christensen, 1986).

Early numerical models neglected the influence of bottom friction on storm surge

propagation. Ignoring the impact of friction is typically acceptable in exceedingly deep

regions of the ocean, however, the influence of bed friction in shallow water areas and

exceptionally shallow over land flow is not to be disregarded without consequential error.

Thus, modern numerical models incorporate the influence of bottom friction via the

Manning formula given in Equation (2-16) in 2-D formulations. Another method utilized

in this laboratory scale representation of flow resistance posed by buildings utilizes the

Darcy-Weisbach formula to calculate the bed shear stress (C_{Db}) in Equation (4-12):

$$C_{Db} = \frac{f' \rho u_m^2}{2} \qquad (4-12)$$

where ρ is the density of water, u_m is the spatially averaged velocity in the local vertical,

and f' is the friction factor. Elimination of C_{Db} by way of combination of Equations (2-

16) and (4-12) demonstrate that the friction factor is a function of the local depth and

Manning's n, which are both directly dependent upon the relative roughness of the

bottom the fluid is flowing over. Therefore, spatially-varying values of the friction factor are utilized to obtain reasonable results in modeling shallow water flows. It should be noted that using the Manning formula to calculate the bottom shear stress may lead to errors when the apparent bottom roughness is not sufficiently small compared to the depth (as is the case with macro-roughness) as indicated in Christensen and Walton (1980).

The influence of the friction factor may be determined for storm surges in unobstructed regions, which may apply to areas that are perennially wet such as the ocean floor and river bottoms, in addition to ephemerally wet land areas like grassy fields and flat, developed regions, which may become entirely inundated in storm surge scenarios. Given that virtually all hurricane-induced surges are within the range of hydraulically rough flow, a velocity profile based upon a modified version of Prandtl's mixing length theory suggested by Christensen (1972) was employed in a laboratory study using:

$$\frac{\overline{u}}{u_f} = 2.5 \ln\left(\frac{29.73\,z}{k} + 1\right) \qquad (4\text{-}13)$$

where $\overline{u}$ is defined as the time-averaged velocity in the direction of flow at z distance from the bottom, u_f is the friction velocity, and k is Nikuradse's equivalent sand roughness (Equation 4-13). The modified version of Prandtl's mixing length theory affords a profile of velocities which satisfies the no-slip condition at the bottom, while the classic velocity profile leads to impossible negative velocities approaching -∞ (Christensen, 1972). Additionally, use in practical applications of 2-D storm surge models dictates that the time-averaged velocity profile be transformed to a depth-

averaged velocity profile. This transformation assumes that the depth-averaged velocity

ideally occurs at a distance of z = 0.368 d from the bottom for the modified logarithmic

vertical velocity profile, where d/k is >1. Using this assumption, the previous equation

becomes:

$$\frac{u_m}{u_f} = 2.5 \ \ln\left(\frac{10.94 \ d}{k} + 1\right) \tag{4-14}$$

The velocity profile in Equation (4-14) relates to the friction factor through substitution

of the Darcy-Weisbach formula into the definition of the friction velocity via Equation

(4-15):

$$\frac{u_m}{u_f} = \left(\frac{2}{f'}\right)^{1/2} \tag{4-15}$$

Solving the above equation for f' and introducing Equation (4-14), yields a general

expression for friction factor for surges in unobstructed regions (Equation 4-16):

$$f' = \frac{0.32}{\left[\ln\left(\frac{10.94 \ d}{k} + 1\right)\right]^2} \tag{4-16}$$

Bottom friction factor for storm surge applications in areas including buildings

and other obstructions is technically complex, especially in areas of high building

density. In terms of friction, buildings may be defined as roughness elements with

significant heights that may protrude through the water layer as a form of macro-

roughness, or simply be comprised of rigid elements of considerable height capable of

creating a form drag that is significantly larger than surface friction within the same area.

In the scenario of a current that flows over an obstructed area where the density is M per unit area, the mean diameter of the obstruction in the projected plane (normal to the flow) is D, and the mean drag coefficient is C_D. The equation below assumes steady or partially-steady flow within the range of rough flow to represent head loss (ΔH) per unit weight of fluid over a bed length of L:

$$\Delta H = f'_e \frac{u^2{}_m}{2g} \frac{L}{R} = f' \frac{u^2{}_m}{2g} \frac{L}{R} (1 - \varepsilon) + M C_D \, dD \, \frac{u^2{}_m}{2g} \frac{L}{R} \tag{4-17}$$

where R is the hydraulic radius, and ε is the fraction of total area occupied by obstructions. An equivalent friction factor, f'_e may be defined to consider the effects of form drag and skin friction simultaneously in the determination of flow resistance. A version of the Darcy-Weisbach equation is introduced from Equation (4-17) to yield:

$$f'_e = f'(1 - \varepsilon) + M C_D \, dD \tag{4-18}$$

where f' is given in Equation (4-16) and may be validated via experimentation. The law of conservation of energy dictates that the total energy head at an upstream location (1) must be equal to the total energy head at an analogous downstream location (2) plus the head loss between the two locations in the following form of the Bernoulli equation:

$$f' = d_1 + \frac{u^2{}_{m1}}{2g} = d_2 + \frac{u^2{}_{m2}}{2g} + \Delta H \tag{4-19}$$

Relation of recorded results of head loss from Equation (4-19) to the Darcy-Weisbach equation (Equation 4-12) ultimately provides Equation (4-20):

$$\Delta H = f'_e \, \frac{u^2_{avg}}{2g} \, \frac{L}{R_{avg}} \tag{4-20}$$

In Equation (4-20), $u_{avg} = \frac{(u_{m1}+u_{m2})}{2}$, and $R_{avg} = \frac{(R_1+R_2)}{2}$; the equivalent friction factor

may be determined for the roughness elements of interest (Wang and Christensen, 1986).

4.2.2 Review of Laboratory Flume Experiment for Flow around Buildings

This review of a laboratory flume experiment entitled "Friction in Hurricane-
Induced Flooding," conducted at the University of Florida in 1983, serves to provide
some insight regarding appropriate bottom friction specification for overland flooding
around buildings like those observed in the ultra-urban environment of New York City
(Wang, 1983). Based upon the need for a more accurate prediction of hurricane-induced
inundation in coastal regions to address applications that help govern land use planning,
flood insurance rate determination, and proper positioning of the construction set-back
line, Wang (1983) developed a methodology for describing the overland friction factor
for flow resistance in urban areas for improved parameterization of over land friction
specification for improved numerical model results. The study utilized a laboratory flume
to place special emphasis on the friction characteristics of buildings, which is the single
greatest source of flow resistance in developed areas (Wang, 1983).

4.2.2.1 Setup and Results of Laboratory Flume Experiment

The presence of buildings in developed areas introduces a form of macro-
roughness, which is insurmountable for shallow water movement to flow over, and
constitutes the principal roughness elements which would significantly affect the

apparent bottom shear stress as well as the wind shear stress during flooding caused by a substantial storm front or hurricane. Typically, buildings are not arranged in uniform patterns, but as building density increases, surface area for necessary infrastructure to service vehicular and foot traffic to those buildings decreases (Figure 4.6). Incidentally, these areas are also the path of least resistance in terms of fluid flow during storm surge scenarios, as roadways and sidewalks are lower elevations than the buildings surrounding them, and provide ideal alternate pathways for a propagating surge blocked by buildings. Buildings may be classified into three categories defined in Wang (1983) (Table 4.1):

1) High-rise buildings are those which have a surface area of $> 10,000 \text{ft.}^2$.

2) Medium-rise buildings are between $2,500 \text{ ft.}^2$ and $10,000 \text{ft.}^2$.

3) Residential buildings are considered to be $< 2,500 \text{ft.}^2$.

Table 4.1. Building dimension parameters drawn and analyzed from orthophotographs of Broward and Dade Counties, Florida, and modeled dimensions for a laboratory flume using three building classifications: high-rise, medium-rise, and residential. N_ℓ is horizontal and N_d is vertical scaling; adapted from Wang and Christensen, 1986.

| Type of Buildings | Orthophotographs of Coastal Buildings | | | | | N_ℓ | Laboratory Flume Model ($N_d = 10$) | | |
| | Appx. Dimension (m) | | Density | | | | Dimension (cm) | | Density |
	Length	Width	#/46,452 m^2	#/acre	Coverage Ratio (*M*)		Length	Width	#/2.1 m^2
High-Rise	69	33	7.19	0.63	0.36	174	39.4	19.1	10
Medium-Rise	31	15	23.62	2.06	0.24	80	39.4	19.1	7
Residential	19	9	68.87	6.00	0.26	48	39.4	19.1	7
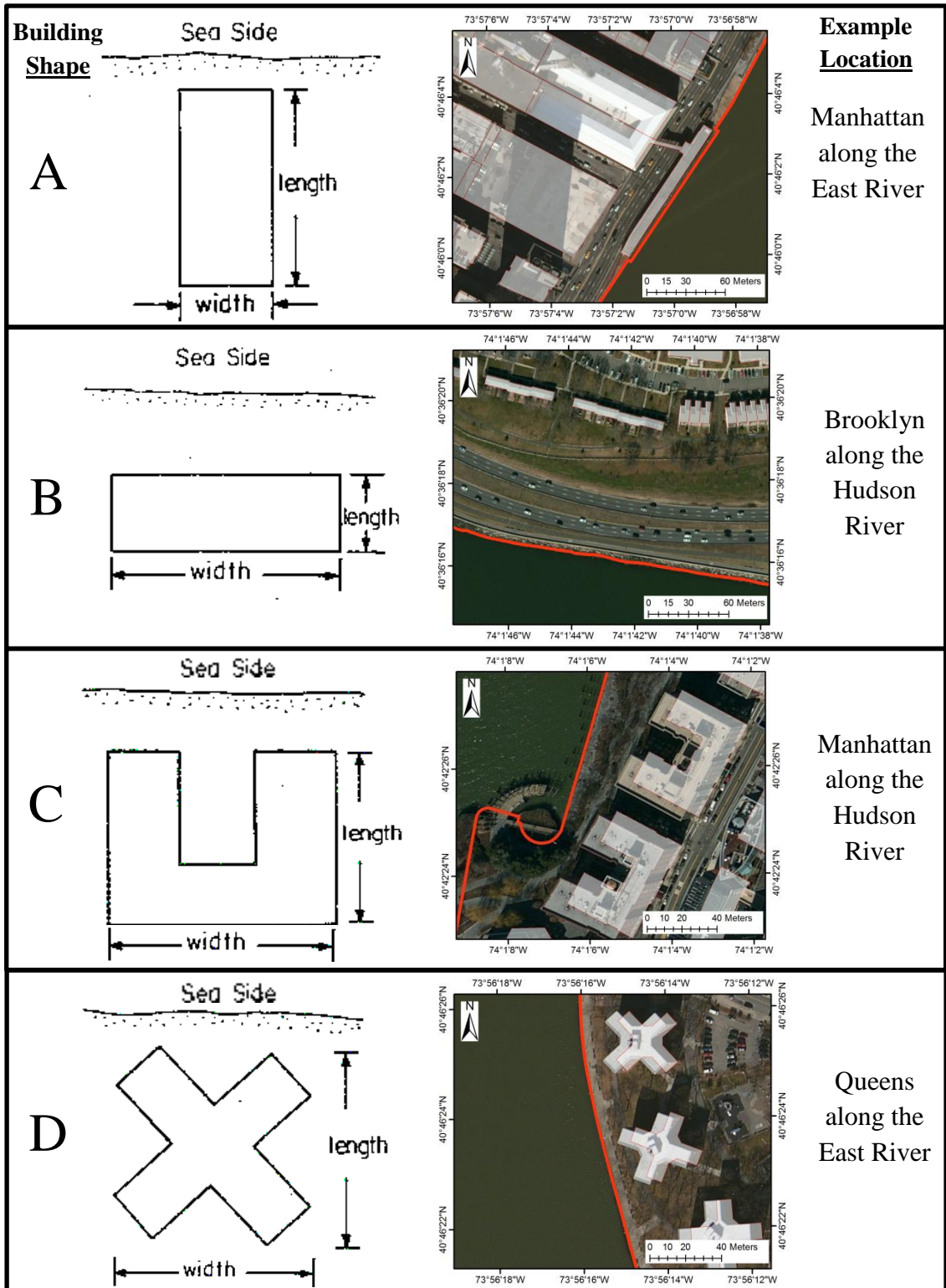
Figure 4.6. Sketch of top view of various outlined building shapes and locations observed in New York City with red highlighted shoreline; drawings adapted from Wang, 1983.

The study by Wang (1983) observed orthophotographs of Broward and Dade Counties in Florida to analyze the dimensions and densities of buildings in coastal areas. Typical building shapes and orientations are shown in Figure 4.6 with comparable building configuration comparisons from New York City. Building shape A, shown in Figure 4.6, was observed to be the shape of the majority of buildings observed (>50% of all buildings surveyed) in their study, as well as in each of the boroughs of New York City. The laboratory experiment made use of standard concrete cinderblocks with dimensions of 19.1 x 39.4cm, with a height of 19.1cm, to represent buildings and placed them into a shallow flume using the scaling outlined in Table 4.1. The experiments are conducted in a flume 2.44m wide x 36.6m long, with a height of 0.81m (Wang, 1983).

Buildings were arranged in staggered and aligned configurations to represent the common building arrangements observed in coastal zones. New York City has almost entirely aligned buildings arranged in city blocks due to its extremely high population density. Configurations 1-13 correspond to building densities and spacing observed with high-rise buildings, configurations 14-21 were used for both medium-rise and residential experimental scenarios (Figure 4.7A-B). Greater than 10 experiments were conducted for each of the 21 patterns shown in Figure 4.7A to calculate the average C_D in varied conditions ranging from Reynolds numbers of 20,000 to 70,000 and Froude numbers of 0.1 to 0.5 regulated via pump and sluice gate. Results obtained for medium rise building areas can be converted using appropriate scaling factors to use in residential areas, given that the two areas are presumed to possess the same relative building distributions with only dimensional differences. The average values of the experimental results for each of the 21 configurations are given in Table 4.2 and shown in Figure 4.8.

High-Rise Building Configurations

Aligned Medium-Rise & Residential Buildings

Staggered Medium-Rise & Residential Buildings
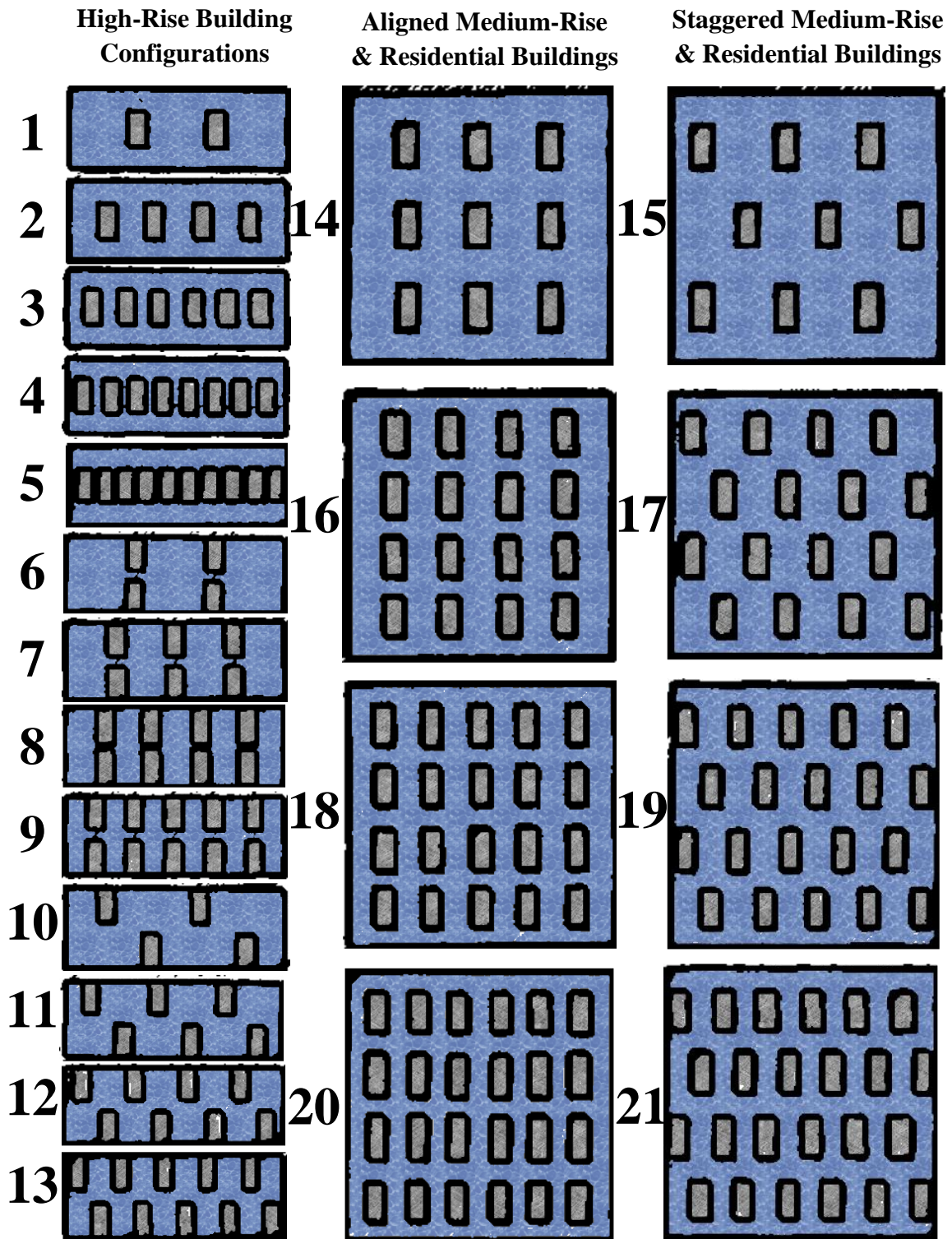
Figure 4.7A. Top view of 21 experimental flume cinderblock building configurations. High-rise configurations have dimensions of 0.87 x 2.44m, and medium-rise and residential building arrangements have dimensions of 2.44 x 2.44m, with fluid flow originating from the top flowing toward the bottom; sketches adapted from Wang, 1983.
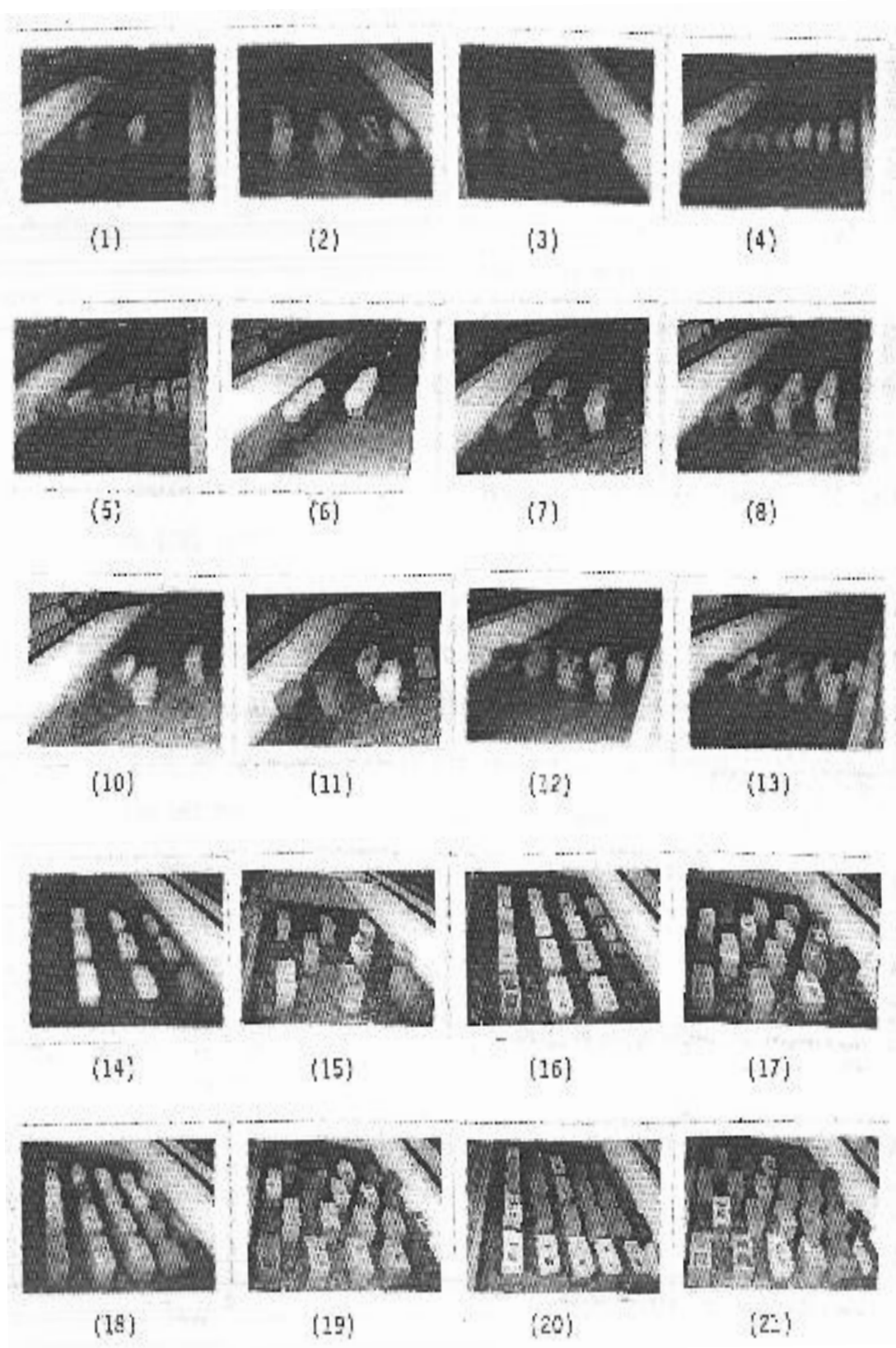
Figure 4.7B. Photographs of 21 flume cinderblock building configurations (Wang, 1983).

94

Diagonal distance (S_d), measured between the buildings in adjacent transverse

rows (from multiple row building configurations 6 - 21), was shown to be positively

correlated with bottom friction, C_{Db}, for both aligned and staggered building

arrangements, as seen in Figure 4.7A-B. The good correlation is a result of the diagonal

spacing, wherein magnitude affords a difference of disposition for the evenly distributed

buildings or roughness elements. Additionally, the diagonal spacing also provides a

relative measure of building density as determined in Table 4.1. Thus, the higher the

density of buildings in a region, the smaller the disposition parameter, S_d/D, will be,

resulting in greater values for drag coefficient, C_{Db}. The disposition parameter of the

staggered pattern is observed to be smaller than the aligned pattern, resulting in a larger

drag coefficient when considering buildings with like dimensions and density (Wang,

1983). Shen (1973) came to the same conclusion in a similar experiment evaluating the

average drag coefficient of two cylinder patterns, aligned and staggered, within the

context of an open channel flow regime, thus validating Wang's (1983) experiment.
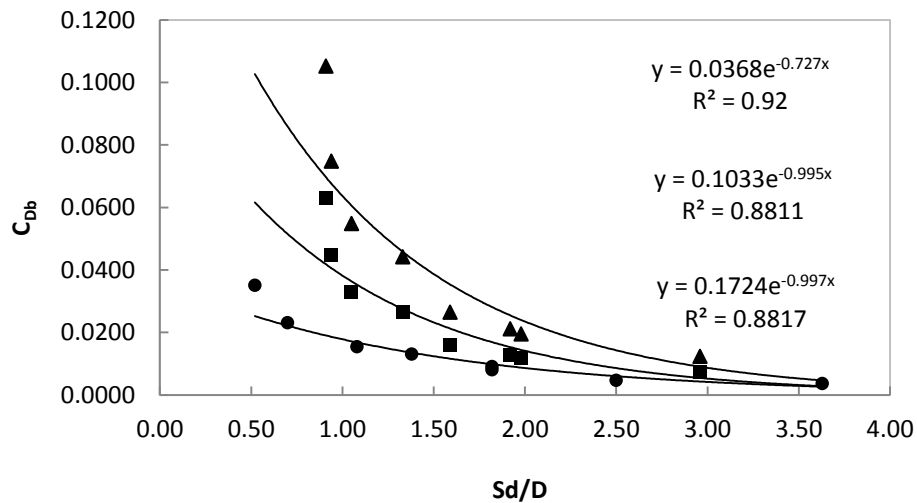
Figure 4.8. Relation between drag coefficient for bottom friction (C_{Db}), and the diagonal
disposition (S_d/D) of buildings ascertained from laboratory flume studies of high-rise ($\bullet$),
medium-rise ($\blacksquare$), and residential ($\blacktriangle$) building configurations; adapted from Wang, 1983.

Table 4.2. Statistical values from experimental flume results for bottom friction in regions obstructed by buildings; adapted from Wang, 1983.

Configuration #	Building Type	f'_e			C_D		
		Mean	Std. Dev	% of Mean	Mean	Std. Dev	% of Mean
1	High-Rise	0.0013	0.0003	23	0.788	0.163	21
2		0.0064	0.0006	38	1.965	0.254	13
3		0.0180	0.0030	17	3.406	0.181	5
4		0.0460	0.0090	20	7.014	1.121	16
5		0.1580	0.0260	16	17.813	1.298	7
6		0.0036	0.0006	17	1.108	0.123	11
7		0.0046	0.0011	24	0.907	0.230	25
8		0.0090	0.0010	11	1.346	0.119	9
9		0.0130	0.0010	8	1.597	0.189	12
10		0.0080	0.0014	18	2.369	0.275	12
11		0.0154	0.0029	19	2.965	0.227	8
12		0.0230	0.0040	17	3.662	0.221	6
13		0.0350	0.0050	14	4.315	0.389	9
14	Medium-Rise	0.0074	0.0011	15	1.232	0.170	14
15		0.0127	0.0030	24	2.082	0.173	8
16		0.0117	0.0020	17	1.088	0.096	9
17		0.0329	0.0067	20	3.040	0.114	4
18		0.0158	0.0018	11	1.181	0.097	8
19		0.0448	0.0072	16	3.355	0.098	3
20		0.0265	0.0038	14	1.586	0.089	6
21		0.0631	0.0112	18	3.926	0.120	3
14	Residential	0.0123	0.0018	15	1.232	0.170	14
15		0.0211	0.0050	24	2.082	0.173	8
16		0.0195	0.0034	17	1.088	0.096	9
17		0.0548	0.0112	20	3.040	0.114	4
18		0.0264	0.0030	11	0.167	0.097	8
19		0.0747	0.0120	16	3.355	0.098	3
20		0.0441	0.0063	14	1.586	0.089	6
21		0.1052	0.0186	18	3.926	0.120	3

4.2.2.2 Application of Flume Results to Sub-Grid Model

The model's specified bottom friction for over land flow is verified by the results of this small scale laboratory experiment to ascertain flow resistance to storm surge induced inundation in the presence of buildings (Wang, 1983). These results were then scaled to average building spacing using dimensional analysis and through proper scaling of building disposition parameters from the laboratory experiment to average building spacing within the city blocks in each New York City borough. Detailed description of the principles of dynamic similarity relating the laboratory experimental results to that of the prototype scale can be found in Appendix B. Separate drag coefficient equations similar to those given in Figure 4.8, may be calculated for each of the three building classifications in New York City comparable to those measured from orthophotographs in Broward County and Dade County, Florida, from Wang, 1983 (Figure 4.6).

Application of these equations requires knowledge of building density and building classification. This information may be calculated for New York City utilizing GIS tools on the building layer embedded within the sub-grid model. Considering that most of the buildings in New York City are aligned in configuration to maximize transportation efficiency, and that virtually all of the buildings along the water or within the flood risk area fall into the classification of high-rise buildings in the ultra-urban metropolis; the following method was utilized to calculate building density for each of the boroughs in New York City in the interest of applying a spatially-varying over land friction coefficient, C_{Db},. This C_{Db} will be specified in the sub-grid model's 2-D formulation using Manning's formula with a spatially varying bottom roughness, n (Table 4.3) by way of a similarity solution described in Appendix B.

Table 4.3. Spatial analysis results for building density and average diagonal building disposition within each New York City borough.

#	Borough	200x200m Cells	Total Cell Area (m^2)	Building Area (m^2)	Coverage Ratio (M)	C_{Db}	n
1	Manhattan	1198	47,920,000.00	19,410,903.63	0.4051	0.2813	0.0978
2	Brooklyn	1271	50,840,000.00	16,159,370.29	0.3178	0.2595	0.0938
3	Queens	1535	61,400,000.00	18,432,395.83	0.3002	0.2551	0.0931
4	Bronx	1101	44,040,000.00	10,685,412.81	0.2426	0.2407	0.0905
5	Staten Island	402	16,080,000.00	3,635,814.19	0.2261	0.2365	0.0896

Using GIS tools, the building areas were retrieved from the vector dataset. Subsequently, the feature to polygon tool was utilized to convert the contour lines to polygons for each building. The resulting polygons were intersected with the exported base grid cell layer to divide up building data extracted from the building contours into 200m x 200m cells to calculate friction parameters for each base grid cell based upon unique building density calculations for each grid cell. Interior terrestrial base grid cells (not including grid cells containing portions of the river) were selected as a representative sample of building density within each 200m x200m base grid square for each of the boroughs within the sub-grid domain. Table 4.3 includes spatial analysis results for building density and analogous measures of C_{Db} with translated values for Manning n using Wang's suggested C_{Db} for high rise buildings in an aligned configuration: $C_{Db} = 0.18 + 1.0M \times 10^4$ (1983). Overland values for Manning n are spatially varying by building density within each New York City borough according to Table 4.3. Building

density ratios calculated from the 200x200m base grid cells for each borough were converted to 1x1m scale to yield C_{Db} values ranging from 0.2365 in Staten Island to 0.2813 in Manhattan. These values translate to Manning *n* values via Equation (2-16) for a range from 0.0896 in Staten Island to 0.0978 in Manhattan (Table 4.3). Standard Manning *n* values of 0.020 in the Hudson River, and 0.030 in the East River and Harlem River to represent bottom drag within the New York Harbor. Both of these values are reasonably close to the average Manning *n* value of 0.025 for clean and straight river channels (Henderson, 1966). In review, provided the use of high-resolution Lidar-derived topography data and extremely accurate vector building data, streets between buildings may be sufficiently resolved within the model sub-grid to intrinsically account for the form drag posed by the storm surge flow around building obstacles. The arrangement and configuration of buildings along with the disposition between rows of buildings along the water's edge vary greatly by shape and size, as noted in Figure 4.6 (Wang, 1983). Each of these building shapes would need to be uniquely accounted for in the model's friction specification if their shape is not resolved within the model grid. This is a task that is either impossible or highly impractical due to computational demand when using the conventional modeling approach. While the inland metropolitan area surrounding New York City is generally structured in a block system to maximize utility for the urban population, buildings adjacent to the water's edge often have unique shapes, being designed to maximize the number of rooms with a view of the adjacent body of water (Figure 4.6). Each of the buildings varies by shape and dimension, and thus has their own unique form drag. This unique form drag is in addition to the friction posed by the ground surface, both of which must be accounted for in the model's friction parameterization if

the model grid does not sufficiently resolve buildings. Thus, the sub-grid model effectively resolves the streets using high-resolution topography to utilize a more universal friction specification.

4.2.3   External Model Forcings

4.2.3.1 Atmospheric Forcing

Atmospheric data for the observation simulation of 2012 Hurricane Sandy in the New York Harbor region were collected in units of m/s from NOAA atmospheric observation data at Bergen Point, New York (NOAA Station # 8519483). Atmospheric observations were subsequently pre-processed and prepared as uniform wind and pressure inputs throughout the small-scale domain. U and V velocities were extracted and wind fields were interpolated to 6-minute time steps, commencing on October 01, 2012, at 00:00 GMT, and ending November 04, 2012, at 00:00 GMT. Atmospheric pressure was converted from mbars to Pascals, and prescribed as a uniform atmospheric pressure input throughout the domain in similar fashion to the prescribed wind inputs.

4.2.3.2 Freshwater River Inflow

Hourly freshwater flows for the Hudson River were obtained from the United States Geological Survey (USGS) and specified as a flux boundary condition. These data were applied uniformly as a forcing along the sides of 9 elements along the northern boundary of the model domain near Wappingers Falls (Station #01372500). The model input has been adjusted by 30 minutes to account for the considerable distance from the station to the edge of the sub-grid domain.

4.2.3.3 Tidal Open Boundary Forcing

Tides are forced via three open boundaries: one to the south, one in the west, and one in the east. The southern open boundary in the sub-grid domain is located at the mouth of the New York Bay into the Raritan Bay leading to the Atlantic Ocean. The open boundary to the west is where the Kill van Kull connects the Newark Bay to New York Bay. The third open boundary lies to the east and connects the East River to the Long Island Sound. In the simulation driven via observation data, the southern boundary is forced using observation data from USGS Rockaway Inlet (Station #1311875), the west boundary uses NOAA Bergen Point (Station #8519483), and the east boundary is forced using water level data from NOAA Kings Point (Station #8516945) shown in Figure 4.1. The forcing data from Rockaway Inlet has been converted from NGVD29 to and delayed by 12 minutes to account for its distance from the southern boundary of the grid at Coney Island, south of the Verrazano Narrows.

CHAPTER 5: Geospatial Data Analysis

5.1   Pre-Processing Development of DEM

The setup and design of the model DEM to be used with the New York City sub-grid includes multiple topography and bathymetry sources with the addition of buildings for the metropolitan area of New York City (Table 5.1). The DEM was primarily configured in GIS ArcInfo v.10.1. The multiple topography datasets collected from the USGS National Elevation Dataset were mosaicked as rasters (1/3 arc sec or ≈10m resolution or better). The mosaic map operation made use of 32-bit float pixel type to preserve a significant number of digits (at least down to mm scale) for both positive and negative value elevations to produce a single geotiff of all USGS data called 'DEM_Hudsonb.tif'. According to the metadata, the primary data source for the USGS data were derived from final return Lidar point cloud data and preprocessed by the USGS to remove objects of the built environment such as city infrastructure and buildings.

Table 5.1. Data sources and resolutions for representing topography and bathymetry for the sub-grid with Lidar-derived topography.

	Data Source	Resolution	Area
Bathymetry	NOAA Coastal Relief Model	3 arc sec (≈90m)	Coastal Regions
	NOAA Bathymetric Survey Data	1/3 arc sec (≈10m)	Hudson River, East River, Kill van Kull, Raritan Bay, and New York Bay
Topography	USGS National Elevation Dataset	1/3 arc sec (≈10m)	Low-elevation areas around the New York Harbor and Raritan Bay
	USGS National Elevation Dataset	1/9 arc sec (≈3m)	Select areas of New York City
	Open NYC Building Inventory	0.1m	New York City Buildings

The resulting raster was projected to NAD83 UTM18N, the desired geographic projection, and retitled 'DEM_Hudsonb_utm18n.tif'. A polygon shapefile was drawn around the area of interest for inclusion in the sub-grid model domain to crop the DEM to include the areas of the Hudson River south to Coney Island and north to Yonkers to include the confluence of the Harlem River with the Hudson River. The shapefile is also bounded in the west by the NOAA-operated gauge at Bergen Point along the Kill van Kull, and east to where the Long Island Sound meets the East River near the NOAA gauge at Kings Point via the ArcGIS editor to produce 'NY_SG_croputm18n proj3HarRvr.shp'. Using this mask polygon, the extract by mask function from the GIS Spatial Analyst toolbox was utilized to crop out the area of interest from the large DEM and crop out the water areas using a combined shoreline layer of New York and New Jersey to create the 'DEM_NYC_2HarRvr2_5m.tif' dataset (New Jersey Shoreline, 2008; New York City Shoreline, 2012).

Finally, the cropped DEM was resampled to 10m resolution 'DEM_NYC_2HarRvr2_5m.tif', and 5m resolution 'HarRvr2_5m.tif' to minimize the interpolation impact within the grid generation software platform when building the sub-grid. In the NAD83 UTM Zone 18N projection, the output cell sizes should be 9.09m and 4.54m, for 10m and 5m resolutions, respectively. The topographic geotiffs were converted to ANSI ASCII format for compatible use with the grid generation software 'A_DEM_HarRvr2_5m.asc'.

Coastal relief data were downloaded as an ArcInfo ASCII file at 90m resolution from NOAA's National Geophysical Data Center and imported into ArcGIS as the base bathymetry DEM: 'DEM_bathy_2HarRvr2'. Higher resolution (≈10m) NOAA digital

bathymetric survey data were collected where available and assimilated into the bathymetry DEM via the merge function while assuring elevation symmetry along the seams. The following digital data surveys were collected from NOAA (NOAA NOS, 2006): H11600 collected in 2006 along the New York Bay and Verrazano Narrows in the south central area of the sub-grid domain, H11353 collected in 2004 along the East River, and H11395 gathered in 2006 along the Hudson River adjacent to Manhattan Island. The merged bathymetry data were then reprojected to NAD83 UTM18N and resampled to 10m and 5m resolution in similar format with the merged topography DEM to produce 'DEM_bathy_2HarRvr2_10m2.asc', and 'DEM_bathy_2HarRvr2_5m2.asc', respectively. The geotiffs were converted to ANSI ASCII format to yield: 'B_DEM_bathy_2HarRvr2_5m2.asc'.

Vector building footprints and building heights were obtained from the GIS repository of New York City, via the NYC DOITT database, last updated in 2013 (New York City Buildings, 2013). The five boroughs of New York City were merged from five vector datasets into one to form 'NYC_Buildings.shp'. The resulting shapefile of building polygons was reprojected to use the same geographic projection used for the topographic and bathymetric DEM: NAD83 UTM18N 'NY_Buildings_utm18nproj.shp'. Using the building footprints layer as a mask polygon, use the extract by mask function in the GIS Spatial Analyst toolbox to create a template geotiff raster of buildings at the highest re-sampled resolution using the building heights field as the elevation above MSL to create: 'HarRvr2_5m_bldg.tif'. The geotiff output for the building layer DEM was exported via ANSI ASCII format for compatible use with Janet, the sub-grid generation software: 'C_DEM_HarRvr2_5m_bldg.asc'.

Within Janet v.2.9.36, the polygon shapefiles were imported to be the template for the sub-grid boundary using 'NY_SG_croputm18nproj3HarRvr.shp'. The polygon editor was utilized to copy the imported boundary polygon to the polygon mask layer for use in building the model boundary. The command to "build regular quad grids" was used to specify an appropriate base grid cell size (200m was used for New York City), setting model depths to be stored at the edges of each cell in the UnTRIM^2 grid. The base grid cell size should be selected unique to each domain to provide at least two base grid cells across the channel of each domain; this grid allows for, on average, approximately 7-8 base grid cells across the Hudson River, 3-4 across most parts of the East River, and 1-2 across the narrow straits of the Harlem River.

Once the regular quadrilateral grid cells have been built, the topography, bathymetry, and building ASCII DEMs were imported into the grid editor. Boundary polygons were subsequently generated for the grid using the previously imported polygon in the polygon mask layer. To complete creation of the land boundary, the system editor was used to edit the boundary markers to set the grid boundary marking the edges completely outside of all mask polygons, and then manually unselecting water boundaries along the south, west, and east as open boundaries, and setting the north boundary along the Hudson River as a flux boundary condition.

The bathymetry layer 'B_DEM_bathy_2HarRvr2_5m2.asc' was then merged with the topography layer 'A_DEM_HarRvr2_5m.asc', to fill in a complete grid with topography and bathymetry. The buildings in layer: 'C_DEM_HarRvr2_5m_bldg.asc', which had been preprocessed out from the original Lidar point cloud data prior to being uploaded as geotiffs to the USGS Seamless Map Server were overwritten back on top of

the merged topography and bathymetry DEM to account for the natural impediment to inundation posed by buildings in the final DEM. Given that the building density is extremely high in New York City, with many of the buildings being exceedingly tall or skyscrapers, using raw Lidar point cloud data would fail to sufficiently resolve streets.

Finally, the sub-grid was generated with the specification of 40 divisions along each base grid cell edge to produce a 5m resolution sub-grid. The combined 5m resolution DEM was subsequently "interpolated" at its native resolution onto the 5m resolution model sub-grid via the digital terrain model module using the natural neighbor (Sibson) interpolation method. The combined topography, bathymetry, and buildings layer were saved as an .xyz point file with 5m spacing, and the sub-grid mesh was saved as a model grid file compatible with UnTRIM^2 for use in modeling inundation caused by Hurricane Sandy in an urban environment: 'NY_bldg_5msg200mbg.grd'.

5.2   Observation Data Compiled during 2012 Hurricane Sandy

Making observations during a hurricane is both physically and technically challenging. Throughout 2012 Hurricane Sandy, six categories of observation data survived and were assembled from various resources for comparative statistical analysis using the metrics described in Appendix A. Results were obtained via sub-grid simulation of the New York Harbor to address 2012 Hurricane Sandy. Model performance was assessed by statistical comparison with a variety of verified field measurements and calculated flood extents from various agencies.

The observation dataset utilized to validate the sub-grid model's predicted flood periods and maximum inundation extents includes:

1)   5 tidal records from 1 USGS and 4 NOAA permanent tide gauges (Figure 4.1), providing both astronomical tide predictions and water level observations, with the calculated difference between these two products being the storm tide

2)   7 overland USGS-recorded rapid deployment gauges installed prior to the event and retrieved post-Hurricane Sandy within the sub-grid domain (Figure 4.1)

3)   73 USGS-collected non-wave-affected high water mark measurements within the New York Harbor sub-grid model domain (Figure 5.1)

4)   80 FEMA-reported inundated school locations indicating water level thickness at specific sites throughout the sub-grid domain (Figure 5.2)

5)   1 FEMA maximum extent of inundation map based upon interpolation of the USGS's high water marks and the best available elevation dataset (Figure 5.3)

6)   12 MTA subway stations recorded as flooding from the street (Figure 5.4).
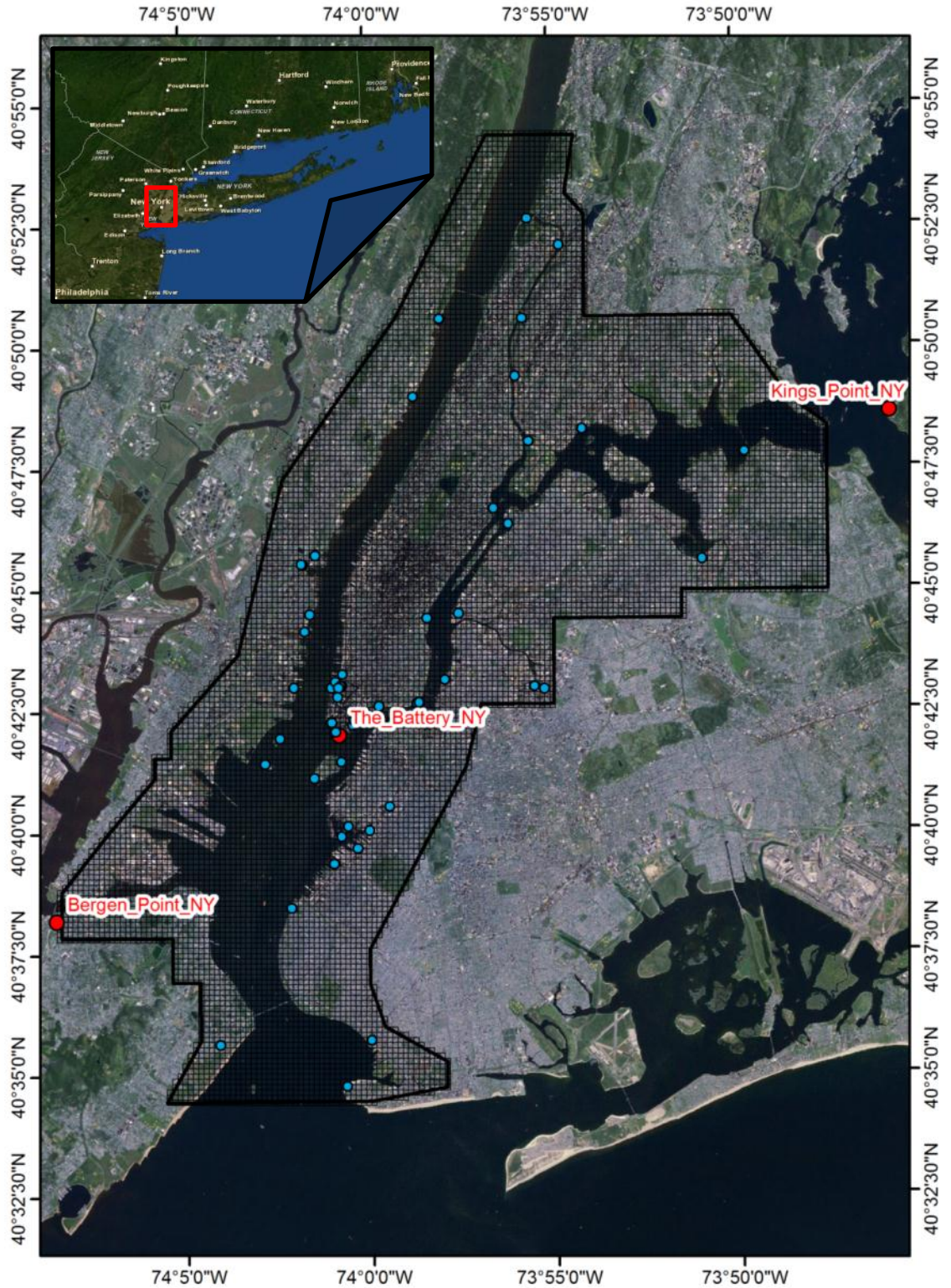
Figure 5.1. Location map of 73 non-wave affected USGS-recorded high water mark sites (**blue**) within the sub-grid domain utilized for spatial verification of model results. High water mark sites were used to verify the maximum spatial extent of inundation via vertical height measurements above the NAVD88 reference datum.
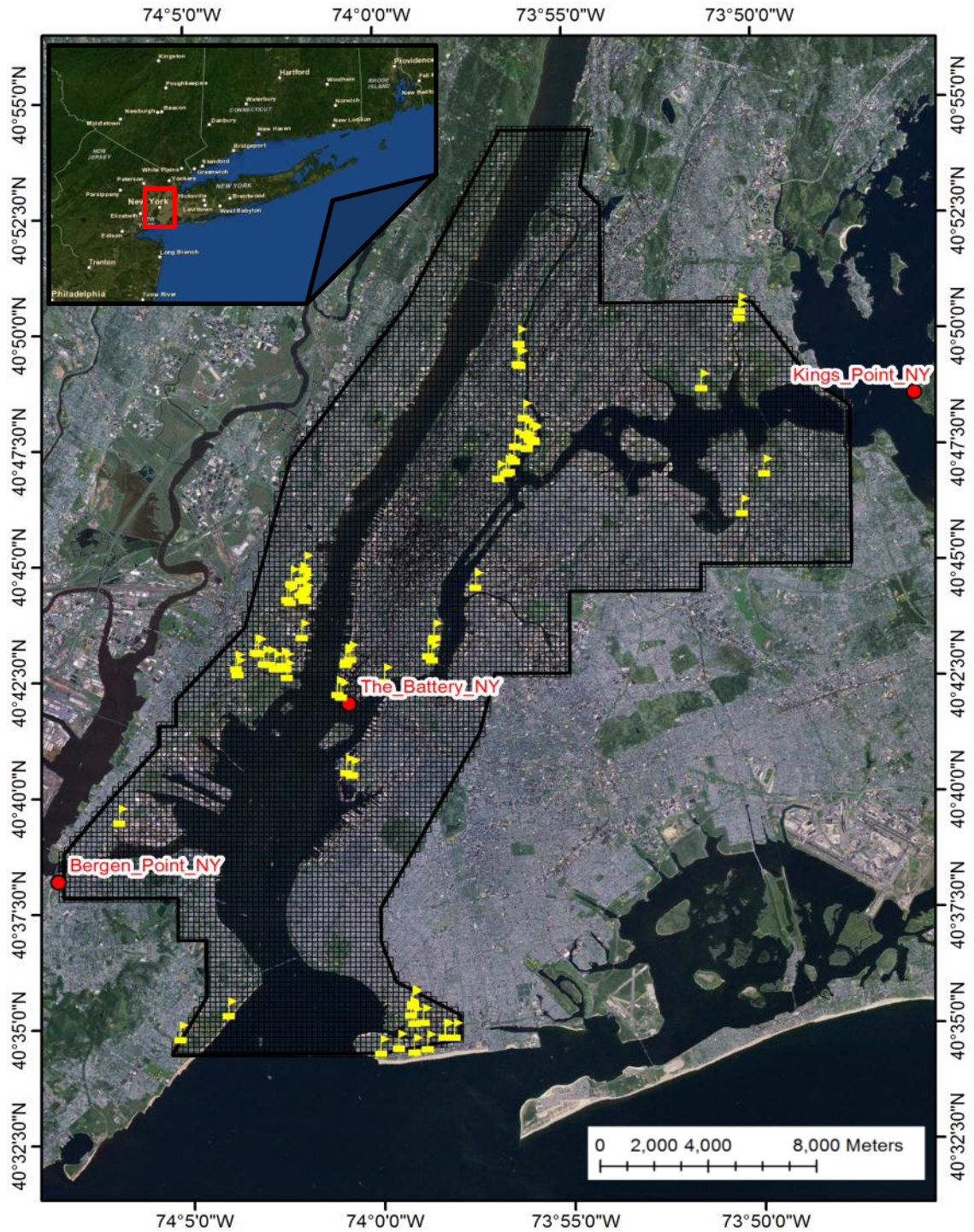
Figure 5.2. Location map of 80 FEMA-reported inundated school sites (**yellow**) within the sub-grid domain utilized for spatial verification of model results. High water marks recorded at critical infrastructure sites are utilized to verify the maximum spatial extent of inundation using vertical height measurements relative to the ground surface.
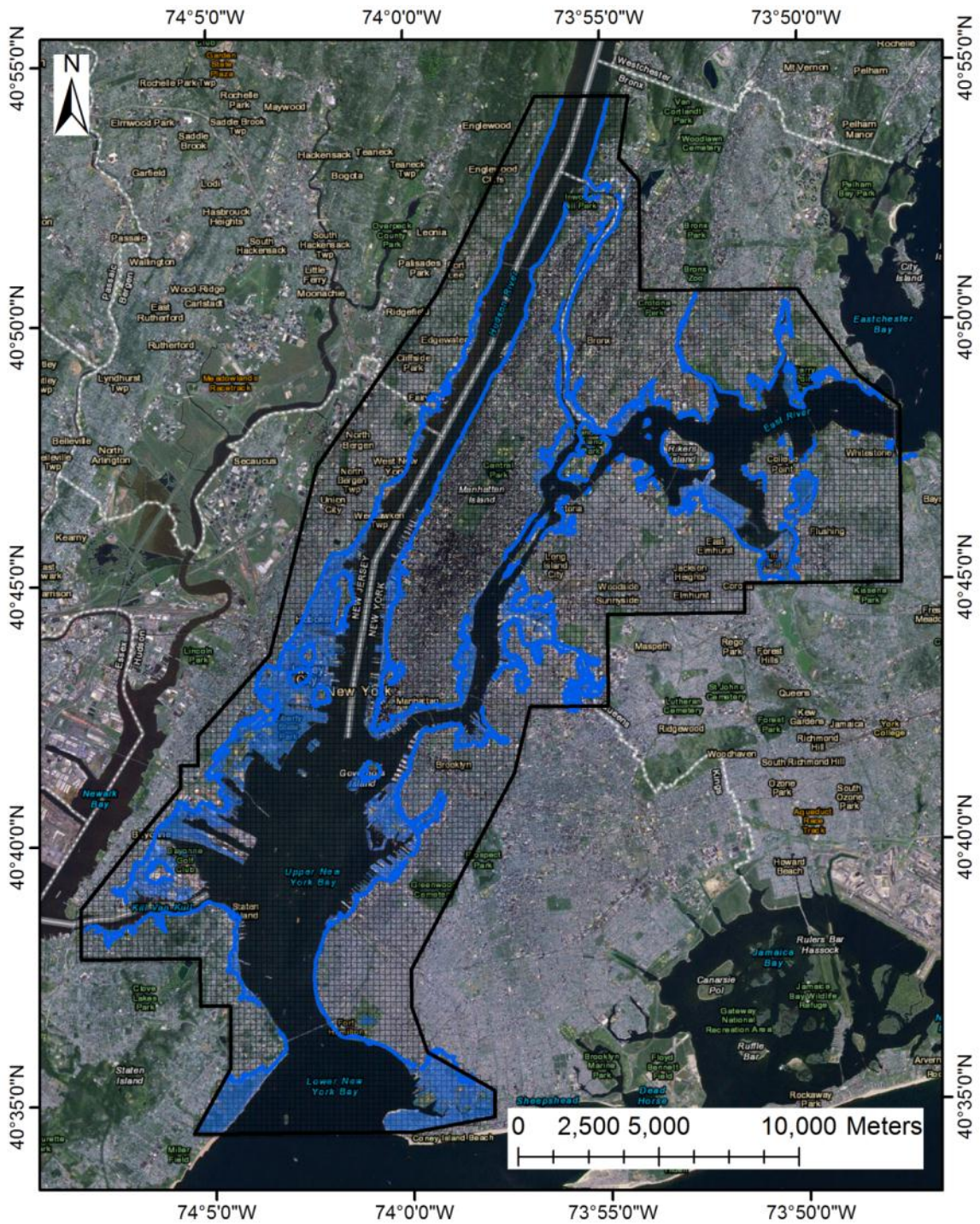
Figure 5.3. Maximum extent of inundation map for areas of New York and New Jersey within the sub-grid of the New York Harbor used for comparison against model results. Produced by FEMA via interpolation of the USGS's high water marks and the best available elevation dataset (FEMA MOTF, 2013).
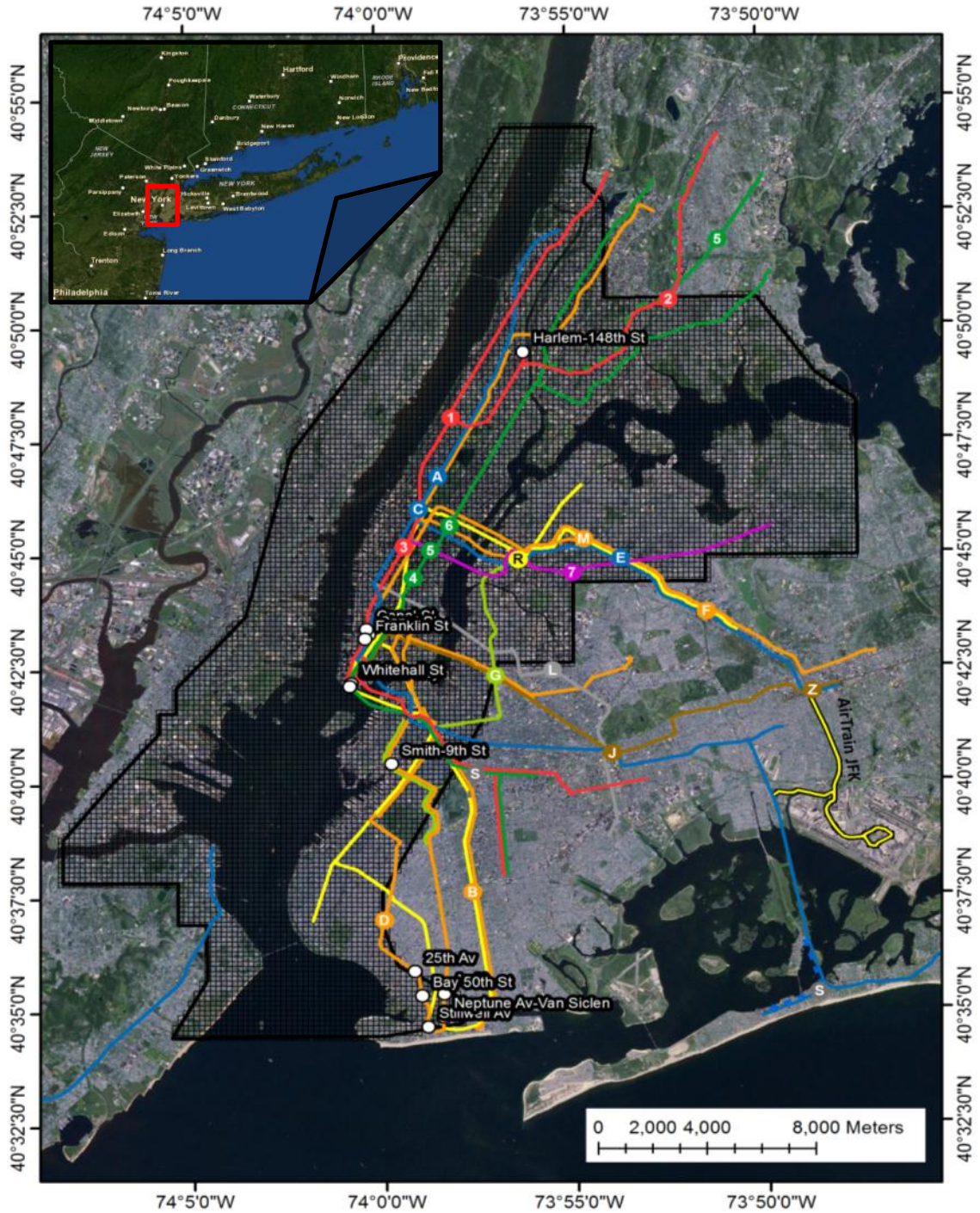
Figure 5.4. Location map of 12 MTA Subway Entrances inundated (white) within the sub-grid domain utilized for spatial verification of model results. These sites are included as areas where substantial evidence exists that flood waters breeched the entrance to the subway system and other critical infrastructure. The labeled sites were used to verify the maximum horizontal spatial extent of inundation. Subway data from Romalewski, 2010.

5.3   GIS Post-Processing and Visualization of Model Results

Creation of a flooding visualization for 2012 Hurricane Sandy in the New York Harbor requires substantial interoperability through GIS-compatible formats, including conversion from UnTRIM^2 unstructured grid element data for water elevations and velocities. Upon conclusion of an UnTRIM^2 model simulation, combined elevation and velocity results are passed to a python script 'untrim2gtiff.py' provided with a copy of the model grid and Geospatial Data Abstraction Libraries (GDAL) for translation of elevations and velocities to a set of geotiffs. One geotiff is produced for each specified model output time step, with resolutions at the scale of the base grid for water elevations and velocities at cell center points throughout the domain. The results of this operation are subsequently passed to a Linux shell script '00_inundationcalcs_nyc.sh', relating the base grid elevations to the topography and bathymetry data of the sub-grid using the open source GIS tool, GRASS, command: r.mapcalc(), resulting in two new sets of geotiff rasters: (1) water elevation data (meters above NAVD88), and (2) water thickness data (m), both at the resolution of the sub-grid (5x5m pixels).

Once both outputs are complete, the script surveys each sub-grid pixel of the output rasters across all time steps to export the maximum recorded value for inundation into 'elevmax.tif' for maximum predicted water elevation, and 'thickmax.tif' for maximum predicted inundation thickness. The 'elevmax.tif' product was used to assess the model maximum water elevation extent against USGS high water mark data (also measured relative to NAVD88), and the 'thickmax.tif' geotiff was utilized for comparison with FEMA's inundated schools dataset (measured relative to the local ground surface).

5.3.1   Distance Differential Assessment Methodology

5.3.1.1 Ideal Test Case for GIS Distance Calculation Methods

A point was selected at Liberty Island within the New York Harbor with two buffers at specified radii of 200m and 300m. The resulting buffer polygons were converted to lines using the polygon to line tool and the construct points toolset in the editor toolset was used to create points at regular 1m intervals along the 200m buffer line to create 1256 points. Finally, the near function was utilized to create a table of distances and angles from each of the constructed regular interval points along the 200m buffer to the 300m buffer line.

Given this ideal test scenario, each of the resulting distances should ascertain that the 'near' distance function properly selects the shortest distance to the 300m buffer. Since this case uses concentric circles, the radial difference should be 100m for all points with the shortest line being drawn at an angle perpendicular to the tangential circumference of the circle (Figure 5.5). Results confirm the mean distance between the two circular polylines is 100.0m with a standard deviation of 0.0m (Table 5.2).

Table 5.2. Location for four points selected for ideal test circle for distance comparison shown in Figure 5.5. Data table includes values for the GIS point ID, shape type (point), distance (m), UTM zone 18N coordinates for the corresponding closest position on the 300m outer circle, and the angle of the distance line calculated relative to 0° at due east.

FID	Shape	NEAR_DIST	NEAR_X	NEAR_Y	NEAR_ANGLE
191	Point ZM	100	580939.164483	4504952.45992	35.409836
418	Point ZM	100	580953.943235	4504630.51961	-29.508197
694	Point ZM	100	580595.500633	4504496.58875	-109.180328
1080	Point ZM	100	580461.70049	4504969.77407	141.639344

(4 out of 1256 Selected)

bufferpoint_for_disttest

Figure 5.5. Ideal test case for distance measurements showing two concentric circles with radii of 200m (in blue) and 300m (in red). The blue circle is comprised of 1256 points evenly spaced 1m apart, with the nearest distances from each blue point to the outer red circle and resulting angles calculated relative to 0° at due east outputting to a GIS table.

5.3.1.2 GIS Distance Calculation Methodology

Creation of an inundation map for 2012 Hurricane Sandy in the New York Harbor

requires substantial interoperability through GIS-compatible formats, including

conversion from UnTRIM^2 unstructured grid element data for water elevations and

velocities. Upon conclusion of an UnTRIM^2 model simulation, combined elevation and

velocity results are passed to a python script, 'untrim2gtiff.py', provided with a copy of

the model grid and GeoDat Abstraction Libraries (GDAL) for translation of elevations

and velocities to a set of geotiffs. One geotiff is produced for each specified model output

time step, with resolutions at the scale of the base grid for water elevations and velocities

at cell center points throughout the domain. The results of this operation are

subsequently passed to a Linux shell script '00_inundationcalcs_nyc.sh', relating the base

grid elevations to the topography and bathymetry data of the sub-grid using the open

source GIS tool, GRASS, command: r.mapcalc(), resulting in an output geotiff raster for

water thickness (measured height from the ground surface to the water's elevation) data

in meters above NAVD88 at the resolution of the sub-grid (5x5m pixels).

Once the geotiff outputs are complete, the '00_inundationcalcs_nyc.sh' script

surveys each sub-grid pixel of the output raster across all time steps to export the

maximum recorded value for inundation into one 'thickmax.tif' for maximum predicted

inundation water thickness. A copy of this layer was converted from a geotiff raster to a

polyline shapefile, extracting and saving the outermost inundation line as 'thickmax_line'

for use in distance comparisons. The 'thickmax_line' shapefile and 'thickmax.tif' geotiff

were subsequently utilized in statistical distance and area comparisons against an

inundation map distributed by the FEMA Modeling Task Force (FEMA MOTF, 2013).

The maximum extent of inundation map product is created from storm surge

sensor data, and field-verified high water mark data collected by the USGS post-

Hurricane Sandy (McCallum et al., 2012). These data products are subsequently utilized

to interpolate a water surface elevation, then subtracted from the best available DEM to

create an inundation grid and surge boundary utilizing a GIS bathtub model for each state substantially affected by the storm. In this sub-grid model comparison, the final released datasets for the 3m-New Jersey and 1m-New York City products released on February 14, 2013, were utilized for spatial comparison with model results (FEMA MOTF, 2013).

The initial distance measurement methodology utilizes the 3m-New Jersey and 1m-New York City clipped data polygons as a mask for inundated areas. In the distance assessment, the outermost inundation extents were interpreted to be the maximum extent of inundation, so as to ignore impediments to flow like buildings. The FEMA maximum inundation extent line was converted from a line to a series of points with 5m regular point spacing (similar to the sub-grid resolution) along the line via the construct points toolset within the ArcGIS10.1 editor. Subsequently, the near/distance calculation feature utilized the standard distance formula to export a table containing shortest distance calculations to the model predicted maximum inundation line for each of the nearly 100,000 5m-spaced points along the FEMA maximum inundation line (Figure 5.6).

The second distance assessment utilizes streets perpendicular to the shore, shoreline shape files for New York City and the State of New Jersey were obtained, clipped with the sub-grid domain boundary, and merged into a single shoreline dataset (New Jersey Shoreline, 2008; New York City Shoreline, 2012). Shorelines cropped by the open boundaries created by river entrances to the New York Harbor from the north, south, west, and east, were joined to seam the gaps to produce a single contiguous shoreline to be utilized for the distance comparison. Finally, the shoreline was converted to a polygon feature using the line to polygon tool for later use in the area comparison for use as a mask layer to remove overwater areas in the observation data and model results.
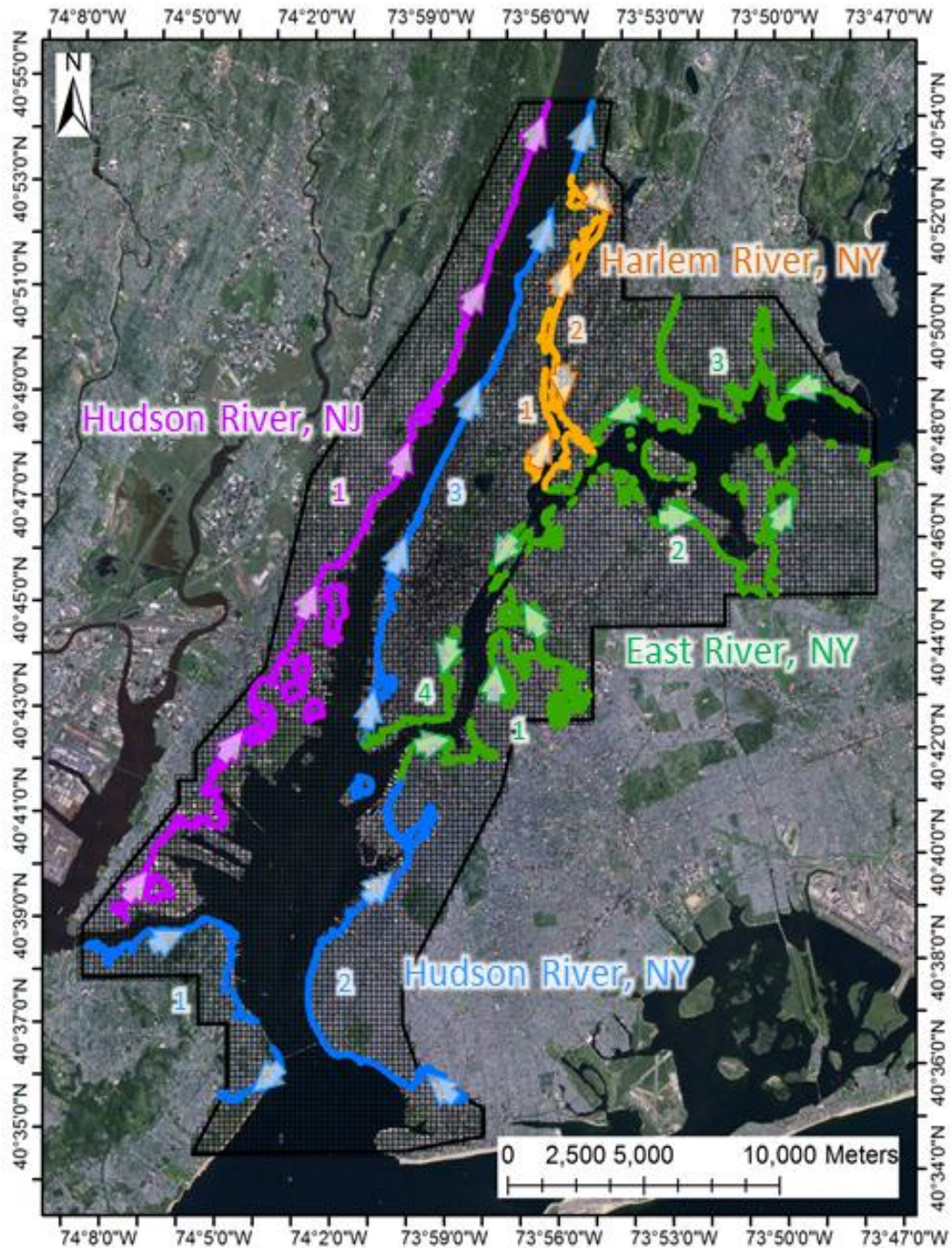
Figure 5.6. Distance measurement map displaying the observed maximum extent of inundation reported by FEMA, separated by color into four regions by river system and state. Numbers and arrows illustrate the direction and order of distance measurements corresponding with the distance table results presented in the next chapter.

5.3.2 Area Difference Comparison Evaluation Process

In preparation for performing an exhaustive area comparison between the FEMA maximum inundation data and the UnTRIM^2 maximum inundation map, both polygon layers were collected and clipped using the shoreline and building layer to remove over-water areas and buildings from both datasets such that only flooded land area is assessed in the comparison. The resulting polygon layers were converted to 5m resolution rasters, and subsequently mosaicked with a raster of the entire region, assigning a default data value for non-inundated sub-grid cell pixels. Notably, without this critical step, the following raster math 'mapcalc' function will only assess the difference of regions shared by both the FEMA inundation raster and the UnTRIM^2 spatial maximum, consequently ignoring the differences (under-predicting and over-predicting regions) between the two rasters due to no-data values. The model result raster is subtracted from the FEMA inundation raster using the difference tool to produce a difference map with the following value table (Table 5.3).

Finally, the resulting difference raster is converted to polygons, without smoothing or otherwise simplifying the polygons, to make use of ArcGIS's area calculation toolset. The total areas are calculated for each polygon and aggregated in a table to provide relevant statistics for total area (m^2) and percent area (%) of matching/intersecting agreement between the FEMA observation data and the model prediction along with errors where the model over-predicted and under-predicted the recorded data. After assessing the total difference areas, the New York Harbor region was separated by river system to address areas analogous to the distance comparison and focus on locations where the model performed well and investigate areas where it did not.

Table 5.3. Value table for two rasters containing model predicted and FEMA observed area of maximum flooding. The difference map for model prediction - FEMA observation yields four field values in the resulting difference map: 2-1=1 (match), 2-3=-1 (over-predict), 3-1=2 (under-predict), and 3-3=0 (no flooding).

Raster Name	Legend ID	Value ID
Model Maximum Inundation	Model Flooded Region	2
	No Result	3
FEMA Maximum Inundation	FEMA Flooded Region	1
	No Result	3

5.4   Google Earth Visualization and Time-Aware Layer Animations

Sub-grid hydrodynamic modeling has the potential to provide quick, high-resolution information about inundation layer thickness and extent, with porting capabilities for time-aware inundation layers. Prior to prominent use of GIS in emergency management applications, the information basis for decisions was limited to the work experience and instinct of individual emergency managers (Post et al., 2005). GIS tremendously expands upon the available resources emergency managers can consider upon evaluating an impending storm system (Garcia et al., 2012; ESRI, 2012). While static maps improve situational awareness, printed paper maps and static images lack interactive capabilities of time-aware layers, and suffer from latency issues. Time-aware layers are noted to have a plethora of applicable uses for disaster management, including improved situational awareness, enhanced ability to make informed decisions regarding evacuations, transportation, and critical facilities closures (ESRI, 2012).

To increase the accessibility of our model results to other scientists, policy-makers, and the general public, all geotiffs are converted to geo-referenced '.png' (Portable Network Graphic) images for use with visualization in Google Earth and other

preeminent online platforms. This option renders the geo-referenced inundation data with

GDAL tool: gdaldem, provided a start date and time (2012-10-27 at 00:00 GMT for 2012

Hurricane Sandy forecast), for 200 iterations of hourly results, creating 6430x8138 pixel

'.png' images at 5m resolution. Utilizing a tree structure of self-referencing Google

(Keyhole Markup Language) '.kml' files with pointers to '.png' images at various stored

resolutions, high-resolution images are broken into tiles at seven different zoom levels

using the GDAL tool: 'gdal2tiles.py', the script's map-tiling algorithm (Figure 5.7).
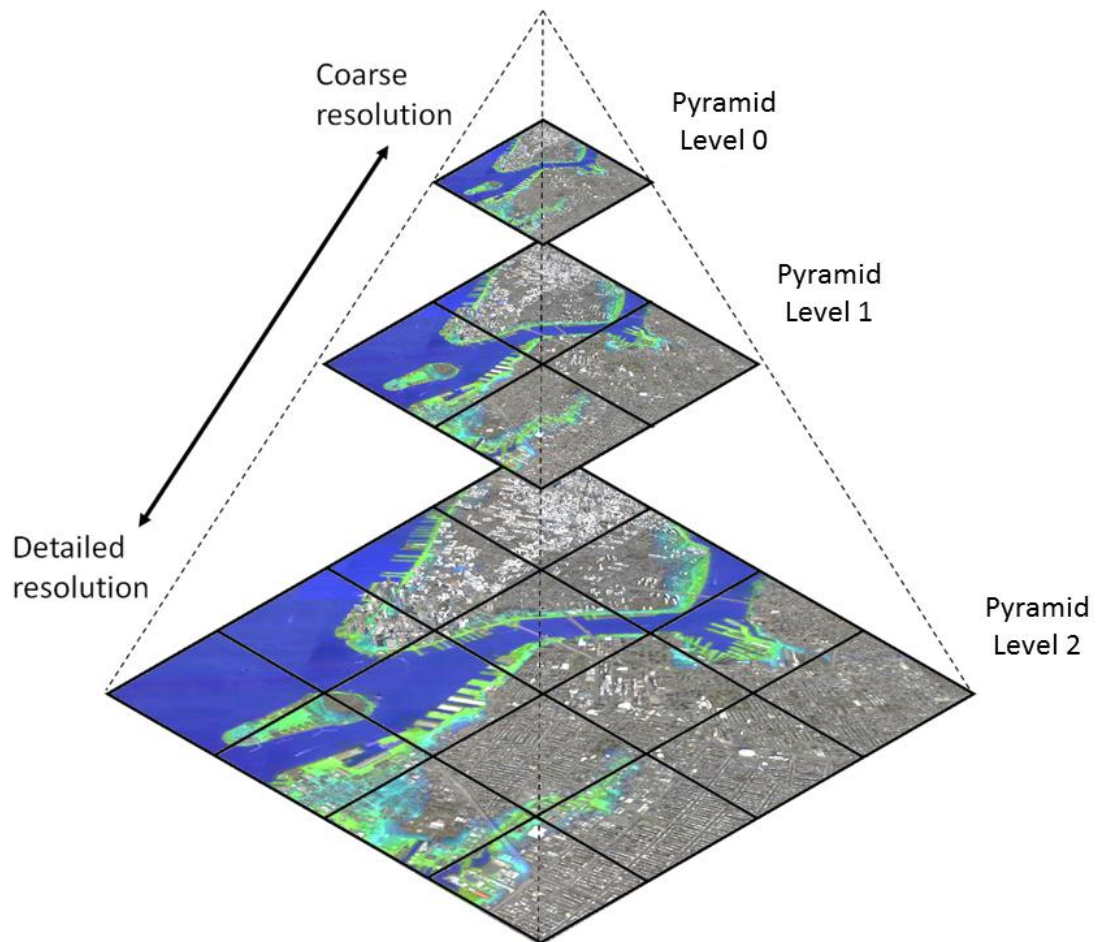
Figure 5.7. Map-tile pyramid example zoomed in on Brooklyn and Southern Manhattan showing 3 zoom levels in the image resolution pyramid: 1 coarse resolution image, 4 less-coarse images, and 16 finer, detailed resolution images for a population of 21 total image tiles (modified tree from Garcia et al., 2012).
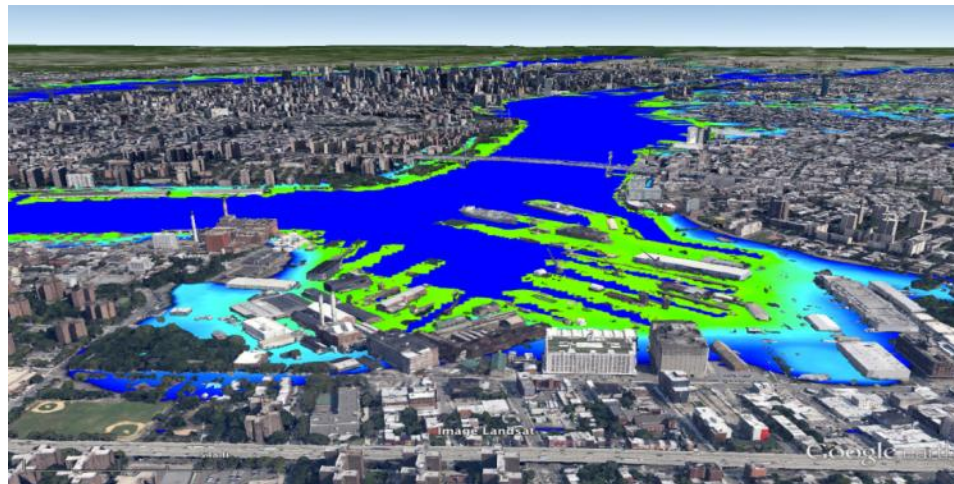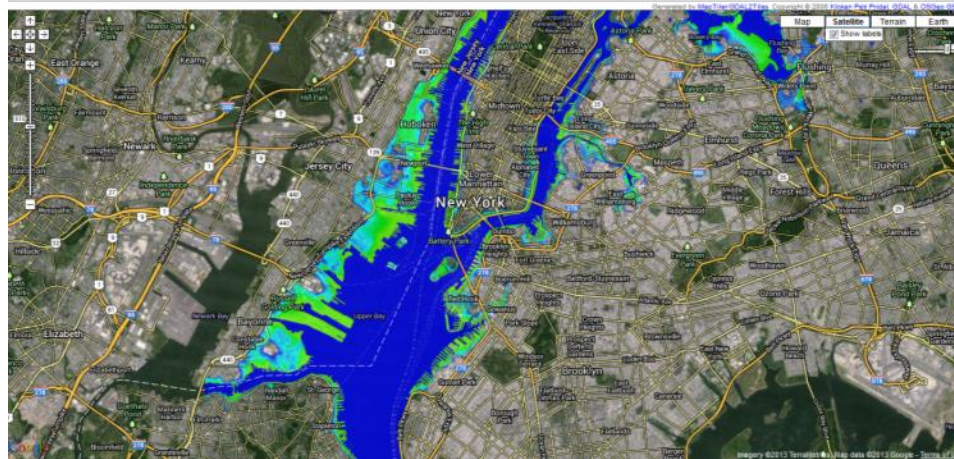
Figure 5.8. Example of UnTRIM^2 model predicted maximum extent of inundation in three prominent online formats, Google Earth (Top) http://web.vims.edu/physical/3DECM/SandyNY/SandyNYMaximums.kmz, Google Maps (Middle) http://web.vims.edu/physical/3DECM/SandyNY/googlemaps.html, and Open Layers (Bottom) http://web.vims.edu/physical/3DECM/SandyNY/openlayers.html.

As illustrated in Figure 5.7, as a region is focused upon by zooming in, higher-resolution '.png' images are loaded from the '.kml' code, with pixel densities ranging from 300m/pixel - 2.4 m/pixel in resolution, proportional to the altitude of the viewer above the globe in Google Earth. With ≈15,000 images per hourly timestamp, over 3 million images would be produced for the full eight day forecast simulation, thus a shortened inundation animation near the peak of the storm surge is most practical. Finally, time-aware metadata is written into a Google Earth KML document to enable time-aware, zoom-able animations in a variety of platforms, including: ESRI's ArcGIS, Google Earth, Google Maps, and Open Layers (Figure 5.8).

In summary, these post-processing procedures rasterize the UnTRIM^2 model's base grid data, combine them with the high-resolution topography and bathymetry stored in the sub-grid, and convert them into usable GIS and Google Earth spatial formats, where the utility of the model predictions may be capitalized upon for statistical spatial comparison and conveniently published in accessible places and formats.

CHAPTER 6: Sub-Grid Inundation Model Comparison with Observation Data

6.1   Water Level Time Series Temporal Comparison

Of the observation data compiled during 2012 Hurricane Sandy, five tidal records assembled from one USGS and four NOAA permanent tide gauges were utilized as a standard for temporal comparison (Table 6.1A). Additionally, seven overland rapid deployment gauges installed and collected by the USGS were utilized as a benchmark for validating the success of the sub-grid inundation prediction in this section (Table 6.1B).

6.1.1   NOAA and USGS Permanent Water Level Gauges

Four of the five permanent water level gauges were utilized to drive the model at three of the open boundaries. Model outputs near the boundary confirmed that the water elevation data is a near perfect match (>99% match) for each of these stations verifying correct forcing at the boundaries (Table 6.1A). The one permanent installation not adjacent to any model boundary reported a significant match of the storm surge height near the center of the grid near the Battery, NY, (Figure 6.1A) with an R^2 of 0.9932, a relative error of 0.47%, and a root-mean-squared error of 7.15cm (Table 6.1A). Stations at the model's east and west boundaries at Kings Point, NY, and Bergen Point, NY, compared well in Figure 6.1B. Due to the loss of the tidal record after the peak of the storm surge at Sandy Hook, NJ, the southern sub-grid boundary was forced using the complete record from the nearby USGS gauge at Rockaway Inlet, NY (Figure 6.1C).

Table 6.1A. Statistical comparison between the model result and verified permanent water level gauges.

Station	R^2	Relative Error (%)	RMS Error (cm)
The Battery, NY	0.9932	0.47	7.15
Kings Point, NY	0.9947	0.31	7.81
Bergen Point, NY	0.9930	0.61	8.32
Rockaway Inlet, NY	0.9904	0.64	8.28
Sandy Hook, NJ	0.9830	1.63	12.83
Mean Value	0.9909	0.73	8.88
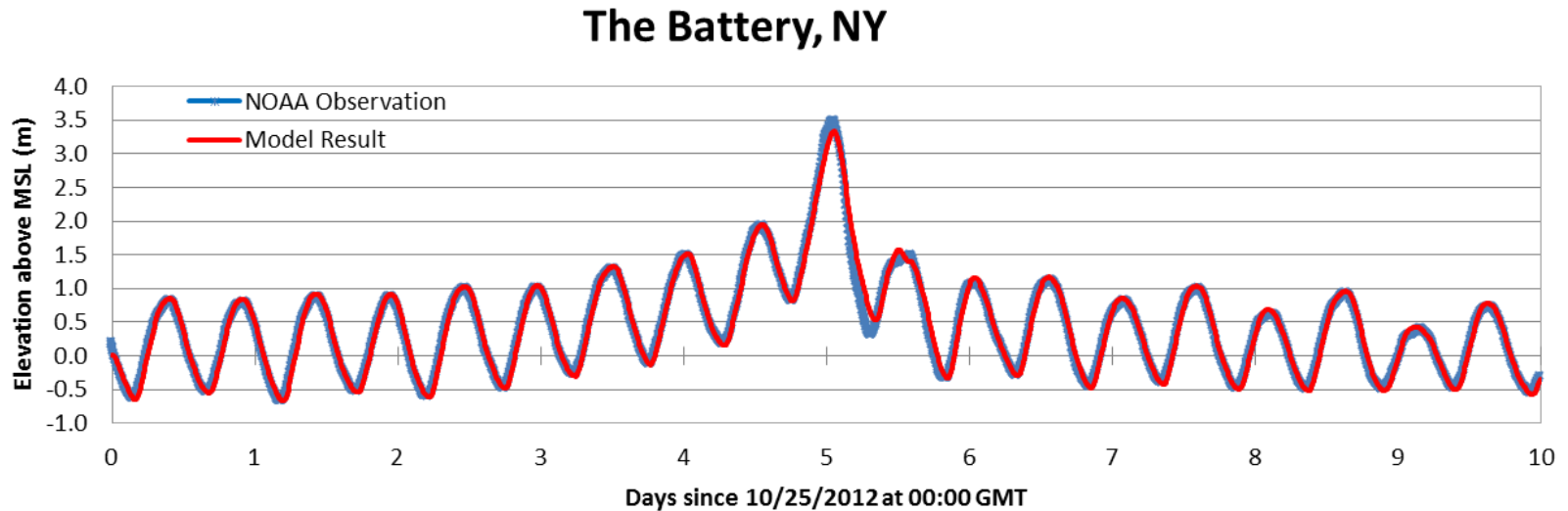
Figure 6.1A. Time series comparison between the water levels predicted by the model and verified USGS and NOAA measurements.
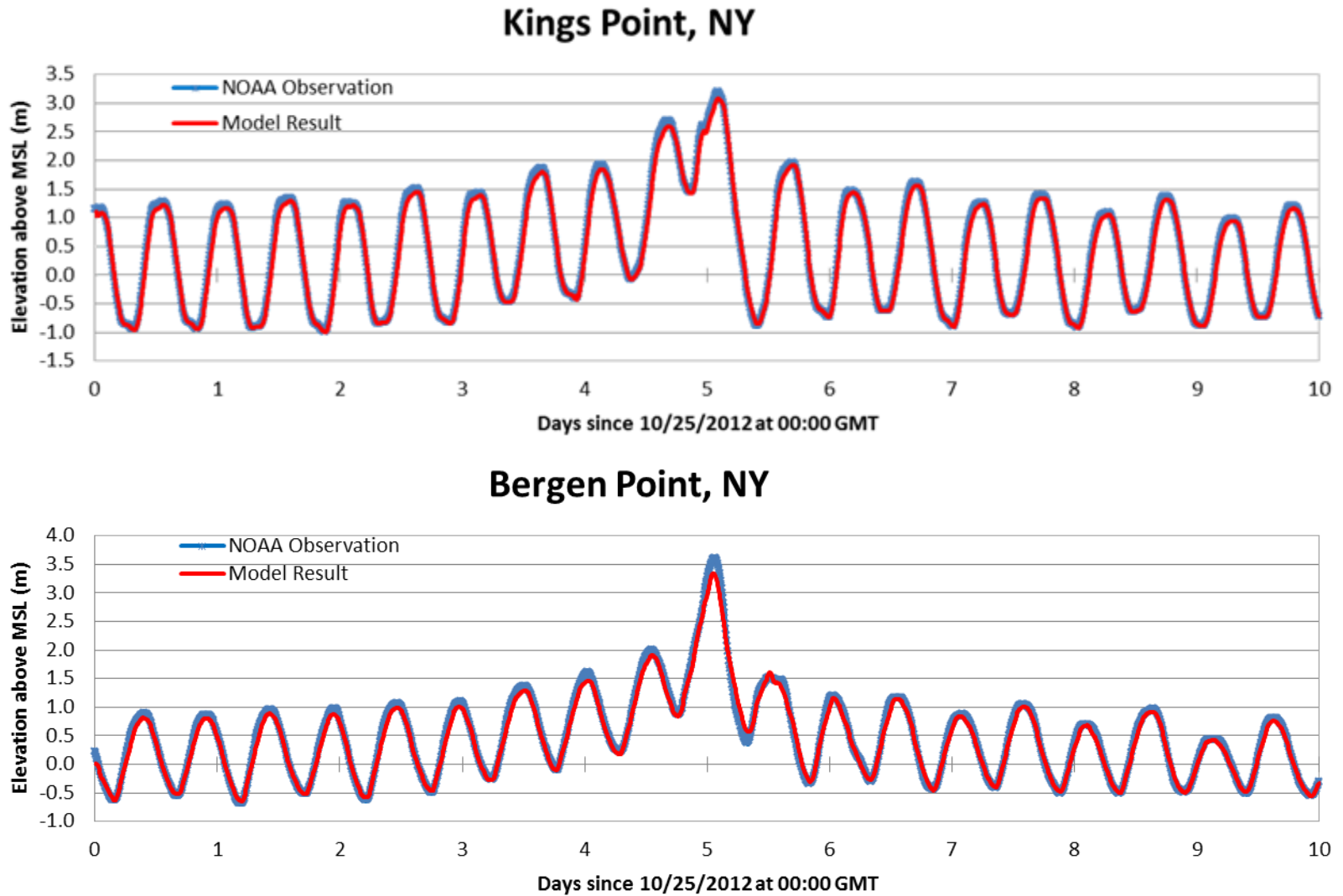
Figure 6.1B. Time series comparison between the water levels predicted by the model and verified NOAA measurements.
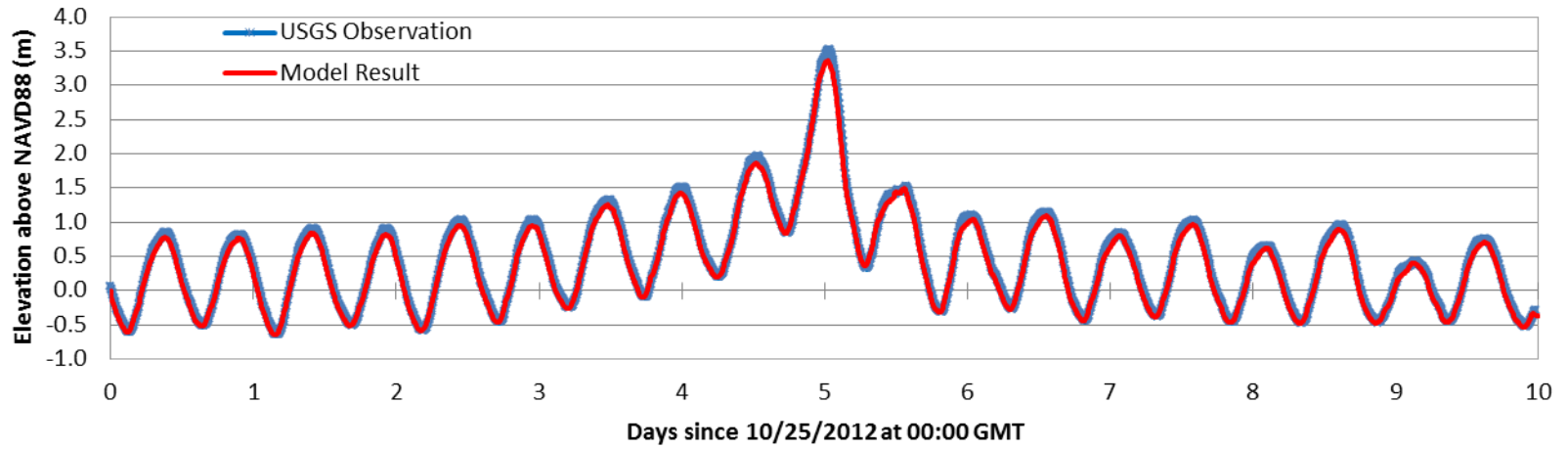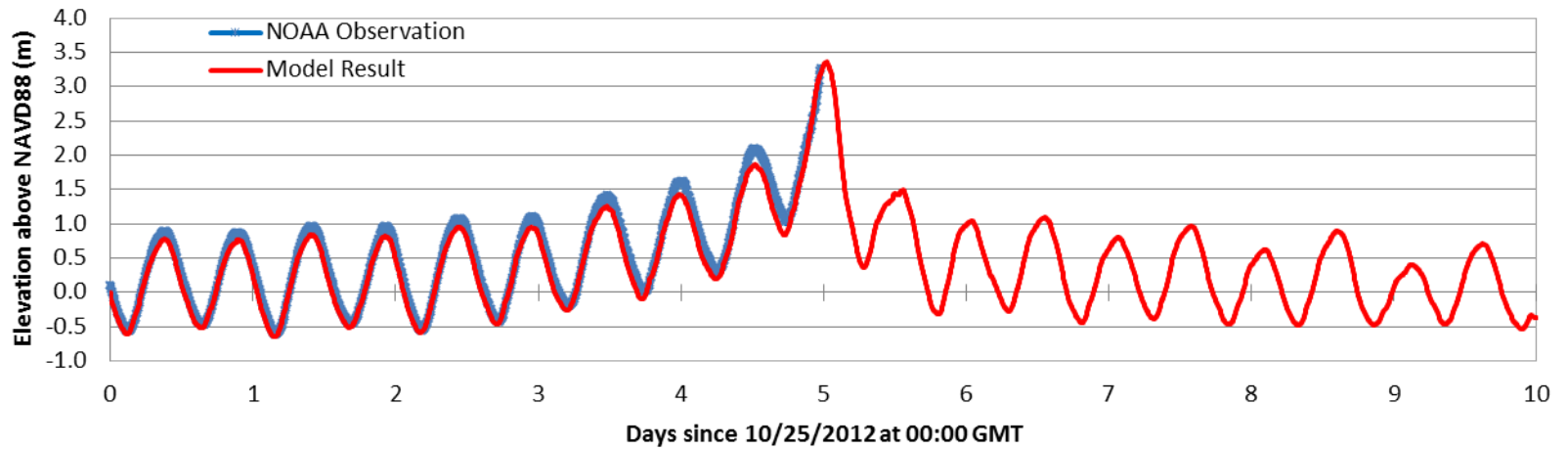
Figure 6.1C. Time series comparison between the water levels predicted by the model and verified NOAA measurements.

6.1.2 USGS Rapid Deployment Water Level Gauges

One of the most straight-forward methods for verification of model results is the use of time series water level observations for a fixed-point comparison. The USGS has expended considerable effort to deploy a comprehensive temporary monitoring network of instruments (Table 6.2) to measure water-levels along the U.S. Atlantic Coast during Hurricane Sandy (McCallum et al., 2013). Seven of these rapid deployment gauges were identified within the extent of the sub-grid domain and were subsequently used for assessment of the model's accuracy for predicting storm surge over land. Inundation comparisons indicated successful comparisons for each of the temporary gauges installed by the USGS prior to the storm's arrival with a mean R^2 of 0.9568, a relative error of 3.83%, and a root-mean-squared error of 18.15cm (Table 6.1B).

Each of the installed gauges recorded data in high-frequency 30-second intervals except for USGS 404810735538063, which recorded data in 6-minute intervals similarly to the permanent gauges noted in the previous section (McCallum et al., 2013). Two stations positioned south of the Verrazano Narrows between the New York Bay and Raritan Bay were heavily impacted by wave interaction, which was reflected in the high-frequency 30-second observation data shown in Figure 6.2. The remaining stations were relatively unaffected by high-frequency wave interaction, thus the high-frequency observation data were decimated to the 6-minute model time step for even comparison of measurements, plotting, and statistics (Figure 6.3A-D and Table 6.1B).

Two gauges remain permanently wet throughout their deployment period, USGS 404810735538063 shown in Figure 6.3B (bottom), and SSS-NY-QUE-001WL in Figure

6.3C (top). The data record for USGS 404810735538063 on Randall's Island at the junction of the Harlem and East Rivers was lost just prior to the peak of the storm surge, leading to a smaller collection of data points for optimal statistical comparison with an R^2 of 0.9538, the highest relative error at 6.07%, and a root-mean-squared error of 21.40cm (Table 6.1A). The observations recorded from SSS-NY-QUE-001WL at Worlds Fair Marina in Queens made use of the conventional non-vented pressure transducer sensor, but in an elongated PVC pipe, allowing for complete measurements of the surge trough amplitude even below -1m relative to NAVD88, which the model moderately under-predicted with an R^2 of 0.9355, a relative error of 4.41%, and a root-mean-squared error of 26.95cm (Table 6.1B).

In all comparisons, it can be observed that the model-simulated results are quite consistent with the measured data both in terms of timing and amplitude. As noted in Figure 6.3A, Figure 6.3B (top), Figure 6.3C (bottom), and Figure 6.3D, the overland gauge is set at a fixed height which can become dry when the water falls below its anchored monitoring position. For each of the five gauges where this observation applies, the model consistently matches the observed water level as it increases and decreases with the tide, passing directly through nearly all of the points where the gauge data stops as the water falls below its datum for measurement and then re-appears. This is another indication of effective performance for the sub-grid model's numerical wetting and drying scheme, and that it was quite accurate in its transition between wet to dry status. Given the record, it is evident that the inundation is co-oscillating with the tidal cycle and the model captured the timing and the depth of the water quite accurately (Table 6.1B).

Table 6.1B. Statistical comparison between the model result and temporary USGS
rapid deployment water level gauges.

Station	R^2	Relative Error (%)	RMS Error (cm)
SSS-NY-KIN-001WL	0.9842	2.78	15.39
SSS-NY-RIC-001WL	0.9286	4.18	19.56
SSS-NY-KIN-003WL	0.9848	1.79	11.93
USGS 404810735538063	0.9538	6.07	21.40
SSS-NY-QUE-001WL	0.9355	4.41	26.95
SSS-NY-QUE-004WL	0.9556	4.50	18.86
SSS-NY-NEW-001WL	0.9554	3.05	12.99
Mean Value	0.9568	3.83	18.15
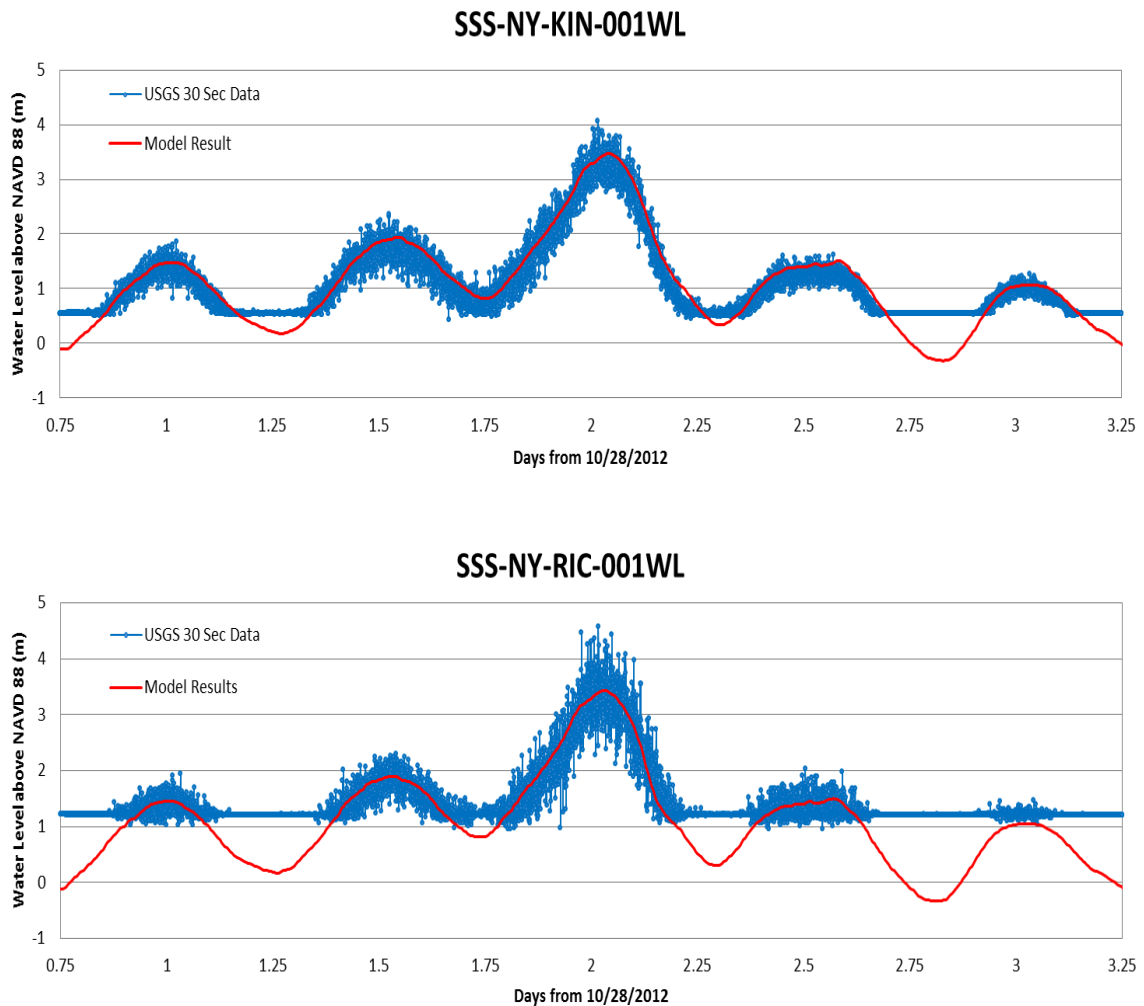
Figure 6.2. Sub-grid model comparisons for 2 wave-affected high-frequency (30-second measurements) USGS observation stations near the mouth of the New York Bay.
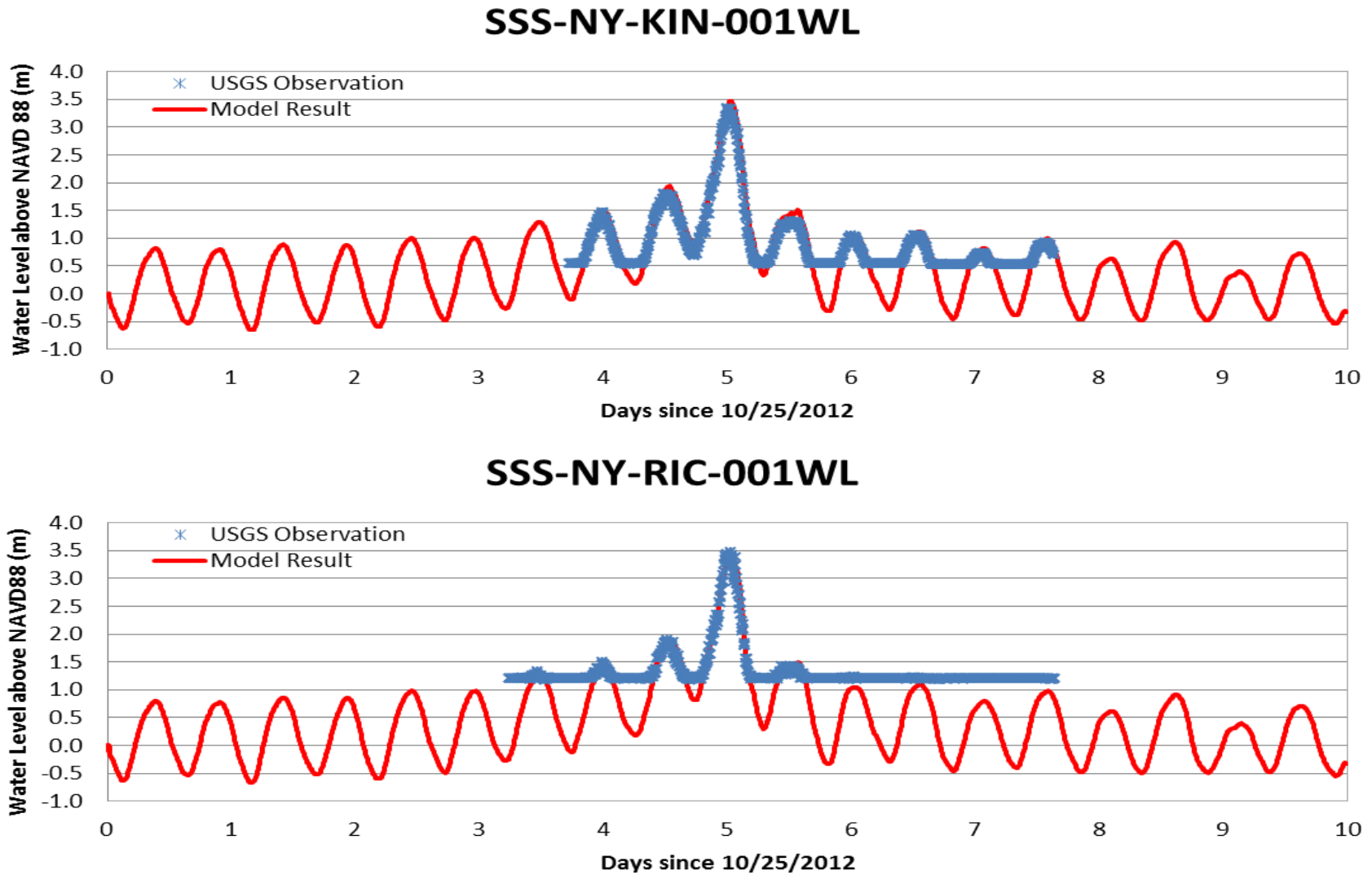
Figure 6.3A. Sub-grid model comparison of inundation water levels with overland USGS rapid deployment gauge observation data.
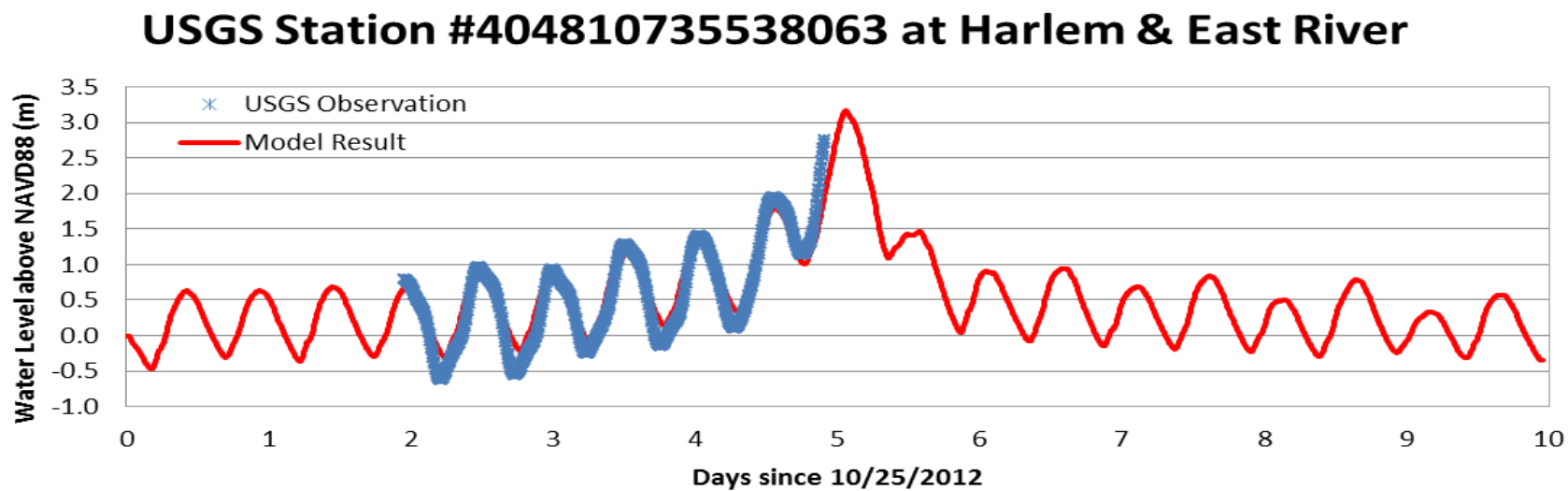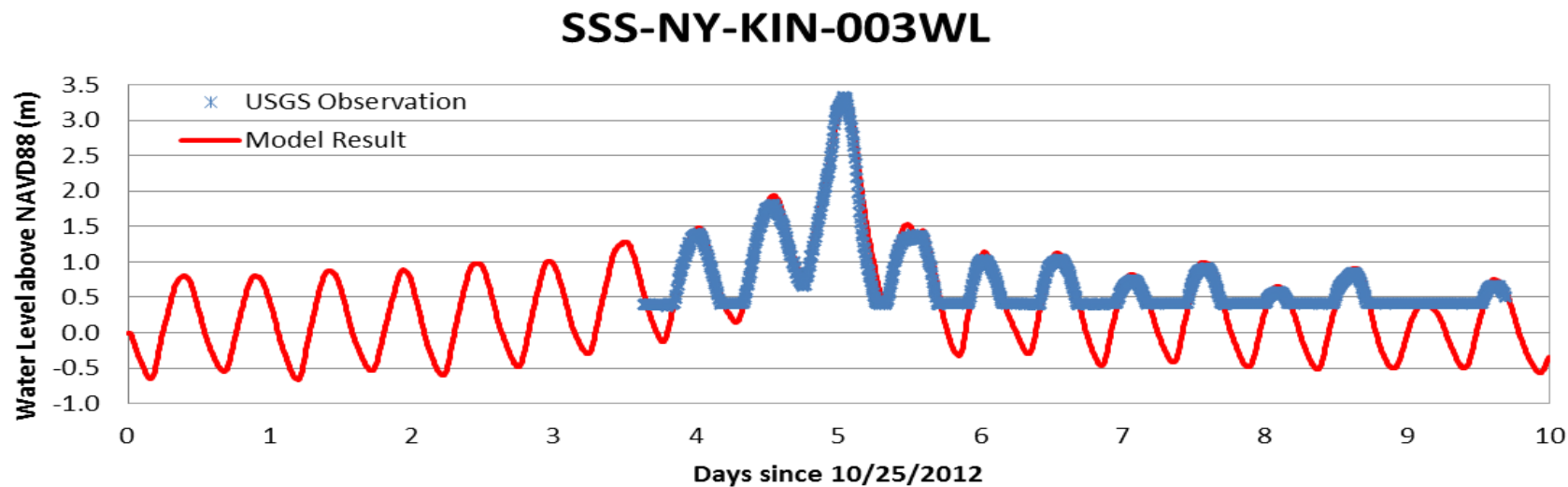
Figure 6.3B. Sub-grid model comparison of inundation water levels with overland USGS rapid deployment gauge observation data.
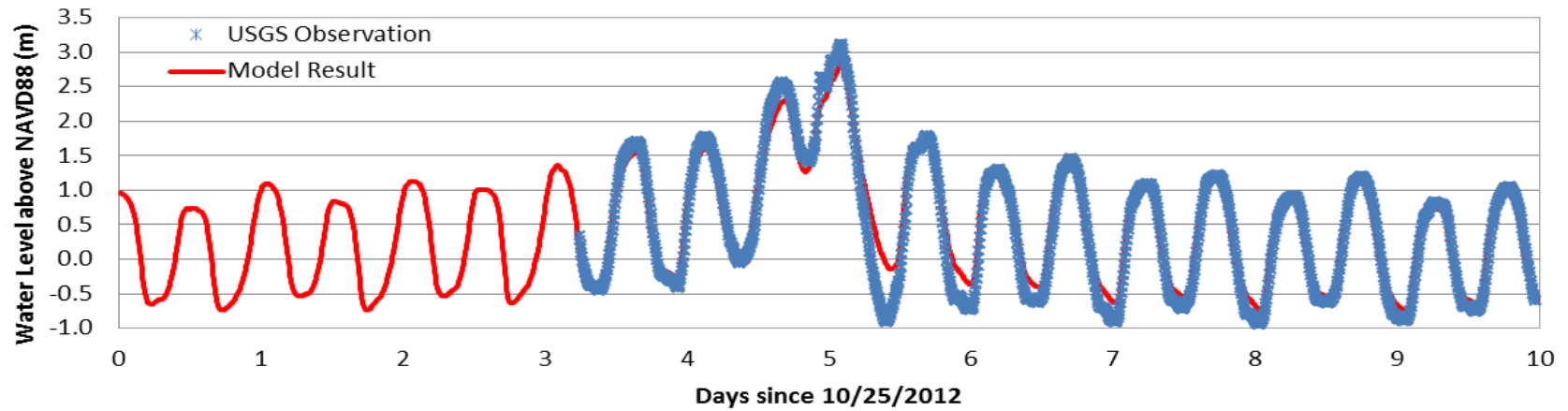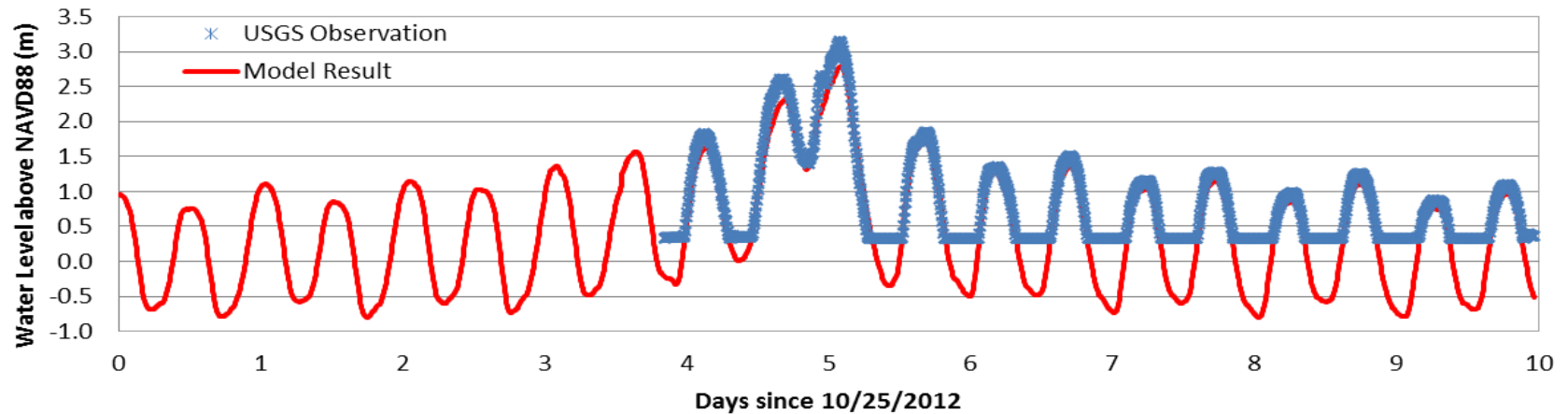
Figure 6.3C. Sub-grid model comparison of inundation water levels with overland USGS rapid deployment gauge observation data.
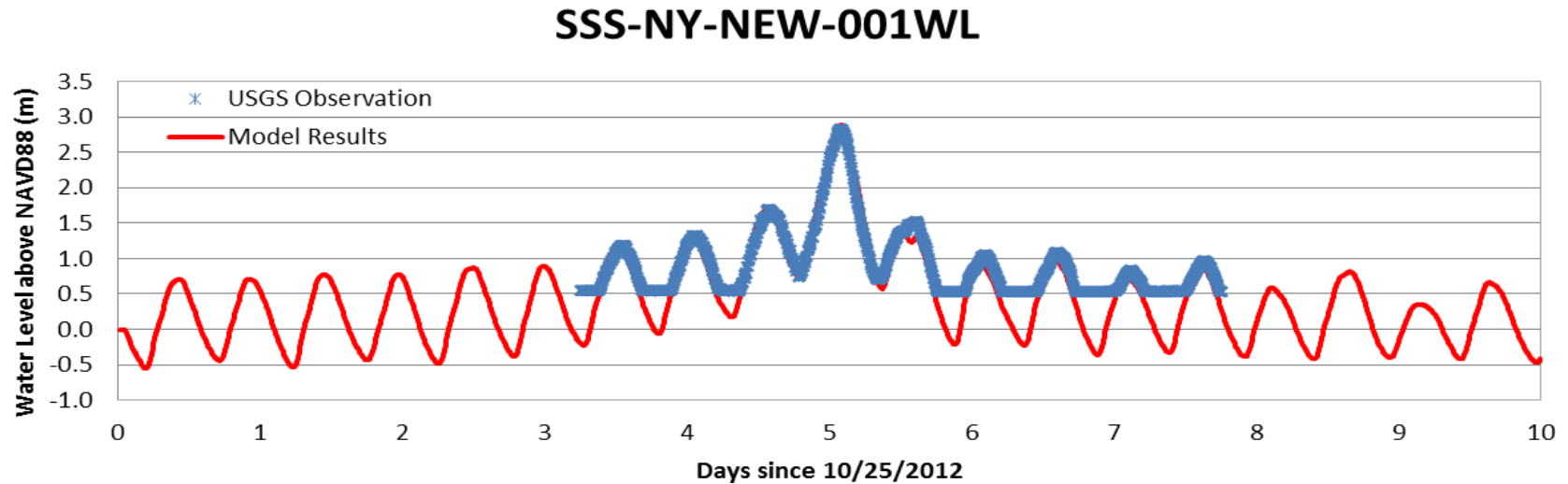
Figure 6.3D. Sub-grid model comparison of inundation water levels with overland USGS rapid deployment gauge observation data.

Table 6.2. Description of USGS temporary rapid deployment gauges with location, data range, peak water level and time.

#	Station Name	Latitude (°N)	Longitude (°W)	Location	Deployment Data Range (GMT)			Peak WL (m)	Peak Time (GMT)	
1	SSS-NY-KIN-001WL	40.58	-74.01	Lower New York Bay at Sea Gate	10/28/2012 6:00	-	11/1/2012 15:30	4.06	10/29/2013	12:23:30 AM
2	SSS-NY-RIC-001WL	40.59	-74.06	Lower New York Bay at South Beach	10/28/2012 6:00	-	11/1/2012 15:30	4.58	10/29/2013	12:23:30 AM
3	SSS-NY-KIN-003WL	40.68	-73.99	Gowanus Canal at Gowanus	10/28/2012 15:20	-	11/3/2012 16:50	3.38	10/30/2013	1:04:30 AM
4	USGS 404810735538063	40.80	-73.93	Harlem River at Randall's Island	10/27/2012 0:30	-	10/29/2012 23:45	No Peak	No Peak	
5	SSS-NY-QUE-001WL	40.76	-73.86	Flushing Bay at Worlds Fair Marina	10/28/2012 6:00	-	11/3/2012 23:30	3.15	10/30/2013	2:06:30 AM
6	SSS-NY-QUE-004WL	40.80	-73.83	Long Island Sound at Whitestone	10/28/2012 6:00	-	11/3/2012 23:30	3.22	10/30/2013	2:06:00 AM
7	SSS-NY-NEW-001WL	40.88	-73.93	Harlem River at Inwood Hill Park	10/28/2012 6:00	-	11/1/2012 18:20	2.90	10/30/2013	2:07:30 AM

133

6.2   Inundation Spatial Comparison

Verification of the spatial extent and depth of flood waters within the New York Harbor sub-grid domain was assessed via comparison of model predicted results with a variety of verified-field measurements from various agencies. First, 73 USGS-collected non-wave-affected high water mark measurements within the New York Harbor were collected for comparison with water level elevation above NAVD88 in meters (Table 6.3A-C). Second, 80 FEMA-collected inundated school locations where flood waters left visible moisture marks indicating water level thickness (measured from the ground to the water marks) at specific sites throughout the sub-grid domain (Table 6.4A-C). Third, a variety of distance and area coverage calculations are utilized to compare model results with FEMA's maximum extent of inundation map, which was based upon interpolation of the USGS's high water marks and the best available elevation data.

6.2.1   USGS High Water Marks

The USGS surveyed 653 independent high water mark locations in the aftermath of Hurricane Sandy ranging from Virginia to Massachusetts. These marks, noted as water stains or debris markings such as dirt or seed lines were used as a benchmark for model comparison considering the maximum extent of inundation. The measurements were typically made along sides of buildings or lamp posts, or via debris lines washed ashore near the ground, and were surveyed relative to NAVD88, with a plurality of measurements collected in New York and New Jersey where the impacts of the storm were the most heavily pronounced. Within the extent of the sub-grid model domain, there were 62 non-wave affected high water mark observation sites for the New York City

Harbor , and 11 non-wave affected marks in the State of New Jersey for comparison. A high water mark was considered to be an independent measurement location if separated by more than 1,000 feet from neighboring high water marks (McCallum et al., 2013).

The model comparisons for high water marks were separated by state and by county, which was a reasonable method for grouping relatively adjacent model results. However, statistics were not computed by county, since the gerrymandered municipal boundaries have minimal impact on the extent of inundation from a hydrodynamic standpoint (Table 6.3A). Most of the high water marks were measured on Manhattan Island (or New York County, abbreviated as NEW in Table 6.3A), with a range in difference between the observed high water mark and maximum water level height reported at that same location by the model ranging from 0.0168 to 0.2639m. Most of the other water marks were collected in Queens (abbreviated as QUE) ranging from 0.0710 to 0.2970m in difference, or in Brooklyn (or Kings County, abbreviated as KIN) ranging in difference from 0.0258 to 0.2788m. The remaining two boroughs surveyed had 3 measurements from the Bronx (abbreviated as BRO) ranging from 0.1187 to 0.2000m, and from 2 measurements from Staten Island (or Richmond County, abbreviated as RIC) ranging from 0.2271 to 0.2971m, with larger differences than the other areas likely due to the proximally close position to the mouth of the New York Bay with some small wave effect noted at these stations (Table 6.3A).

A few high water marks in this area of Staten Island and its analogous position across the Bay on Coney Island near the wave-affected rapid deployment gauges plotted in Figure 6.2 were noted by in the USGS report to be heavily affected by waves. These high water marks were not included in the statistical comparison due to the model not

135

addressing wind-wave interaction, and due to the relative uncertainty of water mark measurements accurately representing the average flood height for prolonged periods in areas frequently buffeted by waves.

In the state of New Jersey, a majority of the 12 high water marks were recorded in Hudson County (abbreviated as HUD in Table 6.3B). The 10 high water marks had a large range in difference from 0.1261 to 0.5290m. The differences in the remaining 2 measurements collected from Bergen County (abbreviated as BER) were also large, with values of 0.5406 and 0.5577m. The large differences were anticipated due to the lack of freely available building height data for the New Jersey side of the Hudson River being represented in the model's DEM. Subsequently, without the building presence in the grid, the modeled flooding extent was greatly exaggerated in places beyond which would have been buffered by high building densities such as in Jersey City, Hoboken, and areas of Bayonne (Table 6.3B).

Aggregated statistics for New York presented in Table 6.3C suggest a very favorable comparison with a $\bar{\varepsilon}$ of -0.0004m indicating no strong leaning towards over-prediction or under-prediction of high water marks by the model. The $\bar{\varepsilon}$ of 0.2150m reported for New Jersey suggests that the model tended to over-predict recorded high water marks by 21.5cm on average. The $|\bar{\varepsilon}|$ was 0.112m for New York and greater than 3x that calculated for New Jersey at 0.364m. The smaller ranges described previously in the high water marks for the different boroughs of New York City logically led to a relatively small σ of 0.085m and an RMSE of 0.120m when compared to σ in New Jersey at 0.256m and an RMSE of 0.347m. The difference of 0.227m is a significant indication that the inclusion of buildings in the model DEM is critical to urban inundation modeling.

136

Table 6.3A. Sub-grid model vertical spatial comparison with 62 non-wave affected USGS-collected high water mark observation sites for the New York City Harbor in meters above NAVD88 for the State of New York. High water mark site IDs and latitude/longitude site measurements adapted from: McCallum et al., 2013: http://pubs.usgs.gov/of/2013/1043/ .

#	HWM Site ID	Latitude	Longitude	Model Result (m)	High Water Mark (m)	Difference (m)
1	HWM-NY-BRO-807	40.8047	-73.9023	3.3610	3.2339	0.1271
2	HWM-NY-BRO-809	40.8154	-73.8386	3.3740	3.2553	0.1187
3	HWM-NY-BRO-810	40.8092	-73.8037	3.3760	3.1760	0.2000
4	HWM-NY-KIN-001	40.6408	-74.0356	3.2050	3.4503	0.2453
5	HWM-NY-KIN-002	40.7164	-73.9249	3.4420	3.3254	0.1166
6	HWM-NY-KIN-504	40.7040	-73.9905	3.3420	3.4473	0.1053
7	HWM-NY-KIN-510	40.7189	-73.9652	3.3790	3.4260	0.0470
8	HWM-NY-KIN-511	40.6688	-74.0096	3.2720	3.4260	0.1540
9	HWM-NY-KIN-604	40.7040	-73.9894	3.3420	3.3467	0.0047
10	HWM-NY-KIN-605	40.7040	-73.9894	3.3420	3.3162	0.0258
11	HWM-NY-KIN-724	40.6652	-74.0127	3.2720	3.4351	0.1631
12	HWM-NY-KIN-725	40.6754	-73.9910	3.2750	2.9962	0.2788
13	HWM-NY-KIN-900	40.6673	-74.0000	3.2730	3.3498	0.0768
14	HWM-NY-KIN-901	40.6611	-74.0056	3.2730	3.4077	0.1347
15	HWM-NY-KIN-902	40.6558	-74.0162	3.2630	3.5022	0.2392
16	HWM-NY-NEW-001	40.7776	-73.9425	3.3950	3.1791	0.2159
17	HWM-NY-NEW-004	40.7631	-74.0005	3.3890	3.1547	0.2343
18	HWM-NY-NEW-005	40.7401	-73.9733	3.3990	3.2949	0.1041
19	HWM-NY-NEW-008	40.6904	-74.0469	3.2960	3.4412	0.1452
20	HWM-NY-NEW-009	40.6897	-74.0439	3.2940	3.4656	0.1716
21	HWM-NY-NEW-010	40.6991	-74.0399	3.3050	3.3863	0.0813
22	HWM-NY-NEW-011	40.6994	-74.0387	3.3100	3.3833	0.0733
23	HWM-NY-NEW-012	40.6909	-74.0125	3.3140	3.3498	0.0358
24	HWM-NY-NEW-013	40.6853	-74.0249	3.2980	3.4199	0.1219
25	HWM-NY-NEW-100	40.7011	-74.0156	3.3170	3.5204	0.2034
26	HWM-NY-NEW-101	40.7011	-74.0150	3.3110	3.4656	0.1546
27	HWM-NY-NEW-102	40.7044	-74.0169	3.3180	3.0541	0.2639
28	HWM-NY-NEW-103	40.7044	-74.0167	3.3180	3.3498	0.0318
29	HWM-NY-NEW-104	40.7031	-74.0069	3.3230	3.4412	0.1182
30	HWM-NY-NEW-105	40.7050	-74.0067	3.3260	3.3741	0.0481
31	HWM-NY-NEW-106	40.7050	-74.0067	3.3260	3.3985	0.0725
32	HWM-NY-NEW-107	40.7050	-74.0064	3.3260	3.4229	0.0969
33	HWM-NY-NEW-108	40.7078	-74.0039	3.3300	3.3741	0.0441
34	HWM-NY-NEW-109	40.7078	-74.0011	3.3330	3.3650	0.0320
35	HWM-NY-NEW-110	40.7078	-74.0022	3.3330	3.3894	0.0564
36	HWM-NY-NEW-111	40.7078	-74.0022	3.3330	3.3680	0.0350
37	HWM-NY-NEW-112	40.7097	-73.9953	3.3420	3.3985	0.0565

38	HWM-NY-NEW-113	40.7108	-73.9781	3.3590	3.4077	0.0487
39	HWM-NY-NEW-114	40.7108	-73.9781	3.3590	3.3101	0.0489
40	HWM-NY-NEW-115	40.7108	-73.9781	3.3590	3.3101	0.0489
41	HWM-NY-NEW-116	40.7111	-73.9772	3.3590	3.3132	0.0458
42	HWM-NY-NEW-117	40.7111	-73.9772	3.3590	3.3132	0.0458
43	HWM-NY-NEW-118	40.7111	-73.9772	3.3590	3.3406	0.0184
44	HWM-NY-NEW-119	40.7111	-73.9772	3.3590	3.3284	0.0306
45	HWM-NY-NEW-120	40.7164	-74.0161	3.3330	3.3162	0.0168
46	HWM-NY-NEW-121	40.7164	-74.0167	3.3330	3.3132	0.0198
47	HWM-NY-NEW-122	40.7181	-74.0147	3.3410	3.4534	0.1124
48	HWM-NY-NEW-123	40.7183	-74.0150	3.3370	3.3680	0.0310
49	HWM-NY-NEW-124	40.7169	-74.0119	3.3400	3.3071	0.0329
50	HWM-NY-NEW-125	40.7169	-74.0125	3.3400	3.2187	0.1213
51	HWM-NY-NEW-128	40.7208	-74.0114	3.3420	3.2888	0.0532
52	HWM-NY-NEW-806	40.7966	-73.9155	3.3570	3.3924	0.0354
53	HWM-NY-NEW-981	40.8006	-73.9265	3.3920	3.1425	0.2495
54	HWM-NY-QUE-001	40.7156	-73.9206	3.4420	3.3162	0.1258
55	HWM-NY-QUE-503	40.7928	-73.8493	3.3730	3.0846	0.2884
56	HWM-NY-QUE-505	40.7417	-73.9590	3.4050	3.2675	0.1375
57	HWM-NY-QUE-506	40.7723	-73.9360	3.4040	3.3315	0.0725
58	HWM-NY-QUE-509	40.7862	-73.9153	3.3680	3.1852	0.1828
59	HWM-NY-QUE-520	40.7964	-73.8290	3.3750	3.3040	0.0710
60	HWM-NY-QUE-603	40.7597	-73.8486	3.3720	3.1943	0.1777
61	HWM-NY-RIC-722	40.6468	-74.0895	3.2600	3.5570	0.2970
62	HWM-NY-RIC-723	40.6412	-74.1359	3.2690	3.4961	0.2271

Table 6.3B. Sub-grid model vertical spatial comparison in meters with 11 non-wave affected USGS-collected high water mark observation sites for the New York City Harbor in meters above NAVD88 for the State of New Jersey.

#	HWM Site ID	Latitude	Longitude	Model Result (m)	High Water Mark (m)	Difference (m)
1	HWM-NJ-BER-415	40.8428	-73.9662	3.4350	2.8773	0.5577
2	HWM-NJ-BER-423	40.8161	-73.9785	3.4240	2.8834	0.5406
3	HWM-NJ-HUD-001	40.7588	-74.0289	3.3850	2.8590	0.5260
4	HWM-NJ-HUD-002	40.7588	-74.0289	3.3850	2.8560	0.5290
5	HWM-NJ-HUD-003	40.7588	-74.0289	3.3850	2.8590	0.5260
6	HWM-NJ-HUD-004	40.7590	-74.0297	3.3850	3.6546	0.2696
7	HWM-NJ-HUD-005	40.7590	-74.0297	3.3850	3.6546	0.2696
8	HWM-NJ-HUD-006	40.7590	-74.0297	3.3850	3.6606	0.2756
9	HWM-NJ-HUD-007	40.7619	-74.0234	3.3850	3.1516	0.2334
10	HWM-NJ-HUD-109	40.7165	-74.0336	3.3280	3.1821	0.1459
11	HWM-NJ-HUD-110	40.7356	-74.0285	3.3570	3.2309	0.1261

Table 6.3C. Statistics table including metrics for mean difference ($\bar{\varepsilon}$), absolute mean difference ($|\bar{\varepsilon}|$), standard deviation (σ), and root-mean-squared error (*RMSE*) for the high water mark comparison with model-predicted peak water levels for New York and New Jersey in the New York City Harbor.

Data Location	$\bar{\varepsilon}$	$|\bar{\varepsilon}|$	σ	*RMSE*
HWM New York	-0.0004	0.112	0.085	0.12
HWM New Jersey	0.215	0.364	0.256	0.347

6.2.2 FEMA Inundated Schools

Inundation attributed to 2012 Hurricane Sandy affected a variety of types of critical infrastructure in New York and New Jersey. The FEMA inundated schools data set is a homeland infrastructure geospatial data inventory of 295 schools flooded during Hurricane Sandy assembled by National Geospatial-Intelligence Agency in partnership with the Department of Homeland Security in 2012. Data for public and private schools in New York were provided by the New York State Department of Education in New York City only. New Jersey public and private schools were furnished via the New Jersey Department of Education with the data being available as a GIS shape file with source: http://184.72.33.183/GISData/MOTF/Hurricane%20Sandy/InundatedSchools_Depth.zip.

Within the study area of the sub-grid domain surrounding the New York Harbor, 80 schools were flooded with recorded water heights reported by FEMA in the aftermath of Hurricane Sandy. The assessments provide general information regarding flood height relative to the ground surface at each school location. These flood heights were compared with the model's output for maximum water thickness (calculated as the difference between the free surface of the flood waters and the topographic ground surface), and

assembled as an additional method for spatial point-to-point comparison for New York in Table 6.4A and New Jersey in Table 6.4B.

Within New York City, most of the inundated schools were located in Manhattan and Brooklyn. The worst flooding was observed at schools neighboring Coney Island Creek along the more coastal areas of New York City. Statistical measures for New York City are reasonably favorable with a $\bar{\varepsilon}$ of 0.0332m, implying no leaning towards over-prediction or under-prediction of inundated schools by the model (Table 6.4C). The $\bar{\varepsilon}$ of 0.3483m reported for New Jersey suggests that the model tended to over-predict recorded high water marks by 34.8cm on average. The $|\bar{\varepsilon}|$ was 0.2769m for New York, compared to 0.4227m calculated for New Jersey. The standard deviations in the two data sets were about equal with 0.3304m for schools in New York and 0.3328m in the model comparison against flood heights at schools in New Jersey (Table 6.4C).

The impact of waves impacted FEMA's inundated schools dataset due to its relation to the USGS high water marks, while the sub-grid model results do not. Thus, regions with higher wave influence may have exaggerated water levels in the FEMA dataset, around the Southern New York Bay and Staten Island, extending the range of the calculated differences between the sub-grid model and the inundated schools for New York (Table 6.4A). The RMSE for the 60 schools in New York City within the sub-grid domain was 0.3293m. Upon comparison with the RMSE of 0.4760m for the 20 schools in New Jersey, the point-to-point evaluation with the New Jersey schools led to 0.1467m more RMSE. As with the other point-to-point comparisons using the USGS high water marks, the RMSE difference of 0.1467m more error in New Jersey is likely attributed to the lack of freely available building data for inclusion in the model's DEM.

140

Table 6.4A. Sub-grid model vertical spatial comparison with 60 FEMA-reported flood heights in meters above the ground at inundated schools within the New York City Harbor for the State of New York. Inundated school information, latitude/longitude, and flood heights adapted from (FEMA MOTF, 2013).

#	Inundated School Site ID	Latitude	Longitude	Model Result (m)	Flood Height (m)	Difference (m)
1	Abraham Lincoln High School	40.5824	-73.9681	0.8166	0.4923	0.3243
2	Academy Of Environmental Science Secondary School	40.7852	-73.9423	0.8412	0.8877	-0.0466
3	Archimedes Academy For Math, Science And Technology	40.8152	-73.8561	0.8238	1.4349	-0.6111
4	Bard High School Early College	40.7183	-73.9761	1.1858	1.5796	-0.3938
5	Battery Park City School	40.7062	-74.0177	2.5644	2.8154	-0.2510
6	Bronx Mathematics Preparatory School	40.8152	-73.8561	0.8238	1.4349	-0.6111
7	Coalition School For Social Change	40.7989	-73.9334	0.6988	1.1482	-0.4494
8	CUNY Borough Of Manhattan Community College	40.7188	-74.0118	1.3489	0.8126	0.5363
9	Expeditionary Learning School For Community Leader	40.5938	-73.9860	0.7845	0.5673	0.2172
10	Frederick Douglass Academy	40.8240	-73.9358	1.6064	1.4853	0.1211
11	Harlem Village Academy Leadership	40.7992	-73.9337	0.7538	1.0969	-0.3431
12	Herbert H Lehman High School	40.8401	-73.8392	0.8949	0.3963	0.4986
13	High School Of Sports Management	40.5938	-73.9861	0.7896	0.5673	0.2223
14	International High School At Lafayette	40.5945	-73.9862	0.7896	0.5672	0.2224
15	Is 174 Eugene T Maleska	40.8151	-73.8561	0.8238	1.4349	-0.6111
16	Is 289	40.7170	-74.0139	2.0012	2.1895	-0.1883
17	Is 303 Herbert S Eisenberg	40.5824	-73.9725	0.8615	0.6794	0.1820

18	Isaac Newton MS For Science	40.7941	-73.9331	0.6189	0.7578	-0.1389
19	John Dewey High School	40.5877	-73.9816	0.7860	0.2319	0.5541
20	John V Lindsay Wildcat Academy Charter School	40.7052	-74.0161	1.2919	1.4333	-0.1415
21	King's Academy	40.8051	-73.9344	0.4670	0.2609	0.2061
22	Kingsborough Early College School	40.5945	-73.9862	0.7896	0.5672	0.2224
23	Lafayette High School	40.5938	-73.9861	0.7896	0.5673	0.2223
24	Life Academy High School For Film And Music	40.5938	-73.9860	0.7845	0.5673	0.2172
25	Life Sciences Secondary School	40.7833	-73.9459	0.5617	0.2617	0.3000
26	Lincoln Technical Institute	40.7841	-73.8289	0.4107	1.0383	-0.6276
27	Manhattan Center For Science & Mathematics	40.7941	-73.9331	0.6210	0.7578	-0.1368
28	Most Precious Blood School	40.5906	-73.9872	0.8437	0.7678	0.0759
29	Mount Carmel-Holy Rosary School	40.7974	-73.9318	0.4678	0.4562	0.0116
30	MS 224 Manhattan East	40.7852	-73.9423	0.8412	0.8877	-0.0466
31	MS 45/Stars Prep Academy	40.7992	-73.9337	0.7538	1.0969	-0.3431
32	New York Center For Autism Charter School	40.7856	-73.9410	2.1529	2.0057	0.1472
33	Pave Academy Charter School	40.6772	-74.0117	0.8702	0.7566	0.1136
34	Promise Christian Academy	40.7699	-73.8390	0.4737	0.6414	-0.1677
35	PS 102 Jacques Cartier	40.7949	-73.9383	0.4249	0.1675	0.2574
36	PS 112 Jose Celso Barbosa	40.7965	-73.9301	1.0888	1.2366	-0.1477
37	PS 126 Jacob August Riis	40.7105	-73.9970	0.4167	0.2440	0.1727
38	PS 146 Ann M Short	40.7895	-73.9389	1.4440	1.6655	-0.2215
39	PS 15 Patrick F Daly	40.6771	-74.0118	0.8620	0.7566	0.1055
40	PS 188 Michael E Berdy	40.5768	-74.0005	0.9212	0.8634	0.0578

41	PS 188 The Island School	40.7197	-73.9775	0.6381	0.2287	0.4094
42	PS 200 The James McCune Smith School	40.8244	-73.9366	0.5660	0.9383	-0.3723
43	PS 206 Jose Celso Barbosa	40.7970	-73.9303	0.9220	0.8365	0.0855
44	PS 212 Lady Deborah Moody	40.5875	-73.9856	0.7136	0.4513	0.2623
45	PS 34 Franklin D Roosevelt	40.7262	-73.9750	0.8947	0.4628	0.4319
46	PS 46 Arthur Tappan	40.8317	-73.9362	0.6378	0.0171	0.6207
47	PS 50 Vito Marcantonio	40.7856	-73.9410	2.6070	2.0057	0.6013
48	PS 52 John C Thompson	40.5824	-74.0883	1.0239	1.0109	0.0130
49	PS 721 Brooklyn Occupational Training	40.5877	-73.9816	0.6757	0.2319	0.4438
50	PS 78	40.7442	-73.9565	0.9679	0.9794	-0.0115
51	PS 90 Edna Cohen	40.5783	-73.9800	4.2535	4.6107	-0.3573
52	PS M094	40.7197	-73.9775	0.6381	0.2287	0.4094
53	Rachel Carson High School For Coastal Studies	40.5823	-73.9719	0.7867	0.6639	0.1228
54	Renaissance High School For Musical Theater And Tech	40.8401	-73.8393	1.0190	0.3963	0.6227
55	Renaissance School Of The Arts	40.7852	-73.9423	0.8412	1.0769	-0.2358
56	River East Elementary	40.7970	-73.9303	0.9220	0.8365	0.0855
57	Smiles Around Us Academy	40.5910	-74.0670	0.9235	1.1537	-0.2302
58	South Brooklyn Community High School	40.6778	-74.0141	0.8419	0.6355	0.2064
59	Stuyvesant High School	40.7178	-74.0138	2.6070	2.8913	-0.2844
60	Urban Peace Academy	40.7992	-73.9337	0.7538	1.0969	-0.3431

Table 6.4B. Sub-grid model vertical spatial comparison with 20 FEMA-reported flood heights in meters above the ground at inundated schools within the New York Harbor for the State of New Jersey. Flood heights adapted from FEMA MOTF, 2013.

#	Inundated School Site ID	Latitude	Longitude	Model Result (m)	Flood Height (m)	Difference (m)
1	Beacon Christian Academy	40.6606	-74.1141	1.0265	0.6970	0.3295
2	Elysian CS Of Hoboken	40.7404	-74.0316	0.9939	0.2455	0.7484
3	Frank R Conwell No 3	40.7172	-74.0475	1.0528	0.6072	0.4456
4	Hoboken Catholic Academy	40.7461	-74.0374	1.4238	1.4382	-0.0144
5	Hoboken High	40.7475	-74.0331	1.3075	1.2346	0.0729
6	Hola Hoboken Dual Language CS	40.7395	-74.0380	1.4228	1.7934	-0.3706
7	James J Ferris	40.7215	-74.0534	0.9981	0.4968	0.5013
8	Kennedy Number 9	40.7213	-74.0522	0.9961	0.4923	0.5038
9	Learning Community CS	40.7157	-74.0450	1.1172	0.9903	0.1268
10	Mustard Seed School	40.7421	-74.0335	1.2137	0.9603	0.2534
11	N J Reg Day Jersey City	40.7157	-74.0621	1.0031	0.4787	0.5244
12	Number 22	40.7137	-74.0616	0.9862	0.4784	0.5078
13	Number 4 Middle School	40.7174	-74.0499	1.0520	0.6542	0.3978
14	Our Lady Of Czestochowa	40.7168	-74.0418	1.1111	0.8092	0.3019
15	Salvatore R Calabro No 4	40.7442	-74.0314	1.1150	0.6808	0.4342
16	St Peters Preparatory School	40.7156	-74.0403	0.9811	0.3178	0.6633
17	The Hudson School	40.7430	-74.0323	1.1787	0.9038	0.2749
18	Thomas G Connors	40.7405	-74.0393	1.4228	1.7822	-0.3594
19	Wallace No 6	40.7512	-74.0312	0.8778	0.0934	0.7844
20	Waterfront Montessori	40.7124	-74.0398	0.9102	0.0709	0.8394

Table 6.4C. Statistics table including metrics for mean difference ($\bar{\varepsilon}$), absolute mean difference ($|\bar{\varepsilon}|$), standard deviation (σ), and root-mean-squared error (*RMSE*) for the high water marks reported in FEMA's inundated schools dataset compared with model-predicted peak water levels for New York and New Jersey in the New York Harbor.

Data Location	$\bar{\varepsilon}$	$|\bar{\varepsilon}|$	σ	*RMSE*
New York Schools	0.0332	0.2769	0.3304	0.3293
New Jersey Schools	0.3483	0.4227	0.3328	0.4760

6.2.3   FEMA Maximum Extent of Inundation Map

Spatial area comparison with FEMA's maximum extent of inundation map was two-fold. This spatial flood coverage map was based upon interpolation of the USGS's field measurements including high water marks and rapid deployment gauges compared in the previous sections and the best available digital elevation data. The field-verified high water mark measurements collected in the aftermath of Hurricane Sandy were utilized to construct an interpolated GIS layer of water surface heights, which was subsequently subtracted from the best available DEM to create a water level thickness layer and a 0m contour for the maximum extent of inundation. These products are comprised of an inundation grid at 1m resolution for New York City and 3m resolution for New Jersey, along with a clipped surge boundary (FEMA MOTF, 2013). The database and GIS products produced by the USGS and FEMA were enormously valuable as a standard for spatial comparison with the sub-grid model results.

These data were collected to calculate distances between the model's predicted maximum flood extent and FEMA's reported maximums (Table 6.5 and Table 6.6), and to compute inundation percent area match statistics for additional spatial verification of the model (Table 6.7). Additionally, 12 MTA subway stations with 41 subway entrances

recorded as flooding from the street in inundated areas directly impacted by Sandy's storm surge were utilized as an additional verification method (Table 6.9).

6.2.3.1 Distance Differential Assessment

Maximum spatial extent of inundation is an especially critical attribute to address in assessing flooding risk. The precision of the maximum horizontal extent of the inundation depends upon the accuracy of the flux estimate and the propagation speed of the long wave associated with the relative variations in water level. Using the unique nonlinear wetting and drying solver within the UnTRIM^2 sub-grid model, transitions between partially wet and dry regions are seamless and perceived to be resolved both accurately and naturally. Therefore, the sub-grid model with the nonlinear solver has the advantage of predicting the maximum extent of the inundation more accurately than advection-based models without an embedded sub-grid to facilitate partial wetting and drying of grid cells in an accurate and timely manner.

Utilizing the global model outputs for elevation and velocities at each model time step via the extensive methods described in the previous chapter, geotiff images were concatenated into animations of the flood water movement in the New York Harbor during Hurricane Sandy. The animations demonstrate seamless street-level flooding through partially wet and partially dry base grid cells with many including tall buildings effectively blocking the flow of water and generating form drag as the water flows around the buildings and through the streets in between. The maximum water levels at each sub-grid cell were calculated to provide a maximum flood extent layer for spatial distance and area comparisons with the FEMA maximum extent of inundation layer.

146

The initial distance comparison utilizing points along the FEMA-clipped maximum extent of inundation line revealed a relatively favorable distance differential with the model-predicted maximum inundation across the sub-grid domain with an absolute mean distance difference of 38.43m (Table 6.5). Upon evaluation of maximum inundation distance by river system, the absolute mean distance indicated minimal difference along the Hudson River and New York Bay region with a 28.876m difference along the New York City Bank, and 36.9m along the lower elevation New Jersey Bank. The Hudson River was divided by state instead of west/east bank due to the lack of freely available building data for the New Jersey side for representation in the sub-grid model DEM (Figure 6.4). The observable difference of 8.024m between the New York bank of the Hudson River (buildings included) and the New Jersey side (bereft buildings) is an indication of the importance of resolving building infrastructure in the model sub-grid for accurate high-resolution inundation prediction.

The average measured distances from the FEMA-reported maximum flood extent points to the model-predicted inundation along the New York bank of the Harlem River were 44.222m, with a 46.779m difference recorded along the East River. The horizontal distance differentials cover a range from 0 to 258.6m (Figure 6.5A-D). Of the four river systems, the East River accounts for a plurality of the point to line distances with 47,283 points out of the total 94,844 points with 5m regular point spacing along the FEMA maximum inundation line. Together, the New York side (21,492 points) and the New Jersey bank (16,396 points) of the Hudson River account for a 32.888m absolute mean distance, the most favorable inundation comparison of the three river systems (Table 6.5).
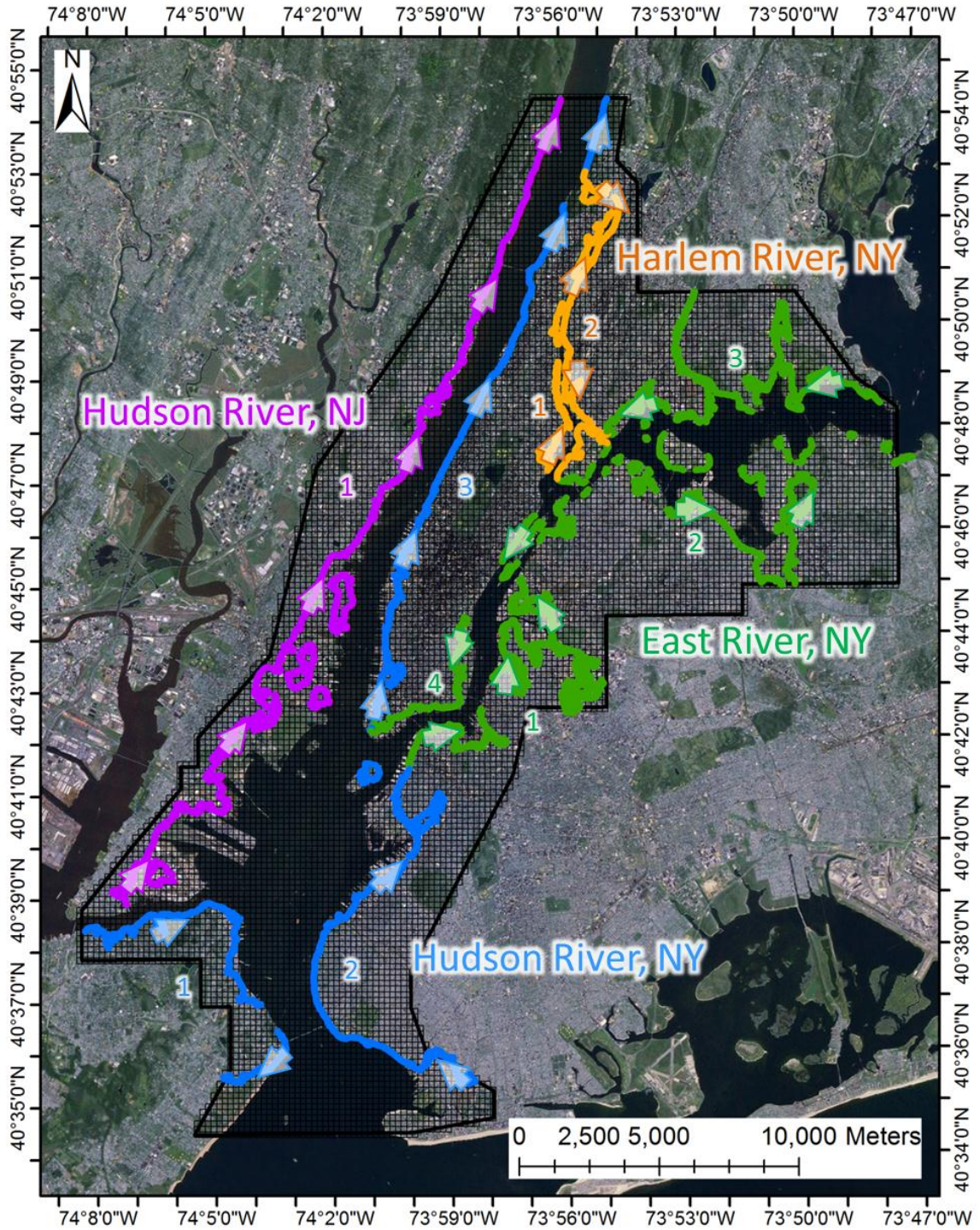
Figure 6.4. Distance measurement map displaying the observed maximum extent of inundation reported by FEMA, separated by color into four regions by river system and state. Numbers and arrows illustrate the direction and order of distance measurements following along each region corresponding with Figure 6.5A-D.
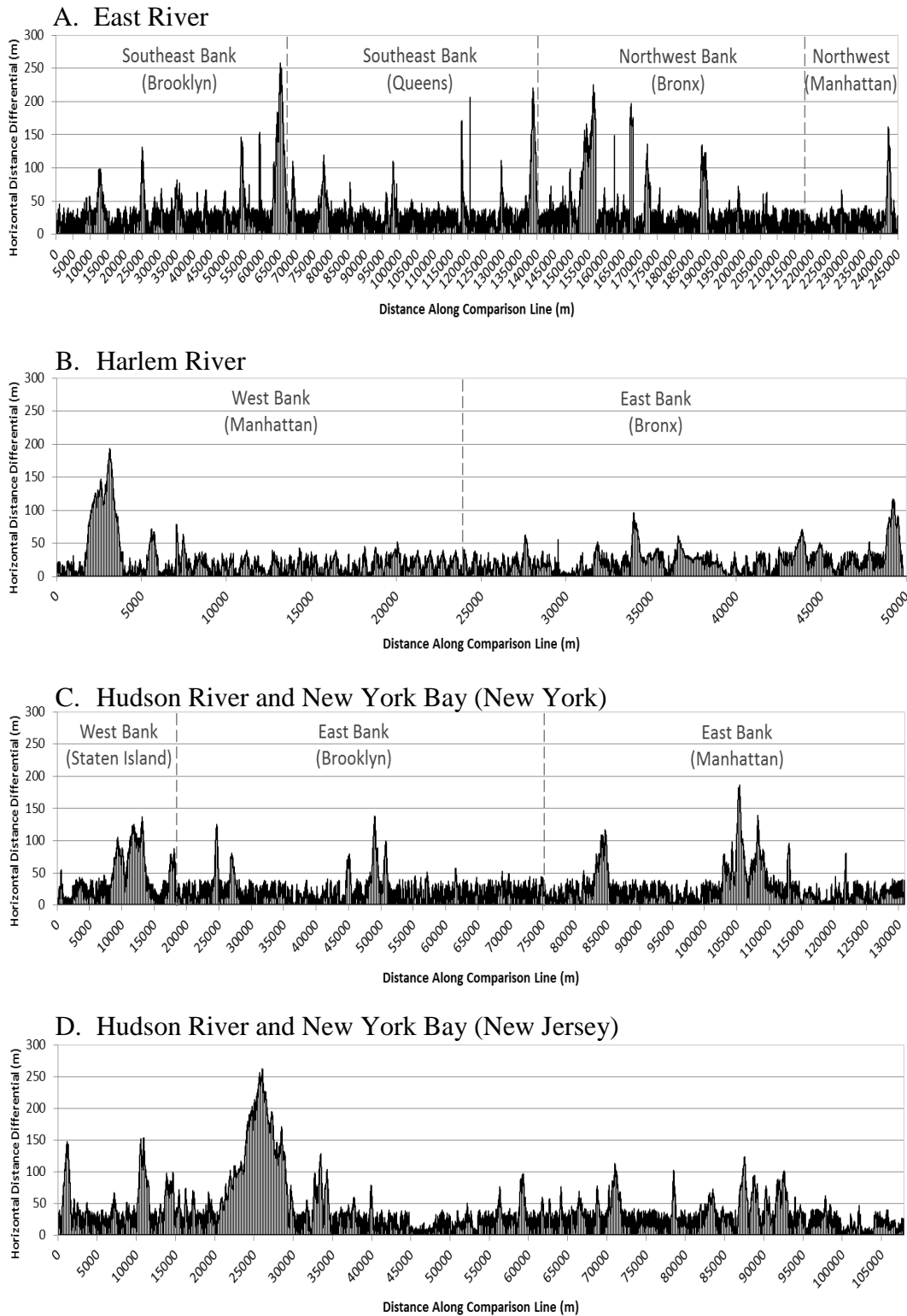
Figure 6.5A-D. Plotted absolute distances to the model's predicted maximum extent of inundation line in reference to the observed maximum extent of inundation line reported by FEMA. Distance measurements are separated into four regions by river system, including: East River (A), Harlem River (B), Hudson River on the New York side (C), and along the New Jersey coast (D).

Table 6.5. Distance difference table with calculated absolute mean distances from the FEMA reported maximum extent of inundation line to the sub-grid model predicted maximum extent line with standard deviations in meters.

Survey Region	# of Points	Abs. Mean Dist.	Std. Deviation
New York			
East River NY	47,283	46.779	58.306
Harlem River NY	9,673	44.222	56.696
Hudson River NY	21,492	28.876	27.017
All New York	78,448	39.959	47.340
New Jersey			
Hudson River NJ	16,396	36.900	30.376
All New Jersey	16,396	36.900	30.376
All Hudson River	37,888	32.888	28.696
Total Across Domain	94,844	38.430	38.858

The second distance comparison via shoreline to FEMA observation (Figure 6.6) and shoreline to sub-grid model prediction (Figure 6.7) along roadways perpendicular to the water's edge revealed an average distance difference of 27.67m, trending toward model under-prediction along 26 sampled roadways throughout the sub-grid domain (Table 6.6). Figures 5.11 and 5.12 indicate that the greatest inundation (>1km inundation from the shoreline) within the sub-grid domain coverage area was observed along the New Jersey Bank of the Hudson River and New York Bay, where elevation is geologically lower than the New York bank. Substantial inundation was also observed near the semi-coastal south end of the domain leading out into Raritan Bay and the Atlantic Ocean. Flooding distances from the shoreline were in relative agreement along most roadways with slightly more over-prediction observed along the East River; likely attributed to the dual surges converging from the Raritan Bay to the south and from the east propagating along the Long Island Sound (Figure 6.7, Table 6.6). Conversely, somewhat more frequent under-prediction was observed along the Hudson River, although many of these occurrences are minute differences (Figure 6.6, Table 6.6).
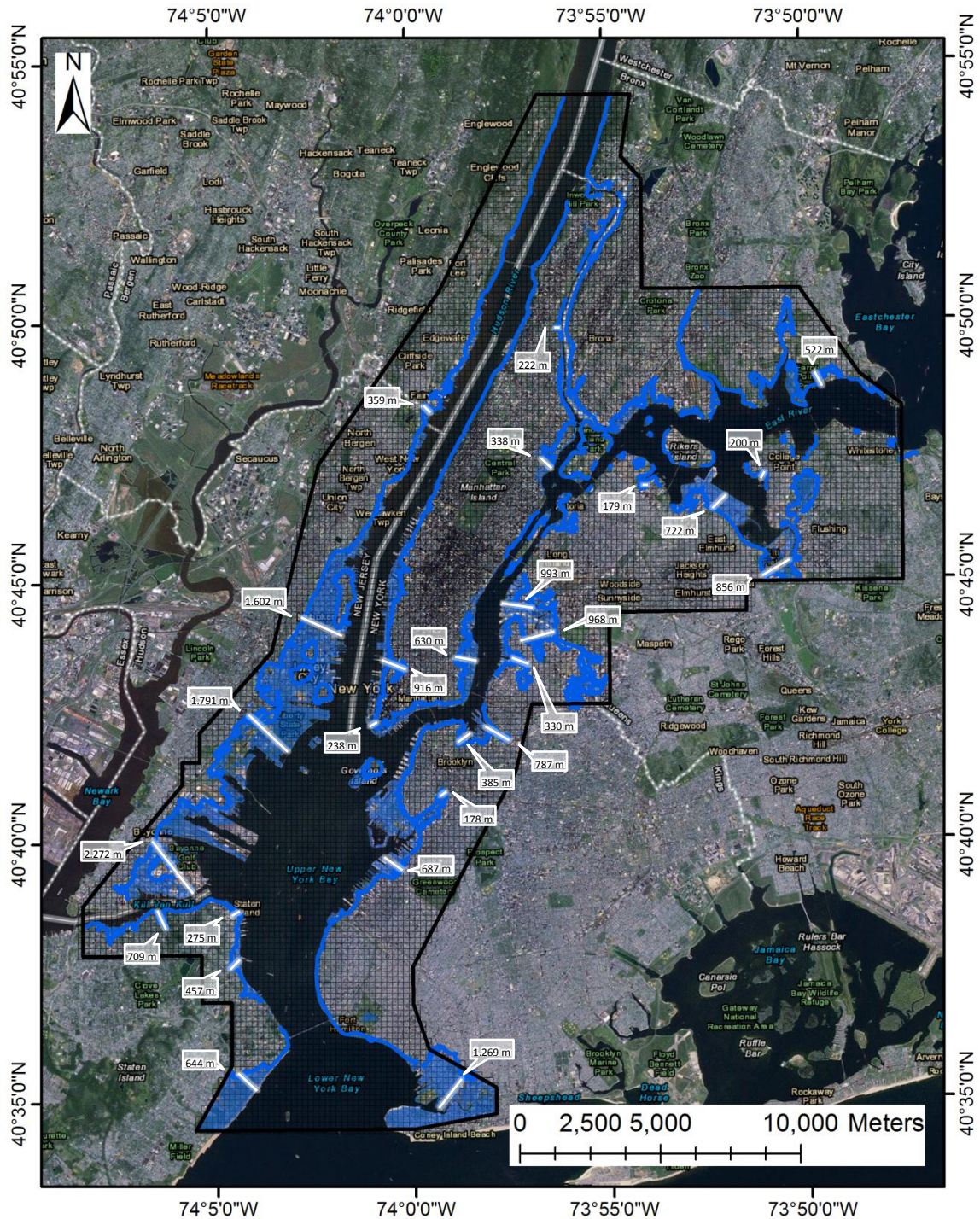
Figure 6.6. Distances measured from the shoreline to the maximum spatial extent of inundation reported by FEMA superposed with inundation distances in meters along streets perpendicular to the shoreline; distance values correspond to the model results in Figure 6.7 and Table 6.2.
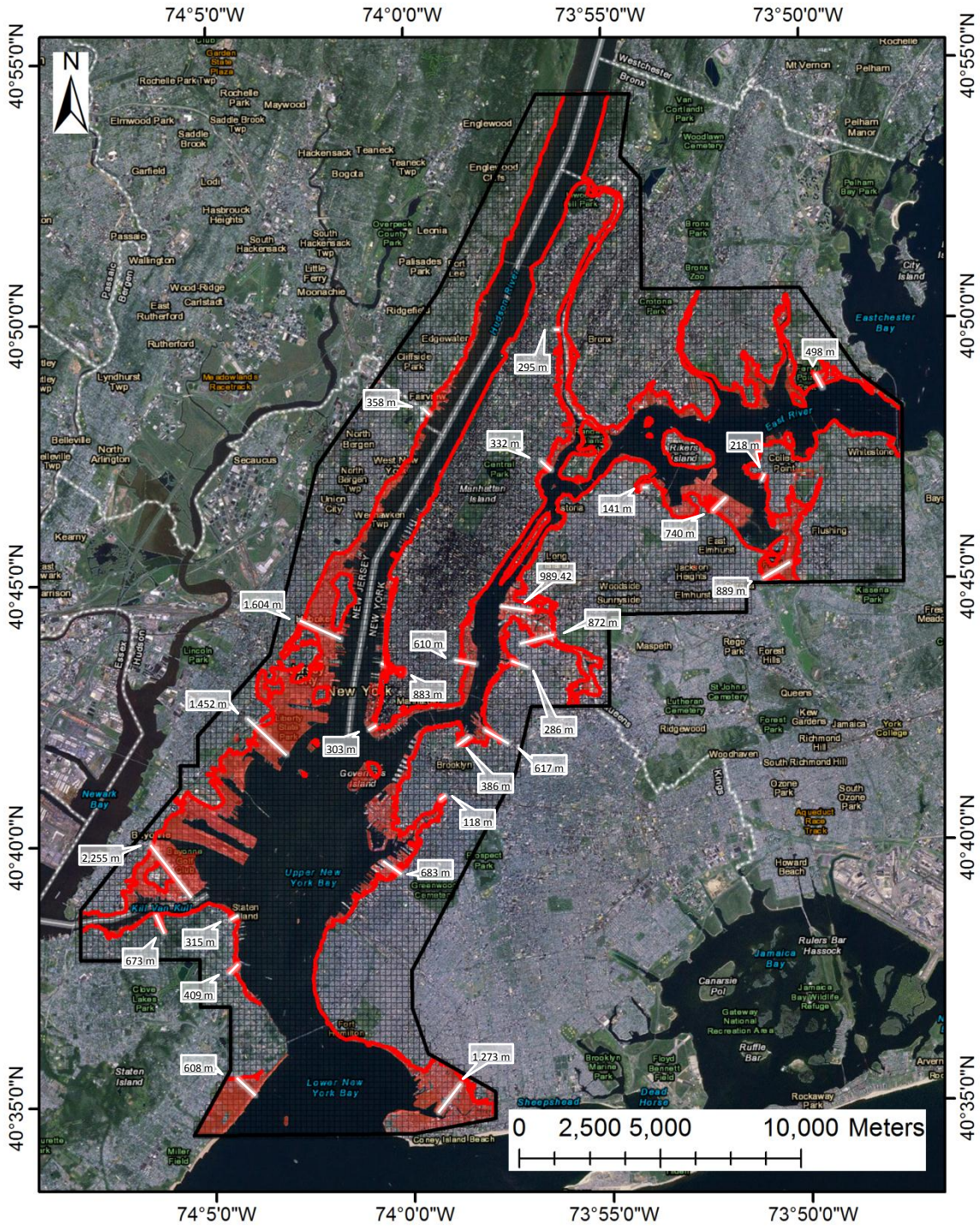
Figure 6.7. Distances measured from the shoreline to the maximum spatial extent of inundation predicted by the sub-grid model superposed with inundation distances in meters along streets perpendicular to the shoreline; distance values correspond to the FEMA observation data in Figure 6.6 and Table 6.6.

Table 6.6. Measured distances along streets perpendicular to the shoreline to the maximum extent of inundation reported by FEMA, distances predicted by the sub-grid model, and calculated differences along streets perpendicular to the shoreline; all units in meters.

#	Roadway	Borough	Dist. FEMA (m)	Dist. Model (m)	Difference (m)	Under/Over
1	Sand Ln.	Staten Island	644.38	608.12	-36.26	Under-predict
2	Water St. & Canal St.	Staten Island	456.52	409.65	-46.87	Under-predict
3	Ferry Terminal Dr.	Staten Island	275.33	315.24	39.91	Over-predict
4	Kissel Ave.	Staten Island	708.79	672.54	-36.25	Under-predict
5	New Hook Rd.	New Jersey	2,272.11	2,254.98	-17.13	Under-predict
6	Thomas McGovern Dr.	New Jersey	1,790.69	1,452.34	-338.35	Under-predict
7	Observer Hwy. to Train Station	New Jersey	1,602.13	1,604.01	1.88	Over-predict
8	S. Independence Way	New Jersey	359.21	357.84	-1.37	Under-predict
9	Canal St. to Broadway	Manhattan	915.66	883.34	-32.32	Under-predict
10	Battery Pl. to Broadway	Manhattan	238.01	302.80	64.79	Over-predict
11	E. 13th St.	Manhattan	629.56	609.83	-19.73	Under-predict
12	E. 110th St.	Manhattan	338.10	331.54	-6.56	Under-predict
13	W. 148th St.	Manhattan	222.08	294.75	72.67	Over-predict
14	Swinton Ave.	Bronx	521.76	498.35	-23.41	Under-predict
15	117th St.	Queens	199.65	218.14	18.49	Over-predict
16	44th St. & Meridian Rd.	Queens	855.92	888.56	32.64	Over-predict
17	102nd St. over LaGuardia Rd.	Queens	722.45	740.03	17.58	Over-predict
18	19th St.	Queens	178.54	140.76	-37.78	Under-predict
19	48th Ave.	Queens	992.54	989.42	-3.12	Under-predict
20	Greenpoint Ave.	Brooklyn	968.34	872.20	-96.14	Under-predict
21	N. 15th St.	Brooklyn	329.86	285.79	-44.07	Under-predict
22	Kent Ave.	Brooklyn	786.52	617.12	-169.40	Under-predict
23	2nd St.	Brooklyn	385.17	386.08	0.91	Over-predict
24	Bond St.	Brooklyn	178.16	118.28	-59.88	Under-predict
25	30th St. off Brooklyn-Queens Expy.	Brooklyn	686.78	683.23	-3.55	Under-predict
26	W. 8th St.	Brooklyn	1,269.25	1,273.07	3.82	Over-predict
		Average	712.60	684.92	-27.67	Under-predict
		Std. Deviation	530.31	503.34	79.86	

6.2.3.2 Area Difference Map Evaluation

The spatial comparison shown in Figure 6.8 resulted in an overall 75.15% spatial match with 11.41% area model over-prediction and 13.44% model under-prediction (Table 6.7). Area comparisons along the main stem of the Hudson River performed reasonably well with a 78.80% match along the New York river banks, and a slightly lower match of 76.73% match along the New Jersey river banks. Flooded area was higher for the New Jersey side of the Hudson River, as the 76.73% matched inundation area corresponded to 17,539,367m^2, while the 78.80% match on the New York side of the river represents 13,076,031m^2 (Table 6.7). The ratio of under-prediction to over-prediction was slightly less than 2:1 for the Hudson River with the New York bank having 13.76% under-prediction, representing 2,283,797m^2, and 7.44% over-prediction signifying a representative area of 1,234,304m^2. The Hudson River banks adjacent to New Jersey observed slightly more error than their New York counterparts with 14.86% under-predicting FEMA's maximum inundation estimates, representing an area of 2,283,797m^2, and 8.41% over-prediction indicating a representative area of 1,922,727m^2.

Inundation area comparisons in along the East River observed a 71.81% match, and the Harlem River had a 70.34% match between the model and FEMA's maximum inundation map. The under-predicted area was approximately the same as the Hudson at 11.20% (2,211,023m^2) and 14.49% (918,108m^2), for the East and Harlem Rivers, respectively. However, the over-predicted areas were approximately double those observed in the Hudson River for New York and New Jersey with 17.00% (3,357,069m^2) for the East River and 15.17% (961,151m^2) for the Harlem River (Table 6.7). The

inundation area of the Harlem River was the smallest due to the smaller and narrower

size of the river, and the higher frequency of over-prediction along the East River is

attributed to the aforementioned convergence of the two storm surges from the south by

Atlantic Coast via the Raritan Bay, and from the east through the Long Island Sound.

Discrepancies between the model predictions and the FEMA flood map are

attributed to DEM differences, and possibly the lack of building representation in the

FEMA maximum inundation map (Figure 6.9). Additionally, the implementation of the

spatial flooding observation data as a derivative "bathtub model" product of USGS-

interpolated high water marks and elevation data without regard for strong water current

velocities or estuarine circulation could account for regions with significant

discrepancies. Such discrepancies can be addressed in both the area and distance spatial

comparisons to minimize the impact of DEM incongruities that are outside of control for

the model to address. Two examples of these discrepancies are shown in Figure 6.9A-B.

Along the New Jersey bank of the Hudson River (Figure 6.9A), two overpasses for I-78

are accounted for in the model's Lidar-derived DEM, but do not allow for flow of water

through the underpass. Thus, the model under-predicts flooding along Thomas McGovern

Drive by 338.35m (Table 6.6), and this discrepancy adversely affected the distance and

area comparisons (Table 6.5 and Table 6.7). Similar roadway infrastructure issues with

the DEM cause inundation along Kent Avenue in Figure 6.9B to be blocked by an

overpass for I-278. This caused the model to under-predict flooding east of the overpass

by 169.4m, and over-predict flooding west of the overpass. Thus, also affecting distance

and area measurements as these infrastructures artificially obstructed fluid movement

(Table 6.5 and Table 6.7).

Figure 6.8. Area comparison with FEMA maximum extent of inundation map in the New York Harbor region during 2012 Hurricane Sandy superposed with satellite imagery. Shaded areas are 5m^2 sub-grid cells highlighted according to whether the sub-grid model over-predicted (red), matched (green), or under-predicted (blue) the spatial extent of inundation coverage reported by FEMA.

Table 6.7. Results of the statistical comparison for inundated areas in the New York Harbor region during 2012 Hurricane Sandy separated by river system and by state. Values are presented as surface areas (m^2) and (% area coverage) for each of the defined categories: match, model under-predict, and model over-predict compared with the FEMA maximum inundation coverage map.

Survey Region	Match	(%)	Under-Predict	(%)	Over-Predict	(%)	Total
New York							
East River NY	14,180,524	71.81	2,211,023	11.20	3,357,069	17.00	19,748,616
Harlem River NY	4,457,765	70.34	918,108	14.49	961,151	15.17	6,337,024
Hudson River NY	13,076,031	78.80	2,283,797	13.76	1,234,304	7.44	16,594,132
All New York	31,714,320	74.31	5,412,928	12.68	5,552,524	13.01	42,679,772
New Jersey							
Hudson River NJ	17,539,367	76.73	3,397,304	14.86	1,922,727	8.41	22,859,398
All New Jersey	17,539,367	76.73	3,397,304	14.86	1,922,727	8.41	22,859,398
All Hudson River	30,615,398	77.60	5,681,101	14.40	3,157,031	8.00	39,453,530
Total Across Domain	49,253,687	75.15	8,810,232	13.44	7,475,251	11.41	65,539,170

If we account for the average distance differential of 38.43m between the FEMA-reported maximum flooding extents and the model-predicted maximum inundation extents, the impact of physical impediments for fluid flow not accounted for in the model's DEM may be minimized. A new methodology could be employed to impose a maximum difference threshold using the average distance differential rounded to 40m. An adjustment of over-predicted and under-predicted flood areas would likely limit the impact of missing or added infrastructure along with Lidar-derived data limitations similar to those noted in Figure 6.9. Utilization of a statistical threshold to minimize the influence of physical impediments for fluid flow not accounted for in the model's DEM using the average distance differential of 38.43m between the predicted and observed maximum flooding extents will be addressed in the next chapter.
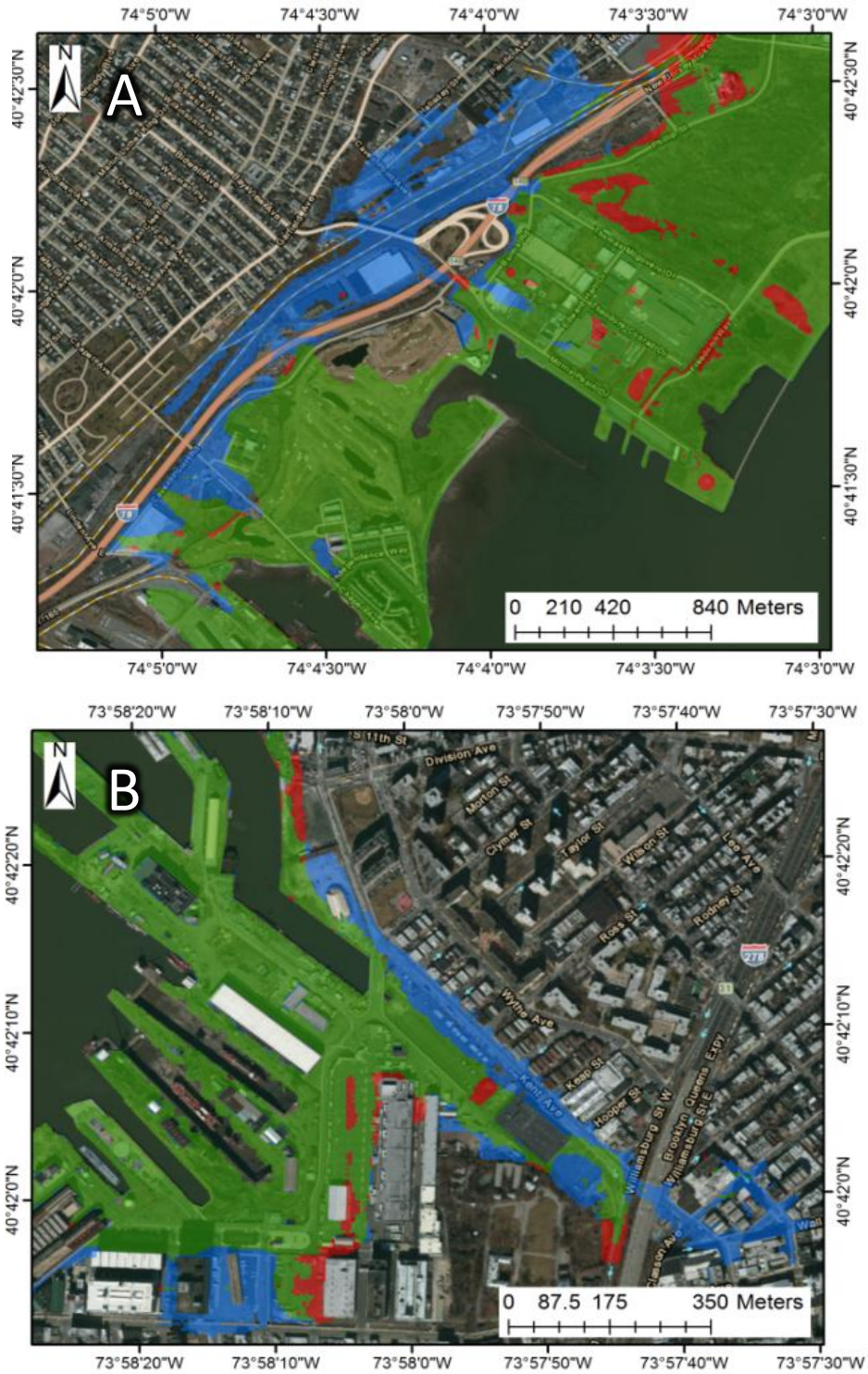
Figure 6.9. Examples of discrepancies between FEMA maximum inundation extents and sub-grid model predicted inundation due to the presence of roadway infrastructure and overpasses blocking fluid movement included in the model's Lidar-derived DEM.

6.3   Sensitivity Tests and Additional Verification

6.3.1   Sensitivity Tests for Grid Resolution

The sub-grid methodology has been described in detail in Chapter 4, and was tested at various base grid resolutions with and without the benefit of sub-grid refinement (Figure 6.10). These tests were performed to determine what difference, if any, is observed in water level predictions resulting from the approximations utilized in the sub-grid conveyance approach. As the base grid resolution increases from 200m to 100m to 50m, an insignificant (<5%) increase in amplitude and a slight promptitude in phase can be observed for water levels with 5m sub-grid refinement for a rapid deployment gauge along the deeply narrow Gowanus Canal in Brooklyn (Figure 6.11). With 5m sub-grid refinement at 200m resolution for the core computational grid, a 40x40 sub-division strategy yielded very comparable results with the 20x20 sub-division of the 100m base grid and the 10x10 nested sub-grid of the 50m base grid (Figure 6.11 and Figure 6.12).

However, the same resolution grids bereft sub-grid refinement compare poorly with the overland inundation observations and with each other. Due to the lack of sub-grid, buildings were unable to be resolved, and subsequently a threshold building height of 5m was imposed prior to using a low-pass filter to smooth the high-frequency building heights. This was done to allow for free movement of the water so inundation could be measured with these broadly interpolated grids without sub-grid refinement (Figure 6.10). When the previous simulations were repeated without 5m sub-grid refinement, the resulting water surface elevations were observed to be significantly more sensitive to grid resolution (Figure 6.13 and Figure 6.14).

This is a consequence of the grid coarsening without sub-grid refinement, as the grid elevations are averaged over a greater area with lower resolutions. The coarser grid meshes give way to tidal decay as the fluid propagates from the grid boundaries to remote shallow reaches of the New York Harbor. The impact of coarsened bathymetry in narrow shallow regions coupled with complex topography yields an unfavorable comparison without sub-grid refinement to resolve these complicated features as observed at rapid deployment gauges located in Brooklyn (Figure 6.13) and in Queens (Figure 6.14).

All runs were conducted on a Dell T3500 PC Workstation with Windows 7 Professional (64-bit edition); an Intel Xeon Quad Core X5570 Processor (2.93GHz); with 24GB RAM running UnTRIM^2 with grid size and run times for a ten-day simulation with global output of water levels and velocities summarized in Table 6.8. As indicated, measurable savings in computational effort can be realized by coarsening the base grid while maintaining detailed sub-grid resolution. As such, the 200m base grid mesh with nested sub-grid will be the grid utilized for the comparisons conducted in New York City.

Without sub-grid specifications, accurate bathymetric and topographic fitting can only be achieved via extremely fine meshes or through the use of heavily distorted unstructured grids. These concessions often have the consequence of having stringent conditions typical of nonlinear systems that must be solved at every time interval. Since overly refined discretization demands a proportionally smaller time step, furthermore contributing to the decreased computational efficiency, it stands to reason that the sub-grid formulation is a useful tool for geophysical fluid dynamics with promising future applications in high-resolution forecast modeling.

With 5m Sub-Grid Refinement

Without Sub-grid Refinement

200m Base Grid

100m Base Grid

50m Base Grid

Topography (m)

14 13 12 11 10 9 8 7 6 5 4 3 2 1 0
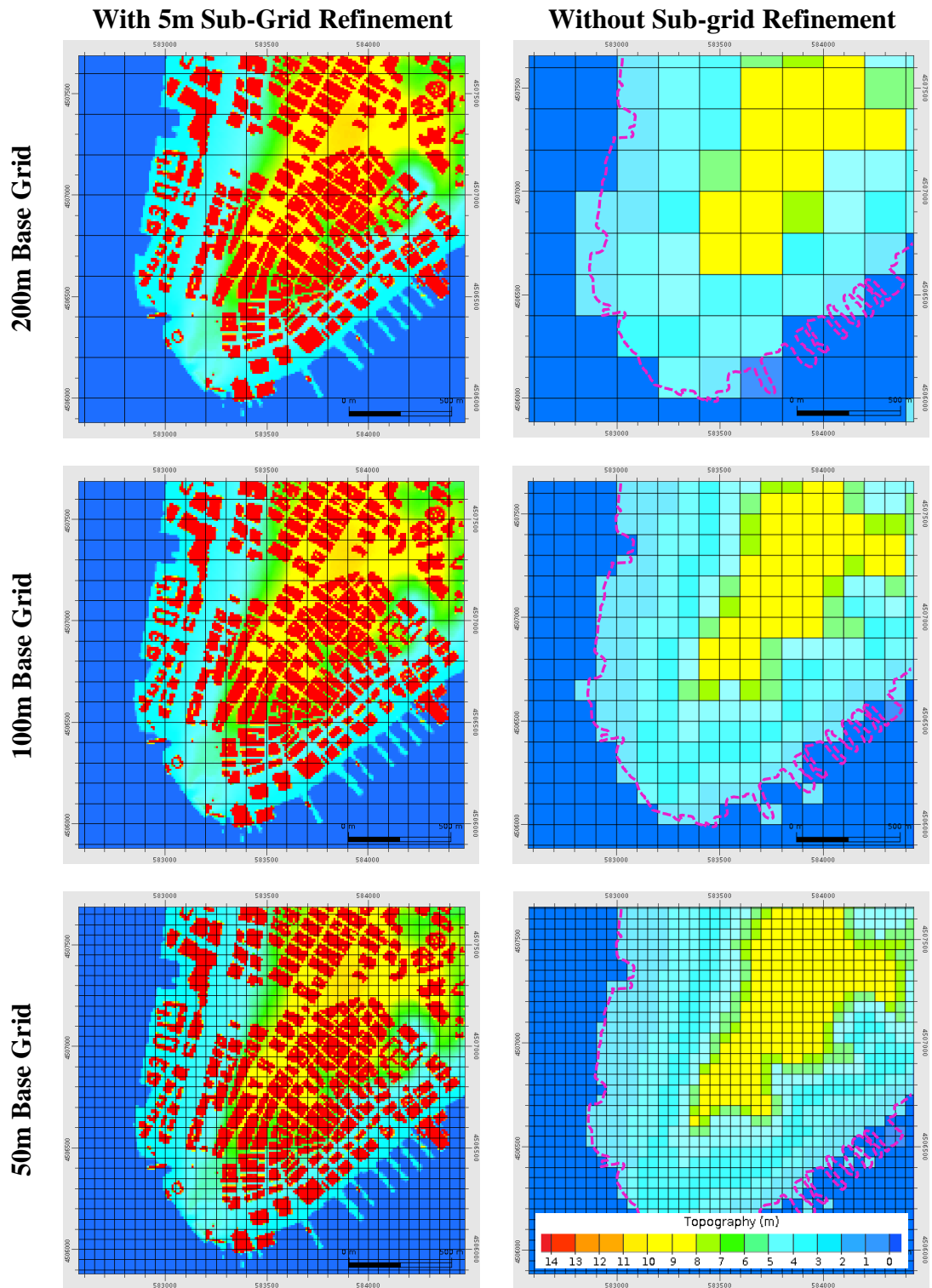
Figure 6.10. Depiction of three UnTRIM^2 model grids with sub-grid refinement (left) and three without sub-grid specifications (right) at 200m (top), 100m (middle), and 50m (bottom) base grid resolution focused on the southern tip of Manhattan near the Battery. Magenta line in figures at right without sub-grid represents the position of the shoreline.
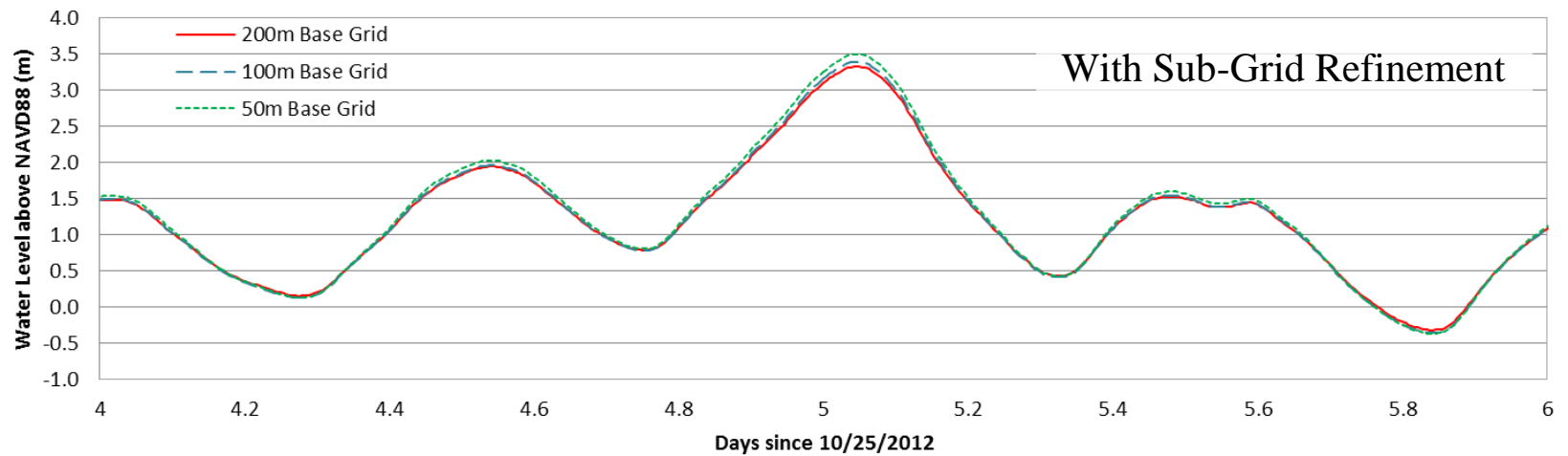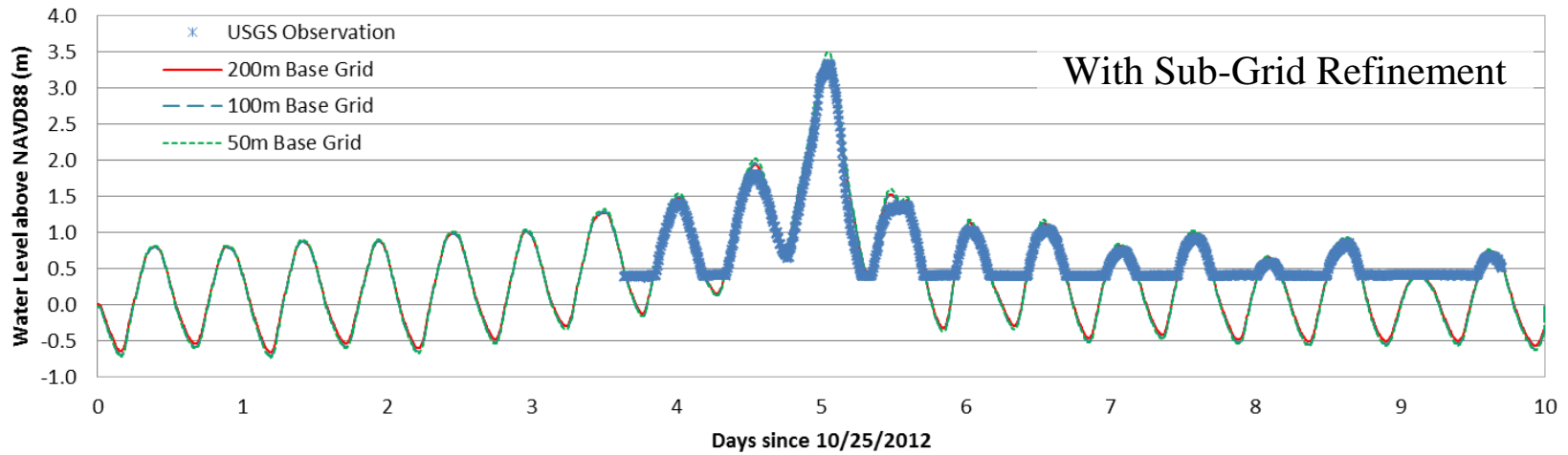
Figure 6.11. Water level recorded for base grids at 200m, 100m, and 50m resolutions with embedded sub-grid at SSS-NY-KIN-003WL. Top plot shows 10-day simulation of 2012 Hurricane Sandy with USGS overland observation gauge; bottom plot focuses on the peak.
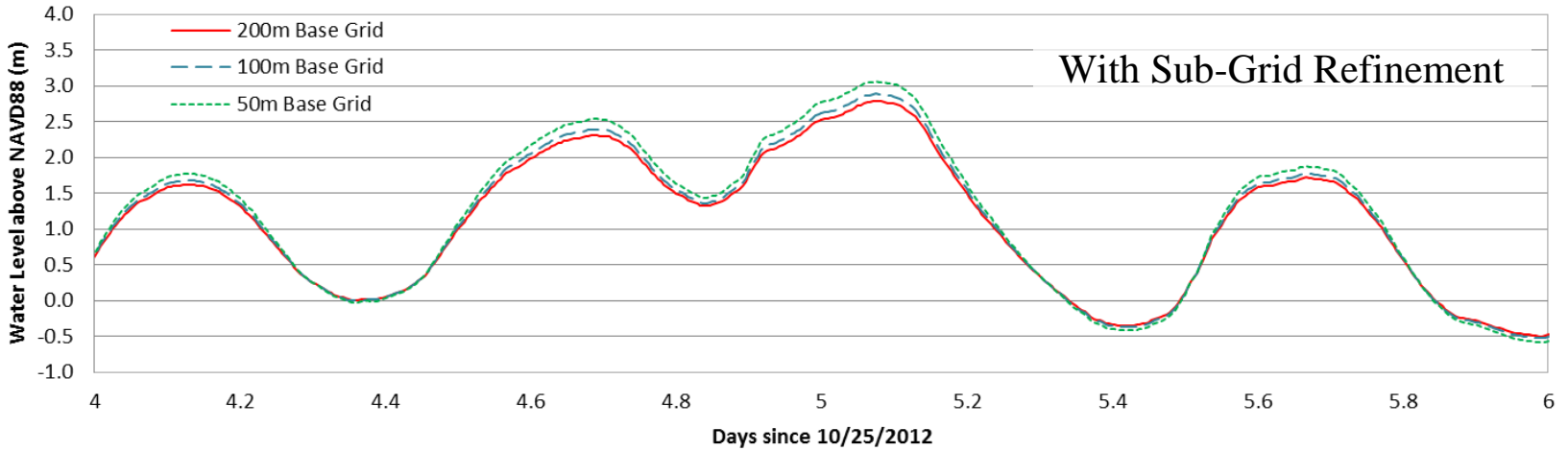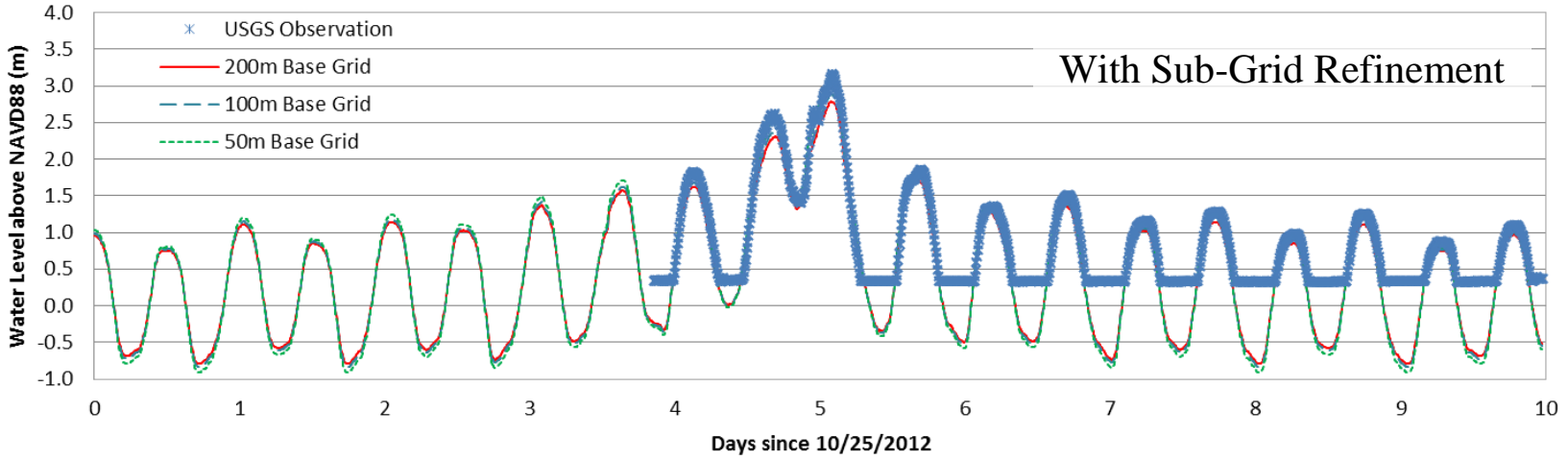
Figure 6.12. Water level recorded for base grids at 200m, 100m, and 50m resolutions with embedded sub-grid at SSS-NY-QUE-004WL. Top plot shows 10-day simulation of 2012 Hurricane Sandy with USGS overland observation gauge; bottom plot focuses on the peak.
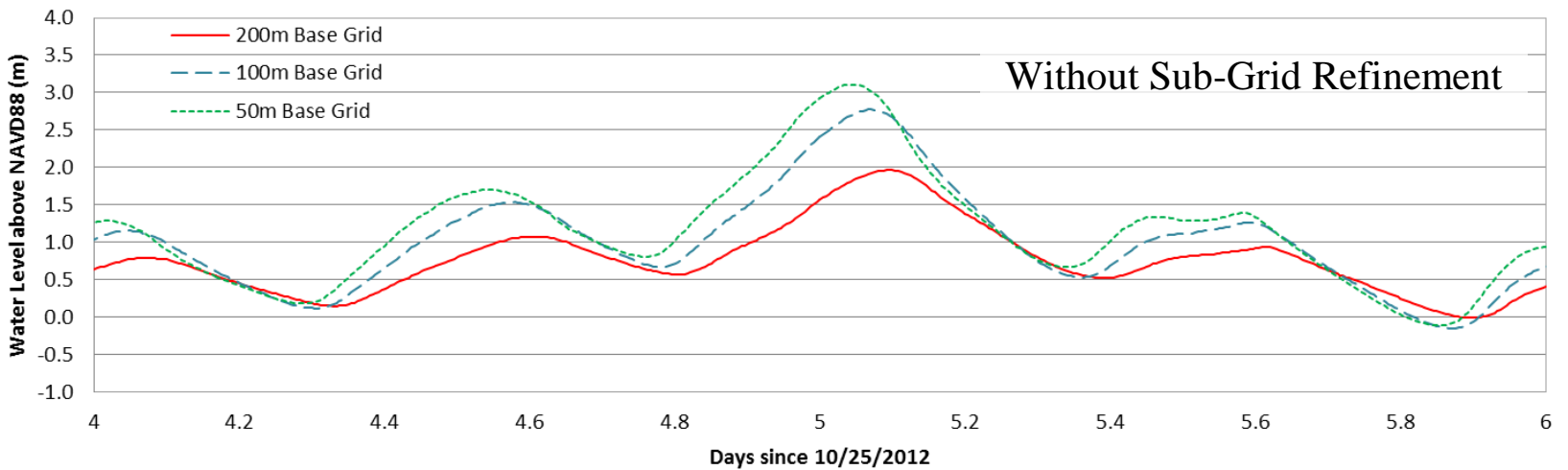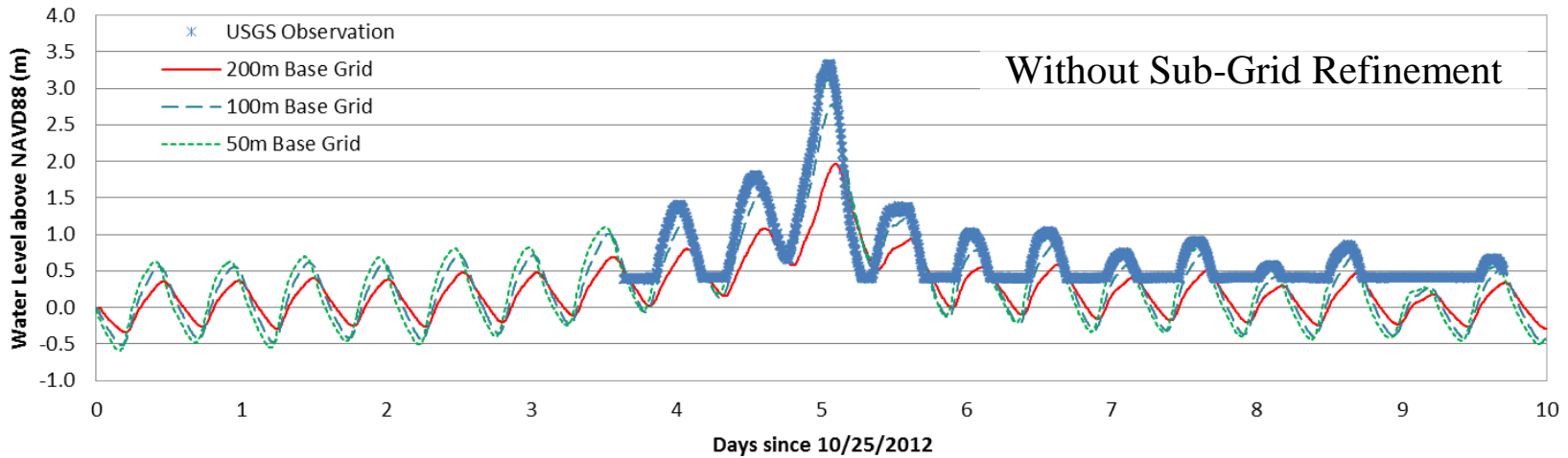
Figure 6.13. Water level recorded for base grids at 200m, 100m, and 50m resolutions without sub-grid at SSS-NY-KIN-003WL. Top plot shows 10-day simulation of 2012 Hurricane Sandy with USGS overland observation gauge; bottom plot focuses on the peak.
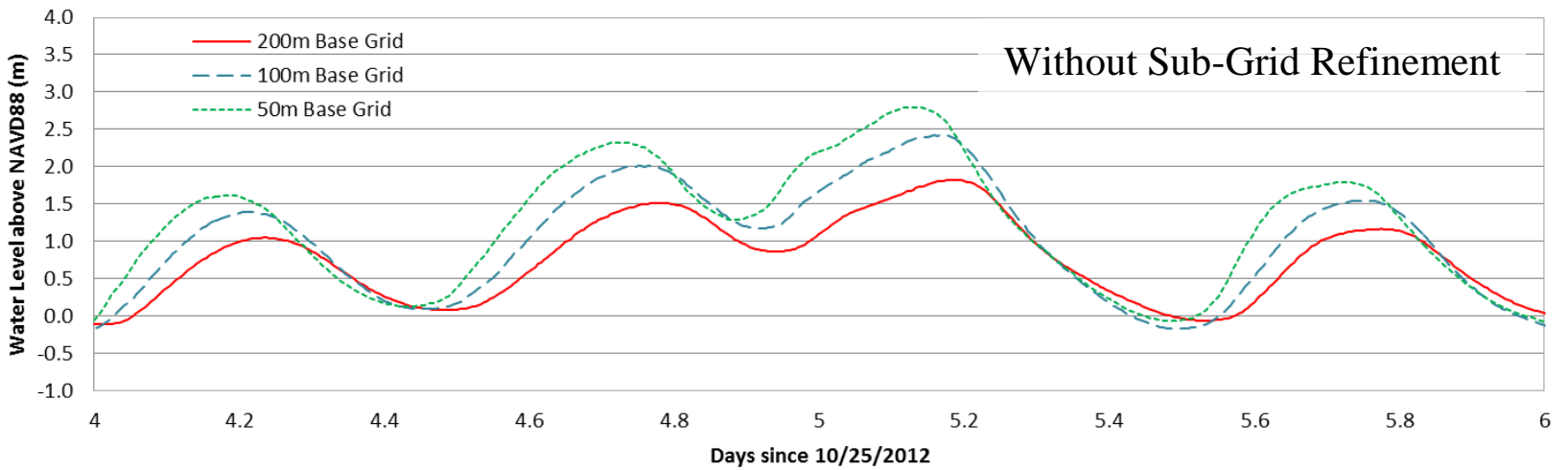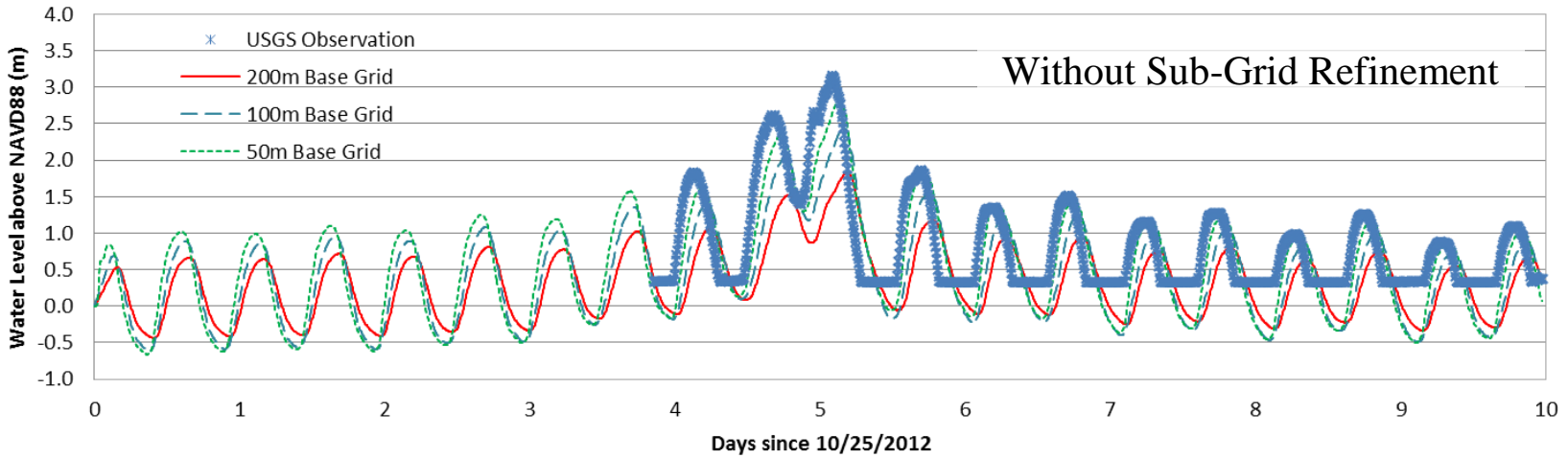
Figure 6.14. Water level recorded for base grids at 200m, 100m, and 50m resolutions without sub-grid at SSS-NY-QUE-004WL. Top plot shows 10-day simulation of 2012 Hurricane Sandy with USGS overland observation gauge; bottom plot focuses on the peak.

Table 6.8 Scaling of model grid size and computation time for each sub-grid simulation.

Grid Resolution (m)	# of Points	# of Sides	CPU Time (min)
50	175059	322523	3737.87
100	45755	87168	504.16
200	11959	23559	68.20

6.2.4   MTA Inundated Subway Entrances Map

The UnTRIM^2 model is utilized in this study to simulate storm surge and inundation caused by 2012 Hurricane Sandy. While a majority of reported flooding during a storm is due to the hurricane's storm surge, smaller portions of the observed inundation may be attributed to precipitation and diverted water to reservoirs or retention ponds by way of storm drains and runoff. Precipitation and percolation through the ground surface as additional model sources and sinks have been previously addressed in in sub-grid modeling efforts at VIMS for more rural settings (Loftis et al., 2013). These sources and sinks were not included in the modeling effort for Hurricane Sandy due to the minimal impact of rainfall relative to the substantial storm surge height in the Harbor, and the complex drainage infrastructure present in the City. Additionally, New York City is home to one of the most complex subterranean mass transit systems in the world. Many areas of the subway system throughout New York City were heavily impacted by the effect of the storm surge bottlenecking up the Hudson and East Rivers (Figure 6.15). Table 6.9 lists 38 known subway entrances flooded by Sandy's storm surge.
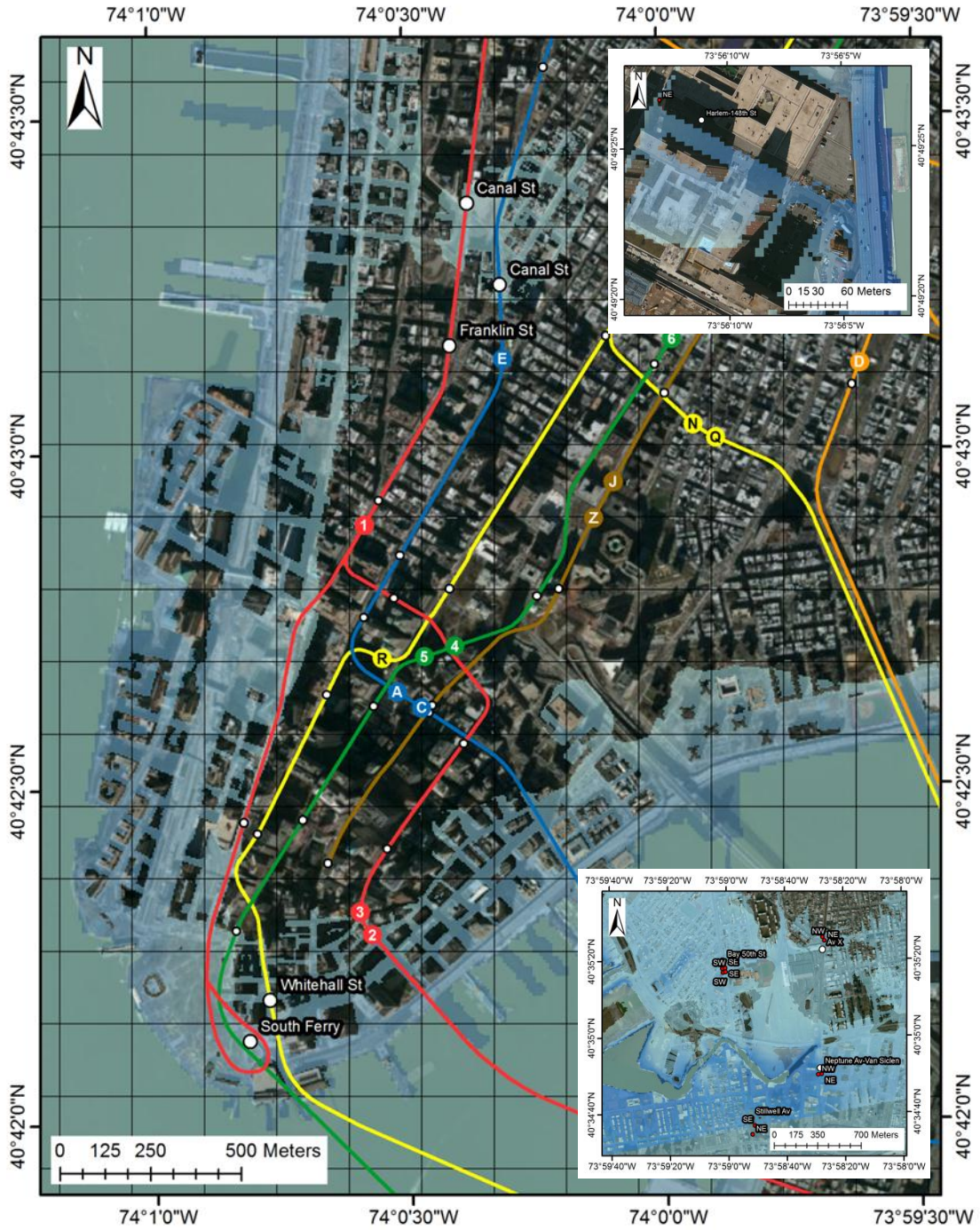
Figure 6.15. Map of subway station entrances impacted by Hurricane Sandy's storm surge along the southern tip of Manhattan, the Upper East Side (top inset), and along Coney Island Creek (bottom inset). Maximum storm surge extent predicted by the sub-grid model is highlighted in blue.

Table 6.9. List of subway station entrances impacted by Hurricane Sandy's storm surge arranged by location and cross street name.

#	Station Name	Latitude	Longitude	Corner	Street NS	Street WE	Subway Line	Division	Primary Route	Entrance Type
1	25th Ave	40.597889	-73.986958	NE	25th Ave	86th St	West End	BMT	D	Stair
2	25th Ave	40.598100	-73.987279	NW	25th Ave	86th St	West End	BMT	D	Stair
3	25th Ave	40.597751	-73.987112	SE	25th Ave	86th St	West End	BMT	D	Stair
4	25th Ave	40.597952	-73.987442	SW	25th Ave	86th St	West End	BMT	D	Stair
5	Ave X	40.590521	-73.974242	NW	McDonald Ave	Avenue X	Culver	IND	F	Stair
6	Ave X	40.590266	-73.974051	NE	McDonald Ave	Avenue X	Culver	IND	F	Stair
7	Bay 50th St	40.588022	-73.983735	SW	Stillwell Ave	Bay 50th St	West End	BMT	D	Stair
8	Bay 50th St	40.588066	-73.983498	SE	Stillwell Ave	Bay 50th St	West End	BMT	D	Stair
9	Bay 50th St	40.588305	-73.983791	SW	Stillwell Ave	Bay 50th St	West End	BMT	D	Stair
10	Bay 50th St	40.588348	-73.983543	SE	Stillwell Ave	Bay 50th St	West End	BMT	D	Stair
11	Canal St	40.720704	-74.004999	NE	Lispenard St	West Broadway	8 Avenue	IND	A	Stair
12	Canal St	40.720758	-74.005399	NW	6th Ave	West Broadway	8 Avenue	IND	A	Stair
13	Canal St	40.721651	-74.005634	SE	St. John La	Laight St	8 Avenue	IND	A	Stair
14	Canal St	40.721967	-74.005133	NE	Thompson St	Canal St	8 Avenue	IND	A	Stair
15	Canal St	40.719870	-74.005038	NE	6th Ave	Walker St	8 Avenue	IND	A	Stair
16	Canal St	40.722569	-74.006080	NE	Canal St	Varick St	Broadway-7th Ave	IRT	1	Stair
17	Canal St	40.722497	-74.005994	NE	Canal St	Varick St	Broadway-7th Ave	IRT	1	Stair
18	Canal St	40.722932	-74.006620	NW	Canal St	Varick St	Broadway-7th Ave	IRT	1	Stair
19	Canal St	40.722878	-74.006518	NW	Canal St	Varick St	Broadway-7th Ave	IRT	1	Stair
20	Franklin St	40.719001	-74.006675	SW	West Broadway	Franklin St	Broadway-7th Ave	IRT	1	Stair
21	Franklin St	40.719918	-74.006620	NE	Varick St	North Moore St	Broadway-7th Ave	IRT	1	Stair
22	Franklin St	40.718965	-74.007121	SW	Varick St	Franklin St	Broadway-7th Ave	IRT	1	Stair
23	Franklin St	40.719251	-74.007058	NW	Varick St	Franklin St	Broadway-7th Ave	IRT	1	Stair
24	Franklin St	40.719888	-74.006925	NW	Varick St	North Moore St	Broadway-7th Ave	IRT	1	Stair
25	Harlem-148th St	40.824069	-73.936981	NE	Adam C. Powell	149th St	Lenox	IRT	3	Door
26	Neptune Ave-Van Siclen	40.580576	-73.974443	NE	West 6th St	Neptune Ave	Culver	IND	F	Stair
27	Neptune Ave-Van Siclen	40.580547	-73.974778	NW	West 6th St	Neptune Ave	Culver	IND	F	Stair
28	Smith-9th St	40.674725	-73.997505	NE	Smith St	9th St	6 Avenue	IND	F	Door
29	South Ferry	40.702033	-74.013149	NE	State St	State St	Broadway-7th Ave	IRT	R	Elevator
30	South Ferry	40.701961	-74.013397	NW	State St	State St	Broadway-7th Ave	IRT	R	Escalator
31	South Ferry	40.701313	-74.013479	SW	State St	State St	Broadway-7th Ave	IRT	R	Stair
32	Stillwell Ave	40.576241	-73.981077	NE	Stillwell Ave	Surf Ave	Brighton	BMT	D	Stair
33	Stillwell Ave	40.576900	-73.980846	SE	Stillwell Ave	Mermaid Ave	Coney Island	BMT	D	Stair
34	Whitehall St	40.701938	-74.012588	SE	Whitehall St	Water St	Broadway	BMT	R	Stair
35	Whitehall St	40.702108	-74.012642	SE	Whitehall St	Pearl St	Broadway	BMT	R	Stair
36	Whitehall St	40.704015	-74.013284	SW	Whitehall St	Pearl St	Broadway	BMT	R	Stair
37	Whitehall St	40.704114	-74.013000	NE	Whitehall St	Pearl St	Broadway	BMT	R	Stair
38	Whitehall St	40.704096	-74.013293	NW	Whitehall St	Pearl St	Broadway	BMT	R	Stair

CHAPTER 7: Discussion and Conclusions

7.1   Overview of Research Performed

7.1.1   Discussion of Large-Scale Storm Tide Model Results

An unstructured model grid with a curvilinear open boundary was developed for the U.S. East Coast with detailed bathymetry in the Hudson and East Rivers, the Long Island Sound, Raritan Bay, and New York Bay, in the interest of modeling 2012 Hurricane Sandy. Different atmospheric model products were used to drive storm surge using the parallel MPI version of the SELFE model. SELFE is an unstructured-grid model, designed for the effective simulation of large-scale ocean circulation over river-to-ocean dimensional scales. The combination of a semi-implicit finite difference method with an Eulerian-Lagrangian advection scheme affords the model ensured stability and computational efficiency to process results over a large domain extent.

The SELFE model accurately predicts tidal propagation along the U.S. Eastern Seaboard and embayments within the model grid with good accuracy. SELFE tidal calibration results spanned 91 days and commenced on 09/01/2012 at 00:00 GMT through 11/30/2012 at 00:00 GMT. The tidal calibration resulted in an excellent overall statistical comparison upon application of the friction parameter adjustments noted in Chapter 3 in accordance with Blumberg et al. (1999). The aggregated statistics comparing the tidal calibration results to the predicted tide values across 10 NOAA tide gauges yielded an average R^2 of 0.9787, a relative error of 2.00%, and a root-mean-squared error of 9.72cm (Table 3.2).

Harmonic analysis decomposed the tidal signal into the relative tidal amplitude and tidal phase between modeled tide and NOAA observed tide for the 8 major harmonic constituents at each NOAA station along the U.S. East Coast. In the tidal amplitude comparison, the SELFE model simulates the amplitude of the dominant M_2 tidal constituent very well at all of the 10 stations with a mean difference of -0.012±0.058m (Table 3.2A). Nearly all of the 10 selected tide gauge stations showed a mean amplitude difference of less than 10% except for Bergen Point, NY (Figure 3.1C), where a 15.6% difference in M_2 tidal amplitude was observed (Table 3.2A). The principal solar diurnal constituent, S_2, had a mean difference of -0.005±0.020m between the modeled tide and NOAA observed tide (Table 3.2A). Differences in tidal phase for the principal lunar and solar semidiurnal constituents, M_2 and S_2, were 0.571±1.980° and -0.799±2.614°, respectively (Table 3.2B). Therefore, the SELFE grid developed for simulating 2012 Hurricane Sandy was deemed capable of modeling the characteristics of long-period wave propagation along the open coast and the New York Harbor, and thus was prepared to effectively simulate the complex dynamics involved with a hurricane storm surge.

Storm tide simulations were successfully conducted for 2012 Hurricane Sandy using the NARR and RAMS model results as atmospheric inputs. Overall statistics using the 24km resolution NARR inputs observed an average R^2 value of 0.8994, a relative error of 11.77%, and a root-mean-squared error of 32.69cm for 10 NOAA gauges (Table 3.3). The 4km RAMS inputs performed noticeably better than the SELFE model simulations driven with the NARR atmospheric inputs at all 10 stations with aggregate statistics yielding an average R^2 value of 0.9402, a relative error of 4.08%, and a root-mean-squared error of 19.22 cm (Table 3.4). Since the RAMS atmospheric inputs

possessed a higher spatial and temporal resolution than the NARR inputs for air pressure and wind speed, it was concluded that generally superior storm tide predictions could be expected from utilizing more reliable or better resolution atmospheric forecast products.

7.1.2 Discussion of Street-Level Sub-Grid Inundation Model Results

Sensitivity tests were conducted to demonstrate the predictive capabilities of the sub-grid model and to determine what difference could be observed in water level predictions resulting from the approximations utilized in the sub-grid conveyance approach described in Chapter 4. As the base grid resolution increased from 200m to 100m to 50m, an insignificant (<5%) increase in amplitude and a slight promptitude in phase was observed in water levels with sub-grid refinement (Figure 6.11 and Figure 6.12). Identical base grids without sub-grid refinement proved to be significantly more sensitive to grid resolution (Figure 6.13 and Figure 6.14). This was largely a result of the grid elevations being averaged over a greater area with lower resolutions, which promoted tidal decay as the fluid propagated from the grid boundaries to remote shallow reaches of the New York Harbor. Sensitivity tests concluded that, without sub-grid specifications, accurate bathymetric and topographic fitting could only be effectively achieved by using extremely fine scale model grids or through the use of heavily distorted unstructured grids.

Street-level sub-grid model performance was assessed via comparison with the following verified field measurements: (1) Temporal comparison of NOAA and USGS permanent water level gauges, and (2) USGS rapid deployment water level gauges, along with a spatial inundation comparison using (3) USGS-collected high water marks, (4)

FEMA-collected data regarding inundated schools, (5) calculated area and distance differentials using FEMA's maximum extent of inundation map, and (6) known locations of inundated MTA subway entrances.

Temporal verification of the sub-grid model results utilized time series observation data compiled during 2012 Hurricane Sandy. Five tidal records assembled from one USGS and four NOAA permanent tide gauges were utilized as a standard for temporal comparison (Table 6.1A). Model outputs near the boundary confirmed that the set of water elevation data is a near perfect match (>99% match) for each of these stations, verifying correct forcing at the boundaries, while the one permanent installation not adjacent to any model boundary near the Battery, NY, reported a favorable match of the storm surge height (Figure 6.1A), with an R^2 of 0.9932, a relative error of 0.47%, and a root-mean-squared error of 7.15cm (Table 6.1A). Storm tide measurements verified the effectiveness of the sub-grid model's wetting and drying scheme via seven overland rapid deployment gauges installed and collected by the USGS with a mean R^2 of 0.9568, a relative error of 3.83%, and a root-mean-squared error of 18.15cm (Table 6.1B).

Spatial verification of the inundation depths predicted by the UnTRIM^2 model were addressed by comparison with 73 high water mark measurements collected by the USGS and by 80 FEMA-reported water level thicknesses at inundated schools throughout the sub-grid domain separated by state. Average statistics for the 73 USGS-recorded high water marks for New York and New Jersey were: -0.0004m and 0.2150m for $\bar{\varepsilon}$, 0.112m and 0.364m for $|\bar{\varepsilon}|$, 0.085m and 0.256m for σ, and 0.120m and 0.347m for root-mean-squared error, respectively (Table 6.3C). Statistical metrics for the 80 FEMA-reported inundated schools for New York and New Jersey were: 0.0332m and 0.3483m for $\bar{\varepsilon}$,

0.2769m and 0.4227m for |ɛ̄|, 0.3304m and 0.3328m for σ, and 0.3293m and 0.4760m for root-mean-squared error, respectively (Table 6.4C). The larger differences and errors reported in the point-to-point comparisons for New Jersey relative to New York were largely due to the lack of building representation in the sub-grid DEM for the New Jersey side of the Hudson River, and were a significant indication that the representation of buildings as a physical impediment to fluid flow is critical to urban inundation modeling.

In addition to the previous sensitivity tests, the time series comparisons, and point-to-point spatial verifications of the sub-grid model's accuracy; maximum flooding extent is an especially critical attribute to address in assessing flooding risk. The relative precision of the maximum horizontal extent of inundation is dependent upon the accuracy of the flux estimate and the propagation speed of the long wave in association with localized variations in water level. Maximum spatial extent of inundation was assessed using FEMA's spatial flood coverage map assembled via interpolation of the USGS's field-verified high water mark data, water level heights reported from rapid deployment gauges, and the best available digital elevation data. These data were collected to calculate distances between the model's predicted maximum flood extent and FEMA's reported flood maximums (Table 6.5), wherein the sub-grid model had an absolute mean distance difference of nearly 40m (38.430m) or eight 5m-resolution sub-grid pixels.

A second distance comparison calculated differences relative to the shoreline for the FEMA flood coverage map (Figure 6.6), and the sub-grid model results and shoreline to sub-grid model prediction (Figure 6.7), along roadways perpendicular to the water's edge. This alternate assessment of distance revealed a mean distance difference of 27.67m, trending toward model under-prediction along 26 sampled roadways throughout

the sub-grid domain (Table 6.6). Figures 5.11 and 5.12 indicate that the greatest

inundation (>1km from the shoreline) within the sub-grid domain coverage area was

observed along the New Jersey Bank of the Hudson River, where elevation is

geologically lower than the New York bank. The final spatial verification calculated a

difference map using the key in Table 5.3 for a complete area comparison, which resulted

in a 75.15% spatial match with 11.41% area model over-prediction and 13.44% model

under-prediction (Figure 6.8 and Table 6.7).

7.1.2.1 Discrepancies between Model Results and Spatial Observation Data

A considerable number of the differences or errors calculated in the spatial

comparisons was attributed to large, but consolidated, areas of over-prediction or under-

prediction resulting from misrepresentation of roadway overpass infrastructure due to the

primary method for topographic data collection being final-return Lidar measurements

(Figure 6.9). Also, DEM differences between the model sub-grid and the one used to

build the FEMA flood map account for other discrepancies noted in the spatial

comparison and are subsequently addressed utilizing an augmented spatial comparison

methodology introduced with updated spatial results and statistics in the next section.

Discrepancies between the model predictions and the FEMA flood map are

attributed to DEM differences, and possibly the lack of building representation in the

FEMA maximum inundation map (Figure 6.9). Additionally, the implementation of the

spatial flooding observation data as a derivative "bathtub model" product of interpolated

USGS high water mark measurements and elevation data without regard for strong water

current velocities or estuarine circulation could account for regions with significant

discrepancies. Such discrepancies can be addressed in both the area and distance spatial comparisons to minimize the impact of DEM incongruities that are outside of control for the model to address.

To provide a representative comparison, in the original distance comparison shown in Figure 6.5A-D, there were 36 total peaks representing differences greater than 100m for the horizontal absolute mean distance evaluation. Throughout the 4 assessment regions covered in the distance comparison, there were 17 locations adjacent to the East River, comprised of 4 of these in Brooklyn, 7 in Queens, 5 in the Bronx, and 1 in Manhattan (Figure 6.5A). There were only 2 places along the Harlem River with distance dissimilarities of greater than 100m between the sub-grid model and the FEMA maximum extent flood map (Figure 6.5B); both of which were located near Randall's Island where the Harlem River joins the East River near the rapid deployment gauge, USGS 404810735538063, shown in Figure 4.1.

There were 8 such discrepancies in the Hudson River along the New York banks of the river, with 3 locations along the west bank bordering Staten Island, with the east banks accounting for 2 locations in Brooklyn, and 3 places in Manhattan (Figure 6.5C). Finally, there were 9 locations along the New Jersey banks of the Hudson River (Figure 6.5D), with one notably large discrepancy covering more than 7500m of differences greater than 100m between the FEMA maximum flooding extent map and the flooding extent predicted by the sub-grid model shown in Figure 6.9A.

Two examples of these discrepancies are shown in Figure 6.9A-B. Along the New Jersey bank of the Hudson River (Figure 6.9A), two overpasses for I-78 are accounted for

in the model's Lidar-derived DEM, but do not allow for flow of water through the underpass. Thus, the model under-predicts flooding along Thomas McGovern Drive by 338.35m (Table 6.6), and this discrepancy adversely affected the distance and area comparisons (Table 6.5 and Table 6.7). Similar roadway infrastructure issues with the DEM cause inundation along Kent Avenue in Figure 6.9B to be blocked by an overpass for I-278. This caused the model to under-predict flooding east of the overpass by 169.4m, and over-predict flooding west of the overpass. Thus, also affecting distance and area measurements as these infrastructures artificially obstructed fluid movement (Table 6.5 and Table 6.7).

7.1.2.2 Revised Spatial Comparison via Augmented 40m Average Inundation

If we account for the average distance differential of 38.43m between the FEMA-reported maximum flooding extents and the model predicted maximum inundation extents, the impact of physical impediments for fluid flow not accounted for in the model's DEM may be minimized. A new methodology may be employed to impose a maximum difference threshold using the average distance differential rounded to 40m. This adjustment of over-predicted and under-predicted flood areas limits the impact of missing or added infrastructure along with Lidar-derived data limitations like those underscored in Figures 6.5A-D and Figure 6.9.

The brief methodology for the recalculation of distances and areas to account for DEM discrepancies utilizing a 40m area difference threshold includes:

1.   Buffering the FEMA maximum inundation extent polyline using the approximate
      average distance difference of 40m.

2.   Merging the polyline buffer with a copy of the original FEMA maximum
      inundation extent to produce a new combined maximum inundation extent with
      40m tolerance.

3.   Extracting/clipping the UnTRIM^2 model inundation extents using the new
      combined maximum inundation extent with 40m tolerance. Steps 1-3 cover
      matching areas which the model under-predicts the spatial observation data.

4.   Repeating steps 1-3 for the UnTRIM^2 model inundation extent layer with respect
      to the FEMA maximum inundation extent layer will also include areas with over-
      prediction using the new 40m threshold adjustment.

5.   Recalculating the geometry in the GIS attribute table to create a new table of areas
      accounting for the 40m maximum discrepancy tolerance.

6.   The data were exported to a spreadsheet to compute updated statistics for distance
      (Table 7.1) and area (Table 7.2).

      Implementation of a 40m distance threshold augmented the overall distance

comparison by an average difference of 17.2m meters for an updated absolute mean

distance of 21.207m. This reduced the absolute mean distances for each of the river

systems to 16.484m for the Hudson River on the New York bank, and 24.079m on the New Jersey side, 18.616m along the Harlem River, and a 19.907m difference between the FEMA observation data and model prediction along the East River. The 40m threshold had a limited effect on the New Jersey coast, making it the new least accurate distance comparison within the sub-grid domain (Table 7.1).

The updated spatial area comparison resulted in an improved 85.17% area (49,253,687m^2) match, indicating agreement between the sub-grid model prediction and the FEMA maximum inundation observation. Over-prediction error is adjusted to 7.57% area (4,376,726m^2), with under-prediction area accounting for 7.27% (4,202,376m^2) of the area attributed to error. This favorable improvement of the model prediction effectively limits the statistical impact of substantial DEM discrepancies on the impact of the model's results as Figure 6.9 illustrates, explaining the two largest distance differences in Table 6.6.

Prior to the 40m distance threshold, these errors along Thomas McGovern Drive in Figure 6.9A, and Kent Avenue in Figure 6.9B are observed as the tallest peaks in the distance plots shown in Figure 6.5D and Figure 6.5A, respectively. These errors also affected data shown in Figure 6.8 and Table 6.7, and are effectively rectified using the 40m adjustment in Tables 7.1 and 7.2.

Table 7.1. Revised distance difference table upon applying a 40m maximum inundation distance threshold with differences to absolute mean distance and standard deviation from previous results noted in italics. All units are in meters.

Survey Region	# of Points	Abs. Mean Dist.	(Diff.)	Std. Deviation	(Diff.)
New York					
East River NY	47,283	19.907	*26.9*	12.984	*45.3*
Harlem River NY	9,673	18.616	*25.6*	12.564	*44.1*
Hudson River NY	21,492	16.484	*12.4*	9.840	*17.2*
All New York	78,448	18.336	*21.6*	11.796	*35.5*
New Jersey					
Hudson River NJ	16,396	24.079	*12.8*	13.048	*17.3*
All New Jersey	16,396	24.079	*12.8*	13.048	*17.3*
All Hudson River	37,888	20.281	*12.6*	11.444	*17.3*
Total Across Domain	94,844	21.207	*17.2*	12.422	*26.4*

Table 7.2. Revised results of the statistical comparison for inundated areas in the New York Harbor region upon applying a 40m maximum inundation distance threshold. Values are presented as surface areas (m^2) and (% area coverage) for each of the defined categories: match, model under-predict, and model over-predict compared with the FEMA maximum inundation coverage map.

Survey Region	Match	(%)	Under-Predict	(%)	Over-Predict	(%)	Total
New York							
East River NY	14,180,524	*83.55*	1,245,757	*7.34*	1,545,862	*9.11*	16,972,143
Harlem River NY	4,457,765	*83.14*	383,500	*7.15*	520,177	*9.70*	5,361,442
Hudson River NY	13,076,031	*88.04*	1,073,436	*7.23*	703,736	*4.74*	14,853,203
All New York	31,714,320	*85.28*	2,702,693	*7.27*	2,769,775	*7.45*	37,186,788
New Jersey							
Hudson River NJ	17,539,367	*84.95*	1,499,683	*7.26*	1,606,951	*7.78*	20,646,001
All New Jersey	17,539,367	*84.95*	1,499,683	*7.26*	1,606,951	*7.78*	20,646,001
All Hudson River	30,615,398	*86.24*	2,573,119	*7.25*	2,310,687	*6.51*	35,499,204
Total Across Domain	49,253,687	*85.17*	4,202,376	*7.27*	4,376,726	*7.57*	57,832,789

7.2   Conclusions

In review, the specific research hypotheses proposed in Chapter 1 were effectively verified in this study. Formulations for the two-dimensional long-wave equation (with hydrostatic assumption) for both the SELFE and UnTRIM[2] models were exceptionally capable of accurately calculating the complex hydrodynamics indicative of the unsteady ocean conditions observed during a tropical storm event like 2012 Hurricane Sandy (Wang et al., 2014).

As anticipated, the inclusion of Lidar-derived topography into the UnTRIM[2] model's sub-grid via GIS significantly increased the effective resolution of the model grid, and was quite capable of effectively resolving buildings in New York City along with narrow creeks and streams classified as 2nd order and above according to Strahler's definition of rivers and mathematical tree structures. Additionally, the inclusion of Lidar-derived topographic measurements was also previously verified in a more rural setting to effectively resolve the dendritic small creeks of the Back River estuary at NASA Langley Research Center in Hampton, VA (Loftis et al., 2013).

An additional implication of this hypothesis was addressed as vector building data were included in the DEM development process to best represent the flooding around buildings observed in the New York City ultra-urban metropolis. The lack of freely available building data for the New Jersey regions of the New York Harbor demonstrated that accurate representation of buildings should be resolved within the model grid for superior spatial flooding projections, as the New Jersey side of the Hudson River observed more pronounced deviations from the FEMA flood map derived from the

USGS-surveyed high water marks used to spatially validate the model (Wang et al., 2014).

The partial wetting and drying scheme utilized in the sub-grid model's inundation algorithm was successfully verified as both accurate and robust during sensitivity tests and throughout the spatial comparison results for the maximum extent of flooding.

Sensitivity tests revealed that there was minimal degradation in model results calculated with the benefit of sub-grid refinement as the base grid resolution increased from 200m to 100m to 50m, while the same model base grids without sub-grid refinement proved to be significantly more sensitive to grid resolution due to the grid elevations being averaged over a greater area with lower resolutions, inciting tidal decay. It was also revealed in a previous modeling effort that sub-grid modeling can replicate the results of a likewise-resolution true grid model in the Capital Mall area of Washington, DC, indicating that there is minimal loss of quantitative accuracy in the sub-grid approach and that it can appropriately match inundation observations (Loftis and Wang, 2012).

To summarize, the primary objectives successfully addressed in this dissertation were:

1. The capabilities of a large-scale storm tide model and a high-resolution sub-grid inundation model were effectively demonstrated in the New York City area during Hurricane Sandy in 2012.

2. With reasonably accurate atmospheric model forcing, it was shown that the U.S. East Coast storm tide model, SELFE, produced accurate water level predictions

upon comparison with NOAA-verified observations with moderate computing resources (using a semi-implicit Eulerian-Lagrangian scheme).

3. This study utilized sub-grid model with a nonlinear solver in a novel approach to high-resolution inundation modeling by incorporating Lidar-derived topographic measurements and buildings directly into the sub-grid. This improved model accuracy to the street-level scale without the high computational costs of simulation on a fully-fledged high-resolution grid.

4. The sub-grid model produced reasonably accurate results upon comparison with field-verified observations collected from various U.S. government agencies including the USGS, NOAA, and FEMA.

5. A multi-faceted verification approach was utilized for spatial comparison with FEMA's maximum inundation extents using GIS tools to calculate distance differentials and flood areas, yielding 21 - 38m mean difference in distance, and 75 - 85% spatial agreement with the sub-grid model results.

6. Sensitivity tests revealed that there was minimal degradation in model results calculated with the benefit of sub-grid refinement as the base grid resolution increased from 200m to 100m to 50m, while the same model base grids without sub-grid refinement proved to be significantly more sensitive to base grid resolution.

7. Finally, there are potential forecast applications for large-scale SELFE model domains to be jointly developed and applied to model storm tide scenarios, in the

interest of generating an operational forecast modeling system with predictive capabilities for street-level inundation. This could be accomplished by exporting water level elevation results from SELFE simulations using forecast results automatically retrieved from atmospheric forecast data repositories. These water level elevations could be automated via script handling to autocombine and format the SELFE binary model results saved at key locations to be utilized as elevation boundary conditions to force the high-resolution street-level sub-grid model to produce spatial coverage maps shown in this dissertation, in less than 2 hours after 30-hour atmospheric forecast data are updated and retrieved.

APPENDICES

Appendix A. Definition of Statistical Formulas for Error Analysis

The following statistical equations have been calculated to evaluate the accuracy of the sub-grid model for both tidal calibrations and storm surge simulations in this study.

Below, x represents the water level time series data, $\bar{x}$ is x's mean time, while subscripts "*mod*" represents the model results and "*obs*" are the observations.

1. The root-mean-square error (RMSE) is defined as:

$$RMSE = \left\{ \frac{1}{N} \sum_{i=1}^{N} (x_{mod} - x_{obs})^2 \right\}^{1/2}$$

2. The mean relative error (RE) is defined as:

$$RE = 100\% \frac{\sum_{i=1}^{N} (\eta_{mod} - \eta_{obs})^2}{\sum_{i=1}^{N} ((\eta_{mod} - \bar{\eta}_{obs})^2 + (\eta_{obs} - \bar{\eta}_{obs})^2)}$$

3. The mean absolute relative error (ARE) is defined as:

$$ARE = \frac{1}{N} \sum_{i=1}^{N} \left(\left| \frac{x_{mod} - x_{obs}}{x_{mod}} \right| \right) * 100(\%)$$

4. The correlation coefficient (r) is defined as:

$$r = \frac{\sum_{i=1}^{N} (x_{mod} - \bar{x}_{mod})(x_{obs} - \bar{x}_{obs})}{[\sum_{i=1}^{N} (x_{mod} - \bar{x}_{mod})^2 \sum_{i=1}^{N} (x_{obs} - \bar{x}_{obs})^2]^{1/2}}$$

Appendix B. Dynamic Similarity to Relate Lab Flume Results to Model

Use of the formulation of the friction factor, f' in equation (4-16), given in Chapter 4, requires some understanding of the influence drag coefficient, C_D, and building density, M. It is also unknown if the friction factor depends upon unspecified flow conditions such as Reynolds number. Without experimentation, it is difficult to know the impact of these parameters in the grand scheme of ascertaining over land friction in inundation scenarios. Therefore, this dissertation utilizes a laboratory flume experiment which analytically verified the impact of form drag and skin friction on shallow water overland inundation (Wang, 1983). In order to make proper use of the suggested bottom friction values proposed in the experiment, dimensional analysis must be conducted in order to guarantee correspondence between the model and prototype. Similarity between the model and prototype dictates that the system should be geometrically, kinematically, and dynamically congruent. Geometric similarity suggests that the ratios of relative lengths and widths be the same. Kinematic similarity implies that kinematic quantities in the model are similar to the prototype. Dynamic similarity dictates that the two systems with geometrically similar boundaries contain the same ratios of all forces acting on the fluid mass.

Based upon Newton's basic dynamic law, which states that force is equal to the rate of momentum, dynamic similarity is achieved when the ratio of inertial forces in the model and the prototype are equal to the vector sum of the forces acting on the two systems. These forces include, but are not limited to: gravitational forces, viscous forces, elastic forces, surface tension forces and phenomena related to fluid-motion. The ratios of these forces must be the same as indicated in Equation (A-1) below:

185

$$\frac{(F_{inertial})_{flume}}{(F_{inertial})_{model}} = \frac{(F_{gravitational})_{flume}}{(F_{gravitational})_{model}} = \frac{(F_{viscous})_{flume}}{(F_{viscous})_{model}} = \frac{(F_{elastic})_{flume}}{(F_{elastic})_{model}} = \frac{(F_{surface\ tension})_{flume}}{(F_{surface\ tension})_{model}} \qquad \text{(A-1)}$$

It is typically impossible to achieve exact dynamic similitude when scaling a laboratory experiment to reality, and thus it is essential to examine the modeled flow dynamics to ascertain which forces are inconsequential to the hydrodynamics of interest. The purpose of reducing the fluid flow to a couple of dominant forces makes the system easier to characterize, and helps to define the most important criteria for dynamic similarity between the model and the prototype. In the case of a model researching the impacts of hurricane storm surge on coastal inundation, elasticity and surface tension are virtually non-present when compared to the other forces acting on the system. Conditions for dynamic similarity are simplified by equating the ratio of the inertial forces to the ratio of gravitational or viscous forces.

In the case of models measuring form drag in turbulent flow with high Reynolds numbers (i.e. inertial forces/viscous forces), viscous forces are of small consequence to the major forces driving the system due to turbulent fluctuations. Thus, viscous forces may be safely neglected in this scenario. The vertical dimension scale and horizontal dimension scale cannot be equal in the case of the prototype and the model ratios, since the flow depth would be insufficient for accurate measurements to be made. Additionally, the viscous forces would become critical to include in such small depths, and could no longer be neglected in shallow flow depths if the same fluid is used for the prototype and model. thus, a model with a different vertical dimension scale than horizontal dimension scale is used to keep the Reynolds numbers in the turbulent flow range. To simplify the problem of similarity, distorted models are often utilized for applications, since

undistorted models may simply be classified as a special case of distorted models. The model scale ratio is defined for the case of dynamic similarity in terms of horizontal length (Equation A-2), vertical depth (Equation A-3), time (Equation A-4), and force (Equation A-5):

$$N_{length} = \frac{L_{flume}}{L_{model}} = \frac{B_{flume}}{B_{model}} \tag{A-2}$$

$$N_{depth} = \frac{D_{flume}}{D_{model}} \tag{A-3}$$

$$N_{time} = \frac{T_{flume}}{T_{model}} \tag{A-4}$$

$$N_{force} = \frac{F_{flume}}{F_{model}} \tag{A-5}$$

where L is the horizontal length, the horizontal width is B, vertical depth is D, time is T, and all forces are labeled as F, with a subscript pertaining to their respective forcing. The force scale for gravity in the horizontal direction of the main flow is described via (Equation A-6):

$$
\begin{aligned}
K_{gravitational} &= \frac{\rho_{flume}\,g_{flume}}{\rho_{model}\,g_{model}} \frac{L_{flume}\,B_{flume}\,D_{flume}}{L_{model}B_{model}\,D_{model}} \frac{(D_{flume}/L_{flume})}{(D_{model}/L_{model})} \\
&= \left(\frac{\rho_{flume}}{\rho_{model}}\right)\left(\frac{g_{flume}}{g_{model}}\right) N_{length}\, N_{depth}{}^2
\end{aligned}
\tag{A-6}
$$

where $K_{gravitational}$ is the gravity force scale, fluid density is ρ, gravitational acceleration is g, and bottom slope is D/L. in a the case of a unidirectional flow, the inertial force may

187

be expressed as a horizontal or virtually horizontal area which may be multiplied by

Reynolds shear stress. Reynolds shear stress is proportional to the fluid density and the

time-averaged value of the product of fluctuation in vertical velocity and the

corresponding velocity fluctuation in the direction of the time-averaged flow resulting in

an inertial force characterized by (Equation A-7):

$$F_{inertial} = \rho \,\overline{u'v'} \times L\,B \tag{A-7}$$

with a scale for the inertial force ($K_{inertial}$) of (Equation A-8):

$$K_{inertial} = \frac{\rho_{flume}\,\left(L_{flume}/T_{flume}\right)\left(D_{flume}/T_{flume}\right)}{\rho_{model}\,\left(L_{flume}/T_{flume}\right)\left(D_{flume}/T_{flume}\right)}\,\frac{\left(L_{flume}\,B_{flume}\right)}{\left(L_{model}B_{model}\right)}$$

$$= \left(\frac{\rho_{flume}}{\rho_{model}}\right)\frac{{N_{length}}^3\,N_{depth}}{{N_{time}}^2} \tag{A-8}$$

where L x B is length x width to yield calculations for area. To maintain dynamic

similarity between the model and prototype, $K_{gravitational}$ should be equivalent to $K_{inertial}$ in

equation (A-6), conditionally represented in the following equation (Equation A-9):

$$N_{depth}\left(\frac{g_{flume}}{g_{model}}\right) = \frac{{N_{length}}^2}{{N_{time}}^2} \quad or \quad N_{time} = \frac{N_{length}}{\sqrt{N_{depth}}} \tag{A-9}$$

where g_{flume} is presumed to be equal to g_{model}. Froude number is commonly utilized to

describe the ratio between gravitational and inertial forces in a system. The time scale

given in equation (A-9) is the similarity requirement for the Froude law in the scenario of

distorted models. The scale ratios of the drag coefficient and friction factor in distorted

Froude models must be determined prior to proper interpretation of experimental results.

The drag force utilized in the flume experiment is characterized by (Equation A-10):

$$F_{drag} = \tau_{drag} \times L\,B = m\,C_D\,dD\,\rho\,{U^2}/{2} \times L\,B \tag{A-10}$$

with a drag force scale in the direction of flow described by (Equation A-11):

$$K_{drag} = \frac{C_{D\,flume}}{C_{D\,model}}\left(\frac{\rho_{flume}}{\rho_{model}}\right) N_{length}{}^3\,N_{depth}\left(\frac{1}{N_{time}}\right)^2 \tag{A-11}$$

(Wang, 1983). K_{drag} is required to be equal to $K_{gravitational}$ to satisfy the ratio of the force scale in the Froude model law. Substitution of Equation (A-9) into Equation (A-11) demonstrates the equality between C_D for the flume and the model (Equation A-12):

$$C_{D\,flume} = C_{D\,model} \tag{A-12}$$

The Darcy Weisbach expression of shear forces is described by Equation (A-13):

$$F_{shear} = f\,\rho\,\frac{U^2}{2}\,L\,B \tag{A-13}$$

where f is the general friction factor, and may be substituted for $f'e$, the equivalent friction factor, or f', the bottom friction factor. The shear force scale is (A-14):

$$K_{shear} = \frac{f_{flume}}{f_{model}}\left(\frac{\rho_{flume}}{\rho_{model}}\right) N_{length}{}^4\left(\frac{1}{N_{time}}\right)^2 \tag{A-14}$$

and K_{shear} must be equal to $K_{gravitational}$ to maintain dynamic similarity. If the time scale is

substituted from (A-9) into the necessitated inequality described in Equation (A-15):

$$\left(\frac{f_{flume}}{f_{model}}\right)\left(\frac{\rho_{flume}}{\rho_{model}}\right) N_{length}{}^4 \left(\frac{1}{N_{time}}\right)^2 = \left(\frac{\rho_{flume}}{\rho_{model}}\right)\left(\frac{g_{flume}}{g_{model}}\right) N_{length}\, N_{depth}{}^2 \quad \text{(A-15)}$$

The scale ratio expression for friction factor is:

$$\frac{f_{flume}}{f_{model}} = \frac{N_{depth}}{N_{length}} \quad \text{(A-16)}$$

A cursory comparison of equation (A-12) and (A-16) demonstrates that the drag

coefficient is identical in the model and the prototype. However, the friction factor of the

flume experiment should be modified by an inverse distortion ratio, N_{depth}/N_{length} (instead

of the typical N_{length}/N_{depth}) in the case of a Froude-distorted model (Wang, 1983). As

indicated in Table 4.1, the values for both N_{depth} (N_d) and N_{length} (N_l) are given, and this

distortion ratio is applied to the final values given for C_{Db}, bottom friction, and

Manning's *n* given in Table 4.3.

LITERATURE CITED

Aldrighetti, E. and P. Zanolli. (2005). A high-resolution scheme for flows in open channels with arbitrary cross-section. *Int. J. Numer. Meth. Fluids*.47: 817-824.

AP (Associated Press). (2012). Hurricane Sandy: Large Sections of Manhattan Left Without Power. October 29, 2012. http://www.oregonlive.com/today/index.ssf/ 2012/10/hurricane_sandy_large_sections.html.

Arumala, J. (2012). Impact of Large-Scale Disasters on the Built Environment. *Leadership Manage. Eng.*, 12(3), 147-150.

Bernier, N. B., and K. R. Thompson. (2006). Predicting the frequency of storm surges and extreme sea levels in the northwest Atlantic. *J. Geophys. Res*., 111, C10009.

Blain, C. A., J. J. Westerink, and R. A. Luettich. (1994). The influence of domain size on the response characteristics of a hurricane storm surge model. *Journal of Geophysical Research*, 99, 18467-18479.

Blake, E. S., T. B. Kimberlain, R. J. Berg, J. P. Cangialosi, and J. L. Beven II. (2013). Hurricane Sandy: Tropical Cyclone Report. National Hurricane Center Report, on February 12, 2013. http://www.nhc.noaa.gov/data/tcr/ AL182012_Sandy.pdf.

Blumberg, A., L. A. Khan, and J. P. St. John. (1999). Three-dimensional hydrodynamic model of New York Harbor region. *Journal of Hydraulic Engineering*, 125(8): 799-816.

Blumberg, A.F., and G. L. Mellor. (1987). A description of a three dimensional coastal ocean circulation model. In N. Heaps (ed.), Three Dimensional Coastal Ocean Circulation Models, *American Geophysical Union*, Washington, D.C., 4:1-16.

Casulli, V. (1999). A semi-implicit finite difference method for non-hydrostatic, free-surface flows, *International Journal for Numerical Methods in Fluids* 30, 425-440.

Casulli, V. (2009). A high-resolution wetting and drying algorithm for free-surface hydrodynamics, *Intl. Journal for Numerical Methods in Fluid Dynamics,* 60, 391-408.

Casulli, V., and R. T. Cheng. (1992). Semi-implicit finite difference methods for three-dimensional shallow water flow. *Int. J. Numer. Meth. Fluids*. 15: 629-648.

Casulli, V., and G. Stelling. (2011). Semi-implicit sub-grid modeling of three-dimensional free-surface flows, *Intl. Journal for Numerical Methods in Fluid Dynamics*, 67, 441-449.

Casulli, V., and R. A. Walters. (2000). An unstructured grid, three-dimensional model based on the shallow water equations, *International Journal for Numerical Methods in Fluids* 32, 331-348.

Casulli, V., and P. Zanolli. (1998). A three-dimensional semi-implicit algorithm for environmental flows on unstructured grids, Univ. of Oxford. *Methods for Fluid Dynamics* 57-70.

Casulli, V., and P. Zanolli. (2002). Semi-implicit numerical modeling of nonhydrostatic free-surface flows for environmental problem, *Mathematical and Computer Modelling* 36, 1131-1149.

Casulli, V., and P. Zanolli. (2005). High resolution methods for multidimensional advection-diffusion problems in free-surface hydrodynamics, *Ocean Modelling* 10, 137–151.

Casulli, V., and P. Zanolli. (2012). Iterative Solutions of Mildly Nonlinear Systems. *Journal of Computational and Applied Mathematics.* Elsevier, 2012.

Cho, K.-H. (2009). A numerical modeling study on barotropic and baroclinic responses of the Chesapeake Bay to hurricane events. Ph.D. Dissertation, Virginia Institute of Marine Science, College of William and Mary.

Cho, K.-H., H. V. Wang, J. Shen, A. Valle-Levinson, Y.-C. Teng. (2012). A modeling study on the response of Chesapeake Bay to hurricane events of Floyd and Isabel, *Ocean Modelling,* 49-50 22-46.

Christensen, B. A. (1972). Incipient Motion on Cohesionless Channel Banks. *Sedimentation* (ed. H. W. Shen). Fort Collins, CO.

Christensen, B. A., and R. Walton. (1980). Friction Factors in Storm Surges over Inland Areas. *Journal of Waterways and Harbor Division of ASCE*. ww2, pp. 261, May 1980.

Cobby, D. M., D. C. Mason, and, I. J. Davenport. (2001). Image processing of airborne scanning laser altimetry data for improved river flood modeling, *ISPRS Journal of Photogrammetry and Remote Sensing*, 56, 121-138.

Comblen, R., S. Legrand, E. Deleersnijder, and V. Legat. (2009). A finite element method for solving the shallow water equations on the sphere. *Ocean Modelling*, 28(1–3), 12-23.

Donelan, M. A., B. K. Haus, N. Reul, W. J. Plant, M. Stiassnie, H. C. Graber, O. B. Brown, and E. S. Saltzman. (2004). On the limiting aerodynamic roughness of the ocean in very strong winds. *Geophysical Research Letters*, Vol. 31, L18306.

Dyer, K. (1986). Coastal and Estuarine Sediment Dynamics. The Fluid Flow, Chapter 3. John Wiley & Sons.

ESRI (Environmental Systems Research Institute). (2012). Answering Emergency Management Information Needs. Winter 2012. http://www.esri.com/news/arcuser/0112/files/gisreadydata.pdf.

FEMA MOTF (Federal Emergency Management Agency Modeling Task Force). (2013). Hurricane Sandy Impact Analysis. http://184.72.33.183/GISData/MOTF/Hurricane%20Sandy/FEMA%20MOTF-Hurricane%20Sandy%20Products%20README%2004182013.pdf.

Flather, R.A., R. Proctor, and J. Wolf. (1991). Oceanographic forecast models. Computer Modeling in the Environmental Sciences. D. G. Famer and M. J. Rycroft (Eds.), Oxford. U.K., 15-30.

Gao, 2012. A Numerical Modeling Study of Storm Surge and Inundation in the
Chesapeake Bay during the November 2009 Mid-Atlantic Nor'easter. Master's
Thesis, Virginia Institute of Marine Science, College of William and Mary.

García, R., J. P. deCastro, E. Verdú, M. J. Verdú, and L. M. Regueras. (2012). Web Map
Tile Services for Spatial Data Infrastructures: Management and Optimization,
Cartography - A Tool for Spatial Analysis, Dr. Carlos Bateira (Ed.), ISBN: 978-
953-51-0689-0. http://www.intechopen.com/books/cartography-a-tool-for-spatial-
analysis/web-map-tile-services-for-spatial-data-infrastructures-management-and-
optimization.

Garratt, .J. R. (1977). Review of Drag Coefficients over Oceans and Continents. *Monthly
Weather Review*. 105: pg. 915-929.

Glahn, B., A. Taylor, N. Kurkowski, and W. Shaffer. (2009). The role of the SLOSH
model in national weather service storm surge forecasting. *National Weather
Digest*, 33(1):3-14.

Gleyzer, A., M. Denisyuk, A. Rimmer, and Y. Salingar. (2004). A fast recursive GIS
algorithm for computing Strahler stream order in braided and nonbraided
networks, *Journal of the American Water Resources Association* 40 (4): 937-946.

Gong, W., J. Shen, and W. G. Reay. (2007). The hydrodynamic response of the York
River estuary to Tropical Cyclone Isabel, 2003. *Estuarine, Coastal and Shelf
Science*, 73: 695-710.

Gong, W., J. Shen, K. H. Cho, and H. Wang. (2009). A numerical model study of barotropic subtidal water exchange between estuary and subestuaries (tributaries) in the Chesapeake Bay during northeaster events. *Ocean Modelling*, 26(3-4): 170-189.

Gutner, T. (2012). Hurricane Sandy Grows To Largest Atlantic Tropical Storm Ever. CBS News WBZ-TV Meteorology Update. October 28, 2012. http://boston.cbslocal.com/2012/10/28/hurricane-sandy-grows-to-largest-atlantic tropical-storm-ever/.

Harris, D.L. (1963). Characteristics of the Hurricane storm surge. Technical Paper No. 48, U. S. Weather Bureau.

Henderson, F. M. (1966). Open Channel Flow. *Flow Resistance*, Chapter 4. MacMillan Publishing Co. Series in Civil Engineering.

Horton, R. E. (1945). Erosional development of streams and their drainage basins: hydro-physical approach to quantitative morphology. *Geological Society of America Bulletin,* 56 (3): 275-370.

Jelesnianski, C.P., J. Chen, and W.A. Shaffer. (1992). SLOSH: sea, lake, and overland surges from hurricanes. National Weather Service, Silver Springs, MD.

Kohut, J. T., S. M. Glenn, and J. D. Paduan. (2006). Inner shelf response to Tropical Storm Floyd. *J. Geophys. Res.*, 111, C09S91.

Kökpinar, M. A. (2004). Flow over a stepped chute with and without macro-roughness elements. *Canadian Journal of Civil Engineering*. 31(5): 880-891.

Le Provost, C., F. Lyard, J. Molines, M. Genco, and F. Rabilloud. (1998). A hydrodynamic ocean tide model improved by assimilating a satellite altimeter-derived data set. *J. Geophys. Res.*, 103, 5513-5529.

Li, M., L. Zhong, W. C. Boicourt, S. Zhang, and D. L. Zhang. (2006). Hurricane-induced storm surges, currents and destratification in a semi-enclosed Bay. *Geophysical Research Letters*, 33, 29.

Loftis, J. D., and H. V. Wang. (2012). Simulation of Coastal Inundation Instigated via Storm Surge, River Discharge, and Precipitation in the Chesapeake Bay Using Sub-grid Modeling with Lidar-Derived Digital Elevation Models. Oceans 2012 Conference, (Conference Poster).

Loftis, J. D., H. Wang, and R. DeYoung. (2013). Storm Surge and Inundation Modeling in the Back River Watershed for NASA Langley Research Center. *NASA Technical Report*: NASA/TM-2013-218046.

Luettich, R. A., J. C. Muccino, and M. G. G. Foreman. (2002). Considerations in the calculation of vertical velocity in three-dimensional circulation models. *Journal of Atmospheric and Oceanic Technology*, 19, 2063-2076.

Luettich, R. (2011). NOAA IOOS Super Regional Storm Surge Testbed - presentation at the U.S. National Hurricane Center on 9/8/2011. Retrieved on April 11, 2012 http://testbed.sura.org/sites/default/files/NHC_talk_9_2011(1).pptx.

Manning, R. (1891). On the flow of water in open channels and pipes. *Transactions of the Institution of Civil Engineers of Ireland*, 20, 161-207.

Masters, J. (2011). Irene's 1-in-100 year rains trigger deadly flooding. *Weather Underground*. Retrieved September 14, 2011. http://www.wunderground.com/blog/JeffMasters/comment.html?entrynum=1908.

McCallum, B. E., S. M. Wicklein, R. G. Reiser, R. Busciolano, J. Morrison, R. J. Verdi, J. A. Painter, E. R. Frantz, and A. J. Gotvald. (2013). Monitoring Storm Tide and Flooding from Hurricane Sandy along the Atlantic Coast of the United States, Submitted October 2012. United States Geological Survey Hurricane Sandy Impact Report. http://pubs.usgs.gov/of/2013/1043/pdf/ofr2013-1043.pdf.

MTA (NYC Metropolitan Transit Authority). (2013). Flood Mitigation Work Begins at 7 Downtown Stations. MTA Bulletin on May 21, 2013. http://new.mta.info/news/2013/05/21/flood-mitigation-work-begins-7-downtown-stations.

New Jersey Shoreline. (2008). Statewide Digital Data Downloads - State of New Jersey. http://www.nj.gov/dep/gis/stateshp.html.

New York City Shoreline. (2012). NYC DOITT GIS Data: NYC Shoreline http://gis.nyc.gov/doitt/dl/gisdata/shp/SHORELINE.zip.

New York City Buildings. (2013). NYC DOITT GIS Data: NYC Building Heights and Footprints. http://gis.nyc.gov/doitt/dl/gisdata/shp/Building_footprints.zip.

Nitsche, M., D. Rickenmann, J. W. Kirchner, J. M. Turowski, and A. Badoux. (2012). Macroroughness and variations in reach-averaged flow resistance in steep mountain streams, *Water Resources Research.* 48, W12518.

NOAA NBDC (National Buoy Data Center). (2012). NBDC Buoy Map for Atmospheric and Oceanic Observations. http://www.ndbc.noaa.gov/.

NOAA NCDC (National Climatic Data Center). (2013). Atlantic Coast Wind Products. http://www.ncdc.noaa.gov/.

NOAA NGDC (National Geophysical Data Center). (1999). ETOPO1 Global Relief Model. http://www.ngdc.noaa.gov/mgg/global/.

NOAA NGDC (National Geophysical Data Center). (2011). 90m Integrated Models of Coastal Relief. http://www.ngdc.noaa.gov/mgg/coastal/grddas01/grddas01.htm. Mid. East Coast http://www.ngdc.noaa.gov/mgg/coastal/grddas02/grddas02.htm. South East Coast http://www.ngdc.noaa.gov/mgg/coastal/grddas03/grddas03.htm.

NOAA NOS (National Ocean Service), (2006). NOS Hydrographic Survey Data Viewer. Hydrographic survey digital database. NYC Surveys. National Oceanic and Atmospheric Administration. http://maps.ngdc.noaa.gov/viewers/nos_hydro/.

NOAA Service Assessment. (2012). Hurricane/Post-tropical cyclone Sandy, October 22-29, 2012. National Weather Service, NOAA, Silver Spring, Maryland.

NOAA Tides and Currents. (2012). Water Levels - Station Selection. http://tidesandcurrents.noaa.gov/stations.html?type=Water+Levels.

NWS (National Weather Service). (2009). November 11-13th, 2009 Nor'easter. National

    Oceanic and Atmospheric Administration. Retrieved October 14, 2010.

    http://www.erh.noaa.gov/er/akq/wx_events/other/November%2011-

    13th%20Noreaster.pdf.

Pawlowicz, R., B. Beardsley, and S. Lentz. (2002). Classical tidal harmonic analysis

    including error estimates in MATLAB using T_TIDE. *Computers Geosciences*.

    28, 929-937.

PBS NOVA. (2012). Inside the Megastorm. TV Documentary; Aired on: November 18,

    2012. http://video.pbs.org/video/2305482040/.

Post, Buckley, Schuh, and Jernigan. (2005). Hurricane Isabel Assessment, a Review of

    Hurricane Evacuation Study Products and Other Aspects of the National

    Hurricane Mitigation and Preparedness Program (NHMPP) in the Context of the

    Hurricane Isabel Response. *NOAA*. Retrieved 2006-11-27.

    http://www.csc.noaa.gov/hes/docs/postStorm/Isabel_PostStorm_Summary.pdf.

Powell, M. D., P. J. Vickery, T. A. Reinhold. (2003). Reduced drag coefficient for high

    wind speeds in tropical cyclones. *Nature*. 422: pg. 279-283.

Powell, M. D. (2006). Drag coefficient distribution and wind speed dependence in

    tropical cyclones. Final report to the NOAA *Joint Hurricane Testbed Program*,

    26 pages.

Reid, R. O. (1990). Water Level Changes: Handbook of Coastal and Ocean Engineering.

    Gulf Publishing, Houston, TX.

Romalewski, S. (2010). MTA subway data in GIS format. Retrieved on June 24, 2013.
http://spatialityblog.com/2010/07/08/mta-gis-data-update/.

Rugaber, C., and Wagner, D. (2011). Damage from Irene appears to be less than feared;
economy could benefit from rebuilding. *AP Economics Writers.* Retrieved August
28, 2011. http://finance.yahoo.com/news/Damage-from-Irene-appears-to-apf-
1228197775.html.

Shapiro, R. (1970). Smoothing, filtering, and boundary effects. *Rev. Geophys.*, 8(2):
359-387.

Shen, H. W. (1973). Flow Resistance over Short Simulated Vegetation and Various Tall
Simulated Vegetation Groupings on Flow Resistance and Sediment Yield.
Environmental Impact on Rivers, *River Mechanics* 3, Fort Collins, Colorado.

Shen, J., H. V. Wang, M. Sisson, and W. Gong. (2006). Storm tide simulation in the
Chesapeake Bay using an unstructured grid model. *Estuarine, Coastal and Shelf
Science*, 68, 1-16.

Shen, J., and W. Gong. (2009). Influence of model domain size, wind direction and
Ekman transport in storm surge development inside the Chesapeake Bay: A case
study if extratropical cyclone Ernesto, 2006. *Journal of Marine Systems* 75, 198-
215.

Shen, T. (2009). Development of a Storm Surge Model Using a High-Resolution
Unstructured Grid. MS Thesis, Virginia Institute of Marine Science, College of
William and Mary.

Smith, A. and R. Katz. (2013). U.S. billion-dollar weather and climate disasters: data sources, trends, accuracy and biases. *Natural Hazards*, 67(2): 387-410.

Stelling, G. and H. Kerncamp. (2010). Personal Communication.

Strahler, A. N. (1952). Hypsometric (area-altitude) analysis of erosional topology, *Geological Society of America Bulletin* 63 (11): 1117-1142.

Strahler, A. N. (1957). Quantitative analysis of watershed geomorphology, *Transactions of the American Geophysical Union* 8 (6): 913-920.

Teng, Y.-C. (2012). Developing an Unstructured Grid, Coupled Storm Surge, Wind Wave and Inundation Model for Super-regional Applications. Ph.D. Dissertation, Virginia Institute of Marine Science, College of William and Mary.

United States Census Bureau. (2012). New York (City) Population, New York. http://quickfacts.census.gov/qfd/states/36/3651000.html.

USDOE (United States Department of Energy). (2012). Hurricane Sandy Situation Report #18. USDOE Report from the Office of Electricity Delivery & Energy Reliability on November 6, 2012. http://www.oe.netl.doe.gov/docs/2012_SitRep18_Sandy_11062012_1000AM.pdf.

Vergano, D. (2012). U.S. Forecast's Late Arrival Stirs Weather Tempest. USA Today on October 30. 2012. http://www.webcitation.org/6BqwAWkIs.

Walsh, M. W. (2011). Irene Adds to a Bad Year for Insurance Industry. *New York Times*. http://www.nytimes.com/2011/08/29/business/irene-damage-may-hit-7-billion-

adding-to-insurer-woes.html?_r=2&scp=20&sq=hurricane%20irene%20new%20jersey&st=cse**.**

Wang, H. V., K. Cho, J. Shen, and Y. Wang. (2005). What has been learned about storm surge dynamics from Hurricane Isabel model simulations? Hurricane Isabel in Perspective Conference, Baltimore, MD., *Conference Proceedings, Chesapeake Bay Consortium*, 117-125.

Wang, H., J. D. Loftis, Z. Liu, D. Forrest, and J. Zhang. (2014). Storm Surge and Sub-Grid Inundation Modeling in New York City during Hurricane Sandy. *Journal of Marine Science Engineering*. (In Press).

Wang, S-Y. (1983). Friction in Hurricane Induced Flooding. Ph.D. Dissertation, University of Florida.

Wang, S-Y., and B. A. Christensen. (1986). Friction in Hurricane Induced Surges. *Coastal Engineering*. Chapter 62.

Westerink, J.J., R.A. Luettich, and J. Muccino. (1994). Modeling tides in the western North Atlantic using unstructured graded grids. *Tellus* 46A: 178-199.

Xu, H., K. Zhang, J. Shen, and Y. Li, (2010). Storm surge simulation along the U.S. East and Gulf Coasts using a multi-scale numerical model approach. *Ocean Dynamics* DOI: 10.1007/s1023601003213.

Zeng, X., M. Zhao, and R. E. Dickinson. (1998). Inter-comparison of Bulk Aerodynamic

    Algorithms for the Computation of Sea Surface Fluxes Using TOGA COARE and

    TAO Data. *Journal of Climate*, 11(10): 2628-2644.

Zhang, K., C. Xiao, and J. Shen. (2008). Comparison of the CEST and SLOSH models

    for storm surge flooding. *Journal of Coastal Research,* 24(2): 489-499.

Zhang, Y. L., A. M. Baptista, and E. P. Myers. (2004). A cross-scale model for 3D

    baroclinic circulation in estuary–plume–shelf systems: I. Formulation and skill

    assessment. *Cont. Shelf Res.* 24, 2187-2214.

Zhang, Y.-L., and A. M. Baptista. (2008). SELFE: A semi-implicit Eulerian-Lagrangian

    finite-element model for cross-scale ocean circulation, *Ocean Modeling*, 21(3-4),

    71-96.

VITA

Jon Derek Loftis

Born on March 20, 1985, in Montgomery, Alabama, USA. Conferred a Bachelor of Science degree in Biology with undergraduate minors in Chemistry and Leadership Studies from Christopher Newport University in 2007. Earned a Master of Science degree in Environmental Science from Christopher Newport University in 2009. Matriculated into the Ph.D. program of the College of William & Mary, School of Marine Science at the Virginia Institute of Marine Science in the Fall of 2009. Co-authored titular portions of his dissertation research in two publications with his Ph.D. adviser prior to graduation: (1) "Storm Surge and Sub-Grid Inundation Modeling in New York City during Hurricane Sandy," published in the Journal of Marine Science and Engineering in March 2014, and (2) a NASA Technical Report #2013-218046 titled, "Storm Surge and Inundation Modeling in the Back River Watershed for NASA Langley Research Center," published in October 2013.